Universitat Autònoma de Barcelona

# Transcriptomic Analysis of White and Brown Adipose Tissue During Non-Shivering thermogenesis

**JORDI RODÓ MORERA**

Universitat Autònoma de Barcelona

DEPARTMENT OF BIOCHEMISTRY AND MOLECULAR BIOLOGY
SCHOOL OF VETERINARY MEDICINE

CENTER OF ANIMAL BIOTECHNOLOGY AND GENE THERAPY

# Transcriptomic Analysis of White and Brown Adipose Tissue During Non-Shivering thermogenesis

JORDI RODÓ MORERA

This PhD thesis has been carried out under the direction of Dr. Fàtima Bosch Tubert and Dr. Verónica Jiménez Cenzano at the Biochemistry and Molecular Biology Department of the Veterinary School of Medicine and at the Center of Animal Biotechnology and Gene Therapy (CBATEG).

**JORDI RODÓ MORERA**

**FÀTIMA BOSCH TUBERT** **VERÓNICA JIMÉNEZ CENZANO**

**June 2019**

**BELLATERRA**

*A totes les persones que han cregut en mi.*

Les coses importants són les
que no ho semblen - Mercé Rodoreda

En primer lloc, volia agrair a la *Dra. Fàtima Bosch* la oportunitat d'haver-me deixat dur a terme aquesta tesis així com el màster sota la seva supervisió. L'estada en el teu grup d'investigació sota unes condicions i un ambient excepcionals m'ha permès créixer com a investigador i formar-me molt polivalentment. Moltes gràcies per la transmetre tant entusiasme i energia per seguir avançant dia rere dia.

Igualment m'agradaria agrair tot el suport rebut per part de la *Dra. Verónica Jiménez*, la meva co-directora de tesis. Moltes gràcies per haver-me ensenyat des de com treballar al laboratori fins a com escriure justificacions de beques. Volia agrair-te especialment la paciència i capacitat de treball admirable que m'han permès arribar a dipositar aquesta tesi.

Finalment mencionar l'ajuda, suport i ensenyança del *Dr. Miquel Garcia*. Saps tant bé com jo que sense aquestes ensenyances que dia rere dia has anat impartint no estaríem aquí. Gràcies per haver-me permès fer-me pesat amb preguntes a vegades obvies, per haver tingut la paciència de buscar nous enfocaments al treball i per haver-me ensenyat una mica més que no cal saber codi per fer alguns anàlisis bioinformàtics sinó molta paciència per treballar amb JAVA.

Aquesta tesis ha estat possible gràcies a les beca predoctoral "Ayudas para contratos predoctorales para la formació de doctores, 2015 (SAF2014-54866-R)" finançada pel "Ministerio de Economia y Competitividad" (MINECO), de la qual he estat beneficiari durant gairebé tres anys (BES-2015-075799). Les investigacions s'han dut a terme gràcies a la financiación rebuda del "Ministerio de Economia y Competitividad" (MINECO) (SAF2014-54866-R), del "Ministerio de Ciencia, Innovación y Universidades" (SAF2017-86266-R), y FEDER, Plan Nacional I+D+I (SAF2014-54866-R), de la Generalitat de Catalunya (2014 SGR 1669, 2017 SGR 01508) i de la European Foundation for the Study of Diabetes (EFSD/MSD European Research Programme on Novel Therapies for Type 2 Diabetes, 2013).

| | |
|---|---|
| **%** | *Percentage* |
| **µL** | *Microlitre* |
| **µm** | *Micrometre* |
| **1,3-BPG** | *1,3-Bisphosphoglycerate* |
| **AAV** | *Adeno-associated viruses* |
| **ADP** | *Adenosine diphosphate* |
| **AIDS** | *Acquired immune deficiency syndrome* |
| **AMS** | *Amsterdam* |
| **ANOVA** | *Analysis of variance* |
| **APE 1** | *Apurinic/apyrimidinic endonuclease 1* |
| **ATP** | *Adenosine triphosphate* |
| **AU** | *Arbitrary Units* |
| **BAT** | *Brown adipose tissue* |
| **BCAA** | *Branched-chain amino acids* |
| **BMI** | *Body mass index* |
| **bp** | *Base pair* |
| **ºC** | *Degree Celsius* |
| ***CA*** | *California* |
| **CAG** | *Promoter of β-actin of chicken and enhancer of the cytomegalovirus* |
| **Cambs** | *Cambridgeshire* |
| **CAT** | *Catalunya* |
| **CBATEG** | *Center of Animal Biotechnology and Gene Therapy* |
| **cDNA** | *Complementary DNA* |
| **CH** | *Switzerland* |
| **$CO_2$** | *Carbon dioxide* |
| **CoA** | *Coenzyme A* |
| **cRNA** | *Complementary RNA* |
| **DE** | *Germany* |
| **DEG** | *Differentially expressed gene/genes* |
| **DHAP** | *Dihydroxyacetone phosphate* |
| **DMEM** | *Dulbecco's modified Eagle's medium* |
| **dmiRT** | *Target sequence of microRNA 1 and microRNA 122a.* |
| **DNA** | *Deoxyribonucleic acid* |
| **dsDNA** | *Double-stranded DNA* |
| **DT2** | *Diabetes tipus 2* |

| | |
|---|---|
| **dTTP** | *2'-deoxythymidine 5'-triphosphate* |
| **dUTP** | *2´-deoxyuridine, 5´-triphosphate* |
| **E.coli** | *Escherichia coli* |
| **ES** | *Spain* |
| **ETF** | *Eletron-transferring flavoprotein* |
| **eWAT** | *Epididymal white adipose tissue* |
| **F-1,6P2** | *Fructose-1,6-bisphosphate* |
| **F-6P** | *Fructose-6-phosphate* |
| **FA** | *Fatty acid/s* |
| **FAD** | *Flavin adenine dinucleotide/s* |
| **$FADH_2$** | *Reduced flavin adenine dinucleotide/s* |
| **FBS** | *Fetal Bovine Serum* |
| **FDA** | *Food and Drug Administration* |
| **FFA** | *Free fatty acid/s* |
| **g** | *Grams* |
| ***g*** | *G-Force* |
| **G-6P** | *Glucose-6-phosphate* |
| **GAP** | *Glyceraldehyde 3-phosphate* |
| **GO** | *Gene ontology* |
| **h** | *Hours* |
| **HE** | *Hessen* |
| **HEK293** | *Human embryonic kidney 293* |
| **HFD** | *High-fat diet* |
| **HH** | *Hamburg* |
| **HIF-1α** | *Hypoxia-inducible factor-1α* |
| **HSL** | *Hormone-sensitive lipase* |
| **iBAT** | *Interscapular brown adipose tissue* |
| **IL** | *Illinois* |
| **IL1β** | *Interleukin 1β* |
| **IL6** | *Interleukin 6* |
| **IMDM** | *Iscove's Modified Dulbecco's Medium* |
| **ITR** | *Inverted terminal repeat* |
| **IV** | *Intravenous* |
| **iWAT** | *Inguinal white adipose tissue* |
| **JP** | *Japan* |

| | |
|---|---|
| **Kb** | *Kilobase* |
| **Kcal** | *Kilocalorie* |
| **LB** | *Lysogeny broth* |
| **LDH** | *Lactate dehydrogenase* |
| ***MA*** | *Massachusetts* |
| **MAD** | *Madrid* |
| **MCT1** | *Monocarboxylate transporter 1* |
| **mg** | *Milligrams* |
| **miR** | *microRNA* |
| **miRNA** | *microRNA* |
| **miRT** | *Target sequences of miRNA* |
| **mM** | *Millimolar* |
| **MODY** | *Maturity-onset diabetes* |
| **$NAD^+$** | *Oxidized Nicotinamide adenine dinucleotide* |
| **NADH** | *Reduce Nicotinamide adenine dinucleotide* |
| **NAFLD** | *Non-alcoholic fatty liver disease* |
| **NL** | *The Netherlands* |
| **nM** | *Nanomolar* |
| **nm** | *Nanometer* |
| **NW** | *North Rhine-Westphalia* |
| **ORF** | *Open reading frame* |
| **pA** | *Polyadenylation signal* |
| **PC** | *Principal components* |
| **PCA** | *Principal component analysis* |
| **PDH** | *Pyruvate dehydrogenase* |
| **PDK** | *Pyruvate dehydrogenase kinase* |
| **PDP** | *Pyruvate dehydrogenase phosphatase* |
| **PEG** | *Polyethylene glycol* |
| **PEP** | *Phosphoenolpyruvate* |
| **PGC-1α** | *Peroxisome proliferator-activated receptor γ coactivator 1α* |
| **PKA** | *Protein kinase A* |
| **PM** | *Perfect match* |
| **PTM** | *Pavlidis template matching* |
| **rAAV** | *Recombinant Adeno-Associated Virus* |
| **RB** | *Roller Bottle/s* |

| | |
|---|---|
| **RBP4** | *Retinol binding protein 4* |
| **RMA** | *Robust multichip average* |
| **RP** | *Rhineland-Palatinate* |
| **RT** | *Room temperature* |
| **RT-PCR** | *Real-Time PCR* |
| **s** | *Seconds* |
| **SAPE** | *Streptavidin-phycoerythrin conjugate* |
| **scAAV** | *Self-complementary AAV vectors* |
| **SNS** | *Sympathetic nervous system* |
| **ssDNA** | *Single-stranded DNA* |
| **SVF** | *Stromal vascular fraction* |
| **T1D** | *Type 1 diabetes* |
| **T2D** | *Type 2 diabetes* |
| **TCA** | *Tricarboxylic acid cycle* |
| **TdT** | *Terminal deoxynucleotidyl transferase* |
| **TG** | *Triglycerides* |
| **TNFα** | *Tumor necrosis factor α* |
| **TYO** | *Tokio* |
| **U** | *Unit of enzymatic activity* |
| **UAB** | *Universitat Autònoma de Barcelona* |
| **UCP1** | *Uncoupling protein 1* |
| **UDG** | *Uracil-DNA glycosylase* |
| **UK** | *United Kingdom* |
| **USA** | *United States of America* |
| **UTR** | *Untranslated region* |
| **UV** | *Ultraviolet* |
| **V** | *Volts* |
| **VA** | *València* |
| **VEGF-A** | *Vascular endothelial growth factor A* |
| **VG** | *Viral genome* |
| **VT** | *Vermont* |
| **WAT** | *White adipose tissue* |
| **WCRF** | *World cancer research fund* |
| **WHO** | *World Health Organization* |
| **WI** | *Wisconsin* |

# I. PRESENTATION

Obesity and type 2 diabetes (T2D) are two closely related diseases that represent a serious health, social and economic problem due to their high prevalence worldwide. Both diseases are also associated with other pathologies that present high mortality. The currently available therapies are not entirely effective and do not suit for all patients in the heterogeneous obese/T2D population. Moreover, existing pharmacological treatments are often associated with important side effects. Thus, the development of new therapeutic strategies for obesity and T2D is crucial.

In the last decades, adipose tissue has been defined not only as a connective tissue but as an organ that plays a central role in the control of energy balance. Furthermore, the proved endocrine and thermogenic functions of adipocytes has renewed interest in the study of this tissue. Non-shivering thermogenesis is based on the generation of heat by means of the uncoupling protein 1. This process has been described as occurring in brown adipose tissue of mice, but recent studies have demonstrated that under certain stimuli, such as prolonged cold exposure, brown fat-like cells (beige adipocytes), appear in some white adipose tissue depots of rodents, and increase energy consumption through non-shivering thermogenesis. This process is known as browning of white adipose tissue. Moreover, the detection of cold-induced BAT in human adults resulted in numerous studies confirming the contribution of BAT to non-shivering thermogenesis and oxidative metabolism in humans. The activation of non-shivering thermogenesis in humans through cold-exposure increases resting energy expenditure, whole-body glucose disposal, insulin sensitivity, and ameliorates glucose metabolism independently of BMI. Thus, the development of new therapeutic strategies aiming to increase metabolic rate such as enhancement of non-shivering thermogenesis via activation of BAT or browning of white adipose tissue (WAT) may hold great potential for the future treatment of obesity and T2D. However, more gene expression studies to gain insight into the molecular mechanisms underlying the cold-induced enhancement of non-shivering thermogenesis, as well as to determine differences between BAT activation and browning of WAT, are needed.

In this study, the transcriptomic response of epididymal and inguinal white adipose depots (eWAT and iWAT, respectively) as well as that of the interscapular brown adipose depot (iBAT) of mice either exposed to 22ºC or 4ºC for the period of 4 days were examined.

Cold exposure increased the metabolic and thermogenic activity of iWAT. In this depot, genes related to glycolysis, tricarboxylic acid cycle, lipolysis, and the degradation of some amino acids presented a high upregulation to maintain the protonmotive power to generate heat. Moreover, the expression of thermogenic-related genes was also highly increased, demonstrating a cold-induced browning of iWAT. The eWAT depot has been reported to be resilient to browning. Thus, the observed metabolic activation of this depot was mild in comparison with that of iWAT, and no relevant enhancement of non-shivering thermogenesis was observed in this depot. Finally, iBAT already presented high expression levels of thermogenic genes because mice were not housed at thermoneutrality.

The detailed study of adipose tissue depots response to cold exposure allowed the detection of different coordinated levels of thermogenic and metabolic induction. The observation that genes related to thermogenesis and metabolism presented a similar expression pattern among samples endorsed the utilization of *pattern matching analysis tools* to unravel *Atp4b* and *1700040L02Rik* as novel genes potentially involved in thermogenesis.

The overexpression of *Atp4b* and *1700040L02Rik* in adipose tissue by means of AAV vectors produced a body weight gain reduction, decreased eWAT, and liver weight, amelioration of white adipocytes hypertrophy, and reduced hepatic steatosis potentially as a result of the detected enhanced thermogenesis in iWAT. Overall, these results indicate a new potential anti-obesogenic role for these genes.

In conclusion, the results from this thesis contributed to a better understanding of the induction of non-shivering thermogenesis in adipose tissue depots in mice. Among the different adipose depots, exploratory data analysis of the gene expression levels of mice exposed from 22ºC to 4ºC determined that iWAT was the depot that responded most significantly to cold exposure. Moreover, as observed in the pathway enrichment and gene ontology analysis, this response was highly coordinated, presenting a high number of genes related to metabolic pathways highly affected. The detailed study of the metabolic pathways led to the detection of a high induction of non-shivering thermogenesis, revealing that both energy production and energy consumption mechanisms were highly synchronized. This in detail study of the adipose tissue also allowed the identification of novel genes potentially involved in non-shivering thermogenesis.

# II. INTRODUCTION

# 1. ADIPOSE TISSUE

The adipose tissue is an organ anatomically disperse composed of multiple discrete areas (fat pads) (Gesta et al., 2007). This tissue contributes to essential functions such as thermogenesis, nutritional homeostasis, energy balance, immune response, and lactation (Cinti, 2012). Furthermore, other functions like organ protection or cushion from mechanical injury have been described (Cinti, 2012; Pond, 1992).

Initially, in the 1940s, adipose tissue was perceived as a connective tissue that contained lipid droplets. Gradually a link with metabolism and nutrient homeostasis was realized. During the 1990s, the discovery of several molecules like TNF-α, leptin or adipsin proved the endocrine function of this organ, showing its central role in the control of the energy homeostasis. From this point forward, the interest in the study of this tissue has renewed in parallel with the alarming increase in obesity incidence.

## 1.1. Adipose tissue components

Although adipocytes can account for more than 90% of fat pad volume, they only account for 20% of the cellular content of the fat pad (Eto et al., 2009). These cells are surrounded, besides the matrix of extracellular proteins, by nerves, lymphatic nodes, small blood vessels and stromal vascular fraction (SVF). SVF comprises multiple cell types, among which: immune system cells, endothelial cells, preadipocytes and fibroblasts (Armani et al., 2010; Cawthorn et al., 2012). Mature adipocytes can be classified in three different types: white adipocytes (Figure 1A), brown adipocytes (Figure 1B) and the more recently described beige adipocytes (Figure 1C) (Petrovic et al., 2010; Wu et al., 2012). These adipocytes are located in two different types of adipose tissue. The brown adipose tissue (BAT) is mainly composed of brown adipocytes, while the white adipose tissue (WAT) can be composed of both, white and beige adipocytes.

## 1.2. Types of adipocytes

### *1.2.1. White adipocytes*

White adipocytes are usually spherical cells characterized by containing low mitochondria content and a unilocular lipid droplet which, as it can occupy more than 90% of the intracellular space, displaces the nucleus at the periphery of the adipocyte (Figure 1A).

The big unilocular lipid droplet maximizes storage capacity in the minimal space of the cell (Figure 1A) (Smorlesi et al., 2012). The diameter of white adipocytes varies between gender, age, and diets. In mice, white adipocytes' diameter ranges from a minimum 10-20 µm to a maximum of 70-80 µm. In the case of humans, this diameter is about 30% larger (Cinti, 2018; Hagberg et al., 2018).

White adipocytes are highly specialized cells in which their main function is the energy storage in the form of free fatty acids (FFA) and triglycerides (TG). In response to metabolic demands of other tissues in situations of energy deficit such as fasting, this adipocyte type can also release FFA and glycerol (Algire et al., 2013; Gesta et al., 2007; Koppen and Kalkhoven, 2010). The release of FFA serves as fuel for other tissues, influencing the regulation of glucose metabolism (Ahmadian et al., 2010).

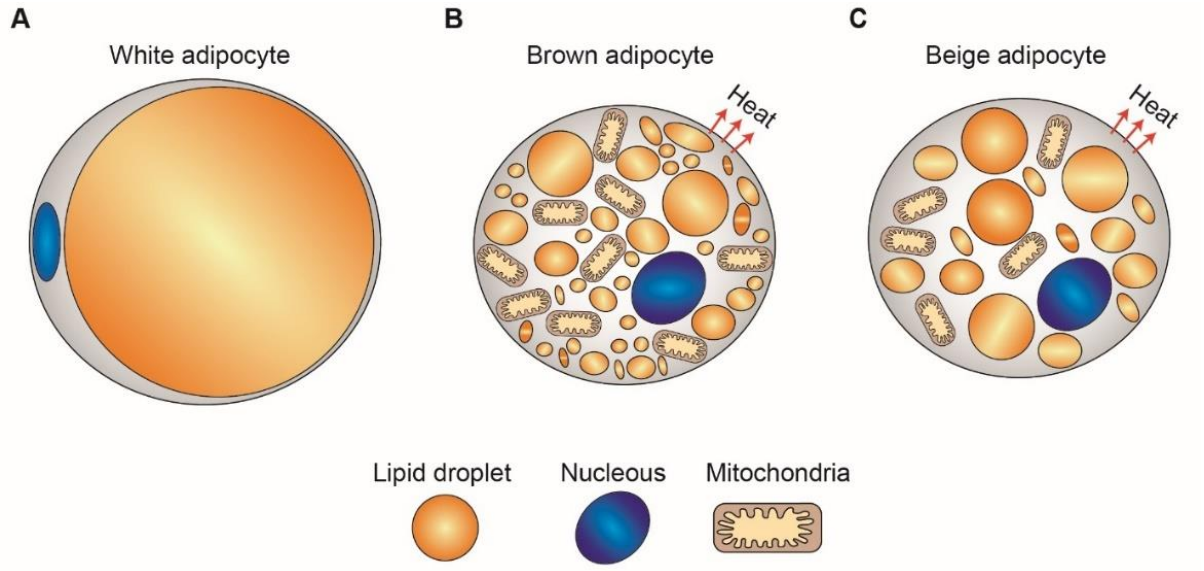


***Figure 1. Types of adipocytes.*** Three different types of adipocytes can be morphologically differentiated due to the number of lipid droplets and mitochondria content. **(A)** White adipocytes contain a unique big lipid droplet and a low number of mitochondria, **(B)** brown adipocytes contain a high number of small lipid droplets and mitochondria content, and **(C)** beige adipocytes contain several lipid droplets and more mitochondria than white adipocytes. Differences in gene expression, function, and lineage origin have been also reported among adipocytes.

White adipocytes are also characterized by its high secretory capacity. These cells can secrete a wide variety of proteins named adipokines, which mediate biological processes via endocrine, paracrine and autocrine manner in several target tissues, such as brain, liver, muscle, pancreas, heart, spleen or lymph nodes. These secreted molecules participate directly in the control of satiety, appetite, the regulation of glucose tolerance,

fat storage, sensitivity to insulin, angiogenesis, cell growth, or inflammation. Concurrently, the pathogenesis of insulin resistance among other diseases has been described to be impacted by variations in the adipokines' gene sequence or by alterations in its secretion (Arner et al., 2018; Booth et al., 2016; de Luis et al., 2018).

### *1.2.2. Brown adipocytes*

Brown adipocytes are typically polygonal with a nucleus eccentrically located but not in the periphery of the cell (Figure 1B). Its diameter is highly variable, ranging from 12 to 50 µm (Cinti, 2009; Gonçalves et al., 2017). This cell type is characterized by containing multilocular lipid droplets and a high number of mitochondria (Figure 1B). These cells are highly specialized in generating heat via non-shivering thermogenesis (Figure 1B) (Cinti, 2018).

The generation of heat is achieved in this cell type by means of the uncoupling protein 1 (UCP1). Usually, mitochondria consume a low rate of oxygen when ADP is absent, but when ADP is present, oxygen consumption strongly increases. Once ADP has been converted to ATP, the respiration rate returns to the initial low rate. ATP is produced in the respiratory chain by the complex V, an ATP synthase. Complex V is located in the inner membrane of the mitochondria and drives the flux of protons from the intermembrane space to the mitochondria matrix through all its transmembrane complexes, generating ATP from ADP + $P_i$. The proton gradient is maintained by the proton pumps of the respiratory chain, which use the electrons obtained in the tricarboxylic acid (TCA) or the β-oxidation as energy source. These electrons will then be converted by a reaction with oxygen to water (Figure 2).

However, isolated mitochondria of brown adipocytes always respire at their maximum rate with a demonstrated lack of regular control over respiration (Calderon-Dominguez et al., 2017; Smith et al., 1966). As in these cells protons re-enter the matrix not only through ATP synthase but also through UCP1, the proton gradient is also released as heat. This uncoupling of the reaction forces the rest of the respiratory chain to restore the proton gradient and so consuming oxygen (Figure 2).

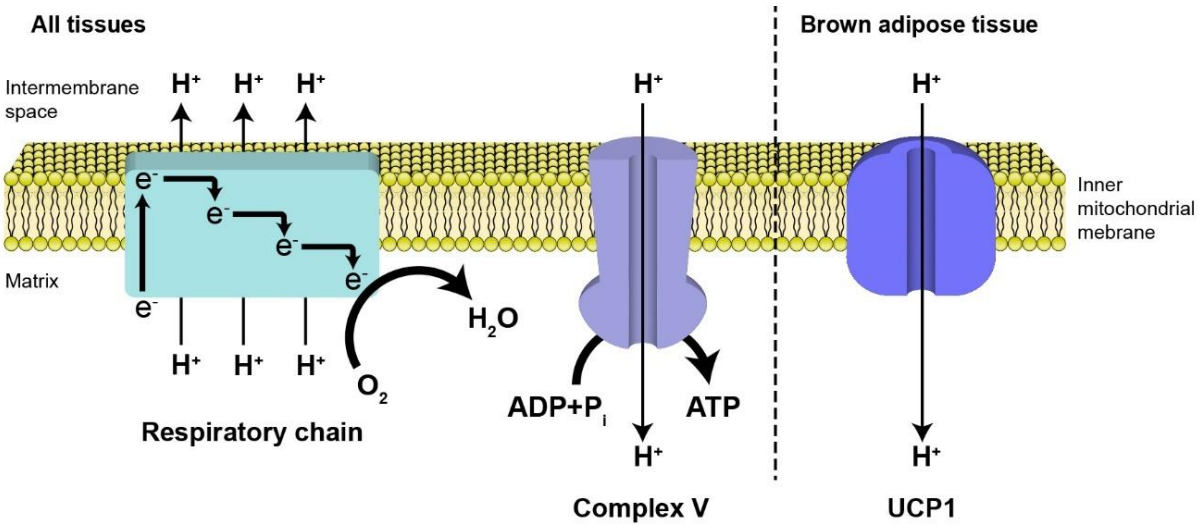


***Figure 2. Respiratory chain and UCP1.*** Scheme illustrating the uncoupling of the respiratory chain in BAT. The translocation of protons from the matrix to the intermembrane space of the mitochondria generates a proton gradient used to generate ATP. In BAT, UCP1 leaks the proton gradient generating energy in form of heat.

### *1.2.3. Beige adipocytes*

Recently, it has been described that under some stimuli, such as prolonged cold exposure or adrenergic stimulation, some clusters of UCP1$^+$ cells with brown fat-like morphology appear within white fat depots (Figure 1C). These cells have been called "brite" or "beige" adipocytes. Beige adipocytes presence varies intensely between depots, being especially this cells expecially numerous in iWAT and retroperitoneal fat (Xue et al., 2007). In basal conditions, beige cells present a white adipocyte-like phenotype, including a large lipid droplet. Under cold exposure or adrenergic signaling, this cell type is transformed into cells presenting BAT-like characteristics, such as UCP1 expression or multilocular lipid droplets (Park, 2014) (Figure 1C).

When comparing mouse brown and beige adipocytes, it has been reported that before thermogenic stimulation brown fat cells have elevated uncoupled respiration and higher basal *Ucp1* expression. Conversely, beige cells have low uncoupled respiration and basal *Ucp1* expression, similar to white fat cells. Nevertheless, cold exposure or β-adrenergic stimulation increases *Ucp1* expression in beige cells to similar levels than those of brown adipocytes (Figure 1C). These results suggest that beige fat cells could be bifunctional, being able to store energy and to turn on heat production under appropriated signals (Wu et al., 2012).

Gene expression pattern of these cells presents remarkably similitudes with brown adipocytes, despite having clear differences. Several mitochondrial and thermogenic genes are expressed in both types of adipocytes, including *Ucp1* (Wu et al., 2012). The appearance of beige adipocytes in WAT is denominated "browning". Nowadays the similarities between rodent brown and beige adipocytes in comparison with $UCP1^+$ positive cells in humans are being studied.

## 1.3. White adipose tissue

White adipose tissue (WAT) is mainly composed of white adipocytes, and some depots also present beige adipocytes. The primary purpose of WAT is to store excess energy in the form of TG for future use. To this end, the expression of specific enzymes during white adipocyte differentiation enables both the accumulation and mobilization of fat (Farmer, 2006; Rosen and Spiegelman, 2000). Fat accumulation is achieved by FA uptake and lipogenesis (*de novo* synthesis of FA), while lipolysis accomplishes fat mobilization. Both processes are well regulated by hormones like catecholamines (Arner, 1999) or insulin (Chakrabarti et al., 2013).

### *1.3.1. Location of white adipose tissue*

WAT can be divided into two subgroups depending on the location of the depots: subcutaneous or intra-abdominal/visceral. This simple distinction is still being referred today due to the different effects of this depot's location on metabolism.

#### *1.3.1.1. Subcutaneous adipose tissue*

The subcutaneous adipose tissue is located beneath the dermis. It is mainly composed of two depots, one located in an anterior and the other on the posterior position (Cinti, 2005). The anterior depot is located suprascapular (Figure 3A), embedding the scapular BAT, while the posterior depot, named inguinal white adipose tissue (iWAT) is located around the hind legs (Cinti, 2005; Zhang et al., 2018) (Figure 3A). In humans, subcutaneous adipose tissue does not localize equally than in mice, as it is localized abdominally, intramuscularly, and gluteofemorally (Chusyd et al., 2016) (Figure 3B). One specific characteristic of the WAT subcutaneous depots is the presence of $Ucp1^+$ cells, the aforementioned beige cells (Figure 1C).

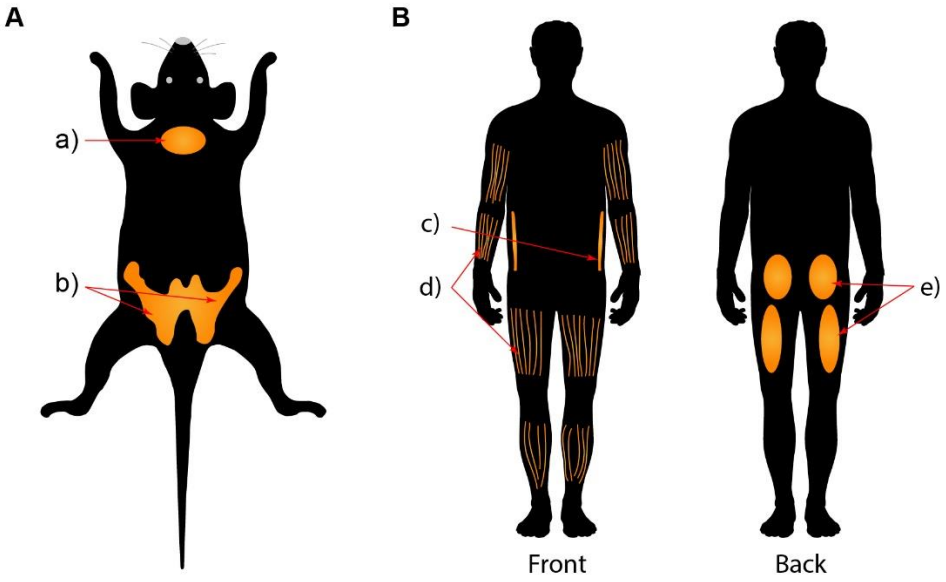


***Figure 3. Location of the subcutaneous white adipose tissue in mice and humans.*** Scheme illustrating the subcutaneous white adipose tissue depots in **(A)** mice; a) suprascapular, b) inguinal, and in **(B)** humans; c) abdominal, d) intramuscular, e) gluteofemoral.

#### *1.3.1.2. Visceral adipose tissue*

The visceral adipose tissue is located in the thoracic and abdominal cavities. Although some depots do not localize equally between humans and mice, the vast majority are shared between both species.

Two adipose depots have been described in the thoracic cavity: epicardial and mediastinal. Epicardial WAT develops in different zones around the heart (Iacobellis et al., 2005), and can be clearly found in humans but hardly in mice (Marchington et al., 1989) (Figure 4B). The mediastinal adipose tissue is found in both humans and mice, in the posterior and superior mediastinum (Figure 4A and B).

Around the digestive system two main depots can be found: mesenteric and omental. The mesenteric adipose tissue is present in both species and is located in the connective tissue of the intestine (Figure 4A and B). In mice, the pancreas is surrounded by the mesenteric adipose tissue and the intestines. The omental adipose tissue is hardly detectable in mice but in humans can be substantial (Figure 4B). Two other adipose tissues depots are present intra-abdominally in both humans and mice, the retroperitoneal and the perirenal adipose tissue. The retroperitoneal adipose tissue is located in the paravertebral position and the perirenal around the kidney (Figure 4A and B). Finally, there is another adipose

tissue depot only present in mice surrounding the reproductive organs, called perigonadal adipose tissue. In females, this depot is divided between the periovarian depot, which surrounds the ovaries and the parametrial depot, which surrounds the bladder, and uterus, (Figure 4A and B). In males, as this tissue surrounds the epididymis, is named epididymal white adipose tissue (eWAT) (Figure 4A and B).

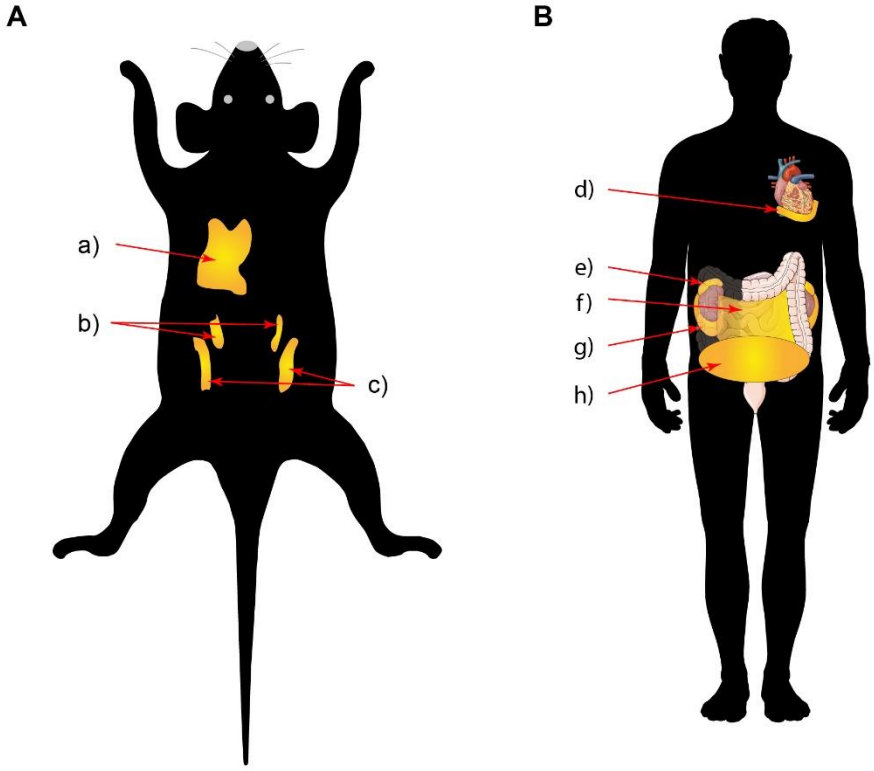


***Figure 4. Location of the visceral white adipose tissue in mice and humans.*** Scheme illustrating the visceral depots of white adipose tissue in **(A)** mice; a) mesenteric, b) retroperitoneal, c) gonadal (periovarian / parametrial / epidydimal), and in **(B)** humans; d) epicardial, e) perirenal, f) mesenteric, g) retroperitoneal, and h) omental.

## 1.4. Brown adipose tissue

Brown adipose tissue (BAT) is composed basically of brown adipocytes. The main function of BAT is to dissipate energy in the form of heat. This function is driven by the presence of the uncoupling protein 1 (UCP1), which uncouples mitochondrial respiration. This process has been described to be important for heat production in newborns, essential for rodents and for hibernating animals (Ballinger and Andrews, 2018; Enerbäck et al., 1997; Lidell, 2019; Lowell et al., 1993). Furthermore, diet-induced thermogenesis in BAT can burn excess of dietary energy consumption (Ho, 2018).

### *1.4.1. Location of brown adipose tissue*

Brown adipose tissue can be found in different locations in mice and in humans. In both species, BAT depots are located mainly in the anterior part (Figure 5). The depots located in the interscapular, infrascapular, ventral spinal, and axillary regions are subcutaneous (Figure 5A). Intrathoracic depots are found around blood vessels, heart, trachea, esophagus, and aorta. Finally, BAT can also be located intraperitoneally, mainly around adrenals and kidneys. In humans, especially in newborns, the distribution of the BAT depots is similar (Figure 5B and C). In newborn humans, BAT has been described to be metabolically active at birth in large interscapular and perirenal BAT depots (Figure 5C) (Lidell, 2019). However, adult humans present an atrophied BAT, with a functional declined of mitochondria and reduced UCP1 activation (Valle et al., 2008).

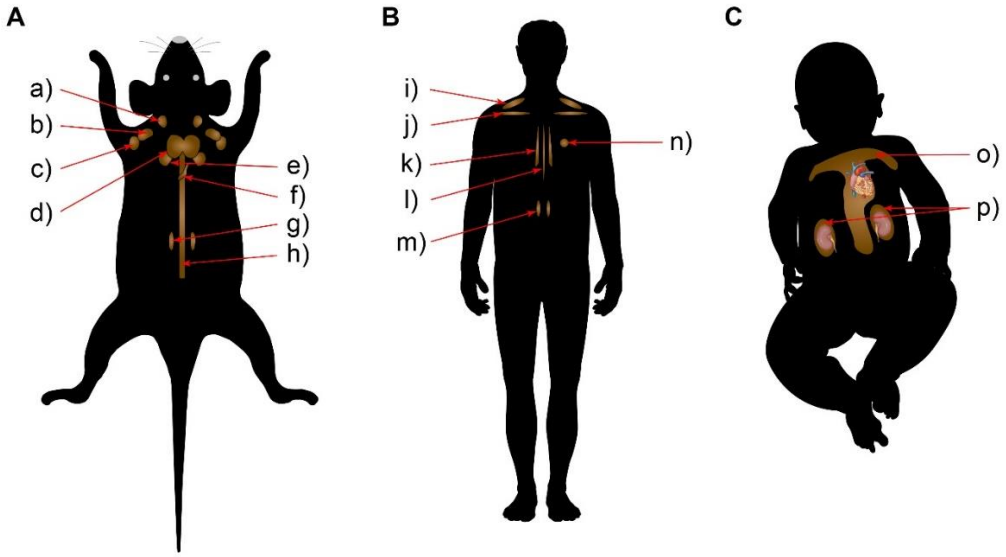


***Figure 5. Location of brown adipose tissue in mice and humans.*** Scheme illustrating the location of the main brown adipose tissue depots in **(A)** mice; a) cervical, b) supraclavicular, c) axillary, d) interscapular, e) infrascapular, f) mediastinal, g) perirenal, h) ventral spinal, in **(B)** adult humans; i) cervical, j) supraclavicular, k) paraspinal, l) mediastinal, m) perirenal, n) paraaortic and pericardic, and in **(C)** newborns: o) interscapular, p) perirenal.

Interscapular brown fat of human infants reassembles rodent classical brown fat (Lidell et al., 2013). However in human adults an increasing brown:beige ratio of cells increases when moving deeper from neck to back (Cypess et al., 2013; Jespersen et al., 2013; Lidell et al., 2013; Sharp et al., 2012; Wu et al., 2012). Furthermore, it has been reported that human BAT shares many histological, functional and molecular characteristics with mice cold-induce beige fat, as the beige cells selective markers TMEM26, CD137, and TBX1 are also expressed in human BAT (Sharp et al., 2012; Wu et al., 2012). One characteristic of all BAT depots is the high vascularization to guarantee enough oxygen supply and metabolites (Hodson, 2014; Shimizu et al., 2014).

## 2. DIABETES MELLITUS

Diabetes Mellitus is a metabolic disease characterized by elevated levels of blood glucose resulting from the body defects of insulin secretion, insulin action or both, leading to the inability to use circulating glucose for energy (American Diabetes Association, 2019c; World Health Organization, 2016). The chronic hyperglycemia leads to several organs' dysfunction and failure over time causing a variety of complications such as nephropathy, retinopathy or cardiovascular disease (Cowie et al., 2017a; Gregg et al., 2016).

Nowadays, diabetes is a major public health problem worldwide, as it has reached epidemic proportions; 425 million people, or 8.8% of adults aged 20-79 years, are afflicted (International Diabetes Federation, 2017). If this trend continues, by 2045 approximately 629 million people aged 20-79 years will have diabetes (International Diabetes Federation, 2017). The World Health Organization considers diabetes as the eighth cause of mortality in both sexes and the fifth in women, being 1.6 times higher in women compared to men despite prevalence in adult men of 20-79 years of age is higher than in women (9.1% in man vs. 8.4% in women) ( International Diabetes Federation, 2017; World Health Organization, 2016). Also, on average, diabetic patients have medical expenditures approximately two-fold higher than healthy people, being spent only in Europe 142.710.993 billion euros as healthcare expenditures (International Diabetes Federation, 2017).

Diabetes is classified by the underlying cause. The majority of diabetic patients can be categorized into two broad etiopathogenetic categories: type 1 and type 2 diabetes. In Type 1 diabetes (T1D), also known as juvenile diabetes or insulin-dependent diabetes, the pancreas no longer produces insulin, or little, as a consequence of the autoimmune destruction of pancreatic β-cells. In Type 2 diabetes (T2D) the peripheral tissues (mainly adipose tissue, skeletal muscle, and the liver) become insulin resistant and there is an inappropriate insulin secretion. The secretion impairment of insulin in T2D is likely due to both cellular dysfunction and mass reduction of β-cells (American Diabetes Association, 2019c).

Besides these two main etiologic groups, the current classification of diabetes includes other less prevalent disorders such as gestational diabetes or diabetes due to monogenic defects in β-cell function. Gestational diabetes was for many years defined as any degree of glucose intolerance that was first recognized during pregnancy, regardless of whether

the condition may have predated or persisted after the pregnancy (American Diabetes Association, 2019c). Monogenic forms of diabetes represent less than 5% of patients and comprise neonatal diabetes and maturity-onset diabetes of the young (MODY). Neonatal diabetes refers to monogenic diabetes with onset before 6 months of age, whereas MODY is characterized by onset before 25 years of age and impaired insulin secretion and almost no alterations in insulin action. These forms of diabetes are inherited in an autosomal dominant pattern (Cowie et al., 2017).

## 2.1. Type 2 diabetes

T2D is the most prevalent form of diabetes as it comprises 90-95% of all diabetic patients worldwide (Centers for Disease Control and Prevention, 2017). As obesity is closely related to T2D, the majority of patients with this kind of diabetes are overweight or obese, and the non-obese T2D patients tend to present an increase in the percentage of fat, mainly distributed in the abdominal region (American Diabetes Association, 2019c). Although T2D was predominantly diagnosed in middle-age or old people, the onset age of the disease has decreased, affecting more and more young people (International Diabetes Federation, 2017). Parallel to the increment of T2D prevalence is the increase of obesity in the population due to environmental changes of sedentary lifestyle (Caspard et al., 2018)(Cheng, 2005).

Frequently, as hyperglycemia in T2D develops gradually and, at earlier stages, is not severe enough to notice diabetes symptoms, the diagnosis of this pathology does not occur during the first years of the disease (American Diabetes Association, 2019c). In addition to the genetic component, the increment of T2D incidence has been multifactorial, and it is related to the aging of populations, the economic development and associated transitions in lifestyle and culture, leading to a growing heterogenicity in the phenotypes and pathophysiology associated with diabetes globally (Gregg et al., 2016; Smith et al., 2010a).

### *2.1.1. Pathogeny of type 2 diabetes*

T2D is a metabolic syndrome characterized by insulin resistance in peripheral tissues and a relative deficiency in the insulin secretion of the pancreatic β-cells leading to sustained hyperglycemia (Ashcroft and Rorsman, 2012; Butler et al., 2003; Yoneda et al., 2013). In response to the insulin resistance, β-cell hyperplasia and hyperinsulinemia occur during

the preclinical period of the disease (Hameed et al., 2015). When sustained hyperglycemia chronifies, β-cells can reach exhaustion as cannot compensate for the insulin needs. In this step, hypotrophy, hyperplasia, dedifferentiation and reduced proliferation of β-cells occur (Cerf, 2015). Furthermore, chronic hyperglycemia also leads to β-cell dysfunction, diminishing signaling, insulin synthesis, and secretion, which finally ends in β-cells apoptosis (Cerf, 2015).

Increased levels of free fatty acids (FFA) in blood circulation is a characteristic of T2D patients (Figure 6) (Reaven et al., 1988). FFA are stored as triacylglycerols (TG) in the adipocytes, and during fasted condition are an essential energy source. Insulin is a negative regulator of lipolysis that limits FFA release from adipocytes through the inhibition of the hormone-sensitive lipase (HSL). In T2D, insulin effect in inhibiting lipolysis and reducing the FFA circulating levels gets notably reduce (Gustafson et al., 2015). Therefore, excessive energy intake and low physical activity cause adipocyte size growth as a response to the TG storage in these cells (Sattar and Gill, 2014). During this adiposity growth, hypertrophied adipocytes become unable to store efficiently more lipids, leading to a TG accumulation in peripheral or ectopic tissues, such as the liver, skeletal muscle or perivascular, omental or pericardial adipose tissue, promoting simultaneously lipolysis (Figure 6) (Guilherme et al., 2008; Loher et al., 2016; Sattar and Gill, 2014). The increased release of FFA from adipocytes also leads to the production of proinflammatory cytokines such as interleukin 1β (IL1β) or tumor necrosis factor α (TNFα). This enhancement in the proinflammatory cytokines release increases even more lipolysis and inhibits the expression of key genes related to insulin signaling and dedifferentiation of adipocytes, affecting through basic molecular mechanisms the insulin resistance in the adipose tissue (Figure 6) (McNelis and Olefsky, 2014).

Although activated macrophages in adipose tissue produce most pro-inflammatory cytokines, other cell types such as B lymphocytes and T cells can also secrete this type of immunomodulatory agents, increasing local and systemic inflammation, thus contributing to insulin resistance (Strissel et al., 2014). The excessive circulating levels of FFA and TG released by adipocytes result in an ectopic accumulation of lipids in non-adipose tissues, which together with TNF-α, trigger peripheral insulin resistance affecting profoundly β-cell mass and function (Kahn et al., 2006). In this insulin resistance state, adipose tissue and skeletal muscle decrease glucose uptake, and insulin can not block adipose tissue lipolysis. Besides, glucose production is increased in the liver as insulin

cannot suppress gluconeogenesis in this tissue. Overt T2D preceding hepatic steatosis is usually associated with obesity, particularly visceral (Taylor, 2008). Obesity represents a determinant cause in the reduction of muscular and hepatic sensitivity to insulin, one of the main contributors to peripheral resistance to this hormone (Birkenfeld and Shulman, 2014; DeFronzo, 2004; McGarry, 2002).

Regarding β-cells, chronic increase of FFA circulating levels in conjunction with hyperglycemia disrupt the kinetics of insulin secretion. Moreover, it impairs glucose stimulus-secretion coupling (with the first phase of insulin secretion loss and the second phase decreased), lower insulin biosynthesis, triggers a deleterious autoinflammatory process in pancreatic islets and promote ß-cell apoptosis (Donath and Halban, 2004; Leahy, 2005). The situation will severely further impact on β cells mass and function (Donath et al., 2010; Hajer et al., 2008; Halban, 2008; Nolan et al., 2011). In response to FFA and circulating pro-inflammatory cytokines in a context of insulin resistance accompanied by eventual β-cell dysfunction, the body's overall energy homeostasis is altered (Nolan et al., 2011) (Figure 6).

In rodents, obesity and insulin resistance are strongly associated with the degree of activity (non-shivering thermogenesis) of BAT. Nearly all experimental rodent models of obesity exhibit diminished or defective BAT function (Hansen and Kristiansen, 2006; Lin and Li, 2004). BAT ablation in mice also reduces energy expenditure and increases obesity in response to a high-fat diet (HFD) (Lowell et al., 1993). Moreover, mice lacking the insulin receptor specifically in BAT show altered insulin secretion and glucose intolerance (Guerra et al., 2001).

In humans, inverse correlations have been established between BAT activity and body mass index (BMI) and/or glycaemia, suggesting a possible role of low BAT activity in obesity and diabetes development (Cypess et al., 2009; van Marken Lichtenbelt et al., 2009; Stefan et al., 2009). Additionally, UCP1 mRNA is reduced in the visceral adipose tissue of obese patients. Moreover, genes characteristically expressed in the brown adipocyte phenotype are underexpressed in subcutaneous WAT of overweighed patients with insulin resistance (Murano et al., 2009). In contrast, a patient that had a large hibernoma (rare, non-malignant tumor made up of essentially brown adipocytes) was reported to lose approximately 7 kg in a year (Allegra et al., 1983).

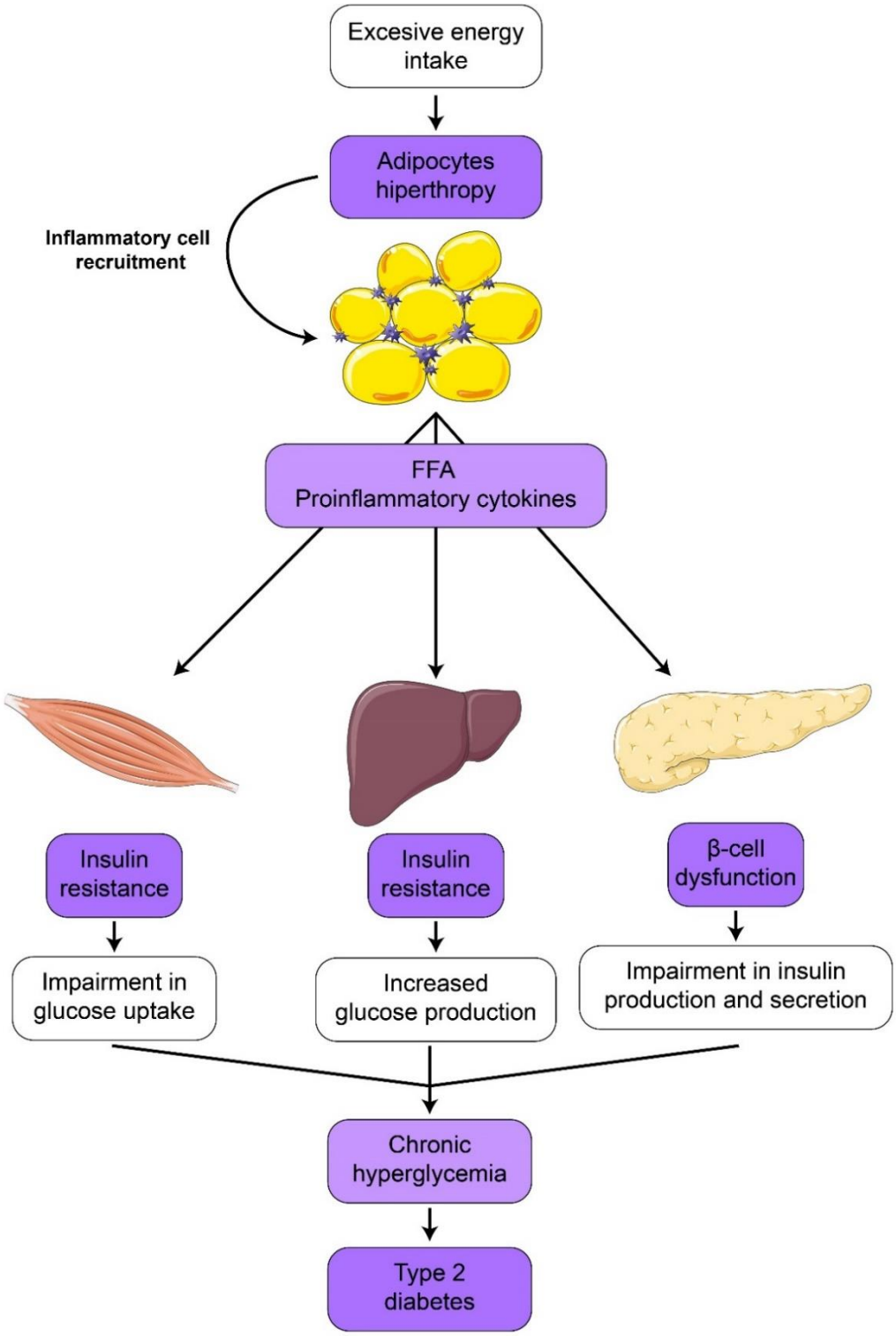


***Figure 6. Key alterations that link obesity and the development of type 2 diabetes***. An excessive energy intake leads to an accumulation of lipids in the adipocytes. This accumulation induces the lack of response to the inhibition of lipolysis by insulin and the recruitment of inflammatory cells that secrete proinflammatory cytokines. The increase of FFA and circulating proinflammatory cytokines causes the ectopic deposit of lipids in skeletal muscle and the liver, inducing insulin resistance in these tissues. Insulin resistance in the muscle and adipose tissue reduces glucose uptake by muscle and in the liver leads to an increase in gluconeogenesis and glycogenolysis, which, altogether contributes to hyperglycaemia. In view of the increase in blood glucose, and to avoid hyperglycaemia, β-cells of the pancreas become hyperplasic to compensate for the demand of insulin. When β-cell dysfunction also occurs, insulin resistance in the aforementioned tissues results in hyperglycemia and the development of T2D.

### *2.1.2. Genetic susceptibility and environmental factors of type 2 diabetes*

Genetic factors contribute clearly to the pathogenesis of T2D (Prasad and Groop, 2015). A genetic contribution can be detected in families with a T2D members, which increases up to 3-fold the risk of developing the disease, or in the high risk of T2D that some ethnic populations have in particular (Cornelis et al., 2015; Ng, 2015; Schäfer et al., 2011). To date, genome-wide association studies (GWAS) have associated more than 60 loci with diabetes (Billings and Florez, 2010; Morris et al., 2012; Robiou-du-Pont et al., 2013; Steinthorsdottir et al., 2014). Each of these loci contains sequence variations that are related to a higher risk of suffering T2D. Even though the molecular mechanisms of several of these genetic variants are not known yet, the influence in the sensitivity or secretion of insulin has been clearly shown in several cases. For example, coding variants of FTO (*Fat mass and obesity-associated protein*), PPARG (*Peroxisome proliferator-activated receptor gamma*), KLF14 (*Krüppel-like factor 14*) or IRS1 (*Insulin receptor substrate 1)* had been reported to be related to high insulin levels in fasted conditions (Voight et al., 2010).

Other genes have been associated with pancreatic β-cell dysfunction, such as GK (*glucokinase*) or MTNR1B (*Melatonin receptor 1B*). Furthermore, insulin secretion defects without marked effects in glycemia can be associated with coding variants of TCF2L2 (*Transcriptor factor 7-like 2*), SLC30A8 (*Solute carrier family 30 member 8*), CDKAL1 (*Cyclin-dependent kinase 5 regulatory subunit associated protein 1-like 1*) and CDKN2A/2B (*Cyclin-dependent kinase inhibitor 2 A, Cyclin-dependent kinase inhibitor 2 B*) (Dimas et al., 2014; Rosengren et al., 2012). As T2D and obesity are tightly related many T2D related loci are also involved with obesity susceptibility, such as in the case of FTO ( Golay and Ybarra, 2005; Karaderi et al., 2015). Besides that, different loci had been identified to increase the risk of being overweight and obese in T2D patients, like ADIPOQ (*adiponectin*), LEPR (*leptin receptor*), IRS2 (*Insulin receptor substrate 2*) or GRB14 (*Growth factor receptor-bound protein 14*) (Kasim et al., 2016).

Among others, the genes that have been detected in GWAS studies are key genes of brown adipose tissue activation such as UCP1 (*Uncoupling protein 1*) or ADRB3 (*β3-adrenergic receptor*) (Brondani et al., 2012b; Kurokawa et al., 2008; Sramkova et al., 2007; Vimaleswaran et al., 2010).

Besides the genetic influence of T2D pathogenicity, risk genetic variants are considered only to increase the susceptibility to of the disease. The main cause of the upsurge of T2D is due to environmental changes associated with lifestyle (Imamura and Maeda, 2011). Consumption of diets with high energy density, typical of the western countries, along with the sedentary lifestyle are the two main factors leading to the development of T2D. Both factors are also responsible for the current obesity epidemic. In particular, ectopic fat accumulation such as fatty liver and visceral fat enlargement, contribute in a more significant way than body mass index (BMI) to the risk of developing T2D. BMI consists of an indirect measure of body fat based on height and weight that applies to adult men and women. This situation fits with the fact that obese people without metabolic dysregulation have lower fatty liver or visceral fat accumulation. Conversely, those who develop T2D having an average body weight or without being obese show ectopic fat accumulation, visceral fat increased and reduced muscle mass (Kolb and Martin, 2017).

Furthermore, multiple other environmental factors that affect the risk of developing T2D independently of adiposity exist. Low-fiber diet multiplies by three the risk of developing T2D and regular intake of sweetened beverages by a 20-30% (Greenwood et al., 2014; Jannasch et al., 2017; Schwingshackl et al., 2017; Wang et al., 2015). Similarly, low physical activity, sedentary behaviors like spending a long-time watching television, exposure to residential traffic, noise or fine air pollution are associated with increased of developing T2D. Cigarettes smokers have also been found to have between a 30 and a 60% higher risk of T2D depending on the number of cigarettes smoked. Stress, depression, anxiety or low socioeconomic status are also factors that influence the risk of suffering from this disease (Kolb and Martin, 2017). Finally, the relationship between certain infections and the development of T2D has also been reported. Hepatitis C can cause hepatic steatosis and with it, resistance to insulin, and T2D. (Lerat et al., 2017). Moreover, Chlamydia pneumoniae infection can cause dysfunction of pancreatic β-cells due to systemic inflammation (Rodriguez et al., 2015). It is also worth mentioning that the acquired immunodeficiency syndrome (AIDS) and anti-retroviral treatments increase systemic inflammation and promote insulin resistance (Dooko et al., 2014).

## 3. OBESITY

The World Health Organization (WHO) defines obesity as an abnormal or excessive fat accumulation that presents a risk to health (World Health Organization, 2018a). Obesity is a complex metabolic disease and one of the most relevant risk factors for insulin resistance and the development of T2D (Kusminski et al., 2016). Obesity has reached epidemic proportions. 1.9 billion adults were overweight in 2016, from which over 650 million of these were obese (World Health Organization, 2018a). Worldwide prevalence of obesity nearly tripled between 1975 and 2016 and, even initially was associated with developed countries, is becoming more prevalent in countries still developing (World Health Organization, 2018a). Each year 2.8 million people die as a consequence of overweight or obesity (The European Association for the Study of Obesity, 2018).

Overweight and obesity not only affect adults but also children. As shown by WHO, in the past four decades the number of obese children and adolescents aged between 5-19 years has increased more than ten-fold worldwide, from 11 million in 1975 to 124 million in 2016 (World Health Organization, 2018a). Furthermore, 213 million children were overweight in 2016 (World Health Organization, 2018a). This increment means, altogether, that almost 340 million or one out of every five (18.4%) children and adolescents aged 5-19 years were overweight or obese globally (World Health Organization, 2018b). Several studies concluded that worldwide excess of weight rise in children and adolescent continues increasing in low and middle-income countries, specially due to the relative rapid transition from underweight to overweight and obesity (Abarca-Gómez et al., 2017; Mekonnen et al., 2018; Muthuri et al., 2014; Rivera et al., 2014). However, in high-income countries, the rise in excess weight has plateaued (Olds et al., 2011; Wabitsch et al., 2014). Early age obesity contributes to an early age development of T2D and is associated with premature death and disability in adulthood. Furthermore, obese children and adolescents have more risk of fractures, hypertension, psychological effects, early markers of cardiovascular disease and insulin resistance (World Health Organization, 2018a).

Obesity develops due to a chronic imbalance in which energy consumption exceeds energy expenditure, leading to an abnormal fat distribution (World Health Organization, 2018a). To classify overweight and obesity in adults, the BMI is used as a simple index for weight-for-height, while for children, age must also be considered before defining overweight or obesity (Eknoyan, 2007). BMI is calculated as the person's weight in kilograms (Kg)

divided by the square of the height in meters (m). For adults, WHO determined in 1993 a BMI between 25-30kg/m² for overweight and a BMI of 30kg/m² or higher for obesity (WHO Expert Committee, 1995; World Health Organization, 2018a). Although BMI is a simple measure widely used in population studies, is not the most convenient measure to predict individual risk as it does not allow to distinguish between muscle or fat-associated weight. To tackle this issue, other methods to determine fat distribution like the circumference of the waist, the ratio between the perimeter of the waist and the hip or more complex imaging techniques, like dual-energy x-ray absorptiometry (DEXA) are presently used (Adab et al., 2018).

## 3.1. Types of obesity in humans

Body fat distribution changes in humans between individuals due to gender, age, hormonal status, ethnics, response to drugs or in concomitant pathologies. This distribution is key for predicting disease associated with obesity (Tchkonia et al., 2013). Two types of obesity can be distinguished depending on the location of fatty depots (Figure 7) (Gesta et al., 2007):

- **Central obesity (apple shape)**: It is characterized by an intra-abdominal/visceral accumulation of fat by increasing its deposition around the viscera in mesenteric, retroperitoneal and omental adipose depots. As this form is more common in men, it is also named android obesity. Individuals who suffer this characteristic fat accumulation show an increase in insulin resistance and glucose tolerance linked to an increased risk of metabolic complication like T2D (Sam, 2018).
- **Peripheral obesity (pear shape)**: It is characterized by a subcutaneous fat accumulation in the thighs and hips. As this form is typical of women, it is also named gynoid. Unlike central obesity, peripheral obesity does not have as much metabolic risk as central obesity, and patients who present this fat distribution form have normal glucose tolerance (Sam, 2018).

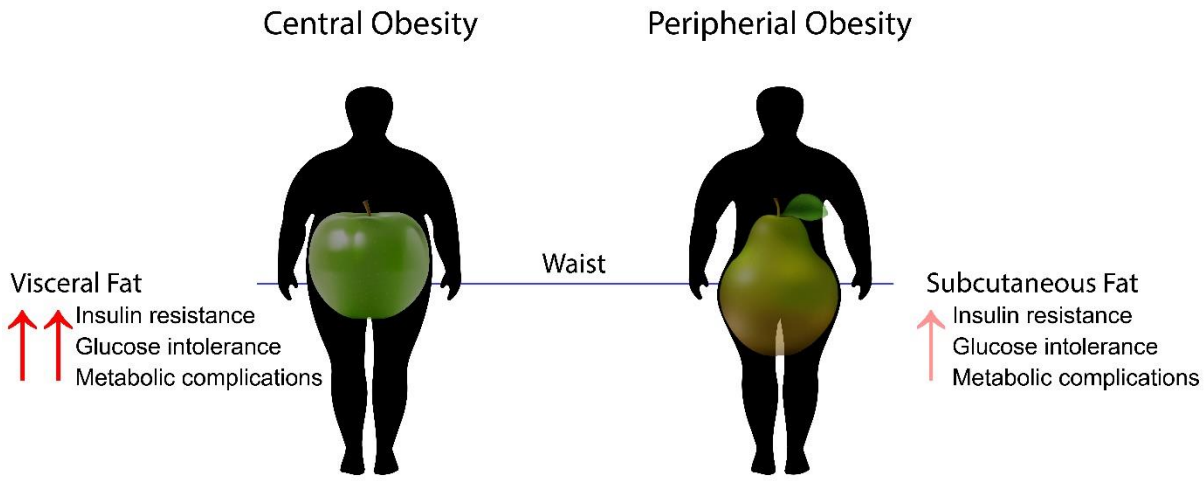


***Figure 7. Obesity classification depending on the fat distribution.*** The increment of fat storage in the intra-abdominal/visceral area (apple shape) promotes metabolic complications, whereas subcutaneous fat storage (pear shape) exerts little or no risk.

## 3.2. Obesity comorbidities

Obesity has been linked with several complications such as high increased risk of T2D and has been associated with other cardiovascular, chronic inflammation and metabolic pathologies, such as non-alcoholic fatty liver disease (NAFLD) (Figure 8), which finally lead to an increased risk of mortality, with an average of life expectancy decrease of 6-7 years (Ghouri et al., 2018; Segula, 2014). Furthermore, obesity and especially visceral fat are also associated with hypertension (Figure 8) (Hall et al., 2018). Hypertension is a major risk of cardiovascular diseases such as ventricular and atrial arrhythmias, ventricular hypertrophy, diastolic and systolic heart failure, cardiac ischemia, and renal and neurological damage (Figure 8) (Black, 2003). It has been shown that the pulmonary tract is also affected by obesity (Figure 8). Especially, obesity has been associated with increased problems due to obstructive sleep apnea or asthma (Carpio et al., 2016; Duarte and Magalhães-da-Silveira, 2015). Other diseases are also related to obesity, such as osteoarthritis, stroke, female infertility, polycystic ovary syndrome, and erectile dysfunction (Esposito et al., 2004; Felson, 1992; Segula, 2014; Song et al., 2004; Tanne et al., 2005) (Figure 8). In addition, the World Cancer Research Fund (WCRF) classifies as "convincing" the association between obesity and endometrial, kidney, pancreas, colorectal, esophagus and breast (postmenopausal) cancer, and "probable" for gallbladder cancer (Kanker and Fonds, 2007) (Figure 8). Some gender differences can be found in obesity secondary complications, as BMI and colon cancer risk are more strongly associated with men than with women (Renehan et al., 2008). The effect of BMI on the

risk of developing some cancers of the female reproductive organs is higher after the menopause (Eliassen et al., 2006).

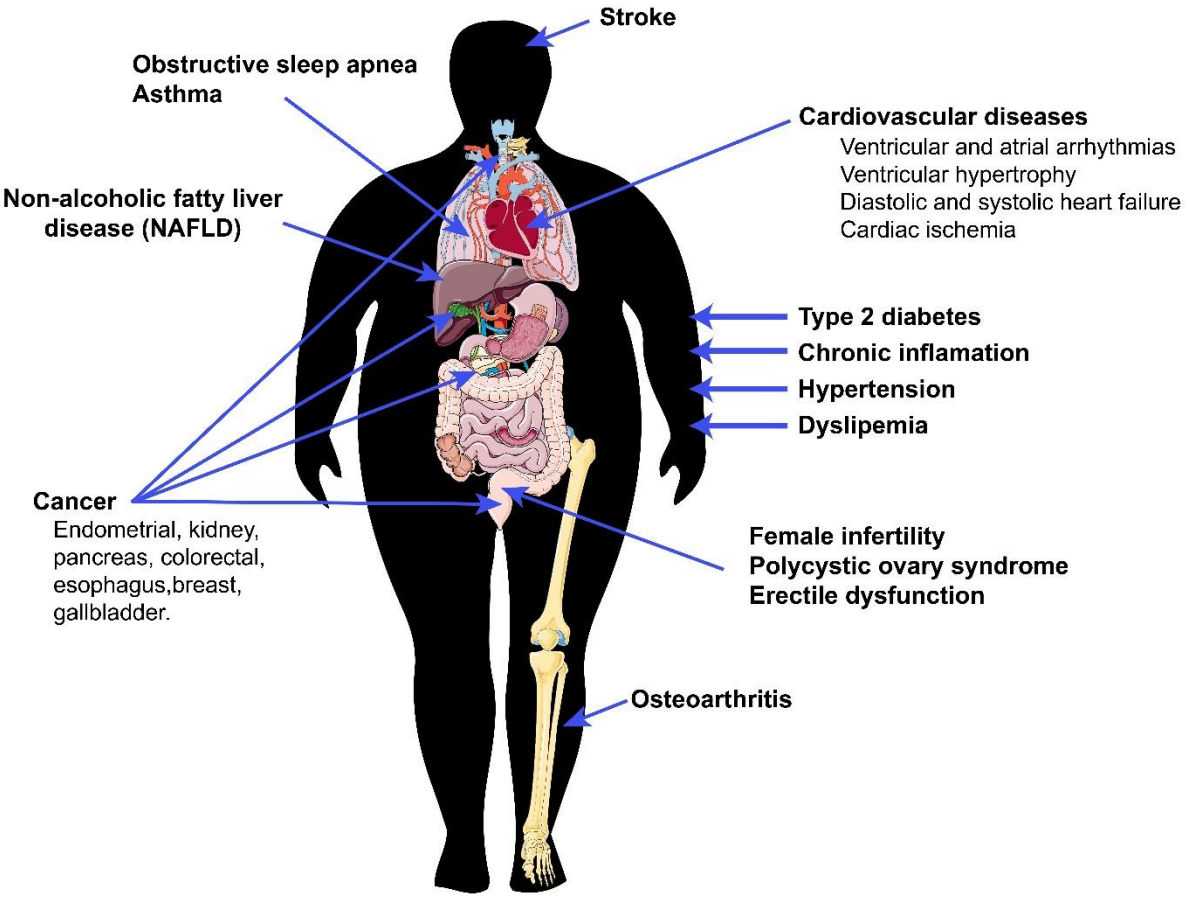


***Figure 8. Diagram of obesity complications.***

# 4. CURRENT TREATMENTS FOR TYPE 2 DIABETES AND OBESITY

The body weight management in obese people has a clear beneficial effect in the treatment of T2D, delaying its progression (Jackness et al., 2013; Knowler et al., 2002; Lim et al., 2011; Pastors et al., 2002; Rothberg et al., 2014; Tuomilehto, 2013; UKPDS Group, 1990; Webb and Wadden, 2017; Wing et al., 2011). Thus, a sustained and modest weight loss improves glycemic control and reduces the need of hypoglycemic drugs in overweight or obese diabetic patients (Pastors et al., 2002; UKPDS Group, 1990; Webb and Wadden, 2017; Williamson et al., 2000).

## 4.1. Current therapies for type 2 diabetic patients

The major objective of T2D treatments aims to decrease circulating glucose levels. The effectiveness of these treatments depends on several factors such as the progression stage of T2D at the moment of the treatment, the level of physical activity of the patient, an adequate intake of nutrients, or the type of drugs used. Once T2D is diagnosed, patients are recommended a lifestyle intervention. This intervention consists of dietary changes and an increase in exercise and cessation of smoking, which clearly reduces the risk of progression of glucose intolerance and insulin resistance (American Diabetes Association, 2019b). However, if this therapy is not followed by the patients as recommended, or if it is not sufficient to reduce circulating glucose levels, patients are given pharmacological treatments. The pharmacological treatment most commonly used is metformin. However, several drugs such as glucagon-like peptide-1 receptor (GLPR1) agonists, inhibitors of dipeptidyl peptidase 4 (DPP-4), sodium-glucose cotransporter 2 (SGLT2) inhibitors, sulfonylureas, thiazolidinediones (TZD) or basal insulin can also be prescribed to control glycemia (American Diabetes Association, 2019c). If in 3 months after metformin treatment the levels of HbA1c are not normalized, treatment with a second drug is recommended. If even with two different treatments prescribed, high HbA1C levels persist, it is recommended to combine both drugs together with the daily administration of multiple doses of basal insulin (American Diabetes Association, 2019a; Inzucchi et al., 2012).

Pharmacologically, metformin belongs to the biguanide class of antidiabetic drugs and is a medication widely used in the treatment of T2D. The treatment with metformin is considered effective, safe and cheap and has been described to reduce the risk of cardiovascular events and even death (Holman et al., 2008; Inzucchi et al., 2012). Its

mechanism of action is based on the suppression of hepatic gluconeogenesis through the sensitization of the liver to insulin, reducing the endogenous production of glucose. Moreover, metformin improves insulin sensitivity in the skeletal muscle, increases satiety and increases the levels of glucagon-like peptide 1 (GLP-1) (Holman et al., 2008; Pryor and Cabreiro, 2015; Tahrani et al., 2011). Since the mechanism via which this drug affects glycemia is not through the stimulus of insulin secretion, the risk of hypoglycemia is low (Holman et al., 2008; Inzucchi et al., 2012). However, metformin is associated with a deficiency of vitamin B12. To avoid health problems related with this secondary effect, it is advisable to periodically monitor patients to control levels of this vitamin, especially in patients suffering from anemia or peripheral neuropathy (Aroda et al., 2016).

GLP-1 is, together with the gastric inhibitory polypeptide (GIP), one of the two primary incretin hormones that are secreted after the ingestion of glucose or nutrients by the intestine to stimulate insulin secretion from pancreatic ß-cells, and, therefore, producing a decrease in blood glucose levels (Seino et al., 2010). This molecule also delays gastric emptying, suppresses glucagon secretion, and decreases appetite, being a candidate to counteract hyperglycemia. However, once GLP-1 reach the bloodstream is inactivated by DPP-4. To use this molecule as an effective drug, different GLP-1 mimetics resistant to inactivation by DPP-4 have been obtained recently. Moreover, inhibitors of DPP-4 have also been generated. The usage of these new molecules results in a longer half-life of GLP-1 (Inzucchi et al., 2012; Mulvihill and Drucker, 2014). Like Metformin, drugs based on the incretin system do not induce hypoglycemia (Inzucchi et al., 2012).

Another mechanism to decrease blood glucose levels is by blocking the reabsorption of glucose in the kidney using inhibitors of SGLT2. These drugs increase the excretion of glucose in urine, which reduces hyperglycemia but promotes urinary tract infections (Zinman et al., 2015). Moreover, other side effects such as an increase in bone reabsorption, which can lead to risk of fractures have been described by some authors (Brunton, 2015). There is controversy regarding this issue.

The sulfonylureas were the first oral drugs used for the treatment of T2D. This drug improves the secretion of insulin by binding to the ATP-sensitive potassium channels ($K_{ATP}$) of pancreatic β-cells (Inzucchi et al., 2012; Turner et al., 1999). Furthermore, sulfonylureas are also capable of suppressing hepatic gluconeogenesis, reducing glycemic levels (Turner et al., 1999). Despite the effectiveness in controlling blood glucose levels,

some adverse events such as an increase in body weight gain or an increased risk of hypoglycemia have been described (Inzucchi et al., 2012).

Thiazolidinediones (TZDs) increase insulin sensitivity in skeletal muscle and reduce hepatic glucose production by activating the heterodimerization of PPAR with the retinoid X receptor (RXR) and by blocking the phosphorylation of Cyclin-dependent kinase 5 (CDK-5) by PPAR (Inzucchi et al., 2012; Yki-Järvinen, 2004). The molecular mechanism by which these drugs counteract hyperglycemia does not increase the risk of hypoglycemic episodes and their effects are longer lasting than those of sulfonylureas and metformin. However, side effects such as weight gain or fluid retention have been described (Inzucchi et al., 2012).

Due to the progressive loss of β-cell mass during the development of T2D, insulin replacement therapy is often required in the treatment of diabetes. The administration of exogenous insulin improves the secretion of endogenous insulin and stabilizes glycemia. In T2D patients, insulin therapy can be combined with one or more of the aforementioned antidiabetic drugs. There are different types of insulin and different administrations methods to maintain normoglycaemia: basal insulin, insulin bolus, premixed insulin, concentrated insulin or even inhaled insulin (American Diabetes Association, 2019c). However, the administration of insulin is linked to a serious risk of hypoglycemia and body weight gain (Turner et al., 1999).

Secondary complications such as arterial hypertension, diabetic retinopathy, foot ulcers or renal complications are tightly related to diabetes. Therefore, it is essential to treat these secondary complications which may appear during the development and progression of T2D. It is worth mention that with a correct pharmacological control of blood glucose and with a lifestyle and diet intervention, T2D patients can have a long and healthy life (American Diabetes Association, 2019b).

## 4.2. Current therapies for obese patients

A decrease in caloric intake along with an increase in energy expenditure is the first intervention in the treatment of overweight and obesity. However, lifestyle intervention to produce healthy changes and to increase physical activity has been described to mainly reduce between 3-5% of most patients' body weight after 4 years (Unick et al., 2013). For this reason, these type of interventions are often accompanied by pharmacological

therapies and even bariatric surgery (Dyson, 2010). Pharmacotherapy against obesity is recommended in individuals with a BMI of at least 27 kg/m$^2$ with some persistent comorbidity or in those subjects with a BMI greater or equal than 30 kg/m$^2$. Pharmacotherapy by itself does not induce an involuntary and substantial loss of weight. Hence, it is considered an adjunct to lifestyle intervention since it can substantially improve weight loss. The effectiveness of a pharmacological treatment against obesity is determined by its ability to reduce 3-5% body weight after 3 months of administration (American Diabetes Association, 2019a).

Nowadays the U.S. Food and Drug Administration (FDA) has approved six anti-obesity treatments that can be adapted to the individual needs of each patient (American Diabetes Association, 2019a, 2019d). Most approved drugs act in the long term, while there is only short-term treatment, the appetite suppressant Phentermine (American Diabetes Association, 2019d). The other approved treatments are: Liraglutide®, Lorcaserin®, Orlistat®, and dual combinations of phentermine-topiramate and naltrexone-bupropion (Astrup et al., 2012; Greenway et al., 2010; Pi-Sunyer et al., 2015; Smith et al., 2010b; Sumithran and Proietto, 2014; Verrotti et al., 2011).

Phentermine belongs to the amphetamine family and acts by suppressing appetite through the activation of catecholaminergic neurons. However, as this drug has the side effect of creating addiction, it can only be administered for a short period of time and in very controlled doses (American Diabetes Association, 2019d).

Liraglutide® is a GLP-1 agonist, and therefore its mechanism of action is the same than incretins. This drug promotes pancreatic insulin secretion, delays gastric emptying and suppresses glucagon secretion. Furthermore, a reduction in appetite and food intake has been described due to anorexic effects at the level of central nervous system. In addition, it has been reported that GLP-1 agonists can restore sensitivity to leptin in obese animals (Astrup et al., 2012; Ladenheim, 2015; Pi-Sunyer et al., 2015).

Lorcaserin® is an agonist of the 5-hydroxytryptamine receptor 2C (5-HT2C). This drug, acting through the hypothalamic neurons, produces pro-opiomelanocortin (POMC), which favors satiety. Moreover, Lorcaserin® also reduces HbA1c levels and risk factors for cardiovascular diseases (Smith et al., 2010b).

Orlistat® is a molecule capable of reducing the digestion of fat at the intestinal level by inhibiting pancreatic and gastric lipases. The treatment with Orlistat® reduces the absorption of fat by the intestine a 30%, improving glycemia and weight of patients (Sumithran and Proietto, 2014).

The combinatory drug phentermine-topiramate, a noradrenaline agonist with inhibitors of carbonic anhydrase, reduces food intake. In addition, this combinatory drug improves the activity of γ-aminobutyric acid (GABA) and norepinephrine receptors, increasing energy expenditure (Verrotti et al., 2011).

The combination of opioid antagonists with a unicyclic aminoketone antidepressant, naltrexone-bupropion, activates POMC neurons through binding to the melanocortin receptor MC4R, antagonizing the effects of the opioid system. Thus, energy consumption is increased and food intake is reduced (Greenway et al., 2010). However, affectations in the mood and an increased likelihood of suicide has been described as adverse effects (Billes et al., 2014).

Bariatric surgery has become the most used alternative to pharmacological treatment due to its rapid efficacy. This type of surgery is recommended in obese patients with severe comorbidities or with a BMI greater than 40 $Kg/m^2$. Currently, deaths due to surgery are below 1% and weight losses of 25-30% are achieved with rapid normalization of blood glucose and blood pressure. However, several disadvantages have been described for the bariatric surgery, such as the intake of a very restrictive nutrient-poor diet which avoid the consumption of fruit and vegetables during a necessary long-term postoperative monitoring. Additionally, increase risk of symptomatic gallstones has been observed in approximately 33% of the patients (Morais et al., 2016). After surgery, patients experience significant weight loss during the honeymoon period that lasts between 18 and 24 months. However, between 17 and 64% patients regain weight after this honeymoon period (Livhits et al., 2011; Odom et al., 2010; da Silva et al., 2016; Tamboli et al., 2014; Weber and Chand, 2018)

Although the treatments described above can reduce the degree of obesity in patients, important side effects have been described, and in some cases, the beneficial effects are only temporary. Thus, it is necessary to develop new treatments for T2D and obesity that present improved efficacy and sustained therapeutic efficacy.

## 4.3. Brown adipose tissue activation and browning of WAT

Obesity is largely due to a sustained imbalance between energy intake and expenditure. The development of new therapeutic strategies aiming to increase metabolic rate such as enhancement of non-shivering thermogenesis via browning of white adipose tissue (WAT) may hold great potential for the future treatment of obesity and T2D.

Under physiological conditions, thermogenic BAT activity is increased by cold-exposure or overfeeding, which activate the sympathetic nervous system (Zafrir, 2013). The release of norepinephrine from the sympathetic nerve endings acts mainly through $\beta_1$ and $\beta_3$-adrenergic receptors in BAT, inducing the thermogenic response and increasing oxidative substrates supply (Ueta et al., 2012). In WAT, cold-exposure and β-adrenergic stimulation lead to the appearance of beige adipocytes (browning) and to an increase in expression of thermogenic genes (Ueta et al., 2012; Wu et al., 2012; Young et al., 1984). However, the capacity of undergoing browning differs between the different WAT depots in rodents. Indeed, while a large accumulation of beige cells can be found in the subcutaneous inguinal adipose tissue during cold exposure, it is rather seldom observed in epididymal/perigonadal adipose tissue (Ferrannini et al., 2016).

### *4.3.1. Effects of cold exposure on energy and glucose homeostasis*

During cold exposure, thermoregulatory mechanisms are activated to maintain constant body temperature in both mice and humans ( Kirov et al., 1996; van Marken Lichtenbelt et al., 2009; Saito et al., 2009). Among others, these mechanisms involve vasoconstriction, activation of shivering by muscle contraction, and non-shivering thermogenesis. Cold exposure is the most powerful physiological stimulus that activates brown fat in both humans and rodents, increasing BAT activity and recruitment, decreasing body fat mass (Yoneshiro and Saito, 2015). Moreover, cold exposure increases resting energy expenditure, whole-body glucose disposal, glucose oxidation and insulin sensitivity in humans (Chondronikola et al., 2014). It has also been shown that, in humans, cold-activated BAT has an impact on glucose metabolism independently of BMI (Matsushita et al., 2014).

### *4.3.2. Therapeutic approaches to increase non-shivering thermogenic activity*

Although the molecular mechanisms underlying BAT activation or browning of WAT are poorly understood, several mouse models over-expressing genes involved in brown adipogenesis or of the uncoupling machinery, or down-regulating inhibitors of these

processes, have demonstrated to increase non-shivering thermogenesis, achieving protection against obesity and insulin resistance. For example, UCP1 overexpression in BAT and WAT has been shown to protect mice from diet-induced obesity (Kopecky et al., 1995). Mice deficient in cell-death-inducing DFF45-like effector A (Cidea) also presented an increase in energy expenditure and were resistant to HFD-induced obesity and diabetes (Zhou et al., 2003). Similarly, overexpression of bone morphogenetic factor 7 (BMP7), an activator of brown adipogenesis, resulted in increased BAT mass and induction of UCP1 leading to an increase in energy expenditure and a reduction in weight gain in mice (Tseng et al., 2008). Moreover, BMP7 was able to induce adipogenesis and UCP1 expression in primary human preadipocytes isolated from subcutaneous white fat (Schulz et al., 2011). Overexpression in adipose tissue of a transcriptional co-regulator of brown-adipose differentiation, PRDM16, induced the browning of WAT, which in turn increased energy expenditure, limited weight gain and improved glucose tolerance in response to HFD (Seale et al., 2011).

Altogether, these data provide compelling evidence that the unraveling and characterization of the intrinsic/extrinsic factors and pathways involved in the browning of WAT and activation of BAT is key to the future development of new therapeutic strategies for obesity and T2D. However, more studies to untangle the molecular activation of non-shivering thermogenesis are needed. Hence, more gene expression analysis to study the activation of this process as well as to determine differences between BAT activation and browning of WAT need to be performed. To this aim, transcriptomic tools such as microarrays are of high utility.

## 4.4. Transcriptomic analysis of adipose tissue depots

As one of the functions of adipose tissue is thermogenesis, several microarray studies have focused on better understanding this biological process or in the discovery of genes that activate thermogenesis in brown or beige adipocytes. To this aim, transcriptomic analysis of transgenic mice overexpressing or silencing genes able to promote or restrict thermogenesis had been widely used (Braga et al., 2014; Dempersmier et al., 2015; Dutchak et al., 2012; Kir et al., 2014). Also, transcriptomic analysis of animals administered with thermogenic compounds such as the PPARγ agonist rosiglitazone, the β3-adrenergic receptor agonist CL-316,243 or JAK inhibitors such as tofacitinib or R406 has been performed due to great potential of these compounds to active/induce BAT or beige fat (Li et al., 2005; Moisan et al., 2014; Ohno et al., 2012). However, these models

do not reflect biological conditions. As mentioned before, in normal conditions *Ucp1* expression is enhanced in response to cold exposure in different species (Chan et al., 2019). Accordingly, cold exposure triggered thermogenesis has been used in different studies with microarrays and RNA-Seq, mainly to study cold tolerance on transgenic mice (Cereijo et al., 2018; Keipert et al., 2017; Mo et al., 2017; Paschos et al., 2018; Seale et al., 2007; Shore et al., 2013; Sustarsic et al., 2018). The solid results obtained with cold exposure activation of thermogenesis allowed the unraveling of new gene functions such as *Cxcl14* or meteorin among others ( Cereijo et al., 2018; Rao et al., 2014). Moreover, these transcriptional studies had allowed to better understand the importance of some genes or lipids in this process such as cardiolipin, *Prdm16* or *Cox-2* (Paschos et al., 2018; Seale et al., 2007; Sustarsic et al., 2018). Other studies had analyzed mice adaptation to mild cold or had described deeply some specific BAT depots (Mo et al., 2017; Shore et al., 2013). However, these studies were not focused on the molecular changes occurring in these depots to adapt to acute cold exposure.

Based on the aforementioned, the usage of transcriptional techniques as microarrays is of enormous utility for a better understanding of the adipose tissue and for unraveling novel gene functions to improve energy consumption. As the molecular mechanisms of cold exposure adaptation such as the enhancement of non-shivering thermogenesis through BAT activation or browning of WAT are poorly understood, more studies are needed to study in detail the responses of different adipose depots to cold exposure, and to identify novel inducers of non-shivering thermogenesis.

# 5. ADENO-ASSOCIATED VIRAL VECTOR-MEDIATED GENE TRANSFER TO ADIPOSE TISSUE

In case of *in silico* unraveling of new potential genes related to thermogenesis, a method to test them *in vivo* is gene transfer. Gene transfer with AAV vectors has proven to be a very useful approach for the study of gene function, offering the benefits of a single administration that can mediate long-term effects.

## 5.1. Adeno-associated viruses biology

Adeno-associated viruses (AAV) are single-stranded small DNA virus that belongs to the family Parvoviridae and the genus Dependoparvovirus. To achieve a productive infection, AAV depends on the co-infection of an auxiliary virus or helper virus (adenovirus, herpes virus, human cytomegalovirus or papillomavirus) (Balakrishnan and Jayandharan, 2014; Carter, 2004). When AAV infects the cells, they integrate into a specific region of human chromosome 19 (19q13.3-qter) (McCarty et al., 2004).

AAV are formed of a protein capsid without lipid envelope of about 18-25 nm in diameter. Due to its small size, its single-stranded DNA (ssDNA) genome is only about 4.7 Kb (Lisowski et al., 2015). The AAV genome consists of inverted terminal repeats (ITRs) and three open reading frames (ORFs) encoding 3 proteins that build the AAV capsid, 4 regulatory proteins, and the assembly activation protein (AAP), a protein discovered recently (Sonntag et al., 2010) (Figure 9).

ITR are palindromic sequences of size 145 bp that flank the AAV genome at its 5 'and 3' ends with a fork structure and act as an origin of replication and packaging signal and integration (Figure 9) (Kotterman and Schaffer, 2014). The ORF Cap encodes three assembly structural proteins (VP1, VP2, and VP3) that form the icosahedral capsid of 60 subunits with the help of assembly activation protein (AAP), expressed from the ORF2 of the Cap gene (Earley et al., 2017; Naumer et al., 2012; Sonntag et al., 2010; Xie et al., 2002) (Figure 9). The ORF Rep encodes four non-structural proteins (REP40, REP52, REP68, and REP78) expressed by splicing variants and alternative promoters. These proteins are crucial for the integration, replication, transcription, and encapsidation of the genome (Figure 9) (Kotterman and Schaffer, 2014).

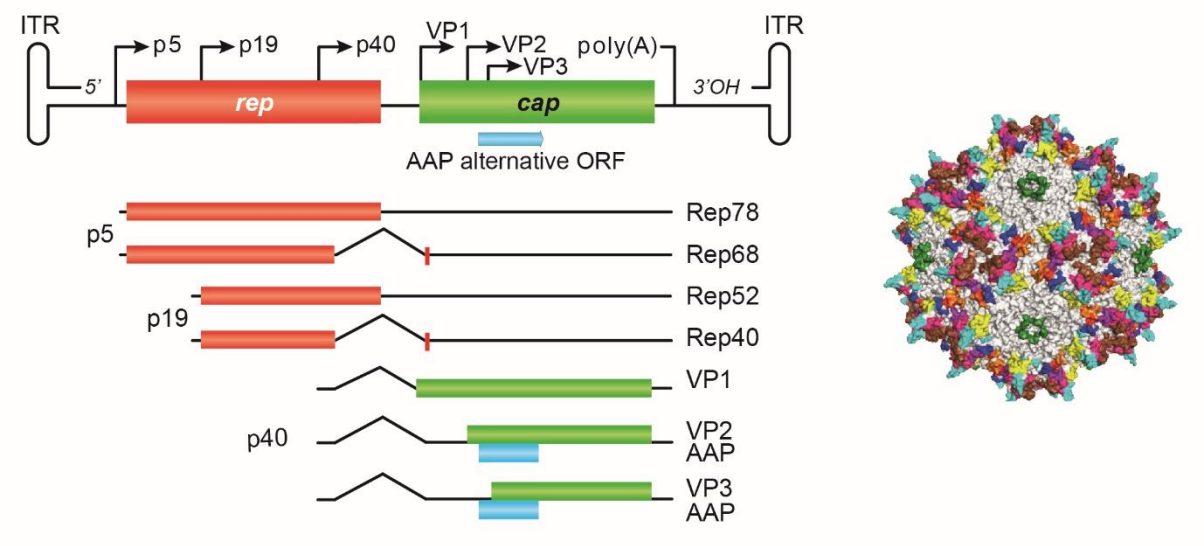


***Figure 9. Illustration of the genome and protein structure of AAV of serotype 2.*** The AAV genome comprises three open reading frames (ORF) flanked by the inverted terminal repeats (ITR). Due to splicing, the ORF Rep encodes four different non-structural proteins, Rep40, Rep52, Rep68, and Rep 78, which are essential transcriptional regulation, replication, virion assembly, and genome integration. The ORF Cap encodes three structural proteins, VP1, VP2 and VP3, and the assembly activation protein, AAP. The promoter p5 transcribed Rep78 and Rep68, the p19 promoter Rep52 and Rep40 and the Cap proteins are transcribed from the p40 promoter. The AAV structure is shown in the right part of the illustration, the VP3 hypervariable regions that match the genetic regions of the AAV genome can be seen colored. Adapted from Samulski and Muzyczka, 2014.

## 5.2. Recombinant adeno-associated viral vectors

Nowadays, despite there are more than 12 different AAV serotypes described, the AAV vectors used in gene therapy are mainly based on the serotype 2 (AAV2) since it is the best characterized (Samulski et al., 1982; Srivastava et al., 1983; Srivastava, 2016). Recombinant AAV vectors are generated by replacing the ORFs of the native viral genome with the expression cassette of interest, flanked by both ITRs. Consequently, the resulting recombinant genome has the ability to be packaged within the capsid but the recombinant AAV vector has a minimal ability to integrate or replicate by itself (Balakrishnan and Jayandharan, 2014; Hirata and Russell, 2000; Snyder et al., 2011). Furthermore, AAV vector transduced cells do not express any viral gene, which contributes to their low immunogenicity.

Recombinant AAV genomes mainly remain episomal in the nucleus of transduced cells (Lisowski et al., 2015). However, in a very low frequency (0.01% - 0.05%), the episomal DNA of the AAV vectors can be randomly integrated into the genome (Li et al., 2011; Smith, 2008; Valdmanis et al., 2012). This situation mainly occurs in areas of active gene transcription or in areas where the endogenous double-stranded DNA of the transduced cell breaks down (Deyle and Russell, 2009; Miller et al., 2004). When the ssDNA genome

of AAV vectors enters the nucleus, it must be converted to double-stranded DNA (dsDNA) to allow expression of the transgene. During this process, the synthesis of the cDNA strand of the AAV genome is a limiting step, so double-stranded genome containing AAV vectors, called self-complementary AAV vectors (scAAV), have been generated by additional genetic modifications to drive faster onset and higher levels of transgene expression (Ferrari et al., 1996; McCarty, 2008; McCarty et al., 2001). However, scAAV present also some issues, as their cloning capacity is reduced by half and their production is much less efficient. Furthermore, the immunogenicity of the scAAV vectors is greater than that of the AAV single-stranded DNA vectors (Martino et al., 2011).

AAV vectors can be produced and purified in the laboratory at high titers. Nowadays the triple transfection system in HEK293, human kidney embryonic cells, is the most used to produce AAV vectors (Ayuso et al., 2010a) (Figure 10). In this system, three plasmids are used to produce the AAV vectors. The first plasmid is the vector plasmid, which contains the therapeutic expression cassette flanked by the ITRs of AAV2. To produce the AAV capsids, the Rep and Cap ORFs are required in *trans*, and are encoded in the second plasmid, which does not contain any ITR to avoid encapsidation. These two plasmids, together with a third plasmid which provides the adenoviral functions necessary for AAV replication, are co-transfected into HEK293 cells. When REP and VP proteins are expressed, the therapeutic construct flanked by the ITRs is replicated and the resulting single-stranded DNA molecules are encapsidated in the formed AAV capsids (Figure 10). Viral particles are then purified from the cell lysate by column chromatography and/or density gradient centrifugation (iodixanol or CsCl) (Ayuso et al., 2010b). The purified preparation of the vector also contains empty capsids. Depending on the packaging efficiency of the vector and the purification method the number of empty capsids varies (Ayuso et al., 2010b). The CsCI gradient purification method is the most efficient in separating empty capsids from those containing genomes (full capsids) (Ayuso et al., 2010b; Pacak et al., 2006; Scallan, 2006). As described by our laboratory (Ayuso et al., 2010b), the precipitation of proteins with polyethylene glycol (PEG) and purification by CsCI significantly reduce DNA and protein impurities, and empty capsids, increasing the purity of the viral preparation and so, the transduction efficiency *in vivo* of these vectors.

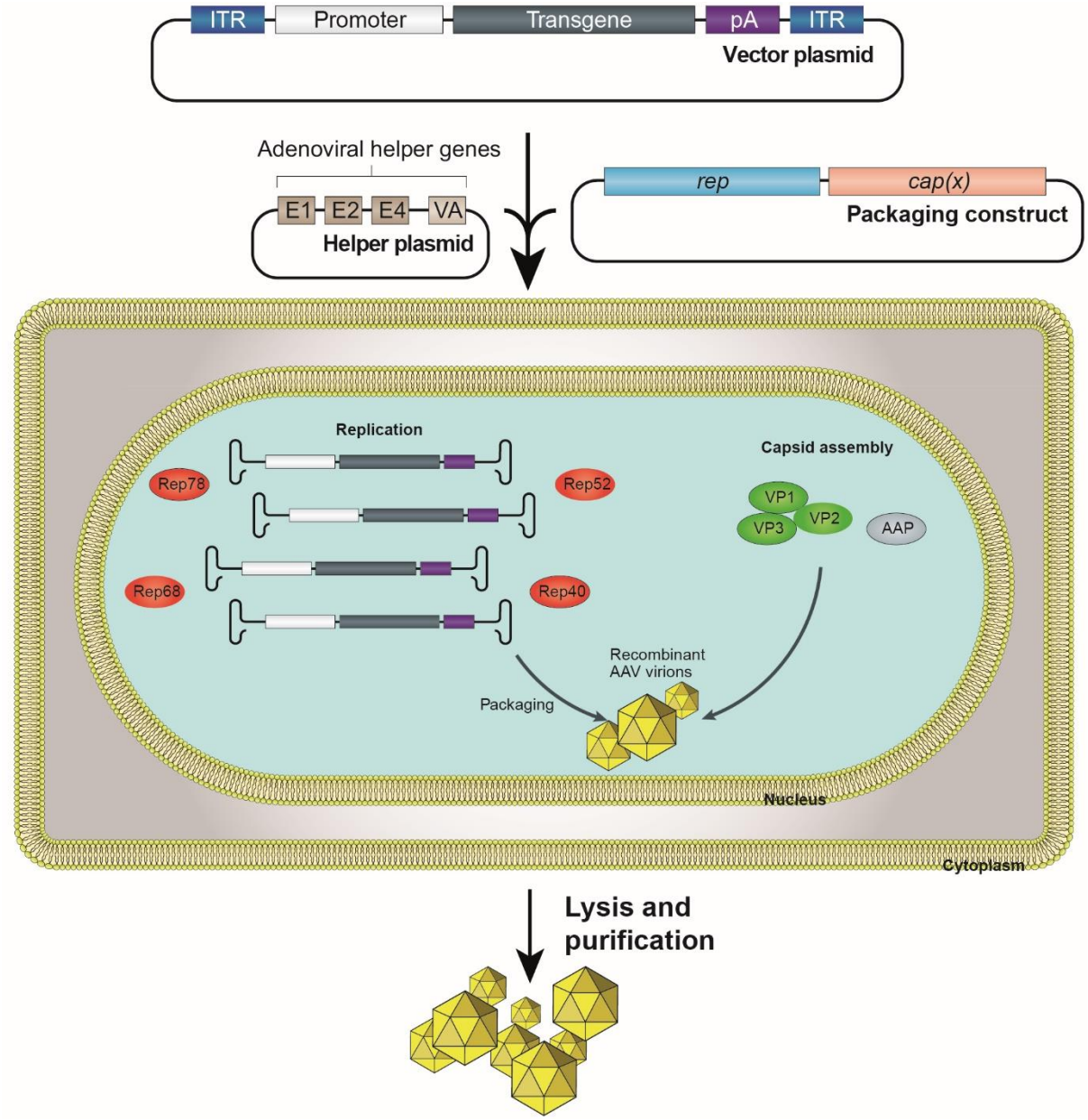


***Figure 10. Triple transfection method to produce recombinant AAV (rAAV)***. Cells are transfected with three different plasmids: the vector plasmid, in which viral Rep and Cap ORFs has been replaced by the viral packing signals (ITRs) flankered transgene, the packaging construct, which provide Rep and Cap genes in *trans*, and lately the helper plasmid, which provides the auxiliary adenoviral functions necessary for the production of AAVs. Subsequently, the vector particles are obtained from the cellular lysate and purified by density gradient or other methods to obtain the full capsids (Adapted from Kotterman and Schaffer, 2014).

The characteristics of the main serotypes of AAV vectors used in gene therapy are described in Table 1. The differences among the various AAV serotypes reside in the capsid proteins (VP1, VP2, and VP3), which with the different cellular receptors and co-receptors determine the binding affinity, affecting its preferential cellular tropism and conferring the infectivity differences among serotypes (Balakrishnan and Jayandharan, 2014).

| Serotype | Origin | Receptor and co-receptors | Tissue Tropism |
|---|---|---|---|
| AAV1 | Human or NHP | N-linked sialic acid | Liver[1], SK[1,2,3], CNS[1,2], respiratory tract[1,2], retina[1], pancreas[1], heart[1,4] |
| AAV2 | Human | HSPG, FGFR1, HGFR, LamR, CD9, integrin $\alpha_v\beta_5$, $\alpha_5\beta_1$, | Liver[1], SK[1], CNS[1], retina[1,2,3], kidney[1] |
| AAV3 | Human or NHP | HSPG, FGFR, HGFR, LamR | Liver[5], HCC[6], SK[1], or inner ear |
| AAV4 | NHP | O-linked sialic acid | CNS[1], retina[1,3], lung[1,2], kidney[1] |
| AAV5 | Human | N-linked sialic acid, PDGFR | Liver, SK[1], CNS[1,3], lung[1,2], retina[1] |
| AAV6 | Human | HSPG, N-linked sialic acid | SK[1,3], heart[1,3,4,7], pancreas[1], respiratory tract[1,2,3] |
| AAV7 | Rhesus macaque | Unknown | Liver[1], SK[1], CNS[1], retina[1] |
| AAV8 | Rhesus macaque | LamR | Liver[1,2,3], heart[1], SK[1], CNS[1,2,3], pancreas[1], retina[1,3], kidney[1], adipose tissue[1] |
| AAV9 | Human | N-linked glycans, LamR | Liver[1], heart[1,2,4], SK[1,3], lung[1], CNS[1,2], pancreas[1], retina[1,2], kidney[1], testicle[1], adipose tissue[1] |
| AAV10 | NHP | Unknown | Liver |
| AAVrh10 | Rhesus macaque | LamR | Liver[1], heart[1], SK[1,3], lung[1], CNS[1,8], pancreas[1], retina[1], kidney[1] |
| AAV11 | NHP | Unknown | Liver |
| AAV12 | NHP | Unknown | Liver[1], heart[1], SK[1,3], lung[1], CNS[8], pancreas[1], retina[1], kidney[1] |

***Table 1. Characteristics of the main serotypes of AAV vectors currently used in gene therapy.*** The differences among serotypes are driven by variations in the capsid proteins (VP1, VP2, and VP3), which determine the cellular tropism by modifying the binding affinity with the different cellular receptors and co-receptors. Tissue tropism in mouse[1], NHP[2], dog[3], pig[4], monkey[4], human[6], sheep[7], rat[8]. NHP, non-human primate; HSPG, heparan sulfate proteoglycan; LamR, 37/67 kDa laminin receptor; FGFR1, fibroblast growth factor receptor 1; HGFR, hepatocyte growth factor receptor, PDGFR, platelet-derived growth factor receptor; EGFR, epidermal growth factor receptor; SK, skeletal muscle; CNS, central nervous system; HCC, hepatocellular carcinoma. Adapted from Balakrishnan and Jayandharan, 2014.

## 5.3. AAV-mediated gene transfer to adipose tissue

In recent years, the genetic manipulation of adipose tissue has been evaluated by means of adeno-associated vectors through various routes of administration.

### *5.3.1. Intra-depot administration*

The route of administration of the AAVs can significantly influence the transduction efficiency of fat depots. In particular, intra-depot administration of eWAT and iWAT has shown high efficient transduction of adipocytes, and the predominant modification of the injected depot (Jimenez et al., 2013). Moreover, the intra-depot administration of BAT has also resulted in a high rate of transduction of brown adipocytes (Jimenez et al., 2013). However, the intra-eWAT, intra-iWAT or intra-iBAT administration with AAV8 and AAV9 resulted in transduction of the liver and heart (Jimenez et al., 2013). To confine the expression of the transgene to adipose tissue, tissue-specific promoters can be used. The adipose-specific mini-aP2 promoter drives transgene expression to adipocytes (Jimenez et al., 2013). The mini-aP2 promoter is composed of the basal promoter and the adipocyte-specific enhancer of aP2 (Graves et al., 1992; Ross et al., 1990). On the other hand, the mini/UCP1 promoter drives the transgene expression specifically in brown adipocytes (Jimenez et al., 2013). This promoter comprises the basal promoter and the adipose-specific enhancer of rat UCP1 (Cassard-Doulcier et al., 1998; Larose et al., 1996).

However, the levels of expression of the transgene when the mini-aP2 or mini/Ucp1 promoters are used have been described to be low in comparison with those obtained with promoters from viral or synthetic origin, such as the CAG promoter (Jimenez et al., 2013). An alternative strategy to restrict the expression of the transgene to the adipose tissue when AAV vectors are administered in intra-depot is to include in the expression cassettes target sequences of miRNAs (miRT) from tissues in which transgene expression wants to be prevented (Jimenez et al., 2013, 2018).Thus, although the cell gets transduced, if the expression cassette contains target sequences for the specific miRNA of the cell type, transcription will be avoided. Nonetheless, if in the target tissue there is no miRNA complementary to the target sequences, the protein of interest encoded in the expression cassette will be translated. AAV8 has been defined as a vector with a high tropism for the liver and heart (Gao et al.; Wang et al., 2010; Zincarelli et al., 2008). Therefore, the addition to the 3' UTR end of the expression cassette of tandem repeats of target sequences of miR-122a and miR-1, which selectively detarget transgene expression from liver and

heart, represses and avoids the expression of the transgene in these tissues (Jimenez et al., 2013, 2018; Mallol et al., 2017).

### *5.3.2. Intravenous administration*

Different serotypes of adeno-associated vectors have been tested to transduce adipose tissue using other routes of administration. The AAV8 and AAV9 serotypes are those that show greater transduction of adipose tissues, achieving the transduction of all adipose deposits in both healthy and obese mice through intravenous systemic administration (Jimenez et al., 2013). Other groups have also reported the robust transduction of white and brown adipocytes in adult mice after the intravenous administration and AAV8 and AAV9 serotypes (Liu et al., 2014; O'Neill et al., 2014). To restrict transgene expression into the adipose tissue, the CAG-dmiRT strategy with the target sequences of miR-122a and miR-1 can also be used in the systemic administration approach (Jimenez et al., 2013).

# III. OBJECTIVES

Obesity and type 2 diabetes (T2D) are two closely related pathologies, the incidence of which has grown exponentially, reaching epidemic proportions in the last decade. Obesity is largely due to a continuous imbalance between energy intake and expenditure. Among other therapeutic strategies, the enhancement of non-shivering thermogenesis to increase metabolic rate through activation of brown adipose tissue (BAT) or via browning of white adipose tissue (WAT) may hold great potential for the future treatment of obesity and T2D. However, activation of BAT and, particularly browning of WAT are not well understood. Hence, more studies to untangle the molecular mechanisms underlying non-shivering thermogenesis are needed. Cold exposure is the unique physiological stimulus that activates thermogenesis both in mice and humans. Microarray analysis of cold-exposed mice could elucidate transcriptomic changes that lead to cold adaptation.

Therefore, the general aim of this thesis was **to fully characterize the transcriptomic profile of white and brown adipose tissue depots during non-shivering thermogenesis**. This general aim was divided into the following specific aims:

1. To perform a comparative transcriptional analysis of eWAT, iWAT, and iBAT in mice after cold exposure.

2. To unravel novel genes potentially involved in non-shivering thermogenesis by analyzing transcriptomic data.

3. To study the effect of the overexpression of key genes identified during the transcriptomic analysis in the adipose tissue of HFD-fed mice.

# IV. RESULTS

# Section I. Study of the response of adipose tissue depots to cold exposure

# 1. GENE EXPRESSION ANALYSIS IN ADIPOSE TISSUE SAMPLES FROM COLD-EXPOSED MICE

It has been described that both cold exposure and $\beta_3$-adrenergic stimulation are potent inducers of non-shivering thermogenesis through activation of BAT and browning of WAT in mice (Chartoumpekis et al., 2011; Lee et al., 2012; Lim et al., 2012). In humans, cold exposure has also been described to activate BAT and the browning of WAT, inducing an increase in energy expenditure (Huttunen et al., 1981; Ouellet et al., 2012; Saito et al., 2009). However, the use of $\beta_3$-adrenergic receptor agonists to activate the BAT has been described with limited success in humans, probably due to differences in the binding characteristics of rodent and human $\beta_3$-adrenergic receptors (Arch, 2008; Clapham and Arch, 2007). Therefore, for a better understanding of the browning of WAT and activation of BAT, and to potentially identify novel intrinsic factors capable of triggering thermogenesis with relevance to humans, this study has focused on the use of cold as a stimulant of non-shivering thermogenesis.

The browning of the WAT occurs in subcutaneous WAT after exposure to cold for 7-10 days in C57Bl6 mice (Vitali et al., 2012; Xue et al., 2009). Nevertheless, after 1 day of cold exposure, rapid induction of thermogenic genes such as *Ucp1* expression occurs in iWAT of 129Sv mice, a strain characterized by their elevated capacity to induce browning of WAT (Barbatelli et al., 2010). The maximal induction of thermogenic genes is reached after 3 days in cold exposure in subcutaneous WAT of 129Sv mice and after 4 days in C57Bl/6 mice (Barbatelli et al., 2010, Jia et al., 2016). Regarding BAT, UCP1 gene expression is highly enhanced after 2 hours of cold exposure, obtaining its maximum expression 24 h after starting cold exposure (Nedergaard and Cannon, 2013).

The browning capacity varies between WAT depots in rodents. In the subcutaneous iWAT, a large accumulation of beige adipocytes can be identified during cold exposure but is rather seldom detected in epididymal/perigonadal adipose tissue (Seale et al., 2011). Hence, for a better study of the browning process and BAT activation, and to identify genes able to induce non-shivering thermogenesis, a comparative transcriptomic analysis between iBAT, inguinal and epididymal fat pads of animals exposed to either cold or to room temperature was carried out.

In this study to analyze the effect of cold exposure on different adipose tissue depots, male 8-week-old C57Bl/6 mice were either exposed to 4ºC or maintained at room temperature (RT) (22 ºC) for 4 days (Figure 11). Body weight and glycemia were measured before and

after cold exposure. Afterward, animals were euthanized and different adipose tissue depots were collected and weighed (Figure 11). iBAT was harvested as an easily accessible depot mainly composed of brown adipocytes, which are known to be highly thermogenic. The iWAT depot was collected as a depot that has been described as having an inducible thermogenic capacity due to the appearance of beige adipocytes under several stimuli. Finally, eWAT was harvested, as it is a well-defined white adipose depot that is more resistant to browning. Next, RNA was extracted from these depots and hybridized to a microarray to quantify gene expression levels (Figure 11).

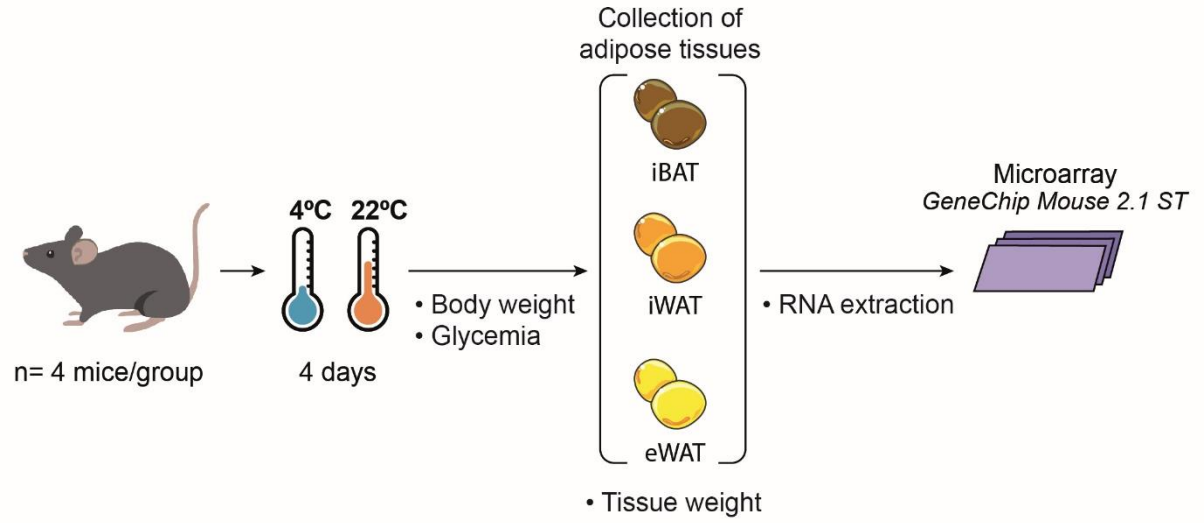


***Figure 11. Experimental Design***. C57Bl/6 mice were either exposed to cold (4ºC) or room temperature (22ºC) for 4 days. Body weight and glycemia were measured before and after cold challenge. Different adipose tissue depots (iBAT, iWAT, and eWAT) were collected from each animal and weighed. RNA was extracted for further microarray analysis using the GeneChip 2.1 ST array.

As expected, the body weight of the animals exposed to RT was not modified after 4 days (Figure 12A, B). In contrast, mice exposed to cold decreased their body weight around 6% (Figure 12A, B). Cold exposure also significantly increased the glycemia of the mice after 4 days, while the animals housed at 22ºC presented similar values, although all animals showed normoglycemic values (Figure 12 C).

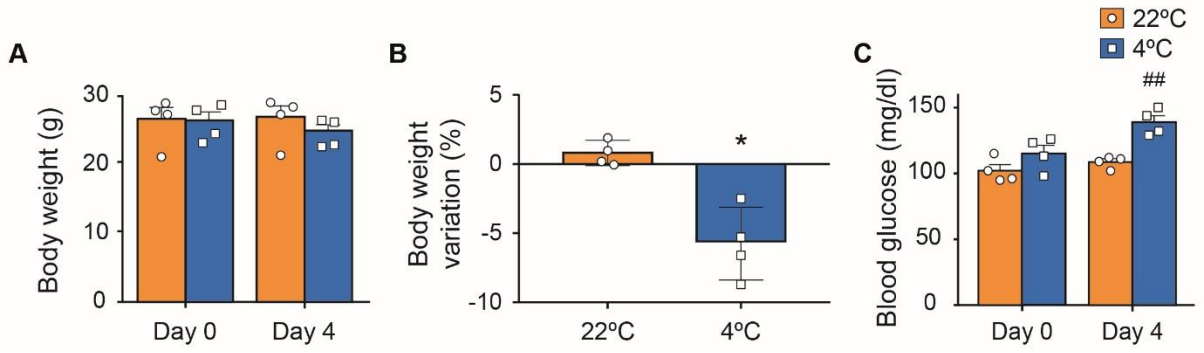


***Figure 12. Assessment of body weight before and after being exposed for 4 days to either 22 or 4ºC.*** C57Bl/6 mice were either exposed to cold (4ºC) or room temperature (22ºC) for 4 days. Body weight and glycemia were measured before and after cold and room temperature exposure. **(A)** Measurements of body weight. **(B)** body weight variation after 4 days of room temperature or cold exposure. **(C)** Blood glucose levels were also measured before and after 22ºC or 4ºC exposure for 4 days. Results are expressed as mean ± SEM. n=4 mice per group. *P <0.05 versus animals exposed to 22ºC. ##P <0.01 versus animals exposed during 4 days at 22ºC.

Adipose tissue depots from mice exposed to either cold or RT presented small differences in tissue weight. When tissue weight was measured and normalized as a percentage of body weight, eWAT of cold-exposed mice showed a lower weight, although not significantly do, in comparison with the same depot of RT-exposed mice. In contrast, iBAT of cold-exposed mice presented a tendency to increase its weight (Figure 13).

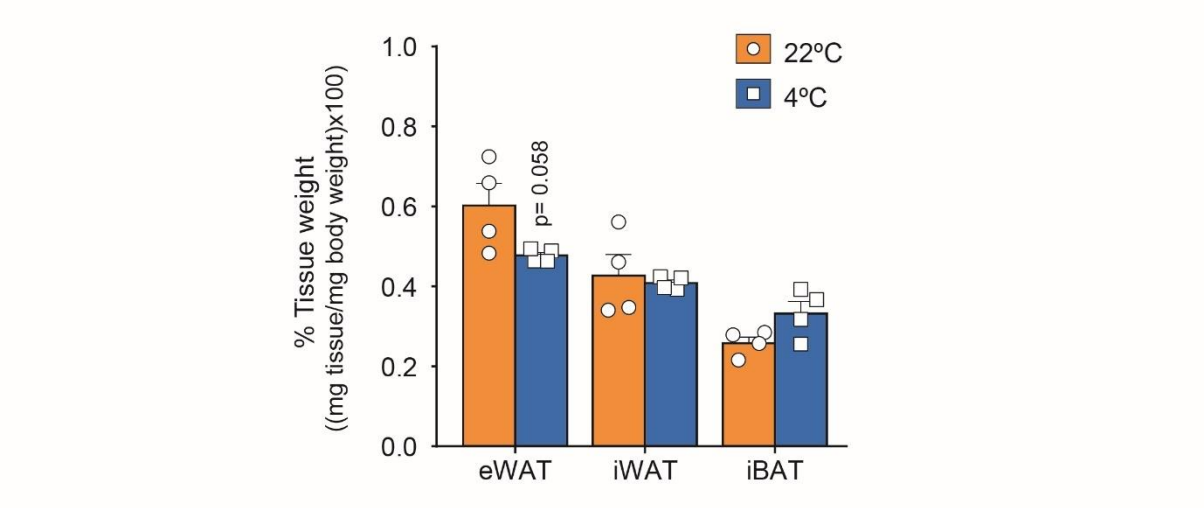


***Figure 13. Adipose tissue depots weight.*** C57Bl/6 mice were either exposed to cold (4ºC) or room temperature (22ºC) for 4 days and, after euthanasia, adipose tissue depots were collected and weighed. Results are expressed as mean ± SEM. n=4 mice per group.

To confirm that 4 days of cold exposure induced the expression of thermogenic genes in iWAT tissue, RNA was extracted and the expression levels of *Ucp1* and *Cidea* were measured by RT-qPCR analyses (Figure 14). Up-regulation of the expression of both genes was observed in the iWAT depot of these mice (Figure 14).

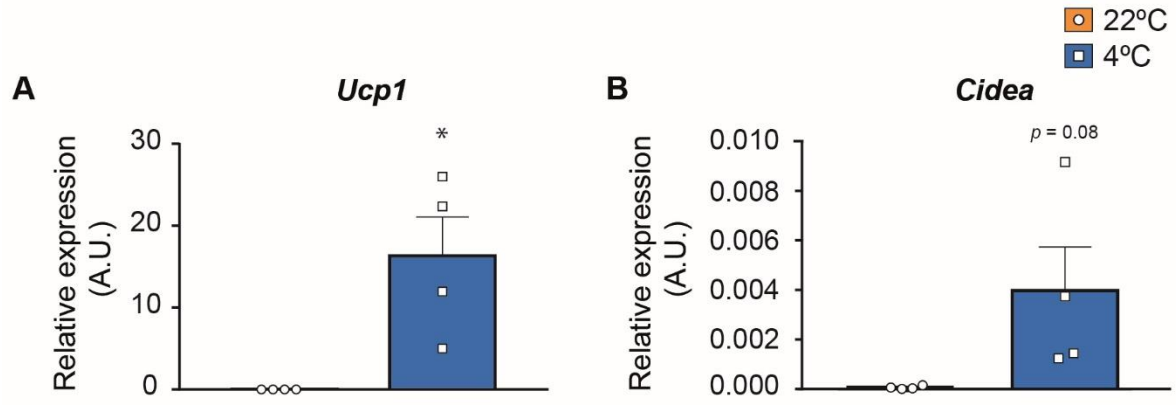


***Figure 14. Expression levels of the thermogenic-related genes Ucp1 and Cidea in iWAT.*** Male C57Bl/6 mice were exposed either to 4ºC or 22ºC for 4 days. RNA from IWAT was extracted and expression levels of **(A)** *Ucp1* and **(B)** *Cidea* were measured by RT-qPCR analysis. AU: Arbitrary Units. The results are expressed as the mean ± SEM. n = 8-10 per experimental group. *P <0.05 versus animals exposed to 22ºC.

In order to analyze the whole gene expression, microarray technology was used. Hence, RNA was extracted from eWAT, iWAT, and iBAT and its quality was evaluated. Due to the good quality of RNA, this was processed to hybridize the microarray GeneChip® 2.1 ST from Affymetrix. Then, the microarray was washed and scanned, and quality control of the obtained values was performed (as explained in VII. MATERIALS AND METHODS). As microarray quality control indicated that data had good quality and there was no bias in the data due to the hybridization, revealing, washing or scanning processes gene expression analyses were then performed.

## 1.1. Exploratory Data Analysis of gene expression patterns

### *1.1.1. Principal Component Analysis*

Gene expression data were then analyzed using *Principal Component Analysis* (PCA) (Figure 16A) as E*xploratory Data Analysis* (EDA). EDA is commonly used for preliminary data analysis, uncovering key features of the data such as patterns and spotting anomalies, such as those triggered by cold exposure. Among other EDA, PCA is a statistical procedure that allows the visualization of the variance by reducing the number

of dimensions of the data. This mathematical method transforms a number of possibly correlated variables into a smaller number of uncorrelated variables called principal components (PC), which equals the number of variables the data have (24 in our study). Components capture all sources of variation and are ranked from high to low, PC1 being the one with the most variability. Each following component has as much of the remaining variability as possible.

The number of PC retained in the visualization (Figure 16A) were chosen based on two extensively used criteria: (1) the retained PC should explain 70% or more of the total amount of variance, and (2) the minimum number of PC should be the one located before the "elbow" of the scree plot of variation (Figure 16B, arrow). PC1 was composed of 59.6% of the variance of all the data, while PC2 was composed of 10.2%. Then, since the sum of PC1 and PC2 variance was almost 70%, and the "elbow" of the scree plot (Figure 16B, arrow) was between PC2 and PC3, plotting PCA with only these two PC is enough to represent the variation of the entirety of the data (Figure 16A).

PCA analysis indicated that the primary source of variation between the samples was the depot of origin (Figure 16A). Among the samples collected from the same adipose tissue depot, cold exposure was also a notable source of variance mainly explained by PC2 values. Samples exposed to cold had higher PC2 values compared to samples from the same tissue of the animals kept at RT. This effect was clearly observed in iWAT, where all the samples from the cold-exposed animals were placed together and separately from the RT exposed ones. Both in iBAT and eWAT, cold exposure did not have that clear an effect. Even though samples from cold-exposed animals moved in the y-axis, those values could not be entirely separated from samples from RT exposed animals. In conclusion, the depot of origin was the main source of variability of gene expression values and, the iWAT depot seemed to be the one most affected by cold exposure.

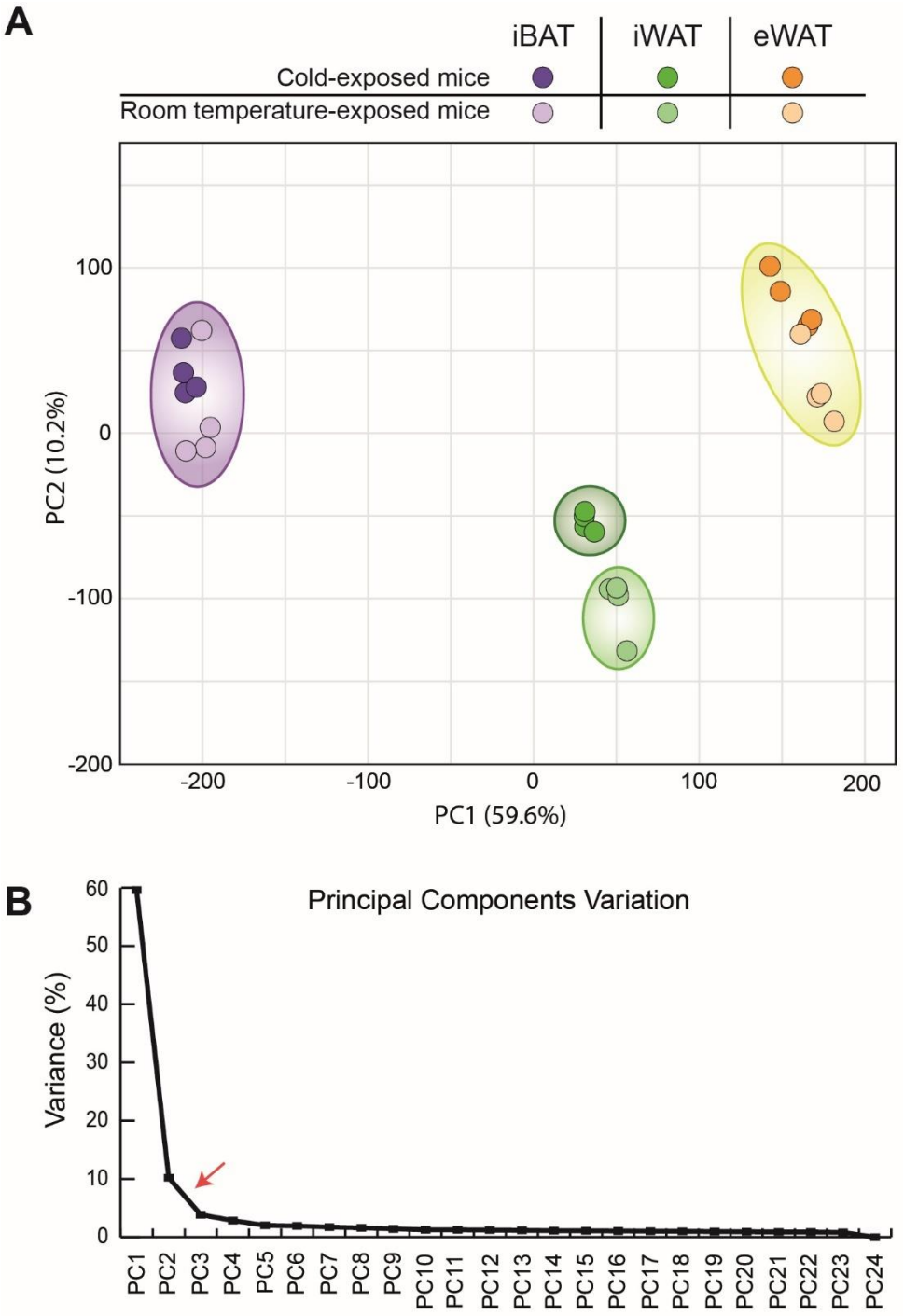


***Figure 16. Visualization of the data variance by Principal Component Analysis (PCA).*** **(A)** PCA score plot of PC1 vs. PC2 for analysis of the different adipose tissue depots from each animal and condition. **(B)** Graphical representation of the variance percentage associated with each principal component. The red arrow indicates the "elbow" of the plot. PC: Principal Component.

### *1.1.2. Correlation Matrix*

After analyzing the principal sources of variance between samples a correlation matrix was created to better determinate the similarities among the different conditions (Figure 17). A correlation matrix is a type of EDA that serves to visualize the correlation coefficient between variables. Each square of the plot indicated the correlation between two samples. This type of analysis is used to summarize and quickly visualize data similarities once these are ordered by resemblance (clustering). Clustering algorithms are a common form of unsupervised learning that group sets of data points into subsets or clusters. The objectives of these algorithms are to create clusters with internal coherency but that are different from each other externally. A correlation matrix was clustered using *hierarchical clustering analysis*. The results of the correlation matrix data indicated that white adipose depots were more similar to one another, even after cold exposure, than as compared to iBAT depot samples. Figure 17 clearly shows that iWAT and eWAT clustered together while iBAT clustered alone. In addition, cold exposure did not produce any major effect on the clustering of either iBAT nor eWAT, as all the samples from these tissues clustered independently of the exposure temperature. However, as in the PCA analysis, data suggested that cold-exposure produced an effect on the gene expression profile of the iWAT depot, reassembling it more consistently with the gene expression pattern of iBAT. Correlation values (representing 1 a perfect positive correlation and 0 no relationship between the two variables) supported this conclusion as the mean of correlation values was 0.97 for inter-iBAT (excluding perfect correlations), 0.93 for iWAT of cold-exposed mice vs iBAT, and 0.91 for iWAT of mice exposed to RT vs iBAT and eWAT vs iBAT. However, while iBAT from both cold and RT-exposed mice clustered together, iWAT from cold-exposed mice was still clustered with the rest of the white adipose depots (Figure 17).

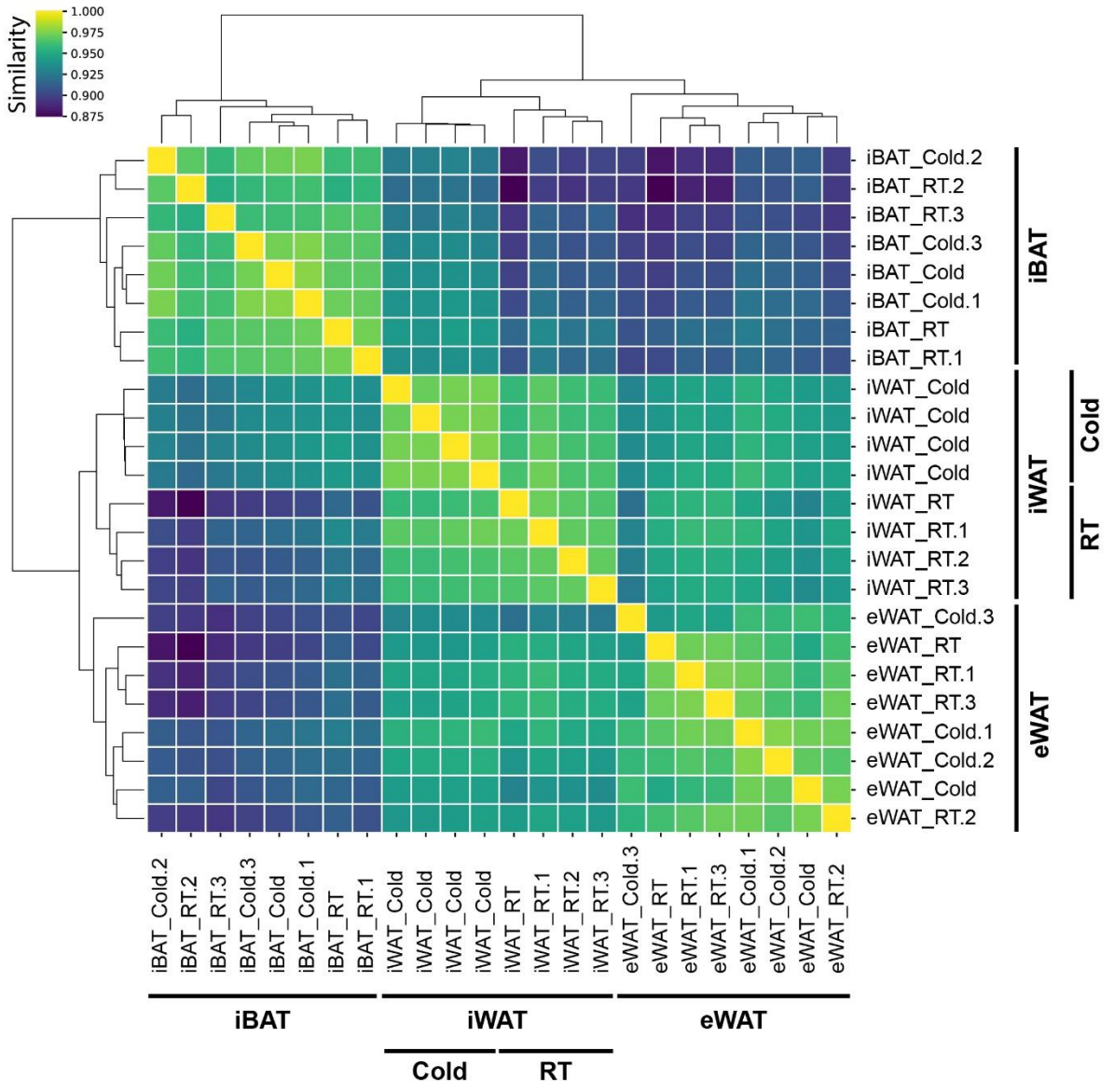


***Figure 17. Correlation matrix of the different adipose tissue depots.*** Dendrogram of the hierarchical clustering (above and on the left of the matrix) revealed the differences and similarities between adipose tissue depots. The Pearson correlation coefficients (r) were represented using a colorimetric scale, indicating 1 a perfect correlation and 0 no correlation between two variables. In yellow the maximum correlation index was represented (r = 1). In blue the minimum correlation index (r = 0.875) was represented. RT: Room temperature.

## 1.2. Differentially expressed genes in adipose depots

Following the exploratory data analysis of gene expression patterns between conditions, gene expression values were studied individually. First, intensity values were normalized by RMA, and chp files were used to perform gene expression analysis using the Applied Biosystems™ TAC software. Using this software, the gene level differential expression analysis was performed to identify genes with different expression levels between conditions, obtaining their statistical values (both ANOVA p-value and the false discovery rate (FDR)). During the analysis, special attention was given to detect differentially expressed genes (DEG), which were the genes whose expression under cold exposure was substantially modified and which showed statistical significance.

The genes that showed differences at gene expression level could be easily visualized by scatter-plot, where statistical significance is represented in the x-axis and magnitude of change in the y-axis (Figure 18A, 19A, and 20A). These scatter-plots are known as volcano plots and allow quick visual identification of how tissues are responding to a stimulus and which genes are the most affected. For this purpose, data was represented in a volcano plot for each depot.

In iBAT, the majority of the identified DEG with statistical significance showed an increased expression in cold-exposed animals in comparison to animals kept at RT (Figure 18A). It was observed that 228 genes were upregulated (highlighted in red) and 79 genes were downregulated (highlighted in green). The most upregulated gene was Mfsd2a with a 19.72-fold change value, followed by Slc25a34, Cyp2b10, Gmpr, and Gm15241 (Figure 18B). Several upregulated genes in the iBAT, such as Bmp8b or Fgf21, have already been described as being induced by cold exposure and to participate in the thermogenic process (Figure 18B). The most downregulated gene was Lctl with a -6.81 fold change value, followed by Svep1, Gpr81, Alb, and 5033411D12Rik (Figure 18B).

**A**

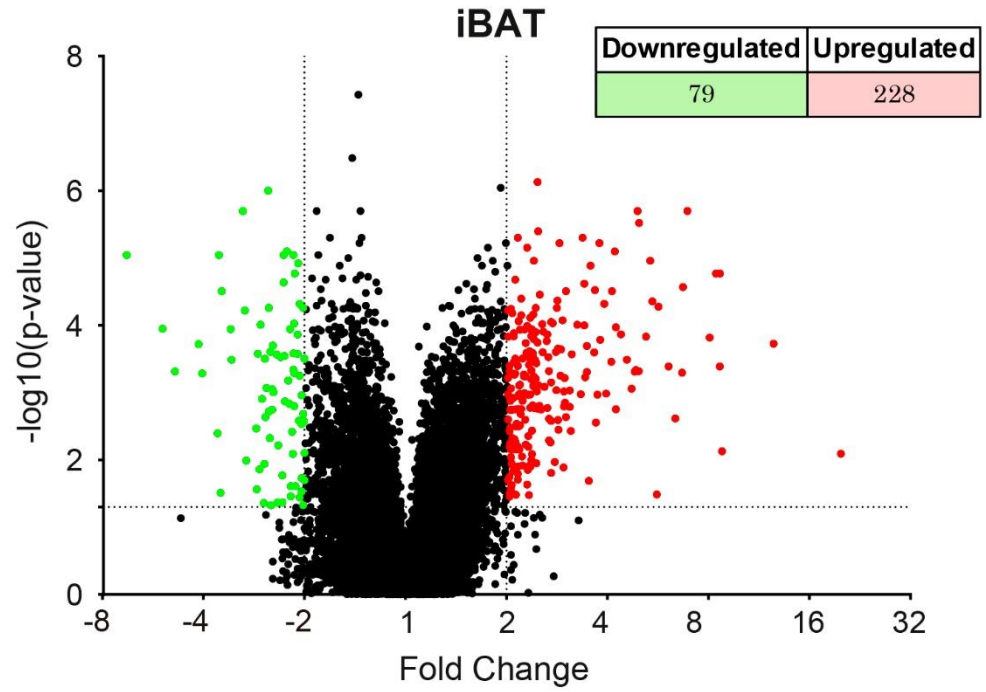


**B**

| Transcript ID | Gene Symbol | Description | FC | p-value |
|---|---|---|---|---|
| 17429632 | Mfsd2a | major facilitator superfamily domain containing 2A | 19.72 | 0.008067 |
| 17432256 | Slc25a34 | solute carrier family 25, member 34 | 12.42 | 0.000187 |
| 17475360 | Cyp2b10 | cytochrome P450, family 2, subfamily b, polypeptide 10 | 8.73 | 0.007423 |
| 17286973 | Gmpr | guanosine monophosphate reductase | 8.6 | 0.000017 |
| 17545756 | Gm15241 | predicted gene 15241 | 8.59 | 0.000407 |
| 17233775 | Tacr2 | tachykinin receptor 2 | 8.37 | 0.000017 |
| 17418141 | Bmp8b | bone morphogenetic protein 8b | 8.02 | 0.000152 |
| 17284114 | Ckb | creatine kinase, brain | 6.88 | 0.000002 |
| 17342999 | Cpne5 | copine V | 6.67 | 0.000027 |
| 17234936 | Hcn2 | hyperpolarization-activated, cyclic nucleotide-gated K+ 2 | 6.63 | 0.000504 |
| 17490899 | Fgf21 | fibroblast growth factor 21; fibroblast growth factor 21-like | 6.33 | 0.002417 |
| 17424279 | Cntfr | ciliary neurotrophic factor receptor | 6.05 | 0.000408 |
| 17459591 | St3gal5 | ST3 beta-galactoside alpha-2,3-sialyltransferase 5 | 5.64 | 0.000053 |
| 17462145 | 8430408G22Rik | RIKEN cDNA 8430408G22 gene | 5.58 | 0.032646 |
| 17458813 | Aqp1 | aquaporin 1 | -3.03 | 0.00006 |
| 17492244 | Ntrk3 | neurotrophic tyrosine kinase, receptor, type 3 | -3.07 | 0.000002 |
| 17358544 | Cd274 | CD274 antigen | -3.32 | 0.000324 |
| 17505863 | Vat1l | vesicle amine transport protein 1 homolog-like (T. californica) | -3.34 | 0.000114 |
| 17404191 | Car3 | carbonic anhydrase 3 | -3.55 | 0.000031 |
| 17229851 | Casq1 | calsequestrin 1 | -3.58 | 0.030833 |
| 17316780 | Angpt1 | angiopoietin 1 | -3.62 | 0.000009 |
| 17548055 | LOC630751 | interferon-inducible GTPase 1-like; cDNA sequence BC023105 | -3.65 | 0.004005 |
| 17218006 | B3galt2 | UDP-Gal:betaGlcNAc beta 1,3-galactosyltransferase, polypeptide 2 | -4.06 | 0.000517 |
| 17290781 | 5033411D12Rik | RIKEN cDNA 5033411D12 gene | -4.16 | 0.00019 |
| 17438886 | Alb | albumin | -4.7 | 0.073351 |
| 17452709 | Gpr81 | G protein-coupled receptor 81 | -4.89 | 0.000483 |
| 17425631 | Svep1 | sushi, von Willebrand factor type A, EGF and pentraxin domain containing 1 | -5.33 | 0.000112 |
| 17518278 | Lctl | lactase-like | -6.81 | 0.000009 |

***Figure 18. Gene expression analysis of the iBAT.*** **(A)** Volcano plot displaying -$\log_{10}$(p-value) vs. fold change of each gene expressed in iBAT, represented by each dot. Red dots highlight the significantly upregulated genes (FC≥2). Green dots highlight the downregulated genes (FC≤-2). The number of significant upregulated and downregulated genes is indicated in the top right corner. **(B)** Table indicating the most affected genes in iBAT, using the same color pattern as in the volcano plot. FC: Fold Change.

A similar number of upregulated and downregulated genes was identified in iWAT tissue, being 241 and 210, respectively (Figure 19A). There were three upregulated genes, *Fabp3-ps1*, *Ucp1,* and *Elovl3*, that stood out among all the others having a fold change value higher than 20 (Figure 19B). In addition, several of the upregulated genes are known to be cold-inducible, such as *Phospho1*, *Gyk* or *Dio2* (Figure 19B). The upregulation of thermogenic and metabolic genes such as *Ucp1*, *Dio2*, *Elovl3*, and *Gyk* confirmed that 4 days of cold exposure enhanced thermogenesis in iWAT. In this tissue, the most downregulated gene was *Ccl8* (-6-fold) (Figure 19B).

In eWAT, a remarkable number of genes were downregulated in response to cold. In particular, 559 genes showed diminished expression levels while only 50 genes had a significantly increased expression over 2-fold (Figure 20A). The identity of several of those downregulated genes was either predicted genes (gene symbol starting with "Gm") or olfactory receptors genes (Figure 20B).

**A**

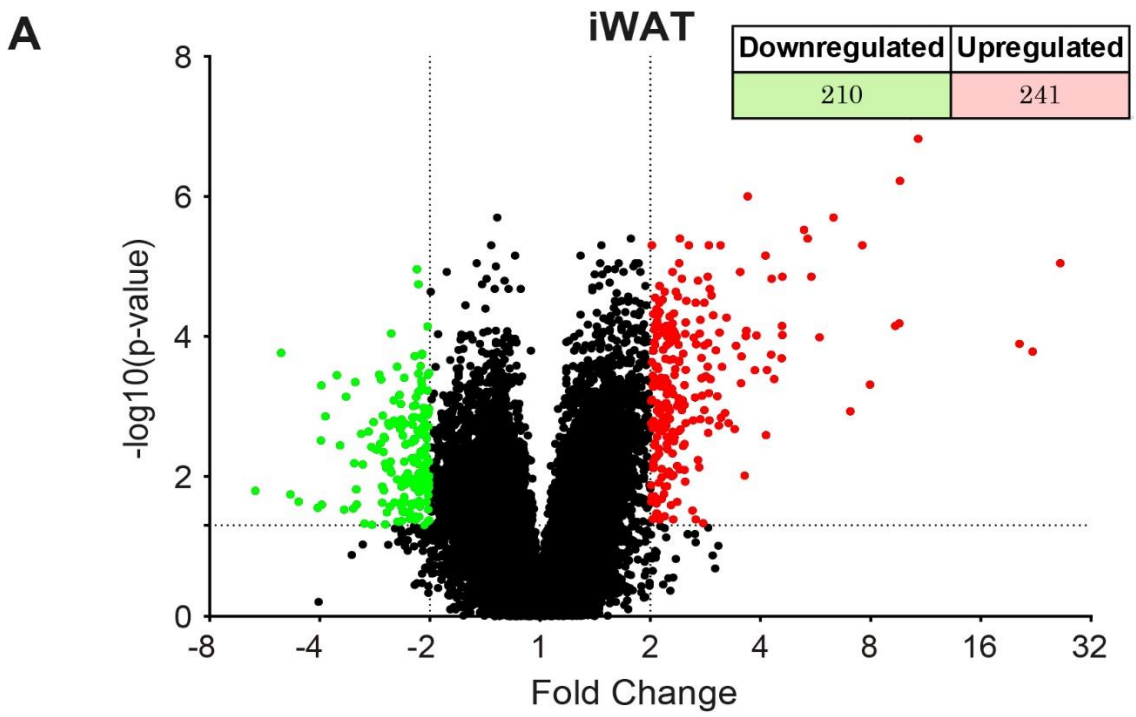


**B**

| Transcript ID | Gene Symbol | Description | FC | p-value |
|---|---|---|---|---|
| 17243761 | Fabp3-ps1 | fatty acid binding protein 3, muscle and heart, pseudogene 1 | 26.38 | 0.000009 |
| 17502899 | Ucp1 | uncoupling protein 1 (mitochondrial, proton carrier) | 22.15 | 0.000165 |
| 17359918 | Elovl3 | elongation of very long chain fatty acids (FEN1/Elo2, SUR4/Elo3, yeast)-like 3 | 20.39 | 0.000128 |
| 17255458 | Phospho1 | phosphatase, orphan 1; zinc finger protein 652 | 10.79 | 0.00000015 |
| 17476288 | Cox7a1 | cytochrome c oxidase subunit VIIa 1 | 9.62 | 0.000000599 |
| 17543045 | Gyk | glycerol kinase | 9.58 | 0.000065 |
| 17329361 | Kng2 | kininogen 2 | 9.34 | 0.000071 |
| 17475360 | Cyp2b10 | cytochrome P450, family 2, subfamily b, polypeptide 10 | 7.97 | 0.00049 |
| 17427860 | Acot11 | acyl-CoA thioesterase 11 | 7.59 | 0.000005 |
| 17282970 | Dio2 | deiodinase, iodothyronine, type II | 7.04 | 0.001177 |
| 17320499 | Chkb | choline kinase beta; carnitine palmitoyltransferase 1b, muscle; cDNA sequence BC0 | 6.33 | 0.000002 |
| 17297750 | Ppif | peptidylprolyl isomerase F (cyclophilin F) | 5.8 | 0.000103 |
| 17464654 | Pdk4 | pyruvate dehydrogenase kinase, isoenzyme 4 | 5.51 | 0.000014 |
| 17315033 | Letmd1 | LETM1 domain containing 1 | 5.38 | 0.000004 |
| 17455801 | Col1a2 | collagen, type I, alpha 2 | -3.39 | 0.000726 |
| 17550576 | mt-Tl2 | mitochondrially encoded tRNA leucine 2 | -3.43 | 0.029989 |
| 17493949 | Folr2 | folate receptor 2 (fetal) | -3.52 | 0.003614 |
| 17411147 | Ifi44 | interferon-induced protein 44 | -3.59 | 0.00036 |
| 17236811 | Lum | lumican | -3.86 | 0.001389 |
| 17532635 | mt-Tt | mitochondrially encoded tRNA threonine | -3.95 | 0.025304 |
| 17548532 | Col1a2 | collagen, type I, alpha 2 | -3.96 | 0.000503 |
| 17450501 | Gbp10 | guanylate-binding protein 10 | -3.97 | 0.003072 |
| 17284512 | Ighv1-9 | immunoglobulin heavy variable v1-9 | -4.03 | 0.623212 |
| 17550580 | mt-Tt | mitochondrially encoded tRNA threonine | -4.05 | 0.028205 |
| 17532629 | mt-Ts2 | mitochondrially encoded tRNA serine 2; mitochondrially encoded tRNA leucine 2 | -4.57 | 0.023001 |
| 17550572 | mt-Ts2 | mitochondrially encoded tRNA serine 2 | -4.81 | 0.018165 |
| 17212461 | Col3a1 | collagen, type III, alpha 1 | -5.1 | 0.000172 |
| 17254065 | Ccl8 | chemokine (C-C motif) ligand 8; c-C motif chemokine 8-like | -6 | 0.01613 |

***Figure 19. Gene expression analysis of the iWAT.*** **(A)** Volcano plot displaying -$\log_{10}$(p-value) vs. fold change of each gene expressed in iWAT, represented by each dot. Red dots highlight the significantly upregulated genes (FC≥2). Green dots highlight the downregulated genes (FC≤-2). The number of significant upregulated and downregulated genes is indicated in the top right corner. **(B)** Table indicating the most affected genes in iWAT, using the same color pattern as in the volcano plot. FC: Fold Change.

**A**

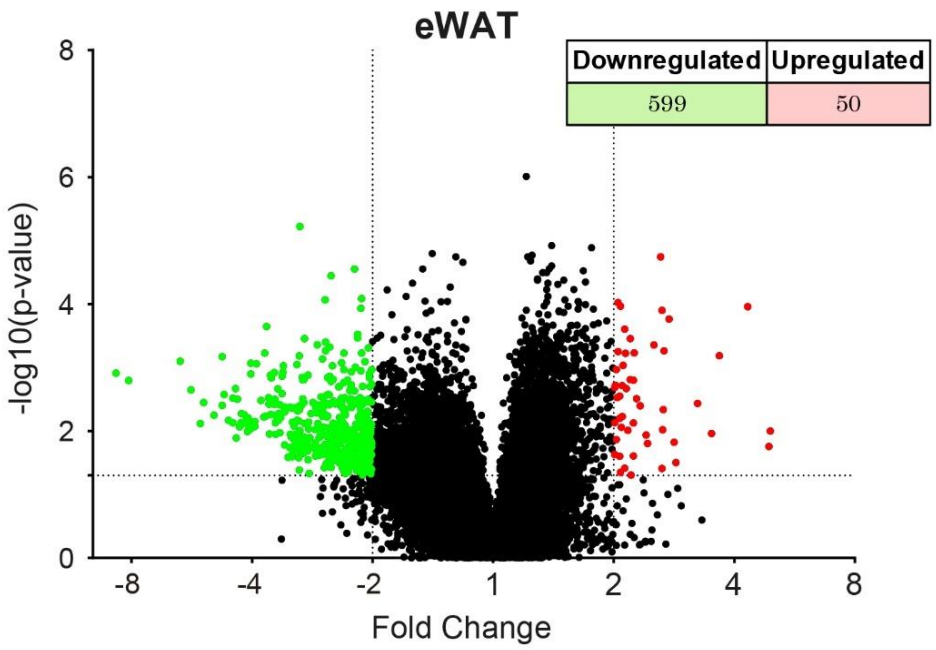


**B**

| Transcript ID | Gene Symbol | Description | FC | p-value |
|---|---|---|---|---|
| 17502899 | Ucp1 | uncoupling protein 1 (mitochondrial, proton carrier) | 4.92 | 0.010001 |
| 17514326 | Gm10722 | predicted gene 10722 | 4.88 | 0.017464 |
| 17497704 | Cox8b | cytochrome c oxidase subunit VIIIb | 4.32 | 0.00011 |
| 17472497 | Gys2 | glycogen synthase 2 | 3.67 | 0.000652 |
| 17373634 | Gm10801 | predicted gene, 10801 | 3.51 | 0.01096 |
| 17382224 | Pax8 | paired box gene 8 | 3.32 | 0.252416 |
| 17421875 | Slc2a5 | solute carrier family 2 (facilitated glucose transporter), member 5 | 3.24 | 0.003666 |
| 17284507 | Igh-VJ558 | immunoglobulin heavy chain (J558 family) | 2.95 | 0.15088 |
| 17516699 | Mpzl2 | myelin protein zero-like 2 | 2.89 | 0.080161 |
| 17514352 | Gm17535 | predicted gene, 17535 | 2.86 | 0.031456 |
| 17514346 | Gm10106* | predicted gene 10106 | 2.83 | 0.015039 |
| 17502233 | Slc27a1 | solute carrier family 27 (fatty acid transporter), member 1 | 2.75 | 0.000172 |
| 17235292 | Rps15 | ribosomal protein S15; 40S ribosomal protein S15-like | 2.73 | 0.099928 |
| 17266302 | Pipox | pipecolic acid oxidase | 2.7 | 0.604116 |
| 17546695 | Gm21627* | predicted gene, 21627 | -4.98 | 0.005629 |
| 17546702 | Gm21627* | predicted gene, 21627 | -4.98 | 0.005629 |
| 17546710 | Gm20736* | predicted gene, 20736 | -4.98 | 0.005629 |
| 17546719 | Gm20824* | predicted gene, 20824 | -4.98 | 0.005629 |
| 17547034 | Gm20824* | predicted gene, 20824 | -4.98 | 0.005629 |
| 17547071 | Gm21088* | predicted gene, 21088 | -4.98 | 0.005629 |
| 17547151 | Gm20824* | predicted gene, 20824 | -4.98 | 0.005629 |
| 17547158 | Gm21627* | predicted gene, 21627 | -4.98 | 0.005629 |
| 17550576 | mt-Tl2 | mitochondrially encoded tRNA leucine 2 | -5.28 | 0.003559 |
| 17407494 | Gm22577 | Predicted geme, 22577 | -5.39 | 0.007616 |
| 17540741 | Gm14527* | predicted gene 14527 | -5.68 | 0.002249 |
| 17540739 | Gm14527* | predicted gene 14527 | -6.05 | 0.000796 |
| 17532629 | mt-Ts2* | mitochondrially encoded tRNA serine 2 | -8.13 | 0.001602 |
| 17550572 | mt-Ts2 | mitochondrially encoded tRNA serine 2 | -8.75 | 0.001224 |

***Figure 20. Gene expression analysis of the eWAT.*** **(A)** Volcano plot displaying -$\log_{10}$(p-value) vs. fold change of each gene expressed in eWAT, represented by each dot. Red dots highlight the significantly upregulated genes (FC≥2). Green dots highlight the downregulated genes (FC≤-2). The number of significant upregulated and downregulated genes is indicated in the top right corner. **(B)** Table indicating the most affected genes in eWAT, using the same color pattern as in the volcano plot. FC: Fold Change; *: probe that can detect more genes other than the principal.

### *1.2.1. Set relationship analyses of differentially expressed genes in iBAT, iWAT, and eWAT*

To further characterize the response of iBAT, iWAT, and eWAT to cold challenge, the relation between DEGs and the adipose depots was studied. For this purpose, *set relationship analyses* represented using Venn Diagrams were performed to identify which DEGs (Figure 18, 19, and 20) were common to more than one of the depots (Figure 21). All the adipose tissue depots studied had some DEGs in common (Figure 21). In the set comprised of white adipose depots (iWAT and eWAT), 65 DEGs appeared, 14 upregulated and 51 downregulated (Figure 21). The iBAT had 51 upregulated and 4 downregulated genes in common with iWAT and 2 upregulated and 2 downregulated genes in common with eWAT (Figure 21). Five DEGs, *B430219N15Rik*, *Scd3*, *Phospho1*, *Lep*, and LOC630751, appeared in all depots (Figure 21).

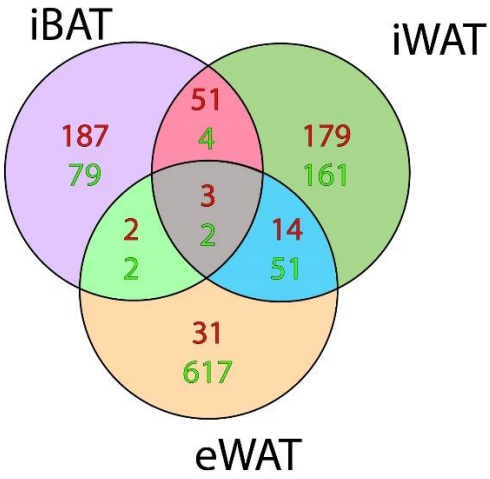


***Figure 21. Set relationship analysis.*** **(A)** Number of upregulated or downregulated genes for each tissue. **(B)** Set relationship analysis reporting the number of DEGs that were common, or not, to the different adipose tissue depots. Highlighted in red: number of upregulated DEGs; Highlighted in green: number of downregulated DEGs.

### *1.2.2. Functional analysis of differentially expressed genes*

The previous results indicated that cold exposure is a potent stimulus that triggers a differential gene expression in the studied fat depots. Therefore, several functional analyses were performed to elucidate the main pathways and gene ontologies affected in all DEGs. First, *pathway enrichment analysis* of all the genes that presented a modified expression in any of the studied tissues was performed. The 15 most significantly enriched pathways were mainly metabolism and related pathways (Figure 22). In particular, central metabolic pathways like the tricarboxylic acid cycle (TCA) with the respiratory electron transport chain were clearly enriched. Moreover, lipid metabolism was strongly

enhanced, with pathways related to fatty acid metabolism, β-oxidation and fatty acid elongation showing very significant p-values. In addition, carbon and pyruvate metabolism were also included in the top-15 significant enriched pathways.

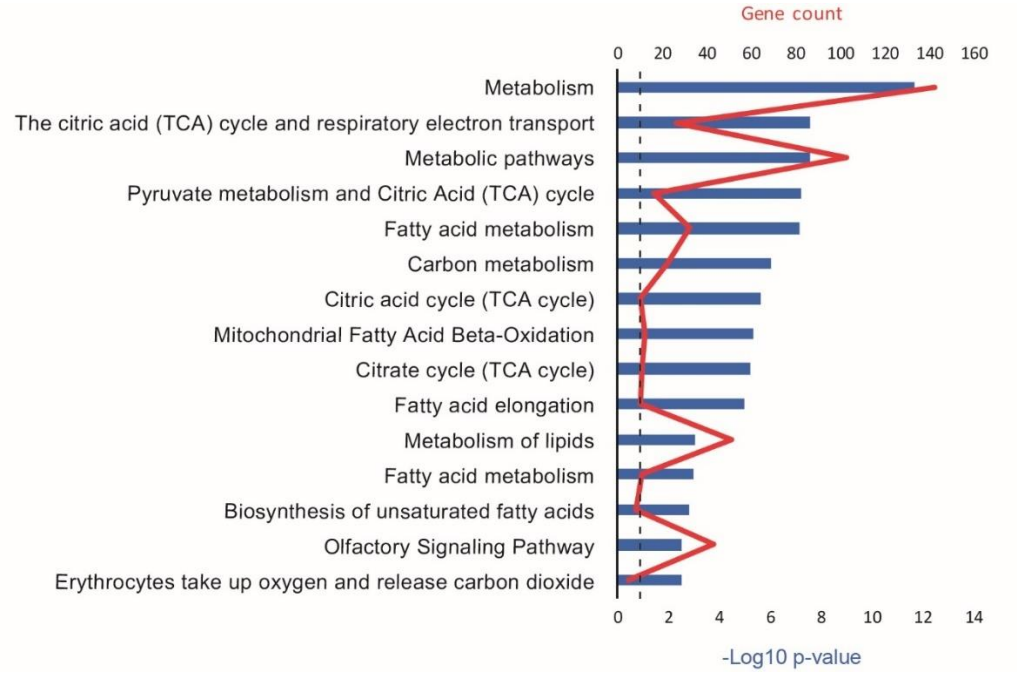


***Figure 22. Most significative enriched pathways of both upregulated and downregulated differentially expressed genes among all the samples.*** -$Log_{10}$ of the p-value is indicated using the bar chart, and the number of enriched genes of each pathway is shown by the line chart. -$Log_{10}$ of 0.05 p-value is indicated by the dashed line.

The results obtained in the *pathway enrichment analysis* were correlated with those obtained by the *gene ontology analysis* (Figure 23). The *gene ontology analysis* elucidates which gene ontology (GO) terms are over-represented in a given set of genes. We found that metabolism played a central role in adaptation to cold challenge in adipose depots (Figure 23). The main over-represented gene ontology was monocarboxylic acid metabolism, which includes: fatty acid metabolic process, lipid carbolic process, tricarboxylic acid metabolic process, and NADH metabolic process.

Other metabolic processes, such as coenzyme metabolism or cofactor metabolism, were also observed in this analysis (Figure 23). Moreover, the cellular response to the different stimulus was reflected in the "response to organic substances", the "sensory perception of chemical stimulus", and the "response to stimulus" gene ontologies. Finally, mitochondrial transport was also over-represented among the DEGs.

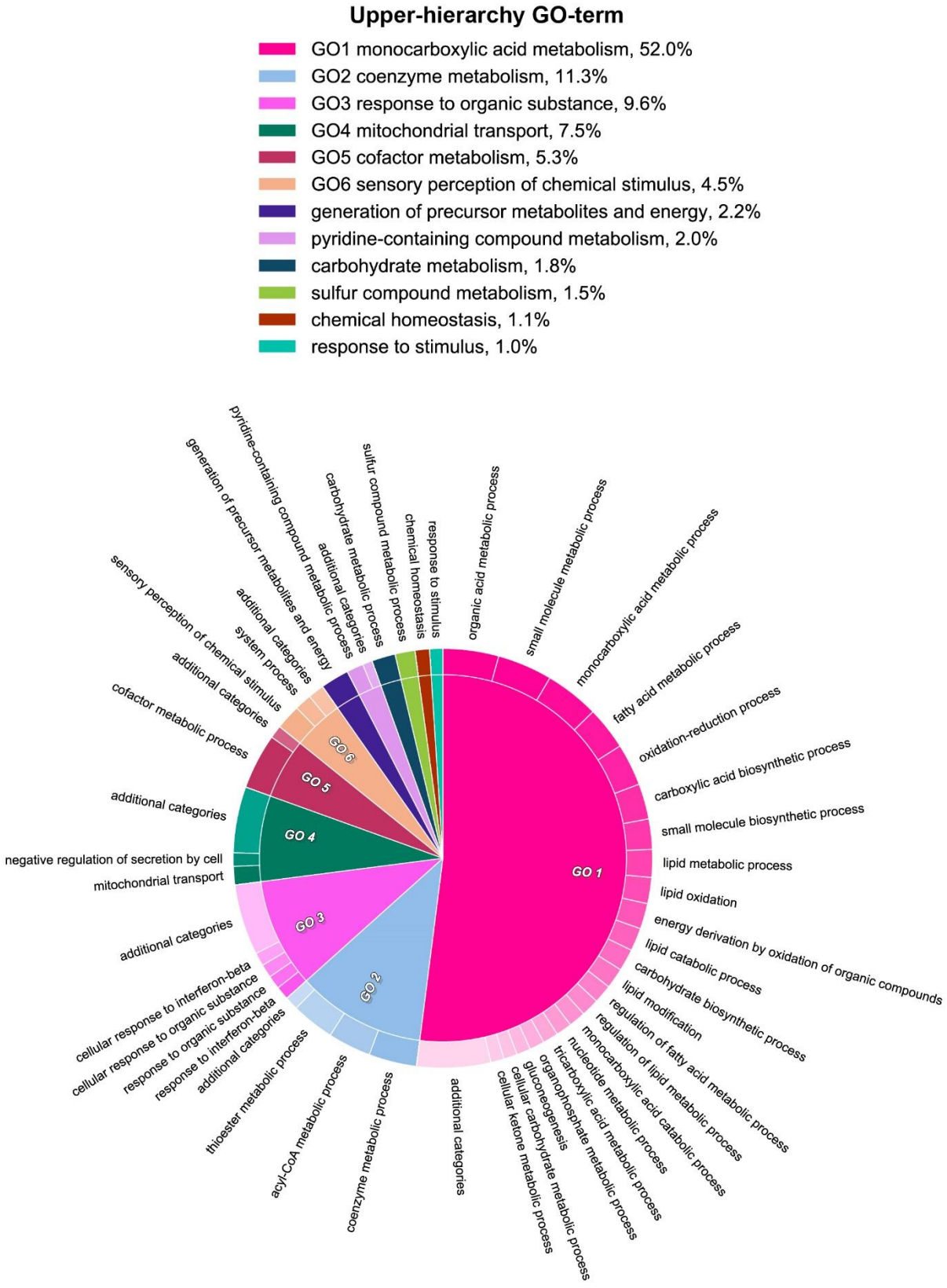


***Figure 23. Circular map summarizing Gene Ontology (GO) biological processes of both upregulated and downregulated differentially expressed genes among all the samples.*** s the arc length of each slice is proportional to the p-value of the GO-term enrichment, the outside slices determine the importance of each GO within the central big slice, which represents the upper-hierarchy GO-term which encompasses all the upregulated minor GO-terms.

Altogether, these results pointed out that the most substantial effect produced by cold exposure on the gene expression profiles of the adipose depots studied was on metabolic pathways. To investigate if the response to cold exposure occurred in a similar manner in all the depots or if differences existed among them, we decided to perform the *logical set relationship analysis* again, studying, in this case, the DEGs for each tissue separately. As shown in Figure 24, iBAT did not show any statistically significant altered metabolic pathway. Nevertheless, pathways related to the transport of small molecules, the SLC-mediated transmembrane transport, and genes related to striated muscle contraction were enriched in this depot, suggesting that the transport of molecules and the remodeling of this depot probably occurred.

On the other hand, expression of metabolic genes in iWAT was strikingly modified by cold exposure, as the top 5 most statistically significant enriched pathways were: 1) the citric acid (TCA) cycle and respiratory chain, 2) pyruvate metabolism and TCA, 3) metabolism, 4) carbon metabolism, and 5) TCA (Figure 24). Finally, the most enriched pathways for eWAT were the olfactory transduction and the olfactory signaling pathway. Different explanations could arise from eWAT results (Figure 24).

Taken together, the second *logical set relationship analysis* indicated that iWAT was the adipose depot with a more coordinated response produced by cold exposure. Despite not being the tissue sharing the highest number of DEGs, the iWAT depot was clearly affecting the *pathway enrichment analysis* of all DEGs together (Figure 22). Instead of being a result impacted by the three depots, the result obtained in this last analysis was the same as the one obtained in the iWAT set of the *set relationship analysis*, indicating the important impact that cold exposure had on this depot (Figures 23, 24). In addition, these results correlate with the ones obtained in the *exploratory analyses* (Figures 16, 17), suggesting that iWAT was the most-responsive tissue to cold challenge in our experimental setting.

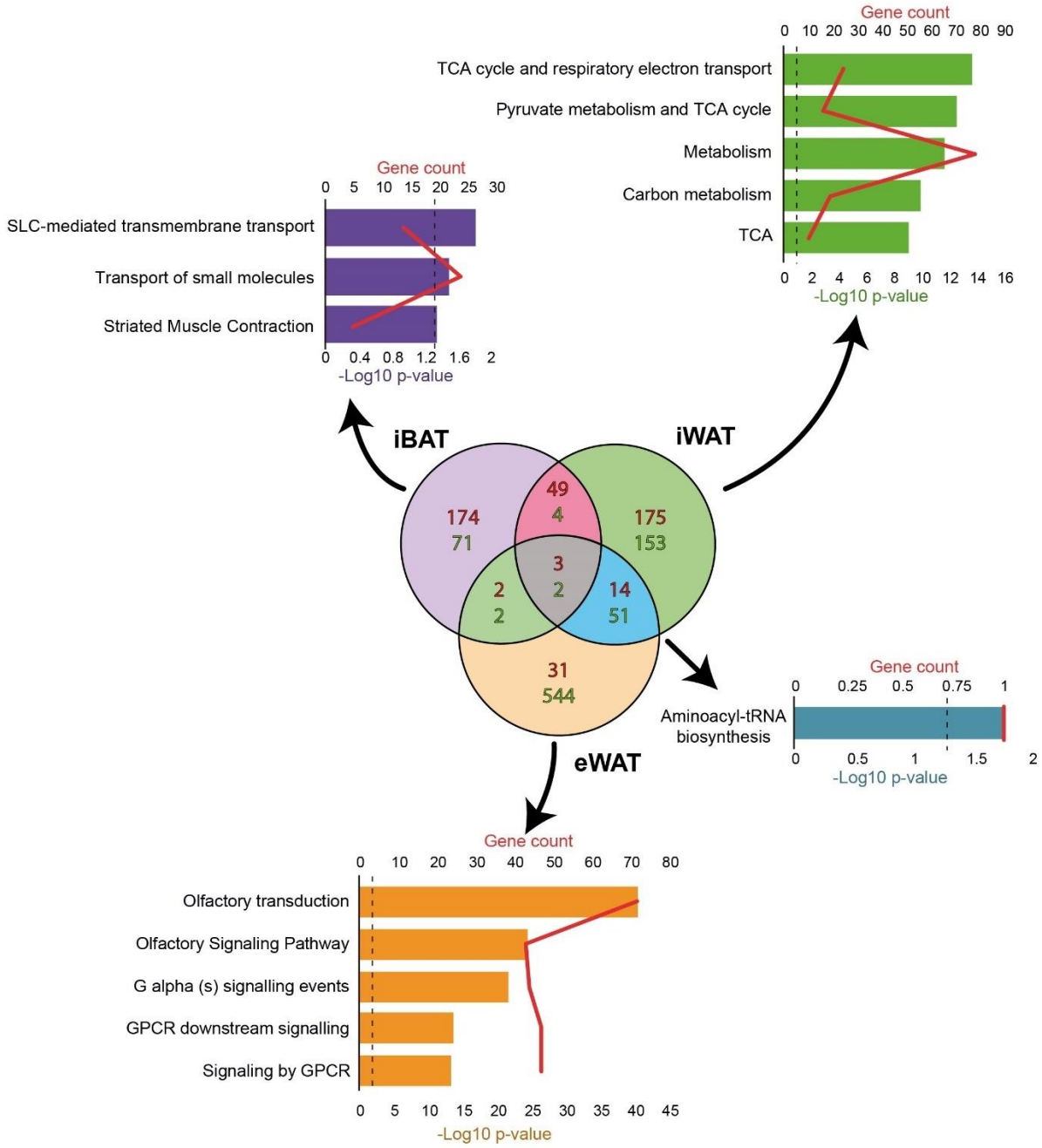


***Figure 24. Most statistically significative enriched pathways of the differential expressed genes of each set.*** - $Log_{10}$ of the p-value is indicated using the bar chart, and the gene number of each pathway enrichment is shown by the red line chart. -$Log_{10}$ of 0.05 p-value is indicated by the dashed line.

# Section II. Effects of cold exposure on metabolic pathways in the different adipose tissue depots iWAT, eWAT, and iBAT

## 1. METABOLIC PATHWAY ANALYSIS OF iWAT

As metabolism was strongly enriched in the *pathway enrichment analysis* of iWAT DEG (Figure 24), we analyzed in detail the metabolic changes in this tissue. To this end, several databases and tools created by the *Kyoto University Bioinformatics Center*, such as the *Kyoto Encyclopedia of Genes and Genomes* (KEGG) or the KEGG mapper tool, were used. First, to obtain a broad view of metabolic changes, the KEGG pathway map 01100 for *Mus musculus* was used since it makes possible the visualization of a substantial part of the metabolism and interactions between different pathways. In the analysis, a mild fold change threshold of ±1.5 was applied to better detect pathways with deregulated genes. Since pathways are comprised of different chemical reactions triggered by enzymes, to detect coordinated metabolic responses special attention was given to pathways in which consecutive genes presented altered above-threshold values rather than pathways in which isolated enzymes were highly deregulated. To afford an easier visualization and thereby analysis, pathways from the KEGG map mmu01100 that contained upregulated genes (FC > 1.5) were highlighted in red and pathways containing downregulated genes (FC < 1.5) were highlighted in green. Fold change values between 1.4 and 1.49 (included) were colored in pink and negative fold change values comprising -1.4 to -1.49 were colored in yellow to better highlight tendencies. A clear snapshot of the metabolic pathways from iWAT that presented gene expression changes in mice under cold exposure is shown in Figure 25. Pathways such as glycolysis, TCA, degradation of amino acids, FA oxidation, and oxidative phosphorylation were clearly enhanced by cold exposure; as the expression of almost every single gene of these pathways increased after cold exposure. After the observation of this enormous effect of cold exposure in upregulating metabolic pathways, in-detail analyses of the pathways glycolysis, TCA, degradation of amino acids, lipolysis, oxidative phosphorylation, and thermogenesis were performed

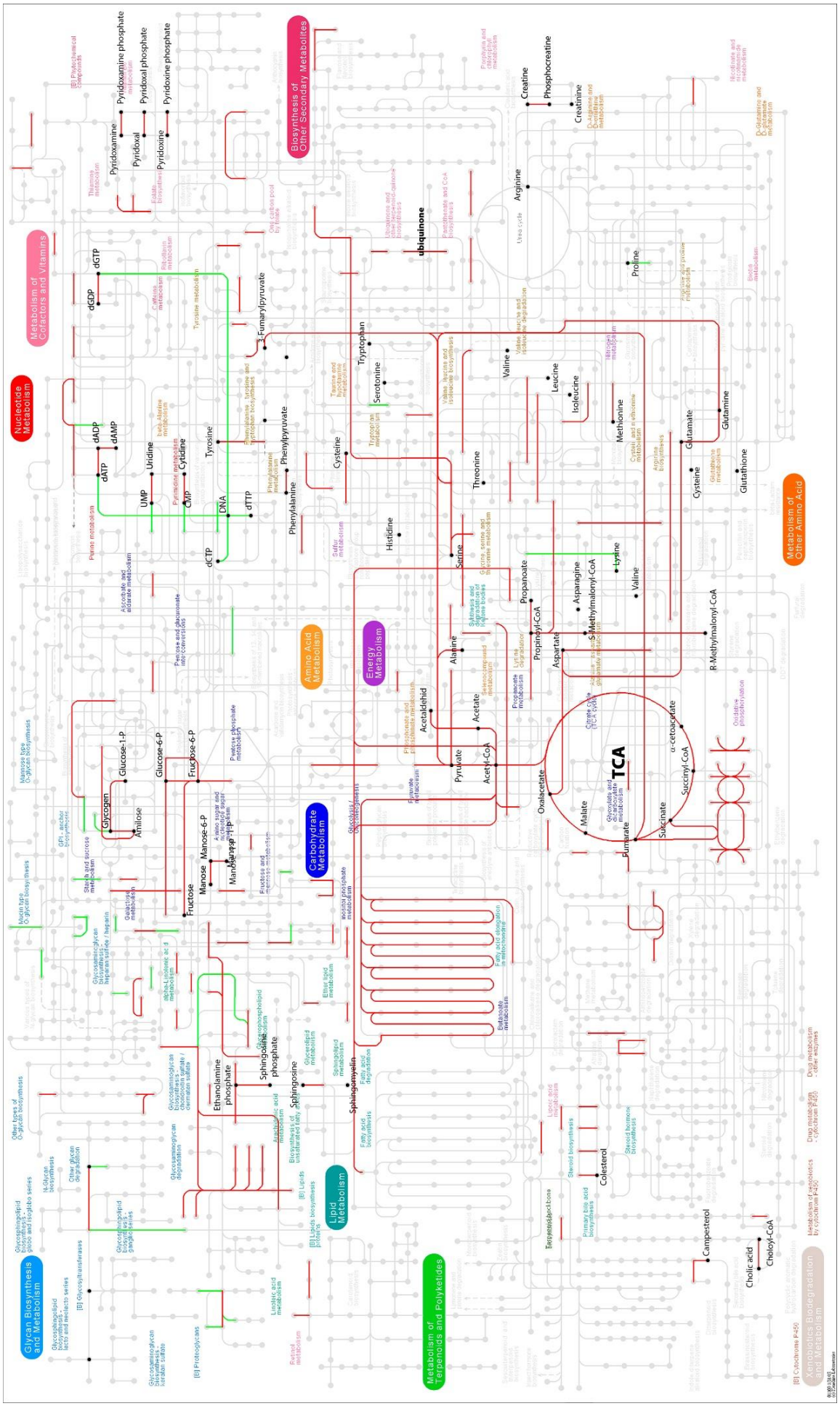


***Figure 25. Metabolic pathways analysis of iWAT of cold-exposed mice.*** The metabolic pathways map mmu01100 from KEGG pathways indicating gene deregulation in iWAT of cold-exposed mice is shown. Highlighted in **Bold**: metabolites; Highlighted in **Red**: upregulated expression in cold exposure of 1.5-fold or higher; Highlighted in **Green**: downregulated expression in cold exposure of -1.5-fold or lower.

## 1.1. Glycolysis

The glucose molecule is well known to be a rich store of chemical energy, which in the presence of oxygen can be broken down, form carbon dioxide and water, and release energy. In living cells, thermodynamics must be considered in order to understand how cells can release energy from glucose molecules. Once a glucose molecule has been transported from the bloodstream into a cell, it is broken down in the cytosol through different biochemical steps ending in the entrance of two pyruvate molecules into the mitochondria. Then, pyruvate is oxidized through the TCA to six molecules of carbon dioxide and water. During these steps, NADH and $FADH_2$ are generated from $NAD^+$ and $FAD^+$ and hydrogen. These hydrogens will ultimately be oxidized to enter the electron respiratory chain, powering the generation of ATP (Brown, 1992).

In mice, the flow of glycolysis is mainly controlled by 3 enzymes that are not in equilibrium: the hexokinase, 6-phosphofructokinase, and pyruvate kinase. Analysis of this pathway in iWAT revealed that cold exposure mediated a remarkable effect in glycolysis (Figure 26). The vast majority of genes codifying for enzymes involved in glycolysis were significantly upregulated, including the three enzymes that control the flow. The first step of this pathway, the phosphorylation of glucose to glucose-6-phosphate (G-6P), was mediated by the *hexokinase*, which had a 1.86-fold change expression for the isoform *hexokinase II* (Figure 26), the main expressed isoform in the adipose tissue (Printz et al., 1993). At the same time, this enzyme can be inhibited by high concentrations of G-6P. Then, *glucose-6-phosphate isomerase* (*Gpi1*) converts G-6P aldose to a ketose giving rise to fructose 6-phosphate (F-6P). Even though this enzyme is in equilibrium, which means it does not control the glycolysis' speed flow, its expression was increased about 80%, reaching a 1,8-fold increase (Figure 26). F-6P is further phosphorylated into fructose-1,6-bisphosphate (F-1,6P2) by *6-phosphofructokinase*. The *6-phosphofructokinase* is an allosteric enzyme that sets the pace of glycolysis. In iWAT samples of cold-exposed mice, expression of both muscular (*Pfkm*) and liver (*Pfkl*) isoforms of this enzyme were increased >2-fold (Figure 26). These two isoforms have been described as being regulated in white adipocytes by insulin signaling, a well-known regulator of glucose consumption, highlighting the importance of this upregulation to increase glucose consumption under cold exposure (Ausina et al., 2018). Thereby, F-1,6P2 is catalyzed in a reversible process by *fructose-bisphosphate aldolase* enzyme, also known as *aldolase*. In iWAT samples of cold-exposed mice, neither *aldolase a*, *b* nor *c* showed an outstanding fold change value, 1.35-fold being the maximum increased value observed for the isoform *a* (Figure 26). This

enzyme produces glyceraldehyde 3-phosphate (GAP) and dihydroxyacetone phosphate (DHAP) from F-1,6P2. GAP is involved in the direct pathway of glycolysis, while DHAP is not. However, in order to avoid losing molecules to generate ATP, the *triose-phosphate isomerase* transforms DHAP to GAP in a rapid and reversible equilibrated reaction. In samples of the iWAT depot of cold-exposed mice, *triose-phosphate isomerase* was increased 1.65-fold (Figure 26), indicating that this pathway was possibly affected by the cold exposure. The metabolic changes produced by both *aldolase* and *triose-phosphate isomerase* enzymes produce two GAP molecules from one single molecule of F-1,6P2, doubling from this step all the glycolysis reactions. Hence, GAP is converted to 1,3-Bisphosphoglycerate (1,3-BPG) by *glyceraldehyde-3-phosphate dehydrogenase*, an enzyme that showed a higher gene expression in samples from the cold exposed condition (1,69-fold increase) (Figure 26). The 1,3-BGP is then processed to 3-Phosphoglycerate by *phosphoglycerate kinase* (2.23-fold change), producing ATP (Figure 26).

Finally, 3-phosphoglycerate is transformed to pyruvate through three reactions catabolized by the enzymes *phosphoglycerate mutase (2,3-diphosphoglycerate-independent)*, *phosphopyruvate hydratase (*also known as *enolase),* and *pyruvate kinase*. All three enzymes presented an increased gene expression, presenting fold change values of 4.36-, 1.44-, and 1.88-fold, respectively (Figure 26). *Pyruvate kinase* is key in the control of the glycolysis' outflow since the reaction catabolized by this enzyme is irreversible and it is regulated by the concentration of ATP. Thereby, elevated ATP concentrations inhibit *pyruvate kinase*, slowing glycolysis in high energy conditions. In addition, *pyruvate kinase* is activated by F-1,6P2 to maintain balance with the oncoming high flux intermediates.

Overall, this gene expression analysis of glycolysis clearly showed significant upregulation of the enzymes involved in this pathway. Among these enzymes, there were some important upregulated genes in iWAT of cold-exposed mice that control the pathway and its flow, *hexokinase*, *6-phosphofructokinase,* and *pyruvate kinase*. These data, in conjunction with the expression of other enzymes, such as *adenylate kinase* or *triose-phosphate isomerase*, indicated that glycolysis was markedly increased in iWAT of mice exposed to cold.


| Transcript ID | Gene Symbol | Description | Fold Change | p-value |
|---|---|---|---|---|
| 17241318 | Hk1 | Hexokinase 1 | 1.13 | 0.305862 |
| 17468018 | Hk2 | Hexokinase 2 | **1.86** | **0.013703** |
| 17292775 | Hk3 | Hexokinase 3 | -1.18 | 0.41372 |
| 17489620 | Gpi1 | Glucose phosphate isomerase 1 | **1.8** | **0.00075** |
| 17314577 | Pfkm | Phosphofructokinase, muscle | **2.28** | **0.0258** |
| 17242376 | Pfkl | Phosphofructokinase, liver, B-type | **2.21** | **0.001404** |
| 17290324 | Pfkp | Phosphofructokinase, platelet | 1.24 | **0.020259** |
| 17496408 | Aldoa | Aldolase A, fructose-bisphosphate | 1.35 | **0.032776** |
| 17425233 | Aldob | Aldolase B, fructose-bisphosphate | 1.27 | 0.300779 |
| 17253599 | Aldoc | Aldolase C, fructose-bisphosphate | 1.11 | 0.238568 |
| 17471011 | Gapdh | Glyceraldehyde-3-phosphate dehydrogenase | **1.69** | **0.024474** |
| 17546512 | Gapdh | Glyceraldehyde-3-phosphate dehydrogenase | **1.48** | **0.029958** |
| 17489289 | Gapdhs | Glyceraldehyde-3-phosphate dehydrogenase, spermatogenic | 1.29 | 0.096218 |
| 17537088 | Pgk1 | Phosphoglycerate kinase 1 | **2.23** | **0.000456** |
| 17344939 | Pgk2 | Phosphoglycerate kinase 2 | -1.05 | 0.336808 |
| 17359466 | Pgam1 | Phosphoglycerate mutase 1 | **4.36** | **0.000408** |
| 17260192 | Pgam2 | Phosphoglycerate mutase 2 | 1 | 0.720514 |
| 17421908 | Eno1 | Enolase 1, alpha non-neuron | **1.44** | **0.027656** |
| 17470846 | Eno2 | Enolase 2, gamma neuronal | 1.08 | 0.561504 |
| 17252183 | Eno3 | Enolase 3, beta muscle | 1.28 | 0.763224 |
| 17360800 | Eno4 | Enolase 4 | -1.02 | 0.773946 |
| 17518007 | Pkm | Pyruvate kinase, muscle | **1.88** | **0.001698** |
| 17399266 | Pklr | Pyruvate kinase liver and red blood cell | 1.03 | 0.806645 |

***Figure 26. Gene expression analysis of genes involved in glycolysis in iWAT.*** On the left part of the figure, a flow chart of the glycolysis pathway is shown. Key steps are highlighted in yellow. The steps of the glycolysis carried out twice per glucose molecule due to the generation of 2 molecules of glyceraldehyde 3-phosphate are indicated with a curly bracket and a "2x" sign. Fold change and statistical values are also specified on the right. Highlighted in **Bold**: statistically significant p-values; Highlighted in **Red**: upregulated expression in cold exposure of 1.5-fold or higher. Adapted from Stryer Biochemistry 8th Edition.

The upregulation of several glycolytic-related genes suggested that glucose uptake into the cell and its consumption may be increased. As glucose can enter the cells through glucose transporters (GLUT), we decided to study their expression. There are several GLUTs, GLUT1 to GLUT5 being the most extensively studied. Of these, GLUT4 is highly expressed in tissues regulated by insulin such as adipose tissue (James et al., 1988). In iWAT, most of the GLUTs did not present changes in gene expression. However, GLUT4, GLUT5, and GLUT8 did present a statistically significant higher expression in iWAT samples from cold-exposed mice (Table 2). Furthermore, GLUT2, GLUT9, and GLUT13 also presented slight statistically significant deregulation of their gene expression values.

| Transcript ID | Gene Symbol | Name | Description | Fold Change | p-value |
|---|---|---|---|---|---|
| 17549664 | Slc2a1 | GLUT1 | Solute carrier family 2 , member 1 | -1.01 | 0.464238 |
| 17396479 | Slc2a2 | GLUT2 | Solute carrier family 2 , member 2 | -1.21 | **0.035492** |
| 17470597 | Slc2a3 | GLUT3 | Solute carrier family 2 , member 3 | -1.11 | 0.440087 |
| 17265096 | Slc2a4 | **GLUT4** | Solute carrier family 2 , member 4 | **1.98** | **0.000656** |
| 17421875 | Slc2a5 | **GLUT5** | Solute carrier family 2 , member 5 | **2.00** | **0.014974** |
| 17383216 | Slc2a6 | GLUT6 | Solute carrier family 2 , member 6 | 1.05 | 0.800941 |
| 17421895 | Slc2a7 | GLUT7 | Solute carrier family 2 , member 7 | 1.12 | 0.267413 |
| 17384082 | Slc2a8 | **GLUT8** | Solute carrier family 2, , member 8 | **1.67** | **0.006429** |
| 17447646 | Slc2a9 | GLUT9 | Solute carrier family 2 , member 9 | 1.15 | **0.021066** |
| 17379683 | Slc2a10 | GLUT10 | Solute carrier family 2 , member 10 | -1.14 | 0.224502 |
| 17232119 | Slc2a12 | GLUT12 | Solute carrier family 2 , member 12 | 1.13 | 0.600047 |
| 17320666 | Slc2a13 | GLUT13 | Solute carrier family 2 , member 13 | -1.38 | **0.004495** |

***Table 2. Gene expression analysis of glucose transporters in iWAT.*** Fold change values of gene expression in cold-exposed mice in comparison with the control group are shown. Highlighted in **Bold**: statistically significant p-values. Highlighted in **Red**: upregulated expression in cold exposure of 1.5-fold or higher.

Once pyruvate is produced, it could be metabolized to different substrates depending on the cellular compartment disposition and the needs of the cell (Figure 27). Some of these substrates are metabolites which can participate directly in the TCA cycle, such as α-ketoglutarate, acetyl-CoA or oxaloacetate. Hence, we next analyzed the expression of genes involved in metabolic reactions related to pyruvate. The mitochondrial enzyme *alanine transaminase*, also known as *alanine aminotransferase* (*Gpt2*), is able to generate α-ketoglutarate and alanine from pyruvate and glutamate in a reversible reaction (*Alanine* + *α-Ketoglutarate* ⇄ *Pyruvate* + *Glutamate*). In our analysis, *Gpt2* gene expression was increased by 56% with a p-value of 0.032 in iWAT samples from cold-exposed mice (Figure 27, Table 3). In addition, pyruvate can be processed to oxaloacetate by the mitochondrial enzyme *pyruvate carboxylase*, whose transcription was increased by

40% in the iWAT (Figure 27, Table 3). These reactions maintain substrates of the TCA cycle. Pyruvate can also be converted to other molecules such as lactate. This step is mediated by the *L-lactate dehydrogenase* and *D-lactate dehydrogenase* enzymes, which isoforms *B* and *D* had a fold change of 3.31 and 1.61 respectively in the iWAT of cold-exposed mice, both upregulations being highly significant (Figure 27, Table 3).

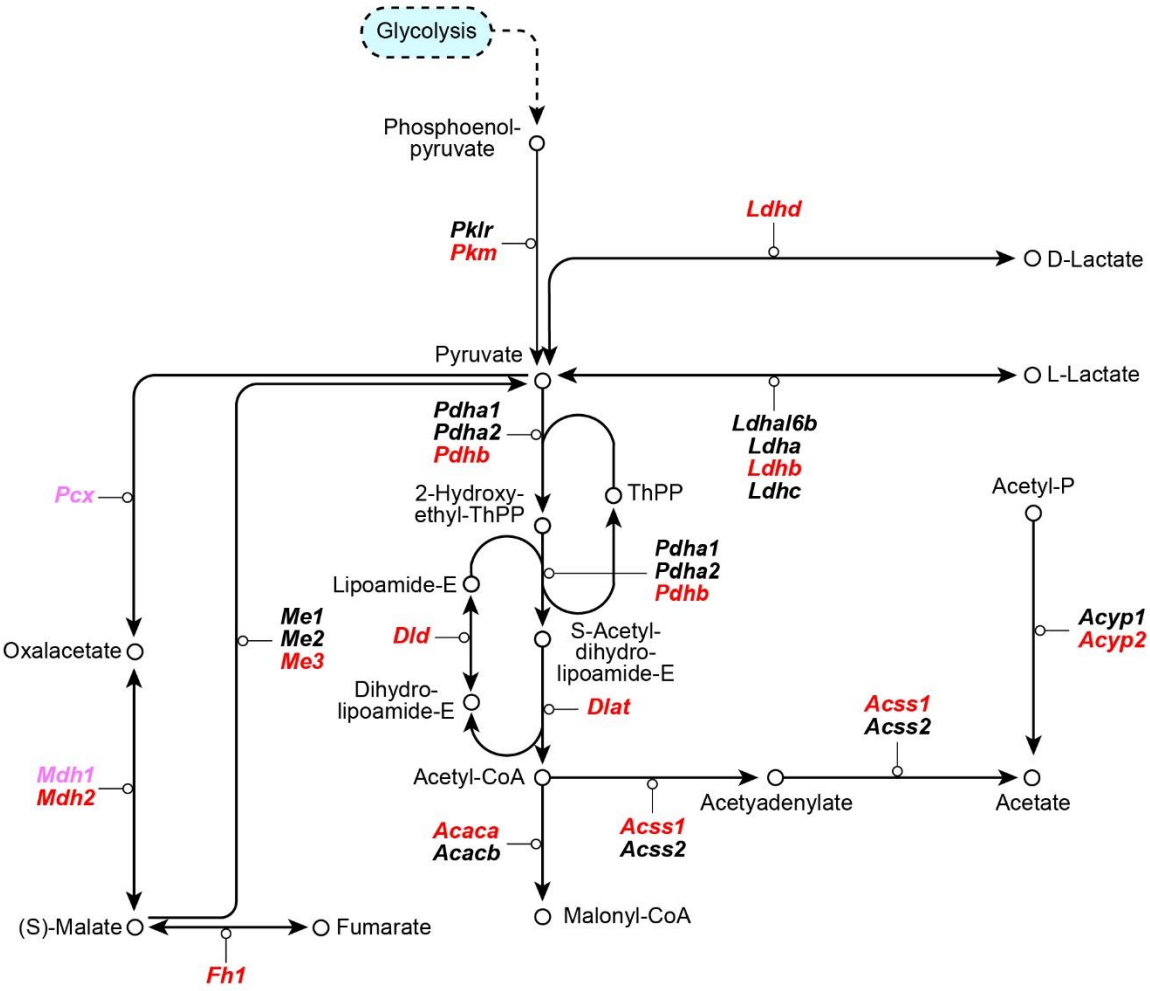


***Figure 27. Expression changes of genes related to the pyruvate metabolism in iWAT mediated by cold exposure.*** The enzymes that metabolize each process are indicated in ***italic bold***. Highlighted in **Black**: no changes in gene expression levels; Highlighted in **Red**: upregulated expression in cold exposure of 1.5-fold or higher; Highlighted in Pink: upregulated expression in cold exposure between 1.4- and 1.49-fold.

| Transcript ID | Gene Symbol | Description | Fold Change | p-value |
|---|---|---|---|---|
| 17254395 | Acaca | acetyl-Coenzyme A carboxylase alpha; acetyl-CoA carboxylase 1-like | 1.04 | 0.351173 |
| 17440826 | **Acacb** | acetyl-Coenzyme A carboxylase beta | **2.01** | **0.001756** |
| 17392690 | **Acss1** | acyl-CoA synthetase short-chain family member 1 | **3.69** | **0.000001** |
| 17378359 | Acss2 | acyl-CoA synthetase short-chain family member 2 | 1.09 | 0.24039 |
| 17282689 | Acyp1 | acylphosphatase 1, erythrocyte (common) type | 1.3 | 0.055234 |
| 17261393 | **Acyp2** | acylphosphatase 2, muscle type | **1.74** | **0.009867** |
| 17526861 | **Dlat** | dihydrolipoamide S-acetyltransferase | **2.33** | **0.000088** |
| 17280498 | **Dld** | dihydrolipoamide dehydrogenase | **1.69** | **0.001312** |
| 17230153 | **Fh1** | fumarate hydratase 1 | **1.57** | **0.000928** |
| 17340493 | Ldhal6b | lactate dehydrogenase A-like 6B | 1.14 | **0.046658** |
| 17478225 | Ldha | lactate dehydrogenase A | -1.34 | **0.048681** |
| 17472517 | **Ldhb** | lactate dehydrogenase B | **3.11** | **0.000005** |
| 17478243 | Ldhc | lactate dehydrogenase C | 1.06 | 0.741787 |
| 17513135 | **Ldhd** | lactate dehydrogenase D | **1.61** | **0.008963** |
| 17260944 | **Mdh1** | malate dehydrogenase 1, NAD (soluble) | **1.47** | **0.003632** |
| 17443310 | **Mdh2** | malate dehydrogenase 2, NAD (mitochondrial) | **2.26** | **0.000052** |
| 17529398 | Me1 | malic enzyme 1, NADP(+)-dependent, cytosolic | 1.15 | **0.03934** |
| 17355391 | Me2 | malic enzyme 2, NAD(+)-dependent, mitochondrial | -1.1 | 0.172056 |
| 17480048 | **Me3** | malic enzyme 3, NADP(+)-dependent, mitochondrial | **1.69** | **0.002599** |
| 17356216 | **Pcx** | pyruvate carboxylase | **1.4** | 0.051221 |
| 17545741 | Pdha1 | pyruvate dehydrogenase E1 alpha 1 | 1.35 | **0.004009** |
| 17410718 | Pdha2 | pyruvate dehydrogenase E1 alpha 2 | -1.1 | 0.05791 |
| 17303400 | **Pdhb** | pyruvate dehydrogenase (lipoamide) beta | **1.67** | **0.004331** |
| 17399266 | Pklr | pyruvate kinase liver and red blood cell | 1.03 | 0.806645 |
| 17518007 | **Pkm** | pyruvate kinase, muscle | **1.88** | **0.001698** |

***Table 3. Expression changes of genes encoding isoenzymes involved in pyruvate metabolism in iWAT.*** Fold change values of gene expression in cold-exposed mice in comparison with the control group. Highlighted in **Bold**: statistically significant p-values. Highlighted in **Red**: upregulated expression in cold exposure of 1.5-fold or higher; Highlighted in Pink: upregulated expression in cold exposure between 1.4- and 1.49-fold.

## 1.2. TCA Cycle

The TCA cycle, also known as the citric acid cycle or Krebs cycle, is the central metabolic hub of the cell (Figure 28). This process does not generate a large amount of ATP molecules, instead, $NAD^+$ and $FAD^+$ are reduced to NADH and $FADH_2$. Thereby, further oxidation of NADH and $FADH_2$ releases electrons that flow through the electron-transport chain and generate a proton gradient across the inner mitochondrial membrane, allowing the generation of ATP by oxidative phosphorylation.

Pyruvate enters the TCA cycle after being transformed into acetyl-CoA (Figure 28). Similarly, TCA can also be fueled with carbohydrates, ketone bodies, fatty acids, and amino acids through acetyl-CoA generation. Furthermore, some cycle metabolites form essential links with pathways such as lipogenesis, gluconeogenesis, and amino acid metabolism. Hence, the regulation of the TCA cycle is a key process in cellular metabolism. The cycle activity is regulated mainly by the *pyruvate dehydrogenase complex* and *isocitrate dehydrogenase* (Figure 28). The trimeric enzyme *pyruvate dehydrogenase*

*complex* (PDC) is the complex formed by *pyruvate dehydrogenase* (*Pdh*), *dihydrolipoyllysine-residue acetyltransferase*, also known as *dihydrolipoamide acetyltransferase* (*Dlat*) and *dihydrolipoyl dehydrogenase*, also known as *dihydrolipoamide dehydrogenase* (*Dld*) (Figure 28). Although PDC is not properly a part of the TCA cycle, it does regulate the flux of glycolytic metabolites towards the cycle. In our analysis, PDC had *Dlat* and *Dld* genes significantly upregulated (more than 1.5-fold), while *Pdha1* was only upregulated 1.35-fold but with statistical significance (Table 3). This trimeric enzyme transfers an acetyl residue to CoA, forming acetyl-CoA and generating NADH in an irreversible reaction. Under conditions of high ratios of ATP/ADP, NADH/$NAD^+$ or acetyl-CoA/CoA, the activity of PDH decreases. Moreover, PDH kinases (*Pdk*) or PDH phosphatases control PDC activity, inhibiting the complex when it is phosphorylated. Different PDH kinases have been described; *Pdk2* and *Pdk4* have been the most extensively studied because their expression is regulated by insulin or starvation. Cold has been described as upregulating the expression of *Pdk2* and fasting as upregulating the expression of *Pdk4*. Glucocorticoids, exercise, and PGC-1α/ERRα or β-adrenergic activation can also upregulate the expression of *Pdk2* and *Pdk4* (Huang et al., 2002). The expression of *Pdk2* and *Pdk4* in iWAT of cold-exposed mice was upregulated 5.51- and 2.74-fold, respectively (Table 4). On the other hand, *[pyruvate dehydrogenase (acetyl-transferring)]-phosphatase*, also known as *pyruvate dehydrogenase phosphatase* (*Pdp1* and *Pdp2*) is stimulated by phosphoenolpyruvate, insulin, and AMP and is competitively inhibited by ATP, NADH, and acetyl-CoA (Huang et al., 1998). In iWAT of cold challenged mice, expression of Pdp1 was unaltered, whereas the expression of *Pdp2* and of the regulatory subunit *Pdpr* was increased 1.43- and 1.39-fold (Table 4).

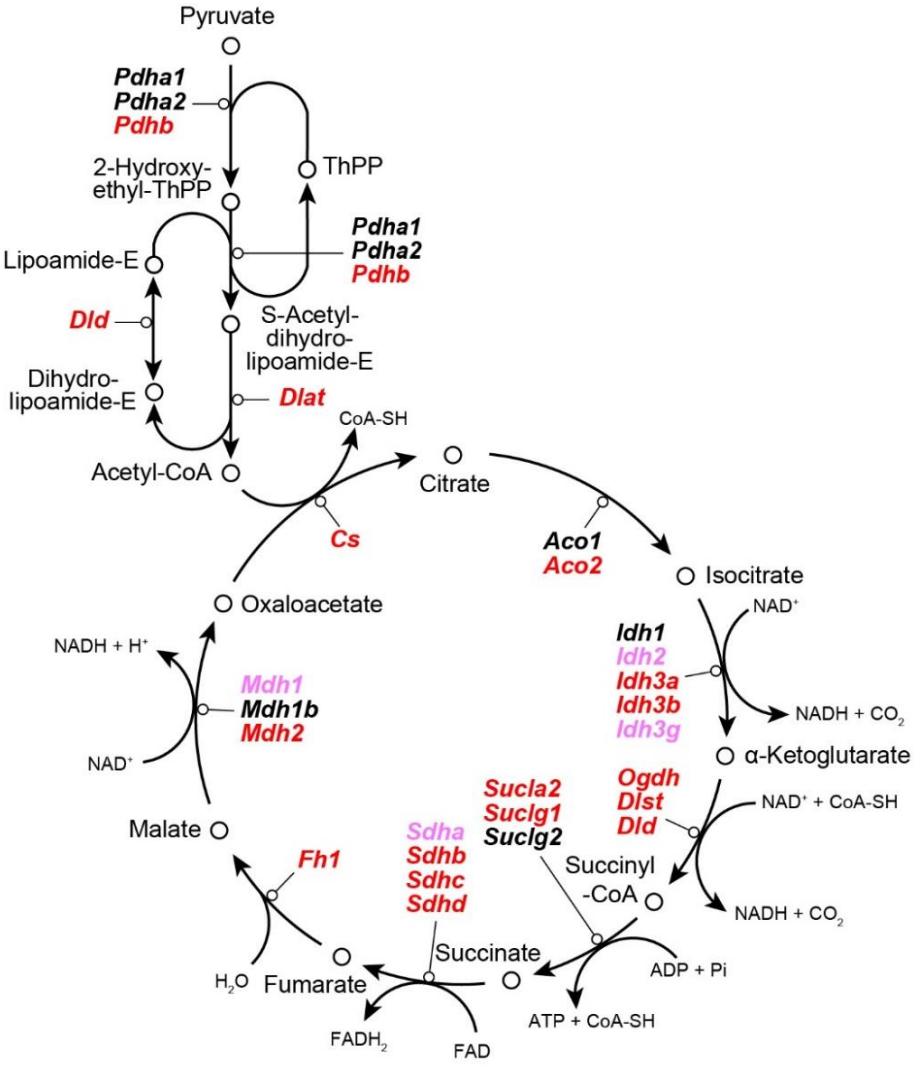


***Figure 28. Expression changes mediated by cold exposure of genes related to the metabolization of pyruvate to acetyl-CoA and the TCA in iWAT.*** The enzymes that metabolize each process are emphasized in ***italic bold***. Highlighted in **Black**: no changes in gene expression levels; Highlighted in **Red**: upregulated expression in cold exposure of 1.5-fold or higher; Highlighted in **Pink**: upregulated expression in cold exposure between 1.4- and 1.49-fold.

| Transcript ID | Gene Symbol | Description | Fold Change | p-value |
|---|---|---|---|---|
| 17371847 | Pdk1 | pyruvate dehydrogenase kinase, isoenzyme 1 | 1.26 | 0.15717 |
| 17268120 | **Pdk2** | pyruvate dehydrogenase kinase, isoenzyme 2 | **2.74** | **0.001529** |
| 17543196 | Pdk3 | pyruvate dehydrogenase kinase, isoenzyme 3 | 1.1 | 0.660076 |
| 17464654 | **Pdk4** | pyruvate dehydrogenase kinase, isoenzyme 4 | **5.51** | **0.000014** |
| 17423321 | Pdp1 | pyruvate dehyrogenase phosphatase catalytic subunit 1 | 1.06 | 0.684604 |
| 17504467 | **Pdp2** | pyruvate dehyrogenase phosphatase catalytic subunit 2 | **1.43** | **0.016337** |
| 17505718 | Pdpr | pyruvate dehydrogenase phosphatase regulatory subunit | 1.39 | **0.006951** |

***Table 4. Pyruvate dehydrogenase kinase and pyruvate dehydrogenase phosphatase isoenzymes in iWAT.*** Fold change values of gene expression in cold-exposed mice compared with the control group. Highlighted in **Bold**: statistically significant p-values. Highlighted in **Red**: upregulated expression in cold exposure of 1.5-fold or higher; Highlighted in **Pink**: upregulated expression in cold exposure between 1.4- and 1.49-fold.

The conversion of pyruvate into acetyl-CoA is the link between glycolysis and cellular respiration, as acetyl-CoA is the fuel of the Krebs cycle. Our results in iWAT samples of cold-exposed mice indicated that to enhance the entrance of pyruvate into the mitochondria, the hetero-oligomeric complex was upregulated; both *mitochondrial pyruvate carrier* isoforms, 1 and 2, were significantly upregulated, approximately 1.6-fold.

The TCA cycle starts with the reaction catabolized by the *Citrate (Si)-synthase*, also known as *citrate synthase*, in which: *Oxaloacetate + Acetyl-CoA → Citrate + CoA + $H_2O$*. In our analysis, this first step was boosted by an increase in the expression of the gene *citrate synthase* of 2.26-fold (Figure 28, Table 5). From citrate, *aconitate hydratase* enzyme produces isocitrate. The mitochondrial isoform *aconitase 2* was upregulated 2.31-fold in iWAT of cold-exposed mice (Figure 28, Table 5). Then, *isocitrate dehydrogenase* performs the first of four oxidation-reduction reactions of the TCA cycle, transforming isocitrate to α-ketoglutarate and producing NADH and $CO_2$. *Isocitrate dehydrogenase* has 5 different isoforms, from which the three $NAD^+$-dependent isoforms of *isocitrate dehydrogenase 3* (*α, β, γ*) were upregulated between 2.2- and 1.45-fold (Figure 28, Table 5). Furthermore, the gene *isocitrate dehydrogenase 2* (NADP+-dependent) presented an upregulation of 1.4-fold (Figure 28, Table 5). As previously indicated, α-ketoglutarate can also be produced from pyruvate and glutamine. This molecule in the Krebs cycle is metabolized by the *oxoglutarate dehydrogenase (succinyl-transferring)* enzyme also known as *α-ketoglutarate dehydrogenase complex*, producing succinyl-CoA, NADH, and $CO_2$. Expression of the three enzymes (*Dld*, *Dlst*, *Ogdh*) that comprise this complex was clearly upregulated in the iWAT samples of cold-exposed mice (Figure 28, Table 5).

As succinyl-CoA is an energy-rich thioester, the conversion of this molecule to succinate also generates ATP; this is the only step of the TCA cycle in which a high phosphoryl-transfer potential molecule is produced. This process is mediated by the *succinyl-CoA synthetase*, which is a heterodimer composed of two forms of the α subunit (*Suclg1*) and two forms of the variable β isoforms encoded by either *Sucla2* or *Suclg2*. This β isoform dimer can result in either ATP-forming (*Sucla2* dimer) or GTP-forming (*Suclg2* dimer). In tissues with high oxygen consumption, reactions positively regulated by ADP are predominant. In iWAT of cold-exposed mice, the genes *succinyl-CoA* α subunit (*Suclg1*) and ADP-requiring *succinyl-CoA synthetase β* subunit (*Sucla2*) were upregulated and showed high expression in this depot (Table 5).

Fumarate is then generated from the oxidation of succinate by *succinate dehydrogenase*, a reaction that generates $FADH_2$. *Succinate dehydrogenase* is an iron-sulfur protein

embedded in the inner mitochondrial membrane that is directly associated with the electron-transport chain. This enzyme is thus the link between the citric acid cycle and ATP formation. $FADH_2$ transfers two electrons directly to the iron-sulfur clusters of the protein, which are passed to the coenzyme Q and later to the ultimate acceptor, molecular oxygen. Following the cycle, hydration of fumarate results in the forming of L-Malate by the *fumarase* enzyme. Finally, the *malate dehydrogenase* converts this molecule to oxaloacetate, producing NADH. In our study, all these TCA enzymes showed a fold change value higher than 1.4, with a p-value statistically significant (Table 5).

| Transcript ID | Gene Symbol | Description | Fold Change | p-value |
|---|---|---|---|---|
| 17412730 | Aco1 | aconitase 1 | -1.09 | 0.999206 |
| 17313394 | **Aco2** | aconitase 2, mitochondrial | **2.31** | **0.000082** |
| 17238433 | **Cs** | citrate synthase | **2.26** | **0.000124** |
| 17280498 | **Dld** | dihydrolipoamide dehydrogenase | **1.69** | **0.001312** |
| 17277352 | **Dlst** | dihydrolipoamide S-succinyltransferase | **2.2** | **0.000454** |
| 17230153 | **Fh1** | fumarate hydratase 1 | **1.57** | **0.000928** |
| 17223863 | Idh1 | isocitrate dehydrogenase 1 (NADP+), soluble | 1.06 | 0.076047 |
| 17492478 | **Idh2** | isocitrate dehydrogenase 2 (NADP+), mitochondrial | **1.45** | **0.000999** |
| 17517390 | **Idh3a** | isocitrate dehydrogenase 3 (NAD+) alpha | **2.2** | **0.000542** |
| 17391608 | **Idh3b** | isocitrate dehydrogenase 3 (NAD+) beta | **1.67** | **0.00057** |
| 17542392 | **Idh3g** | isocitrate dehydrogenase 3 (NAD+), gamma | **1.4** | **0.001989** |
| 17260944 | **Mdh1** | malate dehydrogenase 1, NAD (soluble) | **1.47** | **0.003632** |
| 17223747 | Mdh1b | malate dehydrogenase 1B, NAD (soluble) | 1.13 | 0.753421 |
| 17443310 | **Mdh2** | malate dehydrogenase 2, NAD (mitochondrial) | **2.26** | **0.000052** |
| 17247080 | **Ogdh** | oxoglutarate (alpha-ketoglutarate) dehydrogenase (lipoamide) | **2.74** | **0.000058** |
| 17294377 | **Sdha** | succinate dehydrogenase complex, subunit A, flavoprotein (Fp) | **1.41** | **0.002822** |
| 17420897 | **Sdhb** | succinate dehydrogenase complex, subunit B, iron sulfur (Ip) | **1.64** | **0.00898** |
| 17229629 | **Sdhc** | succinate dehydrogenase complex, subunit C, integral membrane protein | **1.78** | **0.010133** |
| 17526843 | **Sdhd** | succinate dehydrogenase complex, subunit D, integral membrane protein | **2.1** | **0.000419** |
| 17517112 | **Sdhd** | succinate dehydrogenase complex, subunit D, integral membrane protein | **2.05** | **0.000122** |
| 17301899 | **Sucla2** | succinate-Coenzyme A ligase, ADP-forming, beta subunit | **2.23** | **0.000102** |
| 17459716 | **Suclg1** | succinate-CoenzymeA ligase, GDP-forming, alpha subunit | **2.39** | **0.000895** |
| 17548514 | Suclg2 | succinate-Coenzyme A ligase, GDP-forming, beta subunit | -1.02 | 0.975159 |

***Table 5. Core genes of the TCA and its expression changes in iWAT after cold exposure.*** Fold change values of gene expression in cold-exposed mice in comparison with the control group. Highlighted in **Bold**: statistically significant p-values. Highlighted in **Red**: upregulated expression in cold exposure of 1.5-fold or higher; Highlighted in Pink: upregulated expression in cold exposure between 1.4- and 1.49-fold.

## 1.3. Anaplerotic reactions

The TCA cycle is highly relevant for the cell since it generates 3 molecules of NADH and 2 $FADH_2$, which transfer electrons to the $O_2$. This transference of electrons further leads to the generation of a proton gradient across the inner membrane of the mitochondria that enables the production of ATP and, in tissues like iBAT or beige adipocytes, the generation of heat. Heat is produced by the uncoupling protein 1 (UCP1), which uncouples the

respiratory chain and decreases the proton gradient. In cold exposure conditions, the generation of heat is crucial to help to maintain body temperature (Rowland et al., 2015). Consequently, *Ucp1* gene expression gets upregulated, increasing protein levels and uncoupling of the proton gradient function. Thus, the maintenance of the proton gradient to generate ATP and heat is a necessity, and the cell does this by enhancing the metabolism to obtain more electron transfer carriers, such as NADH and $FADH_2$ (Grimpo et al., 2014; Hiroshima et al., 2018). In situations wherein the TCA cycle flux is boosted, it is crucial for the cell to control concentrations of metabolites involved in this cycle inside the mitochondria to ensure the precise functionality of the TCA (Hiroshima et al., 2018). Anaplerotic pathways are chemical reactions that generate intermediates of metabolic pathways, helping to preserve the flux (Lettieri-Barbato, 2019; Murín et al., 2009; Wohlt et al., 1977; Zhang et al., 2017).

In iWAT of cold-exposed animals, anaplerotic pathways seemed to be activated to restore and maintain intermediates of the TCA cycle. Analysis in detail of the different anaplerotic reactions for each intermediate revealed enhancement of the degradation of branched-chain amino acids (BCAA). BCAA are leucine, isoleucine, and valine. Leucine is exclusively ketogenic as its degradation generates acetoacetate and acetyl-CoA (Bhagavan and Chung-Eun, 2015; Brosnan and Brosnan, 2006; Harper et al., 1984). Isoleucine is both ketogenic and glycogenic as its degradation produces both acetyl-CoA and propionyl-CoA (which is converted to succinyl-CoA) (Bhagavan and Chung-Eun, 2015; Brosnan and Brosnan, 2006; Harper et al., 1984). Finally, valine is glycogenic and produced propionyl-CoA (Bhagavan and Chung-Eun, 2015; Brosnan and Brosnan, 2006; Harper et al., 1984). As shown in Figure 29 and Table 6, the expression of most of the genes that encode for enzymes which mediate degradation reactions of leucine and isoleucine to acetyl-CoA was upregulated. Moreover, increased expression of the genes responsible for the degradation of isoleucine and valine to propanoyl-CoA, which lead to the formation of succinyl-CoA through (R)-methyl-malonyl-CoA, was detected (Figure 29, Table 6). Therefore, the high number of statistically significant upregulated enzymes that degrade BCAA in iWAT of the cold exposed animals suggested that these amino acids were degraded, probably to maintain the pool of intermediate molecules of TCA.

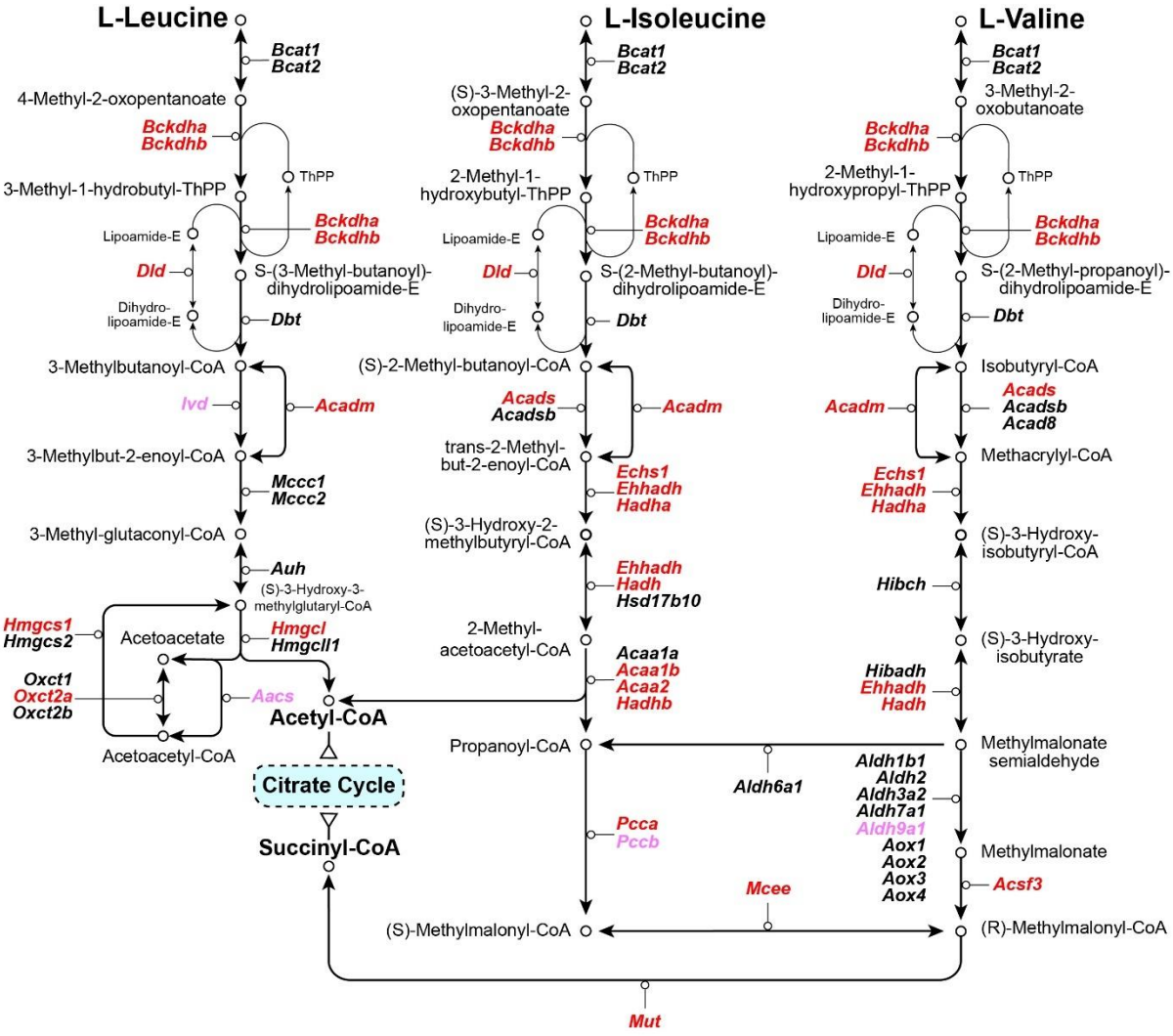


***Figure 29. Expression changes of genes related to the branched-chain amino acids (leucine, isoleucine, and valine) degradation mediated by cold in iWAT.*** From left to right, degradation pathways for the leucine, isoleucine and valine amino acids respectively, and gene expression changes induced by cold exposure indicated. The enzymes that metabolize each process are emphasized in ***italic bold***. Highlighted in **Black**: no changes in gene expression levels; Highlighted in **Red**: upregulated expression in cold exposure of 1.5-fold or higher; Highlighted in Pink: upregulated expression in cold exposure between 1.4- and 1.49-fold. Adapted from KEGG pathway.

| Transcript ID | Gene Symbol | Description | Fold Change | p-value |
|---|---|---|---|---|
| 17442719 | Aacs | acetoacetyl-CoA synthetase | 1.42 | **0.004856** |
| 17523042 | Acaa1a | acetyl-CoA acyltransferase 1A | 1.06 | 0.450507 |
| 17532063 | **Acaa1b** | acetyl-CoA acyltransferase 1B | **2.05** | **0.001961** |
| 17351811 | **Acaa2** | acetyl-CoA acyltransferase 2 (mitochondrial 3-oxoacyl-CoA thiolase) | **2.63** | **0.000104** |
| 17525163 | Acad8 | acyl-CoA dehydrogenase family, member 8 | 1.33 | **0.00142** |
| 17411323 | **Acadm** | acyl-CoA dehydrogenase, medium chain | **1.61** | **0.000963** |
| 17451649 | **Acads** | acyl-CoA dehydrogenase, short chain | **1.5** | **0.001696** |
| 17484014 | Acadsb | acyl-CoA dehydrogenase, short/branched chain | -1.06 | 0.371775 |
| 17506443 | **Acsf3** | acyl-CoA synthetase family member 3 | **1.51** | **0.001701** |
| 17413674 | Aldh1b1 | aldehyde dehydrogenase 1 family, member B1 | 1.11 | 0.113669 |
| 17441949 | Aldh2 | aldehyde dehydrogenase 2, mitochondrial | -1.02 | 0.85944 |
| 17250582 | Aldh3a2 | aldehyde dehydrogenase family 3, subfamily A2 | 1.2 | 0.378418 |
| 17277267 | Aldh6a1 | aldehyde dehydrogenase family 6, subfamily A1 | -1.02 | 0.897558 |
| 17354434 | Aldh7a1 | aldehyde dehydrogenase family 7, member A1 | 1.09 | **0.020836** |
| 17219096 | Aldh9a1 | aldehyde dehydrogenase 9, subfamily A1 | 1.44 | **0.001919** |
| 17212982 | Aox1 | aldehyde oxidase 1 | 1.07 | 0.407452 |
| 17213101 | Aox2 | aldehyde oxidase 3-like 1 | -1.14 | 0.161334 |
| 17213021 | Aox3 | aldehyde oxidase 3 | 1.11 | 0.447884 |
| 17213060 | Aox4 | aldehyde oxidase 4 | -1.17 | 0.392114 |
| 17292612 | Auh | AU RNA binding protein/enoyl-CoA hydratase | 1.21 | **0.004609** |
| 17472678 | Bcat1 | branched chain aminotransferase 1, cytosolic | -1.08 | 0.288891 |
| 17477897 | Bcat2 | branched chain aminotransferase 2, mitochondrial | 1.28 | **0.018921** |
| 17487982 | **Bckdha** | branched chain ketoacid dehydrogenase E1, alpha polypeptide | **1.65** | **0.001461** |
| 17519940 | **Bckdhb** | branched chain ketoacid dehydrogenase E1, beta polypeptide | **1.54** | **0.00053** |
| 17402025 | Dbt | dihydrolipoamide branched chain transacylase E2 | 1.36 | **0.001479** |
| 17280498 | **Dld** | dihydrolipoamide dehydrogenase | **1.69** | **0.001312** |
| 17497612 | **Echs1** | enoyl CoA hydratase, short chain, 1, mitochondrial | **1.79** | **0.001332** |
| 17329220 | **Ehhadh** | enoyl-CoA, hydratase/3-hydroxyacyl CoA dehydrogenase | **3.54** | **0.000468** |
| 17410390 | **Hadh** | hydroxyacyl-CoA dehydrogenase | **1.53** | **0.001646** |
| 17446643 | **Hadha** | hydroxyacyl-CoA dehydrogenase/enoyl-CoA hydratase, alpha subunit | **2.19** | **0.000023** |
| 17435748 | **Hadhb** | hydroxyacyl-CoA dehydrogenase/enoyl-CoA hydratase, beta subunit | **1.79** | **0.00068** |
| 17466919 | Hibadh | 3-hydroxyisobutyrate dehydrogenase | 1.17 | 0.574837 |
| 17212792 | Hibch | 3-hydroxyisobutyryl-CoA hydrolase | 1.39 | **0.002253** |
| 17419980 | **Hmgcl** | 3-hydroxy-3-methylglutaryl-CoA lyase | **1.6** | **0.034485** |
| 17519550 | Hmgcll1 | 3-hydroxymethyl-3-methylglutaryl-CoA lyase-like 1 | 1.1 | 0.908256 |
| 17290173 | **Hmgcs1** | 3-hydroxy-3-methylglutaryl-CoA synthase 1 | **1.65** | **0.004649** |
| 17400862 | Hmgcs2 | 3-hydroxy-3-methylglutaryl-CoA synthase 2 | -1.24 | 0.17029 |
| 17538852 | Hsd17b10 | hydroxysteroid (17-beta) dehydrogenase 10 | 1.24 | **0.042512** |
| 17374648 | Ivd | isovaleryl CoA dehydrogenase | 1.41 | 0.053228 |
| 17404750 | Mccc1 | methylcrotonoyl-CoA carboxylase 1 (alpha) | -1 | 0.346351 |
| 17295503 | Mccc2 | methylcrotonoyl-CoA carboxylase 2 (beta) | -1.21 | 0.323235 |
| 17478883 | **Mcee** | methylmalonyl CoA epimerase | **2.16** | **0.00008** |
| 17345004 | Mut | methylmalonyl-CoA mutase | 1.21 | 0.075687 |
| 17309802 | Oxct1 | 3-oxoacid CoA transferase 1 | 1.08 | **0.030033** |
| 17429685 | **Oxct2a** | 3-oxoacid CoA transferase 2A | **1.64** | 0.18628 |
| 17418154 | Oxct2b | 3-oxoacid CoA transferase 2B | 1.05 | 0.934213 |
| 17302889 | **Pcca** | propionyl-CoA carboxylase, alpha polypeptide | **1.5** | **0.001756** |
| 17530141 | Pccb | propionyl CoA carboxylase, beta polypeptide | 1.44 | **0.006184** |

***Table 6. Expression levels in iWAT of genes participating in the degradation of the branched-chain amino acids.*** Fold change values of gene expression in iWAT of cold-exposed mice in comparison with the control group. Highlighted in **Bold**: statistically significant p-values. Highlighted in **Red**: upregulated expression in cold exposure of 1.5-fold or higher; Highlighted in Pink: upregulated expression in cold exposure between 1.4- and 1.49-fold.

In addition to leucine, isoleucine, and valine, other amino acids participate in the maintenance of the TCA intermediates. Aspartate can generate oxaloacetate by *aspartate transaminase*, which has two isoforms that can be cytoplasmic (*Got1*) or mitochondrial (*Got2*) (Doonan et al., 1984; Ford et al., 1980). This reaction is involved in the malate-aspartate shuttle, in which oxaloacetate is transported to the mitochondria for a temporal conversion to malate by *Mdh1* in the cytoplasm or *Mdh2* in the mitochondria (Figure 30). The conversion of oxaloacetate to malate and, finally, to oxaloacetate again generates $NAD^+$ in the cytoplasm and NADH in the mitochondria, which will be used to maintain the proton gradient. Figure 30 illustrates the entrance of oxaloacetate to the mitochondria that in iWAT of cold-exposed mice was probably enhanced by the significant upregulation of *Got1* (2.67-fold), *Mdh1* (1.47-fold) and *Mdh2* (2.26-fold) (Figure 30, Table 7). Furthermore, the oxoglutarate/malate carrier, *Slc25a11*, had a significant slight increase in gene expression of 1.39-fold (Figure 30, Table 7). Nevertheless, the malate-aspartate shuttle was not fully upregulated since the expression of *Got2* was not modified. In addition, as previously observed, alanine and glutamine can be transformed to pyruvate or α-ketoglutarate by the enzyme *alanine aminotransferase, Gpt2,* (1.56-fold) in a reversible reaction (Figure 30, Table 7).

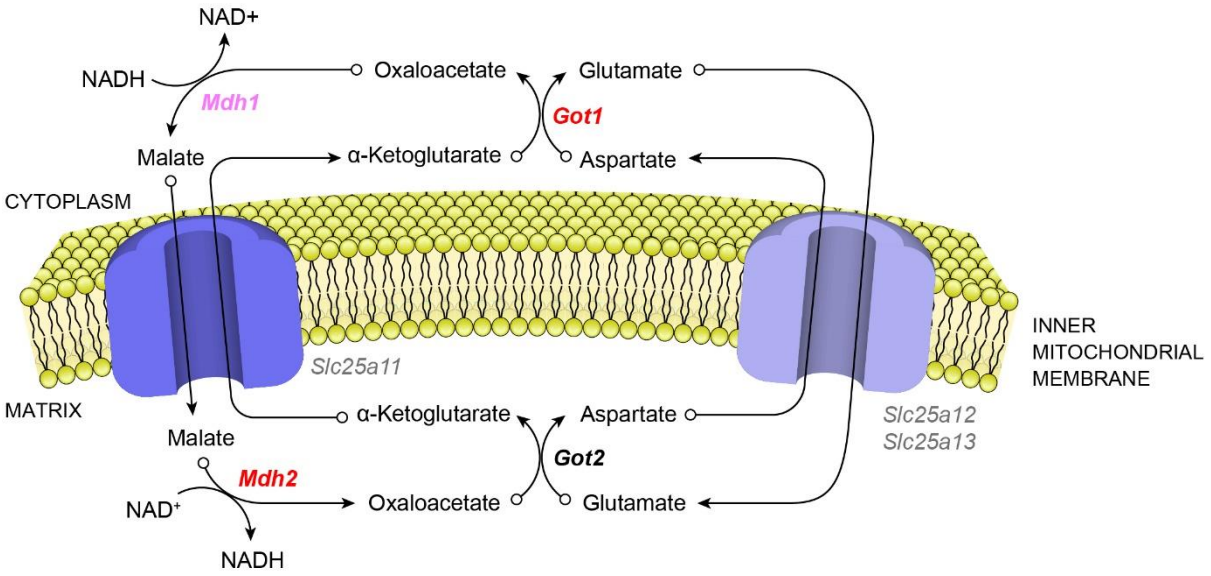


***Figure 30. Schematic representation of the gene expression changes mediated by cold exposure of the malate-aspartate shuttle in iWAT***. Representation of the malate-aspartate shuttle with the metabolites in regular black and the enzymes that metabolize each process in ***italic bold*** and the different transporters and channels in regular grey. Highlighted in **Bold**: no changes in gene expression levels; Highlighted in **Red**: upregulated expression in cold-exposed mice higher or equal than 1.5-fold; Highlighted in Pink: upregulated expression in cold-exposed mice between 1.4- and 1.49-fold.

| Transcript ID | Gene Symbol | Description | Fold Change | p-value |
|---|---|---|---|---|
| 17364932 | **Got1** | glutamate oxaloacetate transaminase 1, soluble | **2.67** | **0.00013** |
| 17512103 | Got2* | glutamate oxaloacetate transaminase 2, mitochondrial | 1.02 | 0.770182 |
| 17260944 | **Mdh1** | malate dehydrogenase 1, NAD (soluble) | **1.47** | **0.003632** |
| 17443310 | **Mdh2** | malate dehydrogenase 2, NAD (mitochondrial) | **2.26** | **0.000052** |
| 17265306 | Slc25a11 | solute carrier family 25 (mitochondrial carrier oxoglutarate carrier), member 11 | 1.39 | **0.010145** |
| 17386396 | Slc25a12 | solute carrier family 25 (mitochondrial carrier, Aralar), member 12 | -1.14 | 0.569582 |
| 17464672 | Slc25a13 | solute carrier family 25 (mitochondrial carrier, adenine nucleotide translocator), member 13 | -1.02 | 0.251213 |

***Table 7. Malate-aspartate shuttle related enzymes with its expression in iWAT.*** Fold change values of gene expression in cold-exposed mice in comparison with the control group. **Bold**: statistically significant p-values. **Red**: upregulated expression in cold exposure of 1.5-fold or higher; **Pink**: upregulated expression in cold exposure between 1.4- and 1.49-fold. *This probe can detect different transcripts.

The degradation of other amino acids as asparagine, aspartate, glutamine, histamine, histidine, phenylalanine, serine, threonine or tyrosine was not as clear as the degradation of BCAA, as shown in Figure 31. However, several genes mediating the degradation of different amino acids were also upregulated, which could mediate its degradation (Table 6, 8).

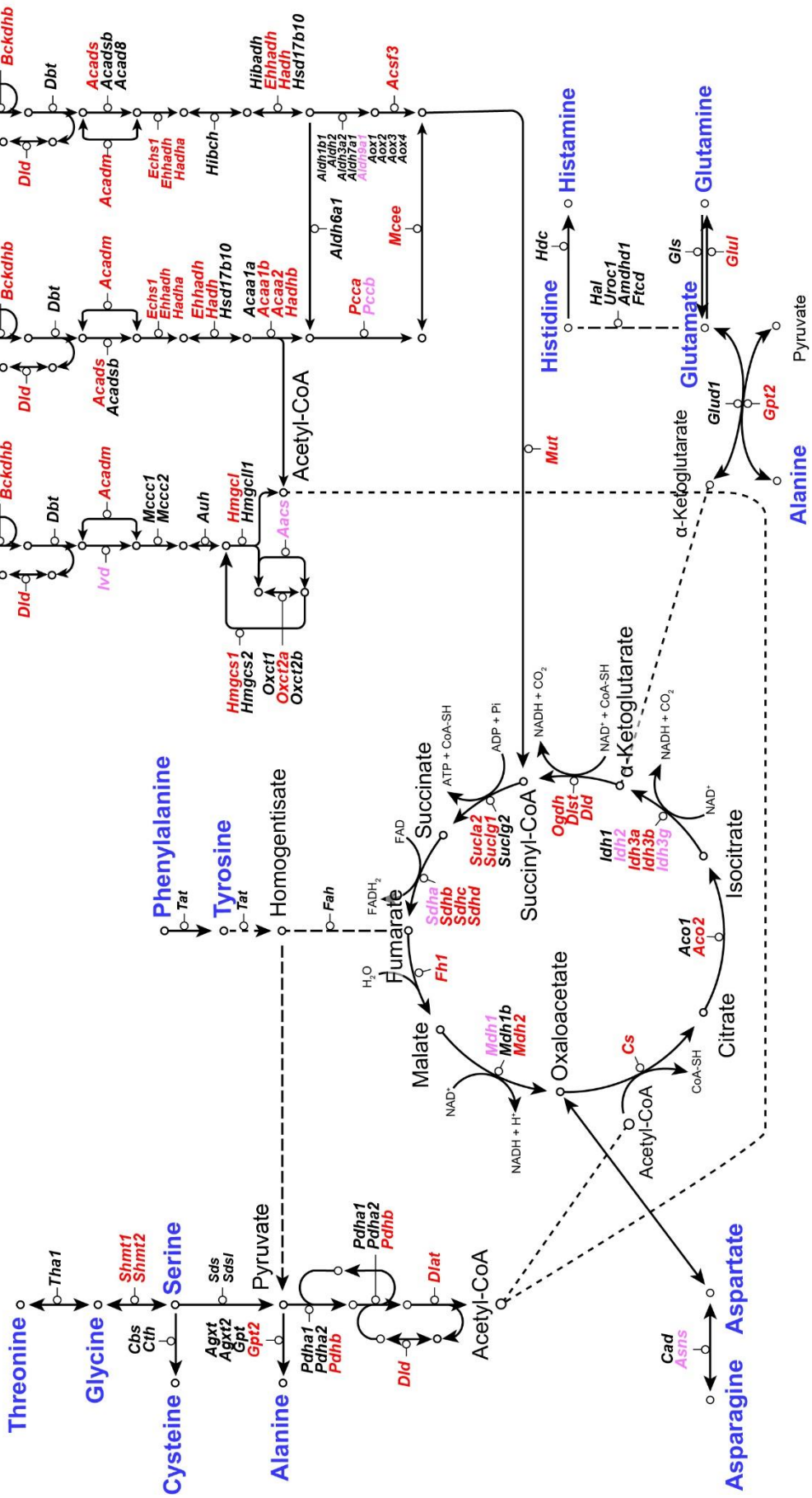


***Figure 31. Expression changes of genes related to the degradation of amino acids in iWAT after cold exposure.*** The enzymes that metabolize each process are emphasized in ***italic bold***. Highlighted in **Blue**: Amino acids; Highlighted in **Black**: no changes in gene expression levels; Highlighted in **Red**: upregulated expression in cold exposure of 1.5-fold or higher; Highlighted in **Pink**: upregulated expression in cold exposure between 1.4- and 1.49-fold. Adapted from KEGG pathway. Short-dashed lines link same metabolites. Long-dashed lines resume several steps.

The enzymes *Shmt1* and *Shmt2* that convert serine to glycine and vice versa had a significant fold change increase of 2.32 and 1.82 respectively, potentially indicating an activated metabolism around both amino acids (Table 8). Analyzing in detail the possible functions of these amino acids in this cold-exposure state, the upregulation of serine-related enzymes was not coincidental, as the serine amino acid has been described as presenting increased levels during cold exposure (López-Soriano and Alemany, 1987). This amino acid has also been described as allosterically activating the *muscular pyruvate kinase*, which was upregulated in iWAT of cold-exposed mice (Chaneton et al., 2012) (Figure 26). Furthermore, besides activating *Pkm*, serine cleavage to glycine has other metabolic functions, contributing to the production of NADPH in a cycle known as the glycine cleavage system. This cycle is mediated by four different enzymes: *Gcsh*, *Dld*, *Gldc,* and *Amt*, which encode the H, L, P, and T proteins (Tedeschi et al., 2013) (Table 9). Under cold exposure conditions, the enzyme responsible for decarboxylating the glycine, encoded in *Gldc* (or P-protein) and the enzyme responsible for reducing $NAD^+$ to NADH, encoded in *Dld* (or L-protein), were upregulated with high statistical significance (Table 8, 9).

| Transcript ID | Gene Symbol | Description | Fold Change | p-value |
|---|---|---|---|---|
| 17215885 | Agxt | alanine-glyoxylate aminotransferase | -1.01 | 0.887939 |
| 17310282 | Agxt2 | alanine-glyoxylate aminotransferase 2 | 1.07 | 0.706286 |
| 17244350 | Amdhd1 | amidohydrolase domain containing 1 | 1.25 | 0.226572 |
| 17464718 | **Asns** | asparagine synthetase | **1.4** | **0.008288** |
| 17435978 | Cad | carbamoyl-phosphate synthetase 2, aspartate transcarbamylase, and dihydroorotase | 1.13 | **0.029493** |
| 17343227 | Cbs | cystathionine beta-synthase | 1.3 | **0.033635** |
| 17411420 | Cth | cystathionase (cystathionine gamma-lyase) | -1.03 | 0.986762 |
| 17526861 | **Dlat** | dihydrolipoamide S-acetyltransferase (E2 component of pyruvate dehydrogenase complex) | **2.33** | **0.000088** |
| 17280498 | **Dld** | dihydrolipoamide dehydrogenase | **1.69** | **0.001312** |
| 17234588 | Ftcd | formiminotransferase cyclodeaminase | 1.01 | 0.476405 |
| 17222880 | Gls | glutaminase | -1 | 0.597213 |
| 17298805 | Glud1 | glutamate dehydrogenase 1 | 1.29 | **0.00497** |
| 17548983 | **Glul** | glutamate-ammonia ligase (glutamine synthetase) | **2.18** | **0.017908** |
| 17312567 | Gpt | glutamic pyruvic transaminase, soluble | 1.12 | **0.047071** |
| 17503446 | **Gpt2** | glutamic pyruvate transaminase (alanine aminotransferase) 2 | **1.56** | **0.032108** |
| 17236552 | Hal | histidine ammonia lyase | -1.14 | 0.88842 |
| 17391094 | Hdc | histidine decarboxylase | -1.05 | 0.650067 |
| 17545741 | Pdha1 | pyruvate dehydrogenase E1 alpha 1 | 1.35 | **0.004009** |
| 17410718 | Pdha2 | pyruvate dehydrogenase E1 alpha 2 | -1.1 | 0.05791 |
| 17303400 | **Pdhb** | pyruvate dehydrogenase (lipoamide) beta | **1.67** | **0.004331** |
| 17263673 | **Shmt1** | serine hydroxymethyltransferase 1 (soluble) | **2.32** | **0.000047** |
| 17245902 | **Shmt2** | serine hydroxymethyltransferase 2 (mitochondrial) | **1.82** | **0.022094** |
| 17272605 | Tha1 | threonine aldolase 1 | 1.21 | 0.095986 |
| 17460785 | Uroc1 | urocanase domain containing 1 | -1.1 | 0.343729 |

***Table 8. Genes participating in the degradation of amino acids in iWAT after cold exposure.*** Fold change values of gene expression in cold-exposed mice in comparison with the control group. Highlighted in **Bold**: statistically significant p-values. Highlighted in **Red**: upregulated expression in cold exposure of 1.5-fold or higher; Highlighted in Pink: upregulated expression in cold exposure between 1.4- and 1.49-fold.

| Transcript ID | Gene Symbol | Description | Fold Change | p-value |
|---|---|---|---|---|
| 17521661 | Amt | aminomethyltransferase | -1.1 | 0.74393 |
| 17280498 | **Dld** | dihydrolipoamide dehydrogenase | **1.7** | **0.00109** |
| 17513325 | Gcsh; LOC674321 | glycine cleavage system protein H (aminomethyl carrier); | 1.22 | 0.35129 |
| 17363865 | **Gldc** | glycine decarboxylase | **1.45** | **0.00281** |

***Table 9. Expression levels in iWAT of genes related to the glycine cleavage system.*** Fold change values of gene expression in cold-exposed mice in comparison with the control group. Highlighted in **Bold**: statistically significant p-values. Highlighted in **Red**: upregulated expression in cold exposure of 1.5-fold or higher; Highlighted in **Pink**: upregulated expression in cold exposure between 1.4- and 1.49-fold.

As previously described, the expression of the *Gpt2*, which encoded an enzyme that mediates the reversible conversion of alanine and α-ketoglutarate to pyruvate and glutamate, was also upregulated, resulting in the generation of two different intermediate metabolites of the TCA cycle (Table 8). The enzyme that generates glutamine from glutamate was also upregulated (*Glul*) (Table 8).

## 1.4. Triglycerides and fatty acid metabolism

### *1.4.1. Mobilization of triacylglycerols*

The degradation of triglycerides to produce FA and, finally, acetyl-CoA has been widely studied, especially in adipose tissue (Figure 32). During cold exposure, the sympathetic nervous system (SNS) releases norepinephrine to the adipose tissue which, through the β-adrenergic receptors, activates adenylate cyclase protein to increase cyclic AMP. In iWAT of cold-exposed mice, gene expression differences were not found in either the β1-adrenergic receptor, the β2-adrenergic receptor or the β3-adrenergic receptor (Table 10). However, the protein responsible for directly activating *adenylate cyclase* through the β-adrenergic receptors' signaling is a Gs protein, whose gene *Gnas* was upregulated (about 50% increase) in iWAT of cold-exposed mice (Figure 32, Table 10). *Adenylate cyclase* also presented some isoforms with an upregulated expression, such as the isoforms 3 (2.31-fold) and 10 (2.19-fold), while others, such as isoform 5 were downregulated (-1.55-fold) (Figure 32, Table 10). *Adenylate cyclase* increases the levels of cAMP that stimulates protein kinase A (PKA). The *Prkaca* gene, which encodes for the catalytic subunit of the protein kinase A (PKA), increased 1.94-fold in iWAT, suggesting an increase in the phosphorylation rate of this protein (Figure 32, Table 10). The enzymes codified by *perilipin* (*Plin1*) and *hormone-sensitive lipase* (*Hsl*) are two of the PKA targets (Anthonsen

et al., 1998; Duncan et al., 2007). The phosphorylation of perilipin, the expression of whose gene presented a 1.23-fold increase in our study, triggers the release of a coactivator for *adipose triglyceride lipase* (*Atgl*), that initiates the mobilization of triglycerides (Figure 32, Table 10). The gene *Atgl,* also known as *Pnpla2*, had its expression increased by 58% (Figure 32, Table 10). The activation of *Atgl* converts triacylglycerol to diacylglycerol and releases FA. Diacylglycerol is then converted to monoacylglycerol and free fatty acids (FFA) by the *hormone-sensitive lipase*. The gene encoding for the *Hsl* presented a significant increase about 1.38-fold (Figure 32, Table 10). Finally, monoacylglycerol is converted to FFA and glycerol by the *monoacylglycerol lipase* or *Mgl*, which had a fold change expression of 1.56 (Figure 32, Table 10). Overall, the enzymes involved in the degradation of triglycerides presented a remarkable upregulation in iWAT, suggesting an increase in the generation of FA.

### *1.4.2. Fatty acid activation and transport to the mitochondria*

In cold-exposed mice, besides the FA obtained from the degradation of triacylglycerol, other results suggested an increased entrance of FA in iWAT. Several FA receptors were highly upregulated, *Slc27a1* for example (2.77-fold) or slightly upregulated, *Slc27a4* or *Slc27a2* (1.27- and 1.24-fold, respectively) (Figure 32, Table 10). However, the large family of fatty acid binding proteins (FABP1–FABP9) that are essential for FA uptake did not present a modified expression of their genes (Figure 32, Table 10).

Once FA are obtained, they must undergo three enzymatic reactions to be oxidized. First, they are activated to fatty acyl-CoA thioesters by a family of isoenzymes of *acyl-CoA synthetases* in the cytoplasm. Of these, the encoding genes for *acyl-CoA synthetases Acls1* and *Acls3* showed 1.25- and 1.36-fold increased expression, respectively. Second, *carnitine palmitoyl transferase 1*, also named *carnitine acyltransferase 1* or *Cpt1*, transforms the fatty acyl-CoA to fatty-acyl-carnitine. *Cpt1b*, with increased gene expression of 6.33-fold in iWAT (Figure 32, Table 10), mediates the entrance of FA to the mitochondria, as fatty acyl–carnitine ester can diffuse across the intermembrane space.

The acyl-carnitine/carnitine cotransporter of the inner mitochondrial membrane allows the entrance to the mitochondrial matrix of fatty-acyl carnitine by moving a molecule of carnitine to the intermembrane space. Finally, *Cpt2* or *carnitine acyltransferase 2* transfers the fatty acyl group from the carnitine to the intramitochondrial CoA (Figure 32). This enzyme had its gene expression increased by 73% in iWAT in cold exposure

conditions. Altogether, the expression levels of genes related to FA transport to the mitochondria suggested that this pathway was increased in iWAT from cold-exposed mice.

### *1.4.3. Fatty acid oxidation*

The oxidation of FA, also known as β-oxidation, takes place inside the mitochondria, where fatty acyl-CoA is converted during several cycles to acetyl-CoA by the removal of successive two-carbon from the carboxyl end (Figure 32). The first step of this process is catalyzed by four different isoforms of the *acyl-CoA dehydrogenase*, each specific isoform for a range of FA chain lengths: *Very-long-chain acyl-CoA dehydrogenase* (*Acadvl*), *long-chain acyl-CoA dehydrogenase* (*Acadl*), *medium-chain acyl-CoA dehydrogenase* (*Acadm*), and *short-chain acyl-CoA dehydrogenase* (*Acads*) (Figure 32). In this process, two electrons from the fatty acyl-CoA are transferred to a flavoprotein (ETF) in the form of $FADH_2$. In the second step of the β-oxidation cycle, water is added to form 3-hydroxyacyl-CoA. In the third step, β-ketoacyl-CoA is formed by the action of *β-hydroxyacyl-CoA dehydrogenase*, also generating NADH. Lastly, the thiolase *acyl-CoA acetyltransferase* splits off the carboxyl-terminal two-carbon fragment from the molecule of CoA, generating acetyl-CoA. Importantly, if the FA chain is composed of 12 or more carbons, these last three steps are catalyzed by a multienzyme complex, the *mitochondrial trifunctional protein* in the inner mitochondrial membrane. This complex is a heterooctamer of $\alpha_4\beta_4$, having the α subunit (*Hadha*) enoyl-CoA hydratase and β-hydroxyacyl-CoA dehydrogenase activities, and the β subunit (*Hadhb*) the thiolase activity. All the genes encoding these enzymes were upregulated in iWAT under cold exposure, with the subunit *Hadha* showing 2.19-fold and *Hadhb* of 1.79-fold (Figure 32, Table 10).

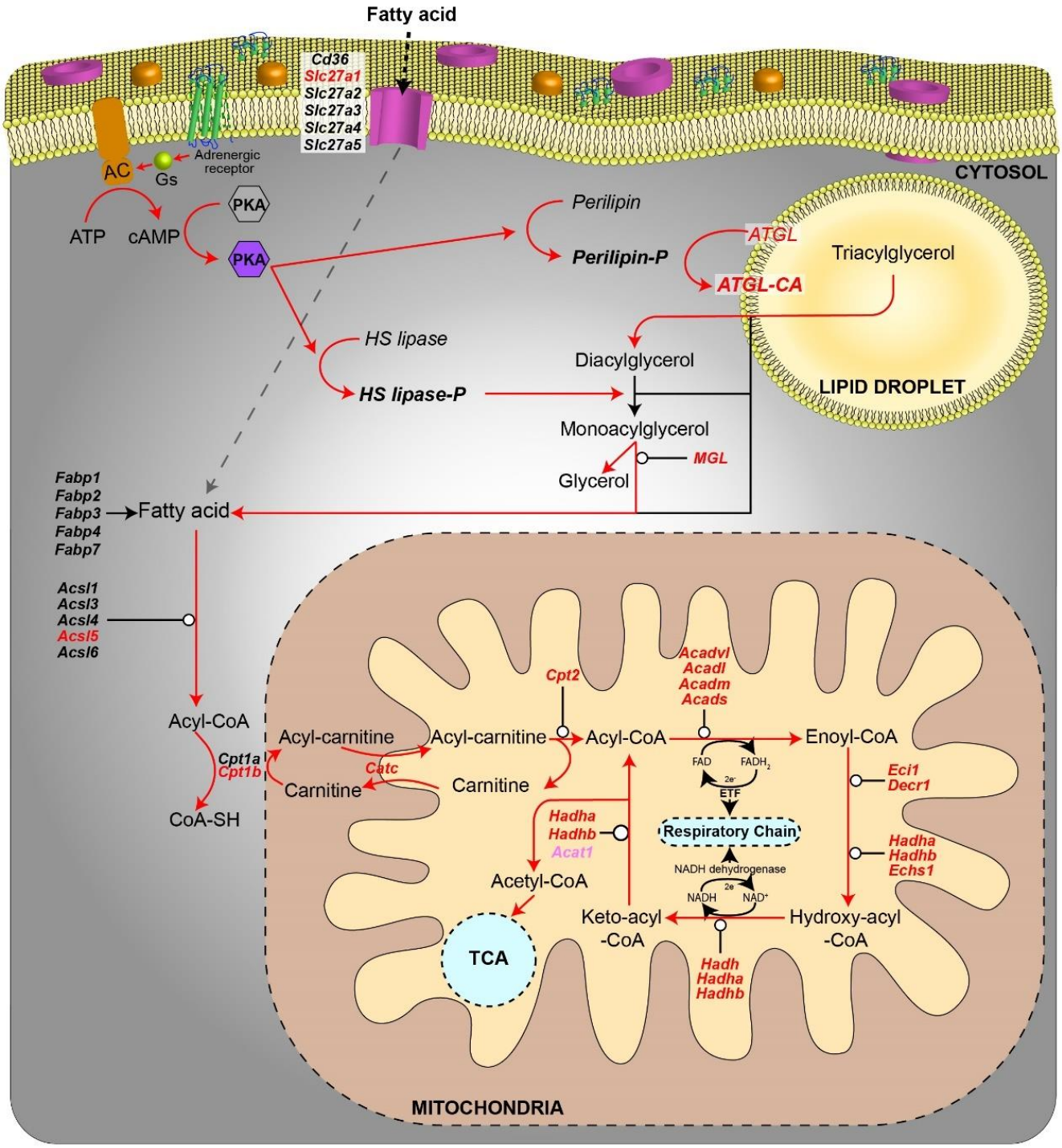


***Figure 32. Schematic representation of the gene expression changes mediated by cold exposure of the triglyceride and fatty acid degradation pathway in iWAT.*** Representation of the triglyceride and fatty acid degradation pathway. The enzymes that metabolize each process are emphasized in ***italic bold***. Highlighted in **Black**: no changes in gene expression levels; Highlighted in **Red**: upregulated expression in cold exposure of 1.5-fold or higher; Highlighted in Pink: upregulated expression in cold exposure between 1.4- and 1.49-fold. Red arrows: potentially enhanced flow; black arrow: potentially normal flow. Dashed lines link same metabolites. Adapted from KEGG pathway.

| Transcript ID | Gene Symbol | Description | Fold Change | p-value |
|---|---|---|---|---|
| 17548916 | **Acadl** | acyl-Coenzyme A dehydrogenase, long-chain | **2.91** | **0.000021** |
| 17411323 | **Acadm** | acyl-Coenzyme A dehydrogenase, medium chain | **1.61** | **0.000963** |
| 17451649 | **Acads** | acyl-Coenzyme A dehydrogenase, short chain | **1.5** | **0.001696** |
| 17265129 | **Acadvl** | acyl-Coenzyme A dehydrogenase, very long chain | **3.02** | **0.000158** |
| 17527123 | Acat1 | acetyl-Coenzyme A acetyltransferase 1 | 1.36 | **0.003926** |
| 17500996 | Acsl1 | acyl-CoA synthetase long-chain family member 1 | 1.25 | **0.023701** |
| 17214685 | Acsl3 | acyl-CoA synthetase long-chain family member 3 | 1.36 | 0.515631 |
| 17545051 | Acsl4 | acyl-CoA synthetase long-chain family member 4 | 1.03 | 0.584309 |
| 17360462 | **Acsl5** | acyl-CoA synthetase long-chain family member 5 | **3.43** | **0.000136** |
| 17249640 | Acsl6 | acyl-CoA synthetase long-chain family member 6 | -1.03 | 0.439315 |
| 17247183 | Adcy1 | adenylate cyclase 1 | -1.09 | 0.495968 |
| 17294086 | Adcy2 | adenylate cyclase 2 | -1.29 | 0.107488 |
| 17273714 | **Adcy3** | adenylate cyclase 3 | **2.31** | **0.000096** |
| 17306877 | Adcy4 | adenylate cyclase 4 | 1.37 | **0.002149** |
| 17325206 | **Adcy5** | adenylate cyclase 5 | **-1.55** | **0.000264** |
| 17321263 | Adcy6 | adenylate cyclase 6 | 1.08 | **0.049496** |
| 17503616 | Adcy7 | adenylate cyclase 7 | -1.1 | 0.730082 |
| 17317533 | Adcy8 | adenylate cyclase 8 | -1.01 | 0.926161 |
| 17327720 | Adcy9 | adenylate cyclase 9 | 1.13 | 0.321262 |
| 17218965 | **Adcy10** | adenylate cyclase 10 | **2.19** | **0.01389** |
| 17360599 | Adrb1 | adrenergic receptor, beta 1 | 1.21 | 0.275350 |
| 17354857 | Adrb2 | adrenergic receptor, beta 2 | -1.21 | 0.780916 |
| 17508544 | Adrb3 | adrenergic receptor, beta 3 | 1.01 | 0.964617 |
| 17521875 | **Catc / Slc25a20** | solute carrier family 25, member 20 | **3.09** | **0.000088** |
| 17445715 | Cd36 | CD36 antigen | -1.03 | 0.101366 |
| 17355915 | Cpt1a | carnitine palmitoyltransferase 1a, liver | -1.04 | 0.818156 |
| 17320499 | **Cpt1b** | carnitine palmitoyltransferase 1b, muscle | **6.33** | **0.000002** |
| 17427961 | **Cpt2** | carnitine palmitoyltransferase 2 | **1.73** | **0.000067** |
| 17423463 | **Decr1** | 2,4-dienoyl CoA reductase 1, mitochondrial | **1.57** | **0.000231** |
| 17497612 | **Echs1** | enoyl Coenzyme A hydratase, short chain, 1, mitochondrial | **1.79** | **0.001332** |
| 17334253 | **Eci1** | enoyl-Coenzyme A delta isomerase 1 | **1.82** | **0.003264** |
| 17459455 | Fabp1 | fatty acid binding protein 1, liver | 1.29 | **0.041520** |
| 17402350 | Fabp2 | fatty acid binding protein 2, intestinal | -1.32 | 0.277936 |
| 17419215 | Fabp3 | fatty acid binding protein 3, muscle and heart | 1.05 | 0.807348 |
| 17404091 | Fabp4 | fatty acid binding protein 4, adipocyte | 1.02 | 0.970035 |
| 17233384 | Fabp7 | fatty acid binding protein 7, brain | -1.02 | 0.175637 |
| 17380306 | **Gnas** | GNAS (guanine nucleotide binding protein, alpha stimulating) complex locus | **1.5** | **0.000417** |
| 17410390 | **Hadh** | hydroxyacyl-Coenzyme A dehydrogenase | **1.53** | **0.001646** |
| 17446643 | **Hadha** | hydroxyacyl-Coenzyme A dehydrogenase | **2.19** | **0.000023** |
| 17435748 | **Hadhb** | hydroxyacyl-Coenzyme A dehydrogenase | **1.79** | **0.000680** |
| 17487927 | Lipe | lipase, hormone sensitive | 1.38 | **0.006436** |
| 17460665 | **Mgll** | monoglyceride lipase | **1.56** | **0.015810** |
| 17492406 | Plin1 | perilipin 1 | 1.23 | 0.141230 |
| 17426981 | **Plin2** | perilipin 2 | **1.66** | **0.000199** |
| 17346216 | **Plin3** | perilipin 3 | **1.56** | **0.002161** |
| 17346125 | Plin4 | perilipin 4 | -1.04 | 0.429856 |
| 17346136 | **Plin5** | perilipin 5 | **3.9** | **0.000097** |
| 17484909 | **Pnpla2** | patatin-like phospholipase domain containing 2 | **1.58** | 0.058636 |
| 17503031 | **Prkaca** | protein kinase, cAMP dependent, catalytic, alpha | **1.94** | **0.000100** |
| 17502233 | **Slc27a1** | solute carrier family 27 (fatty acid transporter), member 1 | **2.77** | **0.000707** |
| 17391089 | Slc27a2 | solute carrier family 27 (fatty acid transporter), member 2 | 1.24 | 0.121447 |
| 17407259 | Slc27a3 | solute carrier family 27 (fatty acid transporter), member 3 | -1.15 | 0.336910 |
| 17368904 | Slc27a4 | solute carrier family 27 (fatty acid transporter), member 4 | 1.27 | **0.030523** |
| 17486589 | Slc27a5 | solute carrier family 27 (fatty acid transporter), member 5 | 1.15 | 0.148656 |
| 17350856 | Slc27a6 | solute carrier family 27 (fatty acid transporter), member 6 | -1.1 | 0.901385 |

***Table 10. Cold-induced expression changes in genes involved in triglycerides and fatty acids degradation in iWAT.*** Fold change values of gene expression in cold-exposed mice in comparison with the group control are shown. Highlighted in **Bold**: statistically significant p-values. Highlighted in **Red**: upregulated expression in cold exposure of 1.5-fold or higher; Highlighted in **Green**: downregulated expression in cold exposure of -1.5-fold or lower.

## 1.5. Oxidative phosphorylation

Oxidative phosphorylation is a process that occurs in the mitochondria and starts with the flow of electrons from NADH and $FADH_2$. Both molecules are generated in all the metabolic processes analyzed previously, especially in the TCA (Figures 26, 28, 30, 32). Four large protein complexes of the inner mitochondrial membrane are responsible for the electron flow in a process called the respiratory chain or electron-transport chain. The respiratory chain generates an electrochemical gradient or proton gradient as three of the complexes use the energy released by the electron flow to pump protons out of the mitochondrial matrix (complex I, complex III, complex IV) (Figure 33). Then, the *ATPase synthase* generates ATP using this gradient (Figure 33).

In iWAT, all the complexes of the respiratory chain presented upregulated expression of subunits suggesting an increased production of the proton gradient (Figure 33, Table 11). Furthermore, genes encoding for subunits of the complex V, the mitochondrial membrane-associated multimeric complex *ATPase synthase* or *F-type ATPase* were upregulated (Figure 33, Table 11). This complex is composed of two different parts, the $F_0$ motor responsible for ion translocation, and the $F_1$ motor responsible for ATP turnover (Figure 33, Table 11). $F_0$ motor consists of at least three subunits (A, B and C), but usually has 9 (A-G, F6, and F8) and $F_1$ motor has the subunit composition $\alpha_3\beta_3\gamma\delta\varepsilon$. In iWAT, genes encoding for subunits of the $F_0$ motor B, C2, C3, D, E, F, and G were upregulated 1.62-, 1.5-, 1.63-, 1.56-, 1.5-, 1.51-, and 1.51-fold, respectively (Table 11). Furthermore, the gene encoding for the subunit C1 was downregulated -1.49-fold. The $F_1$ motor presented the subunits α, β, δ and ε upregulated with their genes upregulated 1.45-, 1.5-, 1.94-, 1.84-, and 1.69-fold (Table 11). The gene encoding for the subunit O or OSCP, which links the subunit A of $F_0$ with the $F_1$ motor, was also upregulated 1.69-fold (Table 11). All these results clearly highlighted the coordinated upregulation of almost all the subunits of the *F-type ATPase* in iWAT of cold-exposed mice, consistent with the key role of this protein to maintain the energy homeostasis.

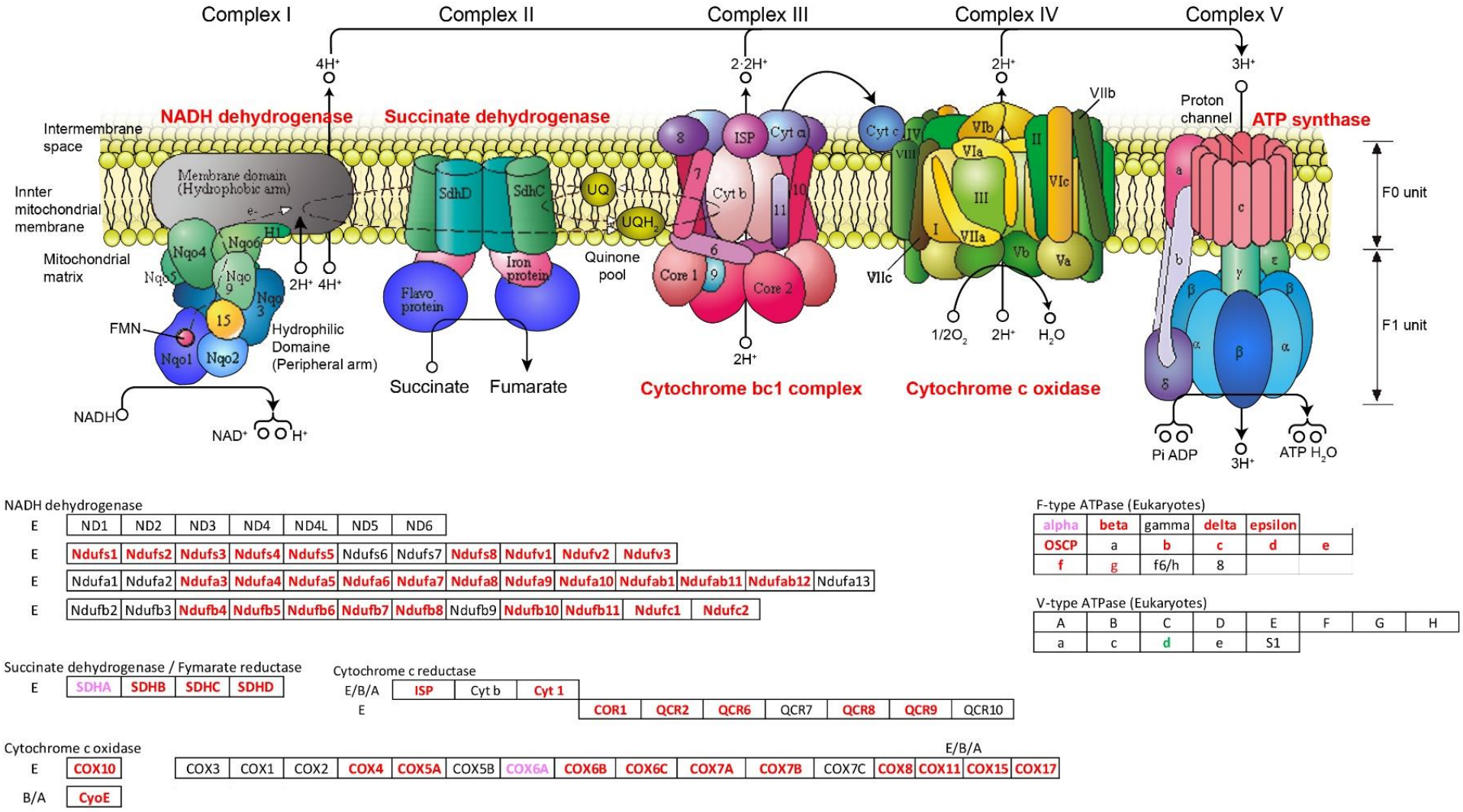


***Figure 33. Expression changes in iWAT induced by cold exposure of the several isoenzymes of the different complexes of the electron transport chain and the ATPase.*** On top of the figure, the different isoenzymes of each complex are showed. Below the schema, all genes encoding for the different complex are indicated, as well as alterations on their gene expression level in cold exposed animals in comparison to room temperature exposed mice. Highlighted in **Black**: no changes in gene expression levels; Highlighted in **Red**: upregulated expression in cold exposure of 1.5-fold or higher; Highlighted in Pink: upregulated expression in cold exposure between 1.4- and 1.49-fold; Highlighted in **Green**: downregulated expression in cold exposure of -1.5-fold or lower. Adapted from KEGG pathway.

| Transcript ID | Gene Symbol | Alias | Description | Pathway | Fold Change | p-value |
|---|---|---|---|---|---|---|
| 17352020 | Atp5a1 | alpha | ATP synthase, H+ transporting, mitochondrial F1 complex, alpha subunit 1 | F-type ATPase | 1.45 | **0.000657** |
| 17238278 | Atp5b | beta | ATP synthase, H+ transporting mitochondrial F1 complex, beta subunit | F-type ATPase | 1.5 | **0.00076** |
| 17235198 | Atp5d | delta | ATP synthase, H+ transporting, mitochondrial F1 complex, delta subunit | F-type ATPase | 1.86 | **0.000009** |
| 17235198 | Atp5d | delta | ATP synthase, H+ transporting, mitochondrial F1 complex, delta subunit | F-type ATPase | 1.86 | **0.000009** |
| 17242839 | Atp5d | delta | ATP synthase, H+ transporting, mitochondrial F1 complex, delta subunit | F-type ATPase | 1.94 | **0.000199** |
| 17242839 | Atp5d | delta | ATP synthase, H+ transporting, mitochondrial F1 complex, delta subunit | F-type ATPase | 1.94 | **0.000199** |
| 17395165 | Atp5e | epsilon | ATP synthase, H+ transporting, mitochondrial F1 complex, epsilon subunit | F-type ATPase | 1.84 | **0.003308** |
| 17395165 | Atp5e | epsilon | ATP synthase, H+ transporting, mitochondrial F1 complex, epsilon subunit | F-type ATPase | 1.84 | **0.003308** |
| 17408863 | Atp5f1 | b | ATP synthase, H+ transporting, mitochondrial F0 complex, subunit B1 | F-type ATPase | 1.62 | **0.001646** |
| 17268289 | Atp5g1 | c | ATP synthase, H+ transporting, mitochondrial F0 complex, subunit c1 (subunit 9) | F-type ATPase | -1.49 | 0.107567 |
| 17340500 | Atp5g2 | c | ATP synthase, H+ transporting, mitochondrial F0 complex, subunit C2 (subunit 9) | F-type ATPase | 1.5 | **0.002566** |
| 17386621 | Atp5g3 | c | ATP synthase, H+ transporting, mitochondrial F0 complex, subunit C3 (subunit 9) | F-type ATPase | 1.63 | **0.001526** |
| 17271891 | Atp5h | delta | ATP synthase, H+ transporting, mitochondrial F0 complex, subunit d | F-type ATPase | 1.43 | **0.022467** |
| 17315713 | Atp5h | delta | ATP synthase, H+ transporting, mitochondrial F0 complex, subunit d | F-type ATPase | 1.56 | **0.002183** |
| 17455083 | Atp5j2 | f | ATP synthase, H+ transporting, mitochondrial F0 complex, subunit F2 | F-type ATPase | 1.51 | 0.116925 |
| 17450741 | Atp5k | epsilon | ATP synthase, H+ transporting, mitochondrial F1F0 complex, subunit e | F-type ATPase | 1.5 | **0.024576** |
| 17332203 | Atp5o | OSCP | ATP synthase, H+ transporting, mitochondrial F1 complex, O subunit | F-type ATPase | 1.69 | **0.007842** |
| 17423577 | Atp6v0d2 | d | ATPase, H+ transporting, lysosomal V0 subunit D2 | V-type ATPase | -2.2 | 0.356331 |
| 17521996 | COR1 | | ubiquinol-cytochrome c reductase core protein 1 | Cytochrome c reductase | 2.66 | **0.000033** |
| 17264107 | Cox10 | | cytochrome c oxidase assembly protein 10 | Cytochrome c oxidase | 2.73 | **0.000091** |
| 17255081 | Cox11 | | cytochrome c oxidase assembly protein 11 | Cytochrome c oxidase | 1.95 | **0.000258** |
| 17364954 | Cox15 | | cytochrome c oxidase assembly protein 15 | Cytochrome c oxidase | 2.65 | **0.000746** |
| 17325581 | Cox17 | | cytochrome c oxidase assembly protein 17 | Cytochrome c oxidase | 1.64 | **0.000537** |
| 17506273 | Cox4i1 | | cytochrome c oxidase subunit IV isoform 1 | Cytochrome c oxidase | 1.73 | **0.000961** |
| 17517727 | Cox5a | | cytochrome c oxidase subunit Va | Cytochrome c oxidase | 2.97 | **0.00005** |
| 17496857 | Cox6a2 | | cytochrome c oxidase subunit VIa polypeptide 2 | Cytochrome c oxidase | 1.44 | 0.378766 |
| 17489223 | Cox6b1 | | cytochrome c oxidase, subunit VIb polypeptide 1 | Cytochrome c oxidase | 1.94 | **0.0027** |
| 17485904 | Cox6b2 | | cytochrome c oxidase subunit VIb polypeptide 2 | Cytochrome c oxidase | 1.6 | **0.009273** |
| 17547698 | Cox6c | | cytochrome c oxidase subunit VIc | Cytochrome c oxidase | 1.49 | **0.003783** |
| 17316436 | Cox6c | | cytochrome c oxidase subunit VIc | Cytochrome c oxidase | 1.65 | **0.013497** |
| 17476288 | Cox7a1 | | cytochrome c oxidase subunit VIIa 1 | Cytochrome c oxidase | 9.62 | **0.000000599** |
| 17529169 | Cox7a2 | | cytochrome c oxidase subunit VIIa 2 | Cytochrome c oxidase | 1.46 | **0.008113** |
| 17537048 | Cox7b | | cytochrome c oxidase subunit VIIb | Cytochrome c oxidase | 1.68 | **0.021343** |
| 17537048 | Cox7b | | cytochrome c oxidase subunit VIIb | Cytochrome c oxidase | 1.68 | **0.021343** |
| 17548981 | Cox7b | | cytochrome c oxidase subunit VIIb | Cytochrome c oxidase | 2.11 | **0.004783** |
| 17548981 | Cox7b | | cytochrome c oxidase subunit VIIb | Cytochrome c oxidase | 2.11 | **0.004783** |
| 17497704 | Cox8b | | cytochrome c oxidase subunit VIIIb | Cytochrome c oxidase | 3.05 | **0.000718** |
| 17264107 | CyoE | | cytochrome c oxidase assembly protein 10 | Cytochrome c oxidase | 2.73 | **0.000091** |
| 17312396 | Cyt1 | | cytochrome c-1 | Cytochrome c reductase | 2.82 | **0.000377** |
| 17291570 | ISP | | ubiquinol-cytochrome c reductase, Rieske iron-sulfur polypeptide 1 | Cytochrome c reductase | 2.26 | **0.00115** |
| 17225564 | Ndufa10 | | NADH dehydrogenase (ubiquinone) 1 alpha subcomplex 10 | NADH dehydrogenase | 1.84 | **0.000285** |
| 17236681 | Ndufa12 | | NADH dehydrogenase (ubiquinone) 1 alpha subcomplex, 12 | NADH dehydrogenase | 1.76 | **0.006867** |
| 17473171 | Ndufa3 | | NADH dehydrogenase (ubiquinone) 1 alpha subcomplex, 3 | NADH dehydrogenase | 1.59 | **0.005139** |
| 17464836 | Ndufa4 | | NADH dehydrogenase (ubiquinone) 1 alpha subcomplex, 4 | NADH dehydrogenase | 1.57 | **0.000708** |
| 17465201 | Ndufa5 | | NADH dehydrogenase (ubiquinone) 1 alpha subcomplex, 5 | NADH dehydrogenase | 1.89 | **0.000784** |
| 17319619 | Ndufa6 | | NADH dehydrogenase (ubiquinone) 1 alpha subcomplex, 6 (B14) | NADH dehydrogenase | 1.61 | **0.003254** |
| 17319619 | Ndufa6 | | NADH dehydrogenase (ubiquinone) 1 alpha subcomplex, 6 (B14) | NADH dehydrogenase | 1.61 | **0.003254** |
| 17370273 | Ndufa8 | | NADH dehydrogenase (ubiquinone) 1 alpha subcomplex, 8 | NADH dehydrogenase | 1.63 | **0.000149** |
| 17370273 | Ndufa8 | | NADH dehydrogenase (ubiquinone) 1 alpha subcomplex, 8 | NADH dehydrogenase | 1.63 | **0.000149** |
| 17384525 | Ndufa8 | | NADH dehydrogenase (ubiquinone) 1 alpha subcomplex, 8 | NADH dehydrogenase | 2.29 | **0.00056** |
| 17384525 | Ndufa8 | | NADH dehydrogenase (ubiquinone) 1 alpha subcomplex, 8 | NADH dehydrogenase | 2.29 | **0.00056** |
| 17471166 | Ndufa9 | | NADH dehydrogenase (ubiquinone) 1 alpha subcomplex, 9 | NADH dehydrogenase | 2.03 | **0.000495** |
| 17495921 | Ndufab1 | | NADH dehydrogenase (ubiquinone) 1, alpha/beta subcomplex, 1 | NADH dehydrogenase | 2.13 | **0.000517** |
| 17342029 | Ndufb10 | | NADH dehydrogenase (ubiquinone) 1 beta subcomplex, 10 | NADH dehydrogenase | 1.71 | **0.000466** |
| 17540490 | Ndufb11 | | NADH dehydrogenase (ubiquinone) 1 beta subcomplex, 11 | NADH dehydrogenase | 1.58 | 0.05587 |
| 17457540 | Ndufb2 | | NADH dehydrogenase (ubiquinone) 1 beta subcomplex, 2 | NADH dehydrogenase | 1.4 | 0.081316 |
| 17330314 | Ndufb4c | | NADH dehydrogenase (ubiquinone) 1 beta subcomplex 4 | NADH dehydrogenase | 1.67 | **0.000074** |
| 17396750 | Ndufb5 | | NADH dehydrogenase (ubiquinone) 1 beta subcomplex, 5 | NADH dehydrogenase | 1.83 | **0.001383** |
| 17424023 | Ndufb6 | | NADH dehydrogenase (ubiquinone) 1 beta subcomplex, 6 | NADH dehydrogenase | 2.08 | **0.000041** |
| 17502944 | Ndufb7 | | NADH dehydrogenase (ubiquinone) 1 beta subcomplex, 7 | NADH dehydrogenase | 1.6 | **0.004527** |
| 17365134 | Ndufb8 | | NADH dehydrogenase (ubiquinone) 1 beta subcomplex 8 | NADH dehydrogenase | 1.99 | **0.002334** |
| 17405133 | Ndufc1 | | NADH dehydrogenase (ubiquinone) 1, subcomplex unknown, 1 | NADH dehydrogenase | 1.51 | **0.005595** |
| 17480343 | Ndufc2 | | NADH dehydrogenase (ubiquinone) 1, subcomplex unknown, 2 | NADH dehydrogenase | 1.58 | **0.001697** |
| 17223685 | Ndufs1 | | NADH dehydrogenase (ubiquinone) Fe-S protein 1 | NADH dehydrogenase | 1.71 | **0.000781** |
| 17229665 | Ndufs2 | | NADH dehydrogenase (ubiquinone) Fe-S protein 2 | NADH dehydrogenase | 1.83 | **0.000414** |
| 17388074 | Ndufs3 | | NADH dehydrogenase (ubiquinone) Fe-S protein 3 | NADH dehydrogenase | 1.76 | **0.000976** |
| 17296336 | Ndufs4 | | NADH dehydrogenase (ubiquinone) Fe-S protein 4 | NADH dehydrogenase | 1.86 | **0.000955** |
| 17325719 | Ndufs5 | | NADH dehydrogenase (ubiquinone) Fe-S protein 5 | NADH dehydrogenase | 1.77 | **0.014108** |
| 17361032 | Ndufs8 | | NADH dehydrogenase (ubiquinone) Fe-S protein 8 | NADH dehydrogenase | 2.26 | **0.001516** |
| 17361056 | Ndufv1 | | NADH dehydrogenase (ubiquinone) flavoprotein 1 | NADH dehydrogenase | 1.7 | **0.00096** |
| 17346802 | Ndufv2 | | NADH dehydrogenase (ubiquinone) flavoprotein 2 | NADH dehydrogenase | 1.91 | **0.000118** |
| 17335865 | Ndufv3 | | NADH dehydrogenase (ubiquinone) flavoprotein 3 | NADH dehydrogenase | 1.78 | **0.000078** |
| 17482484 | QCR2 | | ubiquinol cytochrome c reductase core protein 2 | Cytochrome c reductase | 1.86 | **0.000407** |
| 17428545 | QCR6 | | ubiquinol-cytochrome c reductase hinge protein | Cytochrome c reductase | 1.64 | **0.001286** |
| 17262650 | QCR8 | | ubiquinol-cytochrome c reductase, complex III subunit VII | Cytochrome c reductase | 1.9 | **0.002495** |
| 17260023 | QCR9 | | ubiquinol-cytochrome c reductase, complex III subunit X | Cytochrome c reductase | 1.85 | **0.002721** |
| 17294377 | SDHA | | succinate dehydrogenase complex, subunit A, flavoprotein (Fp) | Succinate dehydrogenase | 1.41 | **0.002822** |
| 17420897 | SDHB | | succinate dehydrogenase complex, subunit B, iron sulfur (Ip) | Succinate dehydrogenase | 1.64 | **0.00898** |
| 17229629 | SDHC | | succinate dehydrogenase complex, subunit C, integral membrane protein | Succinate dehydrogenase | 1.78 | **0.010133** |
| 17517112 | SDHD | | succinate dehydrogenase complex, subunit D, integral membrane protein | Succinate dehydrogenase | 2.05 | **0.000122** |
| 17526843 | SDHD | | succinate dehydrogenase complex, subunit D, integral membrane protein | Succinate dehydrogenase | 2.1 | **0.000419** |

***Table 11. Differentially expressed genes encoding enzymes involved in the respiratory chain in iWAT.*** Fold change values of gene expression in cold-exposed mice in comparison with the control group. Highlighted in **Bold**: statistically significant p-values. Highlighted in **Red**: upregulated expression in cold exposure of 1.5-fold or higher; Highlighted in **Pink**: upregulated expression in cold exposure between 1.4- and 1.49-fold; Highlighted in **Yellow**; downregulated expression in cold exposure between -1.4- and -1.49-fold; Highlighted in **Green**: downregulated expression in cold exposure of -1.5-fold or lower.

## 1.6. Thermogenesis

As cited before in section II 1.1.2., *Ucp1* can also use the proton gradient to generate heat. In iWAT samples of cold-exposed mice, *Ucp1* expression was higher than that observed in the RT exposed mice. Indeed, *Ucp1* expression was increased 22.15-fold, being the second most upregulated gene in iWAT following the *Fabp3-ps1* gene or *fatty acid binding protein 3, muscle and heart, pseudogene 1* (Figure 34, Table 12). This upregulation of *Ucp1* expression was parallel with the activation of other thermogenesis-related genes, such as the *cell death-inducing DFFA-like effector a* (*Cidea*), which was upregulated 2.81-fold, or the *type II iodothyronine deiodinase* (*Dio2*), which was highly upregulated (7.04-fold), or the *peroxisome proliferator-activated receptor gamma coactivator 1-alpha* (*Ppargc1a*), which had a fold change increase of about 4.59 (Figure 34, Table 12). All these upregulations were highly statistically significant (Figure 34, Table 12). Together with the upregulation of thermogenesis-related genes, the significant upregulation of the expression of genes coding for receptors that bind thermogenic activators was also observed. In this regard, *β-Klotho,* that binds FGF21, a well-described potent thermogenic activator, presented a 1.59-fold change increase in iWAT of cold-exposed mice (Figure 34, Table 12). The upregulation of receptors able to bind thermogenic activators may indicate the necessity to activate or maintain thermogenesis to counteract the cold challenge. Together with this induced thermogenic state, iWAT of cold-exposed mice presented a robust three axis metabolite degradation from carbohydrates, FA and amino acids, together with an overexpression of the TCA-related genes (Figure 34). The activation of these different pathways had the mitochondria as a common link, as the cellular energy generation in the form of both ATP and heat is of high importance in these cold-exposed animals (Figure 34).

| Transcript ID | Gene Symbol | Description | Fold Change | p-value |
|---|---|---|---|---|
| 17351457 | **Cidea** | cell death-inducing DNA fragmentation factor, alpha subunit-like effector A | **2.81** | **0.00113** |
| 17282970 | **Dio2** | deiodinase, iodothyronine, type II | **7.04** | **0.001177** |
| 17437765 | **Klb** | klotho beta | **1.56** | **0.017114** |
| 17448001 | **Ppargc1a** | peroxisome proliferative activated receptor, gamma, coactivator 1 alpha | **4.59** | **9.60E-05** |
| 17502899 | **Ucp1** | uncoupling protein 1 (mitochondrial, proton carrier) | **22.15** | **0.000165** |

***Table 12. Expression analysis of thermogenic genes in iWAT.*** The table contains the fold change expression and statistical values for each gene. Highlighted in **Bold**: statistically significant p-values; Highlighted in **Red**: upregulated expression in cold exposure of 1.5-fold or higher.

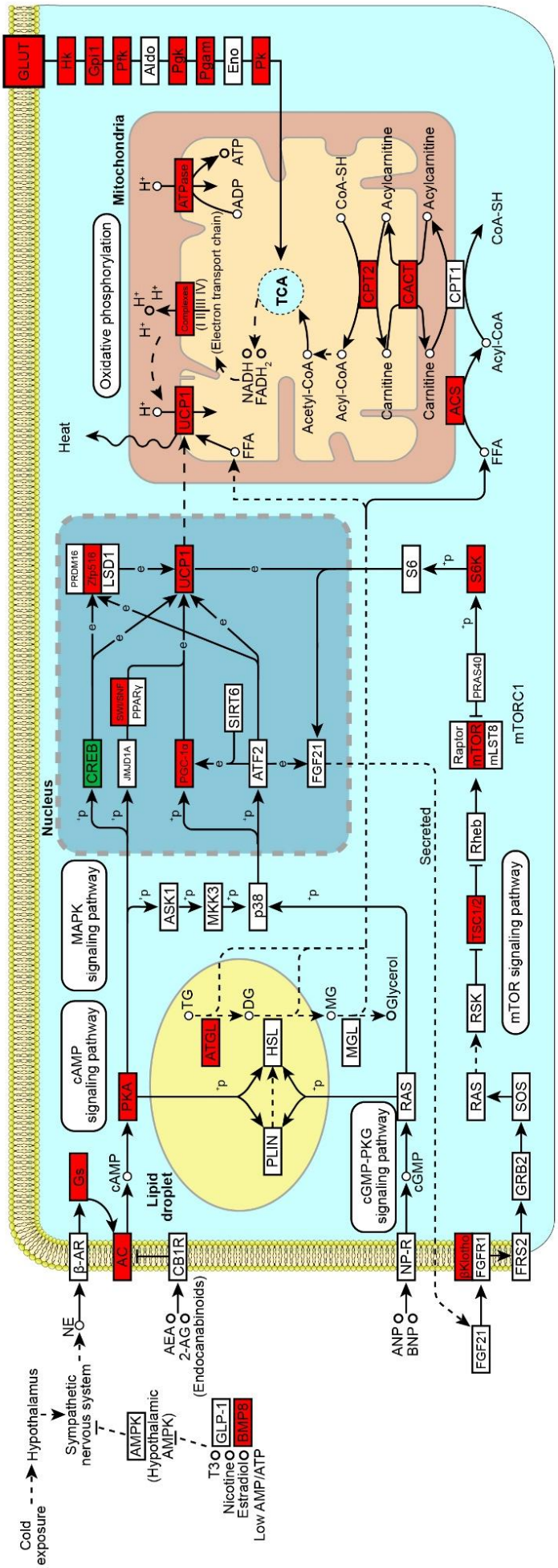


***Figure 34. Expression changes in iWAT of the thermogenesis and metabolic-related genes mediated by cold exposure.*** Enzymes that metabolize each process are framed. Highlighted in **Black**: no changes in gene expression levels; Highlighted in **Red**: upregulated expression in cold exposure of 1.5-fold or higher; Highlighted in **Green**: downregulated expression in cold exposure of -1.5-fold or lower. Adapted from KEGG pathway.

As thermogenesis in iWAT depot occurs in the multilocular beige adipocytes, which present a different morphology when activated, iWAT sections were evaluated. Histological analysis of iWAT showed that cold-exposed animals presented a high number of multilocular adipocytes (Figure 35).

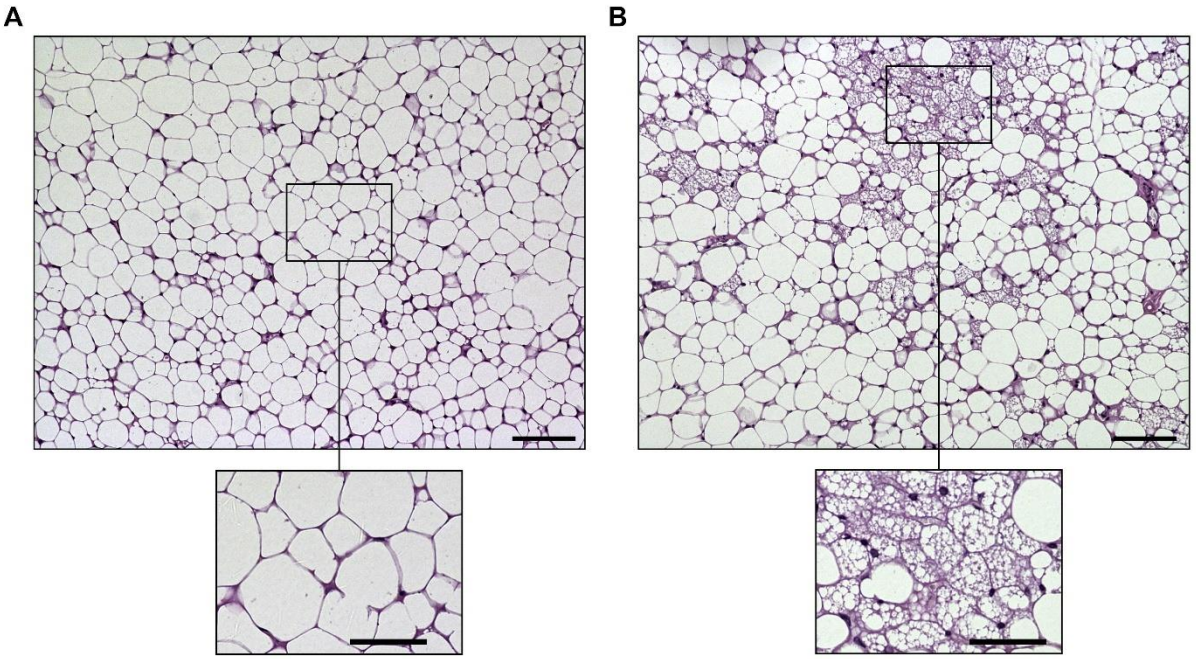


***Figure 35. Histological analysis of iWAT of animals exposed to cold or to room temperature***. Hematoxylin/eosin staining of representative sections of iWAT of C57BL/6 mice exposed to either **(A)** room temperature, or **(B)** cold (4ºC) for 4 days. Scale bars: 100µm and 50µm (inset).

## 2. METABOLIC PATHWAY ANALYSIS OF eWAT

As already described previously, the iWAT analysis allowed to study the process of WAT browning as it presents a coordinated induction of different pathways that lead to an activated-thermogenic state after 4 days of cold-exposure. However, epididymal white adipose tissue depot has been described as presenting different tissue plasticity, being more resilient to browning compared to subcutaneous fat depots as iWAT.

In our study, we found that the epididymal adipose tissue did not present any enrichment in metabolic pathways with statistical significance, in contrast to what was observed in iWAT. Nevertheless, cold adaptation of eWAT was analyzed to determine differences in comparison with iWAT regarding changes in the expression levels of key metabolic genes (Figure 36). The coloring of the changes in expression levels to the KEGG map mmu01100 of eWAT illustrates the importance of lipid metabolism in this tissue during cold adaptation (Figure 36). The processes of fatty acids biosynthesis, elongation, initiation and synthesis presented several genes upregulated as the *fatty acid synthase* or *Fasn*, which presented a 1.81-fold increased expression, or the *3-oxoacyl-ACP synthase* or *Oxsm*, upregulated about 1.43-fold (Figure 36). Other metabolic pathways such as glycolysis or TCA only presented half or less of its related enzymes with differences in expression levels (Figure 36). However, the pyruvate metabolism presented almost all the involved genes upregulated (Figure 36). Finally, the pentose phosphate cycle presented three genes upregulated: *Tkt*, *Pgd,* and *Pgls*, with an increased expression of 2.01-, 1.74- and 1.65-fold, respectively (Figure 36).

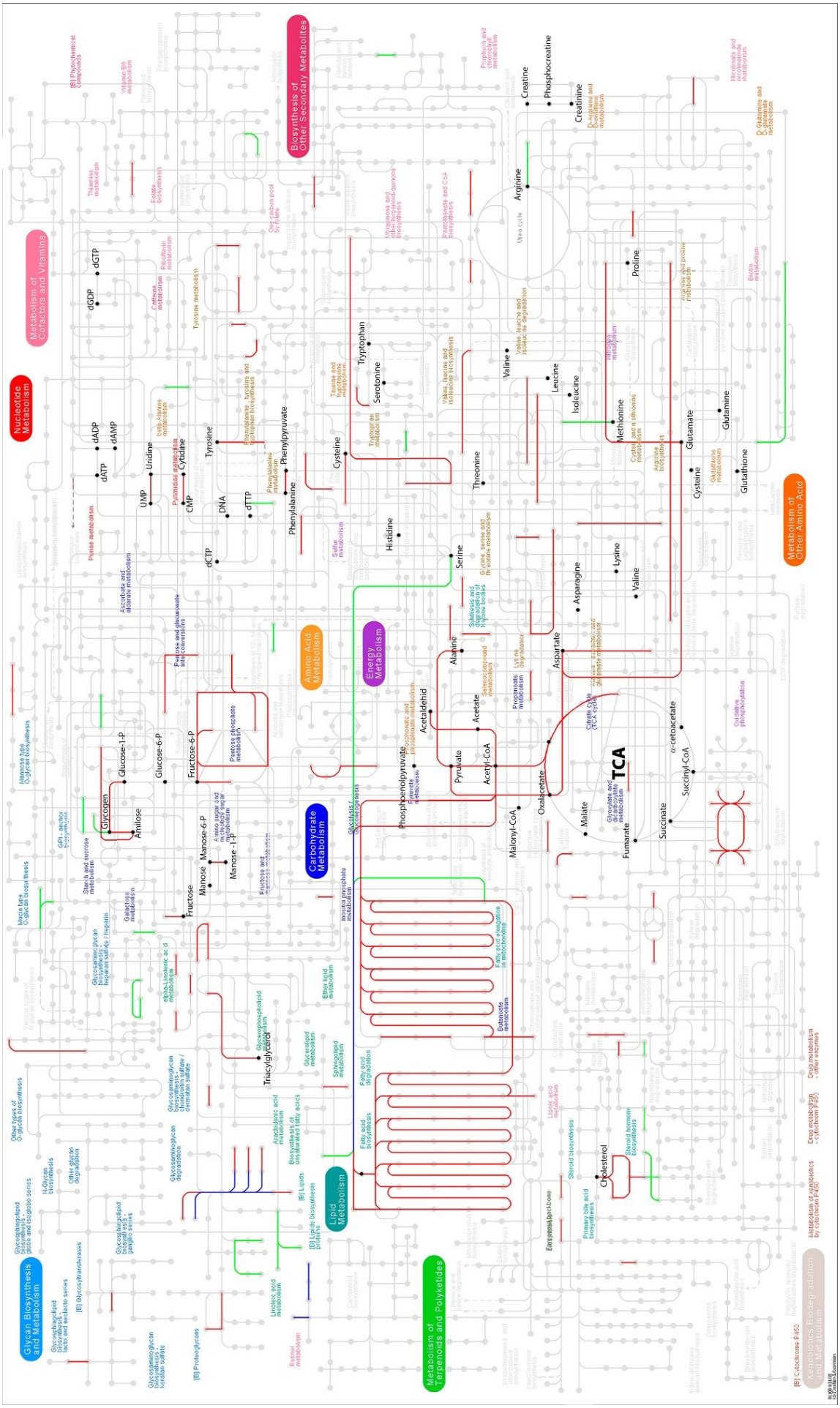


***Figure 36. Metabolic pathways in eWAT of cold-exposed mice.*** Metabolic pathways map mmu01100 from KEGG pathways indicating gene deregulation in eWAT of cold-exposed mice. Highlighted in **Bold**: metabolites; Highlighted in **Red**: upregulated expression in cold exposure of 1.5-fold or higher; Highlighted in **Green**: downregulated expression in cold exposure of -1.5-fold or lower Highlighted in **Blue**: different isoforms presented divergent in fold change values. Adapted from KEGG pathways.

## 2.1. Glycolysis

As indicated in Figure 37, the glycolysis pathway was mildly affected by cold exposure in eWAT. This depot presented only two enzymes with modified expression higher than 1.4-fold. These enzymes were *phosphoglycerate kinase 1* (*Pgk1*) (1.44-fold) and the muscular form of *pyruvate kinase*, *Pkm*, with a 1.4-fold increase (Figure 37). It is worth mentioning that there were several enzymes that presented a statistically significant p-value without having a fold change higher than 1.5, such as *Gpi1* (1.29-fold), *Pfkm* (1.35-fold), *Aldoa* (1.38-fold), *Gapdh* (1.39-fold) (Table 13).

Glucose transporter genes were also deregulated due to cold exposure. The *glucose transporter isoform 5*, or GLUT5, presented a high fold change increase of 3.24 in eWAT samples of cold-exposed mice (Table 13). Moreover, GLUT4 and GLUT8 presented a significant upregulation of 1.39- and 1.26-fold, respectively. In contrast, GLUT13 had its expression downregulated -1.55-fold (Table 13).

| Transcript ID | Gene Symbol | Name | Description | Fold Change | p-value |
|---|---|---|---|---|---|
| 17549664 | Slc2a1 | GLUT1 | Solute carrier family 2 , member 1 | 1.1 | 0.25875 |
| 17396479 | Slc2a2 | GLUT2 | Solute carrier family 2 , member 2 | -1.16 | 0.071003 |
| 17470597 | Slc2a3 | GLUT3 | Solute carrier family 2 , member 3 | -1.34 | 0.640438 |
| 17265096 | Slc2a4 | GLUT4 | Solute carrier family 2 , member 4 | 1.39 | **0.005362** |
| 17421875 | Slc2a5 | **GLUT5** | Solute carrier family 2 , member 5 | **3.24** | **0.003666** |
| 17383216 | Slc2a6 | GLUT6 | Solute carrier family 2 , member 6 | 1.17 | 0.127449 |
| 17421895 | Slc2a7 | GLUT7 | Solute carrier family 2 , member 7 | -1.02 | 0.671138 |
| 17384082 | Slc2a8 | GLUT8 | Solute carrier family 2, , member 8 | 1.26 | **0.041842** |
| 17447646 | Slc2a9 | GLUT9 | Solute carrier family 2 , member 9 | 1.21 | 0.083584 |
| 17379683 | Slc2a10 | GLUT10 | Solute carrier family 2 , member 10 | -1.08 | 0.630375 |
| 17232119 | Slc2a12 | GLUT12 | Solute carrier family 2 , member 12 | -1.16 | 0.125287 |
| 17320666 | Slc2a13 | **GLUT13** | Solute carrier family 2 , member 13 | **-1.55** | **0.008446** |

***Table 13. Gene expression analysis of glucose transporters in eWAT.*** Fold change values of gene expression in cold-exposed mice in comparison with the group control are shown. Highlighted in **Bold**: statistically significant p-values; Highlighted in **Red**: upregulated expression in cold exposure of 1.5-fold or higher; **Green**: downregulated expression in cold exposure of -1.5-fold or lower.

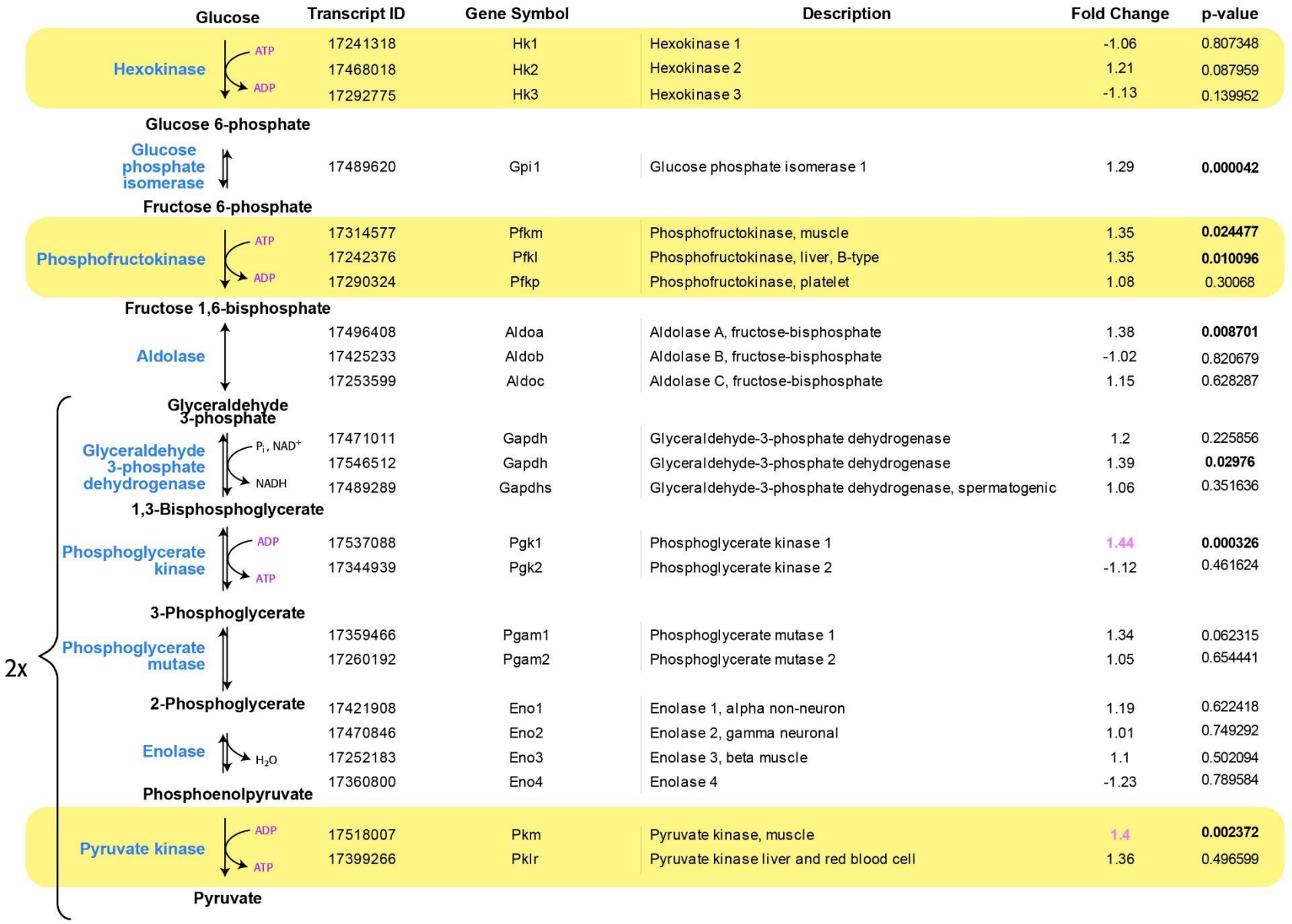


| Transcript ID | Gene Symbol | Description | Fold Change | p-value |
|---|---|---|---|---|
| 17241318 | Hk1 | Hexokinase 1 | -1.06 | 0.807348 |
| 17468018 | Hk2 | Hexokinase 2 | 1.21 | 0.087959 |
| 17292775 | Hk3 | Hexokinase 3 | -1.13 | 0.139952 |
| 17489620 | Gpi1 | Glucose phosphate isomerase 1 | 1.29 | **0.000042** |
| 17314577 | Pfkm | Phosphofructokinase, muscle | 1.35 | **0.024477** |
| 17242376 | Pfkl | Phosphofructokinase, liver, B-type | 1.35 | **0.010096** |
| 17290324 | Pfkp | Phosphofructokinase, platelet | 1.08 | 0.30068 |
| 17496408 | Aldoa | Aldolase A, fructose-bisphosphate | 1.38 | **0.008701** |
| 17425233 | Aldob | Aldolase B, fructose-bisphosphate | -1.02 | 0.820679 |
| 17253599 | Aldoc | Aldolase C, fructose-bisphosphate | 1.15 | 0.628287 |
| 17471011 | Gapdh | Glyceraldehyde-3-phosphate dehydrogenase | 1.2 | 0.225856 |
| 17546512 | Gapdh | Glyceraldehyde-3-phosphate dehydrogenase | 1.39 | **0.02976** |
| 17489289 | Gapdhs | Glyceraldehyde-3-phosphate dehydrogenase, spermatogenic | 1.06 | 0.351636 |
| 17537088 | Pgk1 | Phosphoglycerate kinase 1 | 1.44 | **0.000326** |
| 17344939 | Pgk2 | Phosphoglycerate kinase 2 | -1.12 | 0.461624 |
| 17359466 | Pgam1 | Phosphoglycerate mutase 1 | 1.34 | 0.062315 |
| 17260192 | Pgam2 | Phosphoglycerate mutase 2 | 1.05 | 0.654441 |
| 17421908 | Eno1 | Enolase 1, alpha non-neuron | 1.19 | 0.622418 |
| 17470846 | Eno2 | Enolase 2, gamma neuronal | 1.01 | 0.749292 |
| 17252183 | Eno3 | Enolase 3, beta muscle | 1.1 | 0.502094 |
| 17360800 | Eno4 | Enolase 4 | -1.23 | 0.789584 |
| 17518007 | Pkm | Pyruvate kinase, muscle | 1.4 | **0.002372** |
| 17399266 | Pklr | Pyruvate kinase liver and red blood cell | 1.36 | 0.496599 |

***Figure 37. Gene expression analysis of genes involved in glycolysis in eWAT.*** On the left part of the figure, a flow chart of the glycolysis pathway is shown. Key steps are highlighted in yellow. The steps of the glycolysis carried out twice per glucose molecule due to the generation of 2 molecules of glyceraldehyde 3-phosphate are indicated with a curly bracket and a "2x" sign. Fold change and statistical values are also specified on the right. Highlighted in **Bold**: statistically significant p-values; Highlighted in Pink: upregulated expression in cold exposure between 1.4- and 1.49-fold. Adapted from Stryer Biochemistry 8th Edition.

The pyruvate produced in the cell by the reaction mediated by *pyruvate kinase,* or by other enzymes can be metabolized to different products (Figure 38), as previously indicated (Figure 25). In eWAT, some genes that metabolize this molecule to acetyl-CoA, D-lactate or oxaloacetate were upregulated (Figure 38, Table 14). The conversion from pyruvate to acetyl-CoA is catabolized by the genes that form the PDC (*Pdh, Dlat, Dld*). Among these genes, *Pdha1*, *Pdhb,* and *Dlat* showed a significant expression change of 1.61-, -1.92-, and 1.83-fold, respectively (Table 14). The gene *Ldhd*, which metabolize pyruvate to D-lactate, increased its expression 1-92-fold and had a p-value of 0.006, and the *pyruvate carboxylase* (*Pcx*), which converts pyruvate to oxaloacetate, presented a 1.56-fold increase and a p-value of 0.001 (Table 14). In addition, several molecules can also be converted to pyruvate in order to restore its levels. In eWAT from animals exposed to cold, the enzyme *Me1*, which catalyze the conversion of malate to pyruvate, had its expression increased by 1.49-fold with a p-value of 0.007 (Table 14). Even though several enzymes involved in the pyruvate metabolism presented a modified gene expression, not all the reactions that were affected by cold exposure in the iWAT depot were also affected in the eWAT depot. For instance, the enzymes *Ldhal6b*, *Ldha*, *Ldhb* or *Ldhc*, which mediate the conversion of pyruvate to L-lactate, did not present differences in gene expression levels in eWAT (Table 14). These results suggested that the conversion of pyruvate to acetyl-CoA was probably upregulated. This is noteworthy since PDC regulates the glycolytic metabolites' flux towards the TCA cycle.

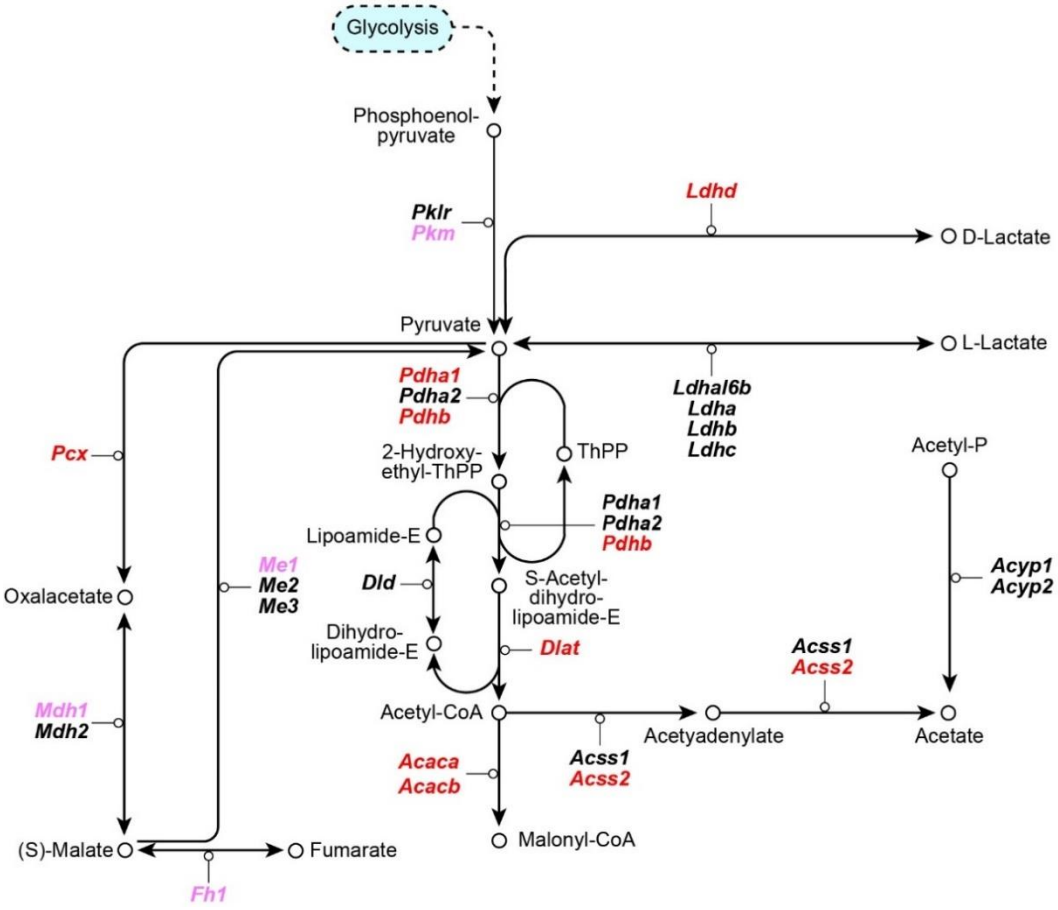


***Figure 38. Expression changes of genes related to the pyruvate metabolism in eWAT mediated by cold exposure.*** The enzymes that metabolize each process are indicated in ***italic bold***. Highlighted in **Black**: no changes in gene expression levels; Highlighted in **Red**: upregulated expression in cold exposure of 1.5-fold or higher; Highlighted in Pink: upregulated expression in cold exposure between 1.4- and 1.49-fold.

| Transcript ID | Gene Symbol | Description | Fold Change | p-value |
|---|---|---|---|---|
| 17254395 | **Acaca** | acetyl-Coenzyme A carboxylase alpha; acetyl-CoA carboxylase 1-like | **1.56** | **0.015587** |
| 17440826 | **Acacb** | acetyl-Coenzyme A carboxylase beta | **1.78** | **0.005325** |
| 17392690 | Acss1 | acyl-CoA synthetase short-chain family member 1 | 1.11 | 0.236648 |
| 17378359 | **Acss2** | acyl-CoA synthetase short-chain family member 2 | **1.94** | **0.007923** |
| 17282689 | Acyp1 | acylphosphatase 1, erythrocyte (common) type | 1.03 | 0.28394 |
| 17261393 | Acyp2 | acylphosphatase 2, muscle type | 1.23 | **0.001748** |
| 17526861 | **Dlat** | dihydrolipoamide S-acetyltransferase | **1.83** | **0.0002** |
| 17280498 | Dld | dihydrolipoamide dehydrogenase | 1.23 | **0.01656** |
| 17230153 | **Fh1** | fumarate hydratase 1 | **1.46** | **0.000128** |
| 17340493 | Ldhal6b | lactate dehydrogenase A-like 6B | 1.12 | 0.088996 |
| 17478225 | Ldha | lactate dehydrogenase A | -1.22 | 0.226112 |
| 17472517 | Ldhb | lactate dehydrogenase B | 1.3 | 0.128981 |
| 17478243 | Ldhc | lactate dehydrogenase C | -1.21 | 0.578118 |
| 17513135 | **Ldhd** | lactate dehydrogenase D | **1.92** | **0.006441** |
| 17260944 | **Mdh1** | malate dehydrogenase 1, NAD (soluble) | **1.47** | **0.000287** |
| 17443310 | Mdh2 | malate dehydrogenase 2, NAD (mitochondrial) | 1.31 | **0.000414** |
| 17529398 | **Me1** | malic enzyme 1, NADP(+)-dependent, cytosolic | **1.49** | **0.007078** |
| 17355391 | Me2 | malic enzyme 2, NAD(+)-dependent, mitochondrial | 1.28 | **0.040228** |
| 17480048 | Me3 | malic enzyme 3, NADP(+)-dependent, mitochondrial | 1.07 | 0.453049 |
| 17356216 | **Pcx** | pyruvate carboxylase | **1.56** | **0.001937** |
| 17545741 | **Pdha1** | pyruvate dehydrogenase E1 alpha 1 | **1.61** | **0.005013** |
| 17410718 | Pdha2 | pyruvate dehydrogenase E1 alpha 2 | -1.02 | 0.483174 |
| 17303400 | **Pdhb** | pyruvate dehydrogenase (lipoamide) beta | **1.92** | **0.001227** |
| 17399266 | Pklr | pyruvate kinase liver and red blood cell | 1.36 | 0.496599 |
| 17518007 | **Pkm** | pyruvate kinase, muscle | **1.4** | **0.002372** |

***Table 14. Genes encoding isoenzymes involved in pyruvate metabolism in eWAT.*** Fold change values of gene expression in cold-exposed mice in comparison with the control group. Highlighted in **Bold**: statistically significant p-values. Highlighted in **Red**: upregulated expression in cold exposure of 1.5-fold or higher; Highlighted in Pink: upregulated expression in cold exposure between 1.4- and 1.49-fold.

## 2.2. TCA cycle

PDC complex is also regulated by phosphorylation (*PDH kinases*) and dephosphorylation (*PDH phosphatases*). In eWAT depot, cold exposure did upregulate the expression of several *PDH kinases*. *Pdk1*, *Pdk2* presented a significantly increased expression after cold exposure of 1.76- and 1.76-fold, respectively, *Pdk3* and *Pdk4* presented a non-significant increase of 1.07- and 1.56-fold, respectively (Table 15). *PDH phosphatase catalytic subunit 2* (*Pdp2)* also presented an upregulated expression of 1.49-fold and the regulatory subunit *Pdpr* a significant 1.3-fold increase (Table 15). In addition, the *mitochondrial pyruvate carrier 1* (*Mpc1)* and 2 (*Mpc2)* were both significantly upregulated approximately 1.98- and 1.59-fold, probably to enhance the entrance of pyruvate into the mitochondria (Table 15).

| Transcript ID | Gene Symbol | Description | Fold Change | p-value |
|---|---|---|---|---|
| 17284037 | **Mpc1*** | mitochondrial pyruvate carrier 1* | **1.98** | **0.002371** |
| 17218955 | **Mpc2** | mitochondrial pyruvate carrier 2 | **1.59** | **0.001125** |
| 17371847 | **Pdk1** | pyruvate dehydrogenase kinase, isoenzyme 1 | **1.76** | **0.000974** |
| 17268120 | **Pdk2** | pyruvate dehydrogenase kinase, isoenzyme 2 | **1.76** | **0.000596** |
| 17543196 | Pdk3 | pyruvate dehydrogenase kinase, isoenzyme 3 | 1.07 | 0.355892 |
| 17464654 | **Pdk4** | pyruvate dehydrogenase kinase, isoenzyme 4 | **1.56** | 0.106974 |
| 17423321 | Pdp1 | pyruvate dehyrogenase phosphatase catalytic subunit 1 | -1.13 | 0.071734 |
| 17504467 | **Pdp2** | pyruvate dehyrogenase phosphatase catalytic subunit 2 | **1.49** | **0.017572** |
| 17505718 | Pdpr | pyruvate dehydrogenase phosphatase regulatory subunit | 1.3 | **0.007757** |

***Table 15. Pyruvate dehydrogenase kinase and pyruvate dehydrogenase phosphatase isoenzymes in eWAT.*** Fold change values of gene expression in cold-exposed mice in comparison with the control group. Highlighted in **Bold**: statistically significant p-values. Highlighted in **Red**: upregulated expression in cold exposure of 1.5-fold or higher; Highlighted in Pink: upregulated expression in cold exposure between 1.4- and 1.49-fold. *This probe can detect different transcripts.

As has been shown before, the TCA cycle in eWAT presented only the gene *Aco2* with high upregulation, entering the cutoff of 1.5-fold increase (Figure 36). However, several mild upregulated enzymes were detected in the second half of the cycle, the steps from succinate to oxalacetate. Starting from the acetyl-CoA entrance into the TCA, the *citrate synthase* (*Cs*) had an upregulated expression of 1.42-fold. Next, the *mitochondrial aconitase*, *Aco2*, also had its expression increased 1.5-fold (Figure 39, Table 16). The following three steps of the TCA did not present any enzyme with its coding gene presenting a clear fold change value. The next enzyme with an important modified expression was *Sdhd* (1.43-fold), linking the citric acid cycle with the energy formation of the respiratory chain (Figure 39, Table 16). However, other subunits that participate in the same step than *Sdhd*, such as *Sdha* or *Sdhb*, presented expression levels increased about 1.36- and 1.37-fold, with high statistical significance (Figure 39, Table 16). After this step, the gene *Fh1*, which its coding enzyme converts fumarate to malate, was also increased about 1.46-fold (Figure 39, Table 16). Malate is then converted to oxaloacetate by the enzyme encoded by *Mdh1*, which had enhanced expression of 1.47-fold (Figure 39, Table 16). Oxaloacetate can be converted to pyruvate, or the cycle can start again. All the genes with a fold change value higher than 1.4 presented statistical significance (Table 16).

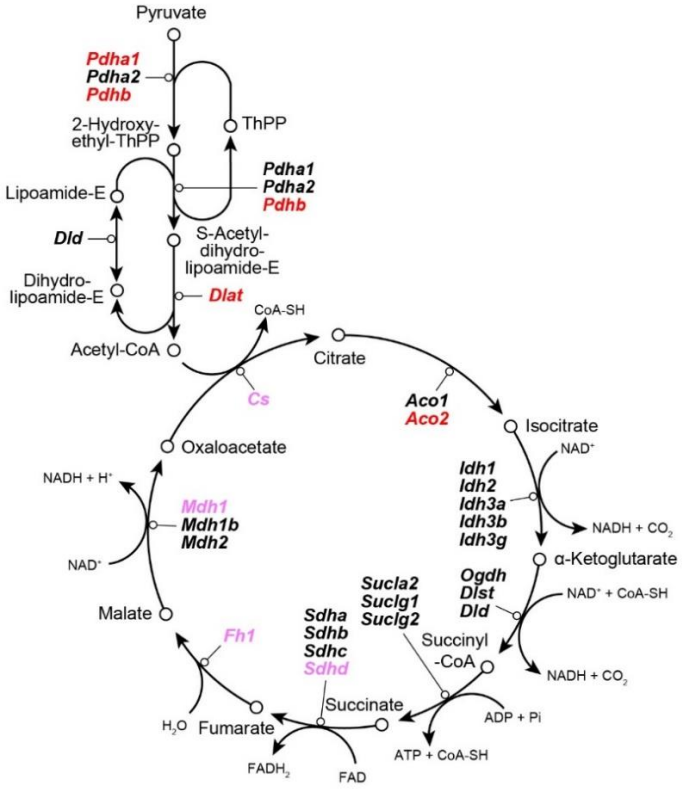


***Figure 39. Expression changes mediated by cold exposure of genes related to the metabolization of pyruvate to acetyl-CoA and the TCA in eWAT.*** The enzymes that metabolize each process are emphasized in italic bold. Highlighted in Black: no changes in gene expression levels; Highlighted in **Red**: upregulated expression in cold exposure of 1.5-fold or higher; Highlighted in Pink: upregulated expression in cold exposure between 1.4- and 1.49-fold.

| Transcript ID | Gene Symbol | Description | Fold Change | p-value |
|---|---|---|---|---|
| 17412730 | Aco1 | aconitase 1 | 1.11 | **0.023983** |
| 17313394 | **Aco2** | aconitase 2, mitochondrial | **1.5** | **0.000509** |
| 17238433 | Cs | citrate synthase | 1.42 | **0.000997** |
| 17280498 | Dld | dihydrolipoamide dehydrogenase | 1.23 | **0.01656** |
| 17277352 | Dlst | dihydrolipoamide S-succinyltransferase | 1.34 | **0.00142** |
| 17230153 | Fh1 | fumarate hydratase 1 | 1.46 | **0.000128** |
| 17223863 | Idh1 | isocitrate dehydrogenase 1 (NADP+), soluble | 1.1 | 0.243558 |
| 17492478 | Idh2 | isocitrate dehydrogenase 2 (NADP+), mitochondrial | 1.04 | 0.670353 |
| 17517390 | Idh3a | isocitrate dehydrogenase 3 (NAD+) alpha | 1.22 | **0.014599** |
| 17391608 | Idh3b | isocitrate dehydrogenase 3 (NAD+) beta | 1.31 | **0.000424** |
| 17542392 | Idh3g | isocitrate dehydrogenase 3 (NAD+), gamma | 1.19 | **0.000518** |
| 17260944 | Mdh1 | malate dehydrogenase 1, NAD (soluble) | 1.47 | **0.000287** |
| 17223747 | Mdh1b | malate dehydrogenase 1B, NAD (soluble) | -1 | 0.755912 |
| 17443310 | Mdh2 | malate dehydrogenase 2, NAD (mitochondrial) | 1.31 | **0.000414** |
| 17247080 | Ogdh | oxoglutarate (alpha-ketoglutarate) dehydrogenase (lipoamide) | 1.27 | **0.011286** |
| 17294377 | Sdha | succinate dehydrogenase complex, subunit A, flavoprotein (Fp) | 1.36 | **0.007605** |
| 17420897 | Sdhb | succinate dehydrogenase complex, subunit B, iron sulfur (Ip) | 1.37 | **0.000148** |
| 17229629 | Sdhc | succinate dehydrogenase complex, subunit C, integral membrane protein | 1.22 | **0.005421** |
| 17526843 | Sdhd | succinate dehydrogenase complex, subunit D, integral membrane protein | 1.39 | **0.002725** |
| 17517112 | Sdhd | succinate dehydrogenase complex, subunit D, integral membrane protein | 1.43 | **0.029554** |
| 17301899 | Sucla2 | succinate-Coenzyme A ligase, ADP-forming, beta subunit | 1.24 | **0.003366** |
| 17459716 | Suclg1 | succinate-CoenzymeA ligase, GDP-forming, alpha subunit | 1.32 | **0.003722** |
| 17548514 | Suclg2 | succinate-Coenzyme A ligase, GDP-forming, beta subunit | -1.13 | 0.752505 |

***Table 16. Genes encoding isoenzymes involved in TCA in eWAT.*** Fold change values of gene expression in cold-exposed mice in comparison with the control group. **Bold**: statistically significant p-values. Highlighted in **Red**: upregulated expression in cold exposure of 1.5-fold or higher; Highlighted in Pink: upregulated expression in cold exposure between 1.4- and 1.49-fold.

### 2.3. Anaplerotic reactions

Similar to the observation made in the iWAT depot, eWAT also presented a considerable number of genes coding for enzymes of the BCAA degradation pathways upregulated (Figure 40, Table 17). The degradation of leucine only presented the enzyme *Bckdha* upregulated (1.51-fold), whereas isoleucine degradation had several steps with enzymes upregulated: *Acads* (1.43-fold), *Ehhadh* (1.92-fold), *Hadha* (1.5-fold), *Hsd17b10* (1.69-fold), *Acaa1b* (1.74-fold) and *Acaa2* (1.4-fold) (Figure 40, Table 17). Finally, the glycogenic degradation of valine was also upregulated in many steps: the expression of *Acads, Aldh2*, *Ehhadh*, *Hadha*, and *Hibch* was upregulated 1.43-, 1.41-, 1.92-, 1.5-, and 1.48-fold, respectively (Table 17). In conclusion, as the enzyme *Bckdha* was upregulated in all the three degradation pathways, gene expression analysis of the BCAA suggested that only isoleucine and valine degradation would be markedly upregulated, forming succinyl-CoA through propionyl-CoA.

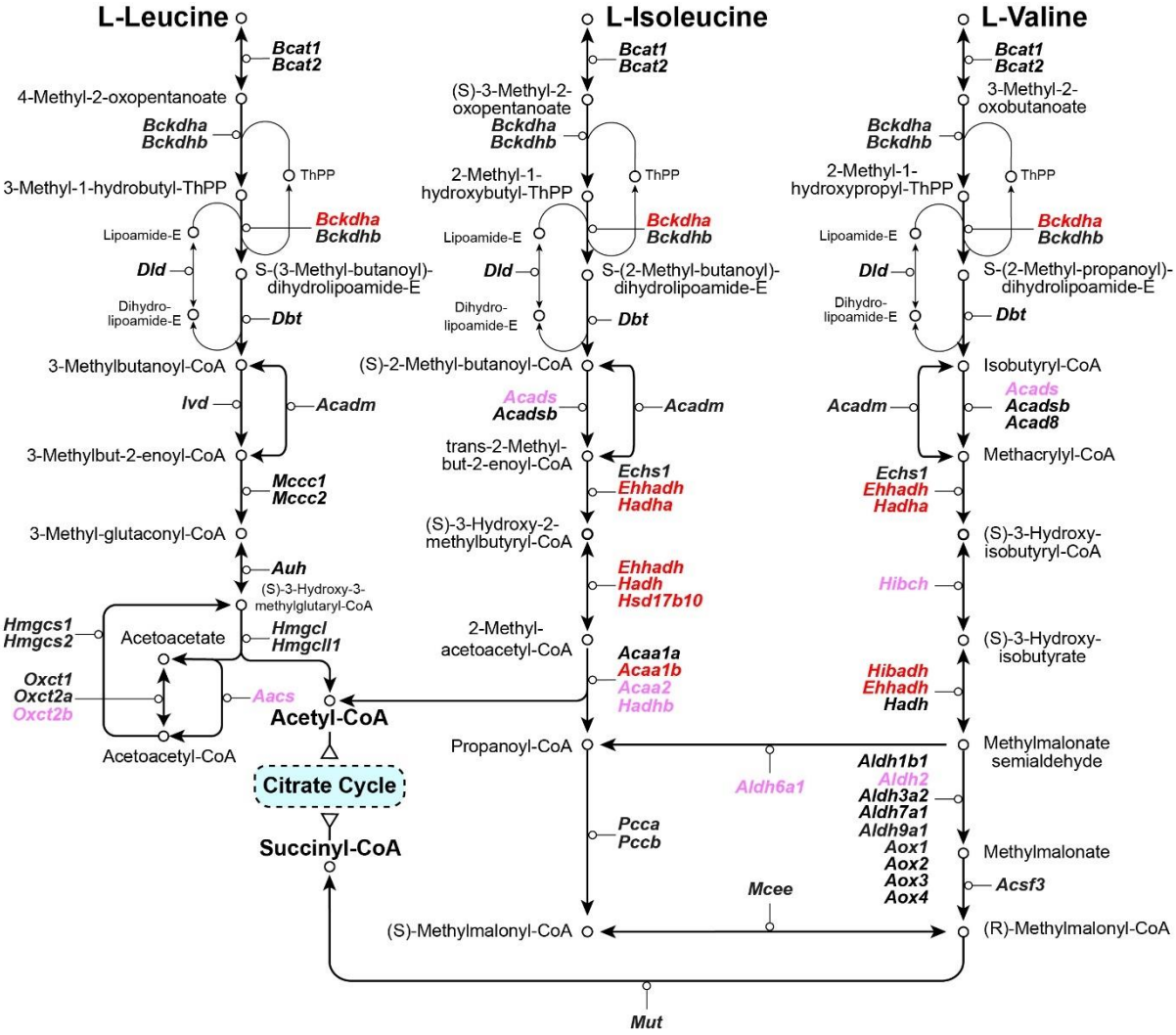


***Figure 40. Expression changes of genes related to the branched-chain amino acids (leucine, isoleucine, and valine) degradation in eWAT.*** From left to right, degradation pathways for the leucine, isoleucine and valine amino acids, respectively, with illustrated gene expression changes induced by cold exposure. The enzymes that metabolize each process are emphasized in ***italic bold***. Highlighted in **Black**: no changes in gene expression levels; Highlighted in **Red**: upregulated expression in cold exposure of 1.5-fold or higher; Highlighted in Pink: upregulated expression in cold exposure between 1.4- and 1.49-fold. Adapted from KEGG pathway.

| Transcript ID | Gene Symbol | Description | Fold Change | p-value |
|---|---|---|---|---|
| 17442719 | Aacs | acetoacetyl-CoA synthetase | 1.4 | **0.001699** |
| 17523042 | Acaa1a | acetyl-CoA acyltransferase 1A | 1.16 | 0.150714 |
| 17532063 | **Acaa1b** | acetyl-CoA acyltransferase 1B | **1.74** | **0.000735** |
| 17351811 | Acaa2 | acetyl-CoA acyltransferase 2 (mitochondrial 3-oxoacyl-CoA thiolase) | 1.4 | **0.000025** |
| 17525163 | Acad8 | acyl-CoA dehydrogenase family, member 8 | 1.31 | **0.002784** |
| 17411323 | Acadm | acyl-CoA dehydrogenase, medium chain | 1.32 | **0.022575** |
| 17451649 | Acads | acyl-CoA dehydrogenase, short chain | 1.43 | **0.001294** |
| 17484014 | Acadsb | acyl-CoA dehydrogenase, short/branched chain | 1.14 | **0.026232** |
| 17506443 | Acsf3 | acyl-CoA synthetase family member 3 | 1.2 | **0.019288** |
| 17413674 | Aldh1b1 | aldehyde dehydrogenase 1 family, member B1 | -1.06 | 0.551017 |
| 17441949 | Aldh2 | aldehyde dehydrogenase 2, mitochondrial | 1.41 | **0.004098** |
| 17250582 | Aldh3a2 | aldehyde dehydrogenase family 3, subfamily A2 | 1.09 | 0.320076 |
| 17277267 | Aldh6a1 | aldehyde dehydrogenase family 6, subfamily A1 | 1.43 | **0.004163** |
| 17354434 | Aldh7a1 | aldehyde dehydrogenase family 7, member A1 | 1.03 | 0.414743 |
| 17219096 | Aldh9a1 | aldehyde dehydrogenase 9, subfamily A1 | 1.29 | **0.025287** |
| 17212982 | Aox1 | aldehyde oxidase 1 | 1.12 | 0.73891 |
| 17213101 | Aox2 | aldehyde oxidase 3-like 1 | -1.12 | 0.167792 |
| 17213021 | Aox3 | aldehyde oxidase 3 | 1.18 | 0.373682 |
| 17213060 | Aox4 | aldehyde oxidase 4 | -1.07 | 0.674936 |
| 17292612 | Auh | AU RNA binding protein/enoyl-CoA hydratase | 1.15 | **0.008094** |
| 17472678 | Bcat1 | branched chain aminotransferase 1, cytosolic | -1.09 | 0.349021 |
| 17477897 | Bcat2 | branched chain aminotransferase 2, mitochondrial | 1.36 | **0.014265** |
| 17487982 | **Bckdha** | branched chain ketoacid dehydrogenase E1, alpha polypeptide | **1.51** | **0.002921** |
| 17519940 | Bckdhb | branched chain ketoacid dehydrogenase E1, beta polypeptide | 1.34 | **0.003194** |
| 17402025 | Dbt | dihydrolipoamide branched chain transacylase E2 | 1.17 | **0.00644** |
| 17280498 | Dld | dihydrolipoamide dehydrogenase | 1.23 | **0.01656** |
| 17497612 | Echs1 | enoyl CoA hydratase, short chain, 1, mitochondrial | 1.3 | **0.001196** |
| 17329220 | **Ehhadh** | enoyl-CoA, hydratase/3-hydroxyacyl CoA dehydrogenase | **1.58** | **0.002007** |
| 17410390 | Hadh | hydroxyacyl-CoA dehydrogenase | 1.17 | **0.000397** |
| 17446643 | **Hadha** | hydroxyacyl-CoA dehydrogenase/enoyl-CoA hydratase, alpha subunit | **1.5** | **0.002189** |
| 17435748 | Hadhb | hydroxyacyl-CoA dehydrogenase/enoyl-CoA hydratase, beta subunit | 1.46 | 0.172737 |
| 17466919 | **Hibadh** | 3-hydroxyisobutyrate dehydrogenase | **1.62** | 0.201123 |
| 17212792 | Hibch | 3-hydroxyisobutyryl-CoA hydrolase | 1.48 | **0.001967** |
| 17419980 | Hmgcl | 3-hydroxy-3-methylglutaryl-CoA lyase | 1.23 | 0.069996 |
| 17519550 | Hmgcll1 | 3-hydroxymethyl-3-methylglutaryl-CoA lyase-like 1 | -1.27 | 0.128187 |
| 17290173 | Hmgcs1 | 3-hydroxy-3-methylglutaryl-CoA synthase 1 | 1.12 | 0.436023 |
| 17400862 | Hmgcs2 | 3-hydroxy-3-methylglutaryl-CoA synthase 2 | -1.17 | 0.150307 |
| 17538852 | **Hsd17b10** | hydroxysteroid (17-beta) dehydrogenase 10 | **1.69** | **0.004402** |
| 17374648 | Ivd | isovaleryl CoA dehydrogenase | 1.39 | **0.035342** |
| 17404750 | Mccc1 | methylcrotonoyl-CoA carboxylase 1 (alpha) | 1.14 | 0.061111 |
| 17295503 | Mccc2 | methylcrotonoyl-CoA carboxylase 2 (beta) | 1.19 | **0.001674** |
| 17478883 | Mcee | methylmalonyl CoA epimerase | 1.23 | **0.0335** |
| 17345004 | Mut | methylmalonyl-CoA mutase | 1.25 | 0.072501 |
| 17309802 | Oxct1 | 3-oxoacid CoA transferase 1 | 1 | 0.873842 |
| 17429685 | Oxct2a | 3-oxoacid CoA transferase 2A | 1.26 | 0.077445 |
| 17418154 | Oxct2b | 3-oxoacid CoA transferase 2B | 1.46 | 0.198526 |
| 17302889 | Pcca | propionyl-CoA carboxylase, alpha polypeptide | 1.39 | **0.011733** |
| 17530141 | Pccb | propionyl CoA carboxylase, beta polypeptide | 1.35 | **0.004911** |

***Table 17. Branched-chain amino acids degradation-related gene expression in eWAT.*** Fold change values of gene expression in cold-exposed mice in comparison with the control group. Highlighted in **Bold**: statistically significant p-values. Highlighted in **Red**: upregulated expression in cold exposure of 1.5-fold or higher; Highlighted in Pink: upregulated expression in cold exposure between 1.4- and 1.49-fold.

As described previously, not only these amino acids can generate intermediate molecules of the TCA. As shown in Figure 30, the malate-aspartate shuttle also generates other intermediary proteins of the TCA. In eWAT, only the gene *Mdh1* presented a significant upregulation of 1.47-fold (Figure 41, Table 18).

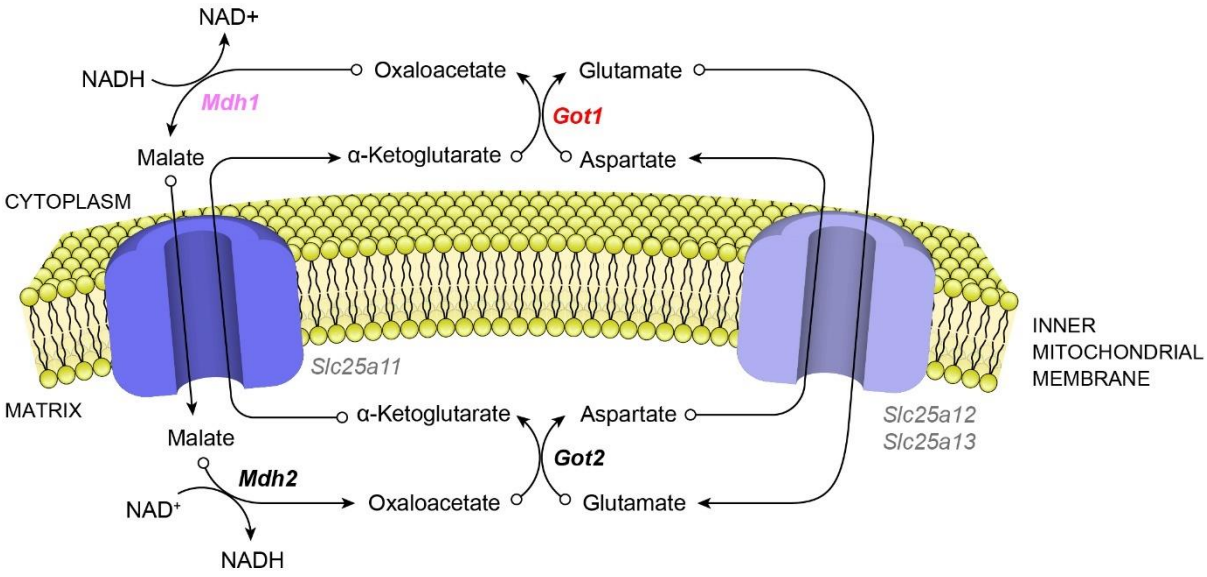


***Figure 41. Schematic representation of the gene expression changes mediated by cold exposure of the malate-aspartate shuttle in eWAT.*** Representation of the malate-aspartate shuttle with the metabolites in regular black and the enzymes that metabolize each process in ***italic bold*** and the different transporters and channels in regular grey. Highlighted in **Bold**: no changes in gene expression levels; Highlighted in **Red**: upregulated expression in cold-exposed mice higher or equal than 1.5-fold; Highlighted in Pink: upregulated expression in cold-exposed mice between 1.4- and 1.49-fold.

| Transcript ID | Gene Symbol | Description | Fold Change | p-value |
|---|---|---|---|---|
| 17364932 | **Got1** | glutamate oxaloacetate transaminase 1, soluble | **1.67** | 0.069844 |
| 17512103 | Got2* | glutamate oxaloacetate transaminase 2, mitochondrial | 1.11 | 0.352644 |
| 17260944 | **Mdh1** | malate dehydrogenase 1, NAD (soluble) | **1.47** | **0.000287** |
| 17443310 | Mdh2 | malate dehydrogenase 2, NAD (mitochondrial) | 1.31 | **0.000414** |
| 17265306 | Slc25a11 | solute carrier family 25 (mitochondrial carrier oxoglutarate carrier), member 11 | 1.11 | **0.020291** |
| 17386396 | Slc25a12 | solute carrier family 25 (mitochondrial carrier, Aralar), member 12 | -1.06 | 0.398007 |
| 17464672 | Slc25a13 | solute carrier family 25 (mitochondrial carrier, adenine nucleotide translocator), member 13 | 1.08 | 0.907223 |

***Table 18. Malate-aspartate shuttle related enzymes with its expression in eWAT.*** Fold change values of gene expression in cold-exposed mice in comparison with the control group. Highlighted in **Bold**: statistically significant p-values. Highlighted in **Red**: upregulated expression in cold exposure of 1.5-fold or higher; Highlighted in Pink: upregulated expression in cold exposure between 1.4- and 1.49-fold. *This probe can detect different transcripts.

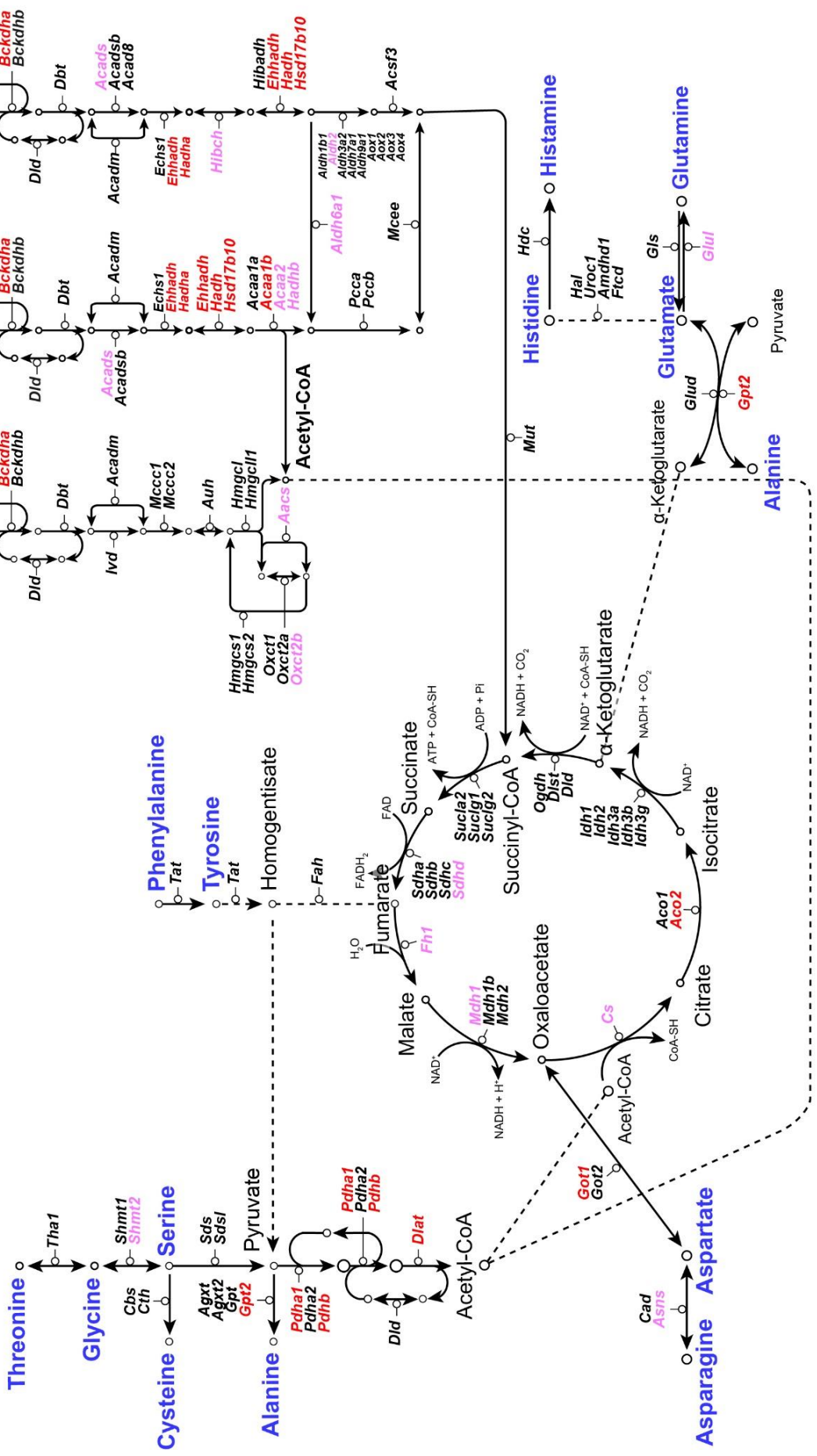


***Figure 42. Expression changes of genes related to the degradation of amino acids in eWAT after cold exposure.*** The enzymes that metabolize each process are emphasized in ***italic bold***. Highlighted in **Blue**: Amino acids; Highlighted in **Black**: no changes in gene expression levels; Highlighted in **Red**: upregulated expression in cold exposure of 1.5-fold or higher; Highlighted in **Pink**: upregulated expression in cold exposure between 1.4- and 1.49-fold. Adapted from KEGG pathway. Dashed lines link same metabolites.

## 2.4. Triglyceride and Fatty acid metabolism

Cold exposure triggers lipolysis through β-adrenergic receptors. Cold-induced changes in gene expression of genes involved in TG and FA degradation are depicted in Figure 43 and Table 20.

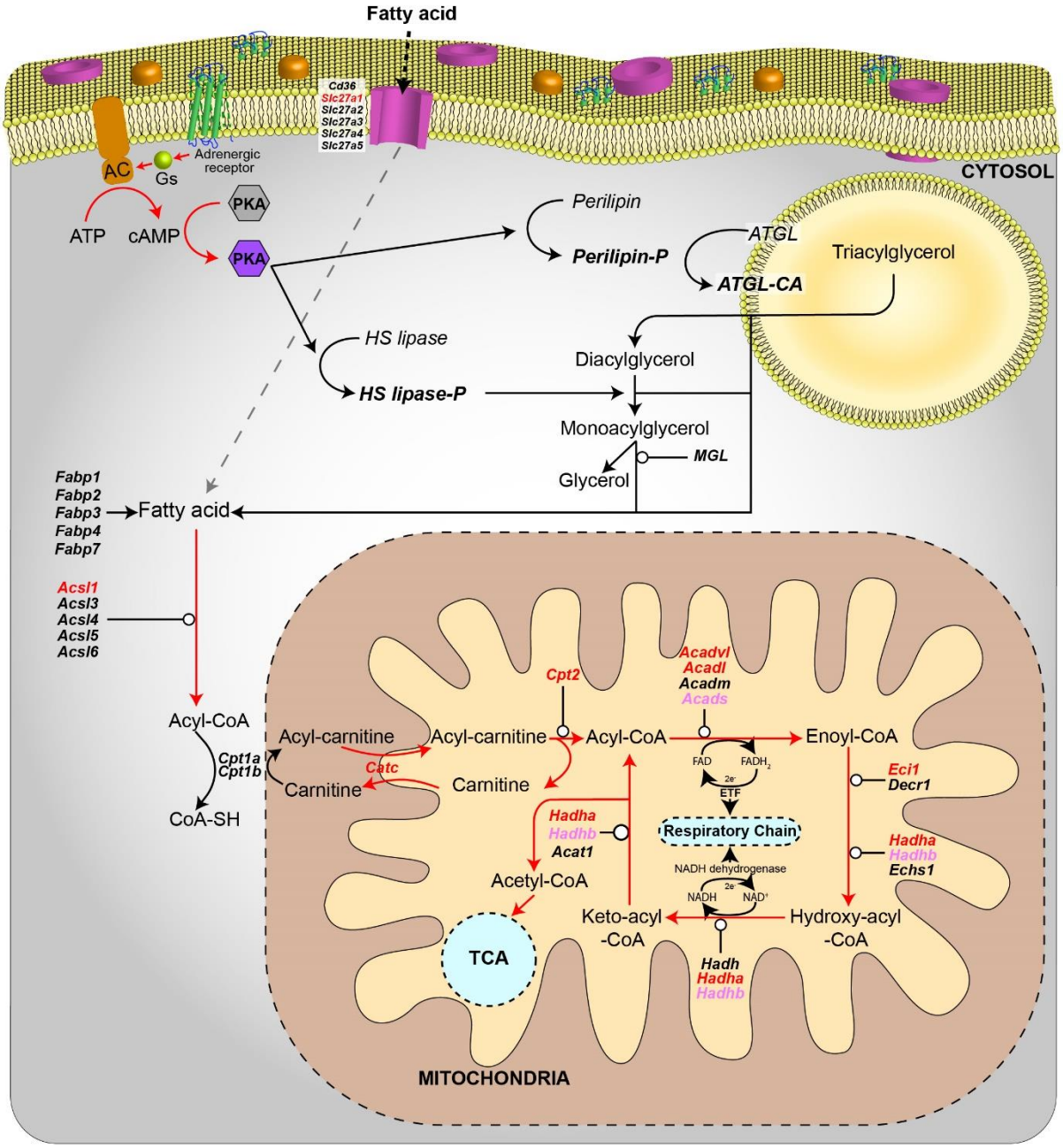


***Figure 43. Schematic representation of the gene expression changes mediated by cold exposure of the triglyceride and fatty acid degradation pathway in eWAT.*** Representation of the triglyceride and fatty acid degradation pathway. The enzymes that metabolize each process are emphasized in ***italic bold***. Highlighted in **Black**: no changes in gene expression levels; Highlighted in **Red**: upregulated expression in cold exposure of 1.5-fold or higher; Highlighted in Pink: upregulated expression in cold exposure between 1.4- and 1.49-fold. Red arrows: potentially enhanced flow; black arrow: potentially normal flow. Dashed lines link same metabolites. Adapted from KEGG pathway.

| Transcript ID | Gene Symbol | Description | Fold Change | p-value |
|---|---|---|---|---|
| 17548916 | **Acadl** | acyl-Coenzyme A dehydrogenase, long-chain | **1.59** | **0.001849** |
| 17411323 | Acadm | acyl-Coenzyme A dehydrogenase, medium chain | 1.32 | **0.022575** |
| 17451649 | **Acads** | acyl-Coenzyme A dehydrogenase, short chain | **1.43** | **0.001294** |
| 17265129 | **Acadvl** | acyl-Coenzyme A dehydrogenase, very long chain | **1.57** | **0.000218** |
| 17527123 | Acat1 | acetyl-Coenzyme A acetyltransferase 1 | 1.15 | **0.002107** |
| 17500996 | **Acsl1** | acyl-CoA synthetase long-chain family member 1 | **1.52** | **0.007254** |
| 17214685 | Acsl3 | acyl-CoA synthetase long-chain family member 3 | 1.01 | 0.950178 |
| 17545051 | Acsl4 | acyl-CoA synthetase long-chain family member 4 | 1.14 | 0.168704 |
| 17360462 | Acsl5 | acyl-CoA synthetase long-chain family member 5 | 1.04 | 0.806418 |
| 17249640 | Acsl6 | acyl-CoA synthetase long-chain family member 6 | -1.11 | **0.019049** |
| 17247183 | Adcy1 | adenylate cyclase 1 | -1.03 | 0.755947 |
| 17294086 | **Adcy2** | adenylate cyclase 2 | **-1.47** | **0.001797** |
| 17273714 | Adcy3 | adenylate cyclase 3 | 1.39 | **0.026481** |
| 17306877 | Adcy4 | adenylate cyclase 4 | 1.29 | 0.056191 |
| 17325206 | Adcy5 | adenylate cyclase 5 | -1.22 | 0.241966 |
| 17321263 | Adcy6 | adenylate cyclase 6 | 1 | 0.733712 |
| 17503616 | Adcy7 | adenylate cyclase 7 | 1.02 | 0.80506 |
| 17317533 | Adcy8 | adenylate cyclase 8 | 1.16 | 0.994441 |
| 17327720 | Adcy9 | adenylate cyclase 9 | 1.07 | 0.111236 |
| 17218965 | **Adcy10** | adenylate cyclase 10 | **1.84** | **0.002202** |
| 17360599 | Adrb1 | adrenergic receptor, beta 1 | -1.08 | 0.56843 |
| 17354857 | Adrb2 | adrenergic receptor, beta 2 | 1.32 | 0.160033 |
| 17508544 | Adrb3 | adrenergic receptor, beta 3 | -1.11 | 0.171269 |
| 17521875 | **Catc / Slc25a20** | solute carrier family 25, member 20 | **1.5** | **0.001364** |
| 17445715 | Cd36 | CD36 antigen | -1.02 | 0.171889 |
| 17355915 | Cpt1a | carnitine palmitoyltransferase 1a, liver | -1.13 | 0.133928 |
| 17320499 | Cpt1b | carnitine palmitoyltransferase 1b, muscle | 1.36 | **0.000991** |
| 17427961 | **Cpt2** | carnitine palmitoyltransferase 2 | **1.5** | **0.000042** |
| 17423463 | Decr1 | 2,4-dienoyl CoA reductase 1, mitochondrial | 1.32 | **0.000603** |
| 17497612 | Echs1 | enoyl Coenzyme A hydratase, short chain, 1, mitochondrial | 1.3 | **0.001196** |
| 17334253 | **Eci1** | enoyl-Coenzyme A delta isomerase 1 | **1.6** | **0.000825** |
| 17459455 | Fabp1 | fatty acid binding protein 1, liver | 1.05 | 0.911004 |
| 17402350 | Fabp2 | fatty acid binding protein 2, intestinal | -1.28 | 0.065232 |
| 17419215 | Fabp3 | fatty acid binding protein 3, muscle and heart | -1.09 | 0.688923 |
| 17404091 | Fabp4 | fatty acid binding protein 4, adipocyte | -1.02 | 0.56515 |
| 17233384 | Fabp7 | fatty acid binding protein 7, brain | -1.12 | 0.059506 |
| 17380306 | Gnas | GNAS (guanine nucleotide binding protein, alpha stimulating) complex locus | 1.04 | 0.344212 |
| 17410390 | Hadh | hydroxyacyl-Coenzyme A dehydrogenase | 1.17 | **0.000397** |
| 17446643 | **Hadha** | hydroxyacyl-Coenzyme A dehydrogenase | **1.5** | **0.002189** |
| 17435748 | **Hadhb** | hydroxyacyl-Coenzyme A dehydrogenase | **1.46** | 0.172737 |
| 17487927 | Lipe | lipase, hormone sensitive | 1.16 | **0.003875** |
| 17460665 | Mgll | monoglyceride lipase | 1.1 | 0.14904 |
| 17492406 | Plin1 | perilipin 1 | 1.07 | 0.294631 |
| 17426981 | Plin2 | perilipin 2 | 1.31 | **0.011787** |
| 17346216 | Plin3 | perilipin 3 | 1.1 | 0.133634 |
| 17346125 | Plin4 | perilipin 4 | -1.18 | 0.108409 |
| 17346136 | Plin5 | perilipin 5 | 1.12 | 0.065475 |
| 17484909 | Pnpla2 | patatin-like phospholipase domain containing 2 | 1.33 | **0.000706** |
| 17503031 | Prkaca | protein kinase, cAMP dependent, catalytic, alpha | 1.3 | **0.020291** |
| 17502233 | **Slc27a1** | solute carrier family 27 (fatty acid transporter), member 1 | **2.75** | **0.000172** |
| 17391089 | Slc27a2 | solute carrier family 27 (fatty acid transporter), member 2 | -1.03 | 0.827655 |
| 17407259 | Slc27a3 | solute carrier family 27 (fatty acid transporter), member 3 | -1.11 | 0.329363 |
| 17368904 | Slc27a4 | solute carrier family 27 (fatty acid transporter), member 4 | 1.39 | **0.005578** |
| 17486589 | Slc27a5 | solute carrier family 27 (fatty acid transporter), member 5 | -1.39 | 0.470255 |
| 17350856 | Slc27a6 | solute carrier family 27 (fatty acid transporter), member 6 | -1.32 | **0.044374** |

***Table 20. Cold-induced expression changes of genes involved in triglycerides and fatty acids degradation in eWAT.*** Fold change values of gene expression in cold-exposed mice in comparison with the control group are shown. Highlighted in **Bold**: statistically significant p-values. Highlighted in **Red**: upregulated expression in cold exposure of 1.5-fold or higher; Highlighted in **Pink**: upregulated expression in cold exposure between 1.4- and 1.49-fold.

### *2.4.1. Mobilization of triacylglycerols*

In eWAT, no statistically significant differences were detected in the expression of β-adrenergic receptors, as the *β1-adrenergic receptor* (*Adrb1*) presented an expression of -1.08-fold, the *β2-adrenergic receptor* (*Adrb2*) of 1.32-fold and the *β3-adrenergic receptor* (*Adrb3*) of -1.11-fold (Figure 43, Table 20). The *Gs protein*, that mediates the internal signaling of these receptors, did not present an altered expression either (1.04-fold) (Figure 43, Table 20). However, despite the *Gs protein* was not upregulated, its target protein *adenylate cyclase* presented in the isoform 10 (*Adcy10*) and in the isoform 3 (*Adcy3*) increased expression of 1.84-, and of 1.39-fold, respectively (Figure 43, Table 20). *Adenylate cyclase* transforms ATP to cAMP, thereby activating the *protein kinase A* (PKA). The catalytic subunit alpha of this protein was mildly upregulated (1.3-fold) (Figure 43, Table 20). The expression of genes encoding these two proteins was not highly altered in eWAT, presenting the different *perilipin* isoforms (*Plin1* to *Plin5*) fold change values between -1.18 and 1.31, and the *HS lipase* (*Lipe*) presented an expression increase of 1.16-fold (Figure 43, Table 20). The phosphorylation of *perilipin* triggers the release of a coactivator for *adipose triglyceride lipase* (ATGL), which presented a 1.33-fold increased expression (Figure 43, Table 20). This gene is also known as *Pnpla2* or *patatin-like phospholipase domain containing 2*. This protein together with the *monoglyceride lipase* (*Mgl*), which had a fold change value of 1.1, transforms triacylglycerol to FA and glycerol (Figure 43, Table 20). The potential activation of this process triggered by cold in eWAT may result in the mobilization of TG, being metabolized to FA. Moreover, FA can be uptaken from the extracellular space by FA transporters. Among the different FA transporters, the *Slc27a1* presented a fold change increase of 2.75 and the *Slc27a4* a fold change increase of 1.39 (Figure 43, Table 20). The *large family fatty acid binding proteins* (*FABP1–FABP9*) did not present any expression differences between eWAT from mice exposed to cold or to RT (Figure 43, Table 20).

### *2.4.2. Fatty acids activation and transport to the mitochondria*

Once FA has been generated or internalized, *acyl-CoA synthetase*, which presented its gene *Acsl1* increased 1.52-fold (Figure 43, Table 20), mediates the conversion of the FA to fatty acyl-CoA thioester, the first step to oxidize FA. To enter the acyl-CoA into the mitochondria, *Cpt1* transforms fatty acyl-CoA thioester to fatty acyl-carnitine. *Cpt1a* presented a -1.13-fold and *Cpt1b* a fold increase of 1.36-fold (Figure 43, Table 20). Then, acyl-carnitine enters the mitochondria through the *acyl-carnitine/carnitine transporter*

(*Catc*), which was also upregulated (1.5-fold). Finally, the *carnitine acyltransferase 2*, or *Cpt2*, which was upregulated 1.5-fold, converts the fatty acyl-carnitine to fatty acyl-CoA. In summary, these results seemed to indicate an upregulation of the FA activation and transport into the mitochondria.

### *2.4.3. Fatty acids oxidation*

Enzymes involved in all four steps of β-oxidation of FA were upregulated in eWAT as a result of cold exposure (Figure 43, Table 19). In the first step, in which two electrons are transferred to the ETF, the expression of all the different enzymes, *Acadvl*, *Acadl,* and *Acads*, with the exception of *medium-chain acyl-CoA dehydrogenase* (*Acadm*), was highly upregulated (Figure 43, Table 20). In the second step, in which water is added to form 3-hydroxyacyl-CoA, the three enzymes *Eci1*, *Hadha*, *Hadhb* presented its gene upregulated more than 1.4-fold (Figure 43, Table 20). The formation of β-ketoacyl-CoA was also likely enhanced as the expression of both genes, *Hadha* and *Hadhb* were upregulated (Figure 43, Table 20).

## 2.5. Fatty acid biosynthesis

In eWAT, several enzymes involved in the biosynthesis of fatty acids presented an upregulated expression as a result of cold exposure (Table 21). The ATP citrate lyase (*Acly*), which was significantly upregulated 2.24-fold (Table 21), metabolizes citrate to acetyl-CoA. Afterward, malonyl-CoA is generated by the enzymes *Acaca* and *Acacb* (Lehner and Quiroga, 2016), which had fold change values of 1.56 and 1.78, respectively (Table 21). Finally, the fatty acid synthase or *Fasn* (1.44-fold) (Table 21) generates palmitate (hexadecanoic acid) through different repeated steps (Lehner and Quiroga, 2016). Palmitate is then transported to the endoplasmic reticulum and elongation and desaturation process occurs to generate longer chain FA and unsaturated FA (Bond et al., 2016). Fatty acid elongation uses fatty acyl-CoA and malonyl-CoA as substrates, so fatty acyl-CoA synthetases add CoA to activate the FA. In eWAT, the fatty acyl-CoA synthetase *Acsl1* was upregulated 1.52-fold (Table 21). Afterward, different enzyme elongates the fatty acyl-CoA. First, the initial and rate-limiting step is performed by the ketoacyl-CoA synthases named ELOVLs (elongation of very long chain fatty acids) which condenses a malonyl-CoA to acyl-CoA (Bond et al., 2016). In eWAT, both *Elovl3* and *Elovl6* were significantly upregulated 1.73- and 2.1-fold, respectively (Table 21). Two of the other three types of genes related to the elongation process, such as the genes that encode for KAR,

and Hsd17b12, were significantly upregulated 1.41-fold in eWAT. Moreover, the gene that encodes for the trans-2,3-enoyl-CoA reductase, *Tecr*, was significantly upregulated 1.54-fold, but the genes that encode for the different β-hydroxyacyl-CoA dehydratase (*Hacd*) did not have its expression highly deregulated after cold exposure (Table 21). The desaturation process is then performed by stearoyl-CoA desaturases (Scd) and fatty acid desaturases (Fads) (Bond et al., 2016). Within these enzymes, the genes *Scd2*, *Fads1*, and *Fads3* presented an expression increase of 1.41-, 2.24-, and 1.54-fold, respectively (Table 21).

| Transcript ID | Gene Symbol | Description | Fold Change | p-value |
|---|---|---|---|---|
| 17269521 | **Acly** | ATP citrate lyase | **2.24** | **0.001584** |
| 17500996 | **Acsl1** | acyl-CoA synthetase long-chain family member 1 | **1.52** | **0.007254** |
| 17214685 | Acsl3 | acyl-CoA synthetase long-chain family member 3 | 1.01 | 0.950178 |
| 17545051 | Acsl4 | acyl-CoA synthetase long-chain family member 4 | 1.14 | 0.168704 |
| 17360462 | Acsl5 | acyl-CoA synthetase long-chain family member 5 | 1.04 | 0.806418 |
| 17249640 | Acsl6 | acyl-CoA synthetase long-chain family member 6 | -1.11 | **0.019049** |
| 17417767 | Elovl1 | elongation of very long chain fatty acids (FEN1/Elo2, SUR4/Elo3, yeast)-like 1 | 1 | 0.676969 |
| 17292058 | Elovl2 | elongation of very long chain fatty acids (FEN1/Elo2, SUR4/Elo3, yeast)-like 2 | -1.13 | 0.454554 |
| 17359918 | **Elovl3** | elongation of very long chain fatty acids (FEN1/Elo2, SUR4/Elo3, yeast)-like 3 | **1.73** | **0.022489** |
| 17529307 | Elovl4 | elongation of very long chain fatty acids (FEN1/Elo2, SUR4/Elo3, yeast)-like 4 | -1.09 | 0.247621 |
| 17519598 | Elovl5 | ELOVL family member 5, elongation of long chain fatty acids (yeast) | 1.32 | 0.051691 |
| 17402558 | **Elovl6** | ELOVL family member 6, elongation of long chain fatty acids (yeast) | **2.1** | **0.005905** |
| 17289717 | Elovl7 | ELOVL family member 7, elongation of long chain fatty acids (yeast) | -1.08 | 0.962296 |
| 17388573 | Hsd17b12 | hydroxysteroid (17-beta) dehydrogenase 12 | 1.23 | 0.068528 |
| 17381892 | **Hacd1** | 3-hydroxyacyl-CoA dehydratase 1 | **1.74** | 0.277883 |
| 17325198 | Hacd2 | 3-hydroxyacyl-CoA dehydratase 2 | 1.1 | 0.117609 |
| 17528229 | Hacd3 | 3-hydroxyacyl-CoA dehydratase 4 | 1.01 | 0.445325 |
| 17427051 | Hacd4 | 3-hydroxyacyl-CoA dehydratase 3 | 1.16 | **0.034758** |
| 17510906 | Tecr | trans-2,3-enoyl-CoA reductase | 1.19 | **0.026035** |
| 17365098 | Scd1 | stearoyl-Coenzyme A desaturase 1 | -1.18 | 0.157642 |
| 17549342 | **Scd2; Mir5114** | stearoyl-Coenzyme A desaturase 2; microRNA 5114 | **1.41** | **0.000216** |
| 17359678 | Scd3 | stearoyl-coenzyme A desaturase 3 | 1.01 | 0.31173 |
| 17359698 | Scd4 | stearoyl-coenzyme A desaturase 4 | 1.37 | **0.016376** |
| 17357460 | **Fads1** | fatty acid desaturase 1 | **2.24** | **0.003457** |
| 17362595 | Fads2 | fatty acid desaturase 2 | 1.11 | 0.084352 |
| 17357444 | **Fads3** | fatty acid desaturase 3 | **1.54** | **0.005191** |

***Table 21. Expression of genes encoding enzymes involved in fatty acids biosynthesis in eWAT.*** Fold change values of gene expression in cold-exposed mice in comparison with the control group. Highlighted in **Bold**: statistically significant p-values. Highlighted in **Red**: upregulated expression in cold exposure of 1.5-fold or higher; Highlighted in Pink: upregulated expression in cold exposure between 1.4- and 1.49-fold.

## 2.6. Oxidative phosphorylation

In eWAT, the different complexes that form the electron respiratory chain presented several subunits upregulated due to exposure to cold. Less than half of the subunits of the *NADH dehydrogenase,* the *cytochrome c reductase* or the *cytochrome c oxidase,* presented a deregulated gene expression (Figure 44, Table 22). In contrast to iWAT, in eWAT these results suggested that the proton gradient flow was mildly induced by cold exposure. ATPases did not present any subunits with a modified expression as indicated in Figure 44 and Table 22.

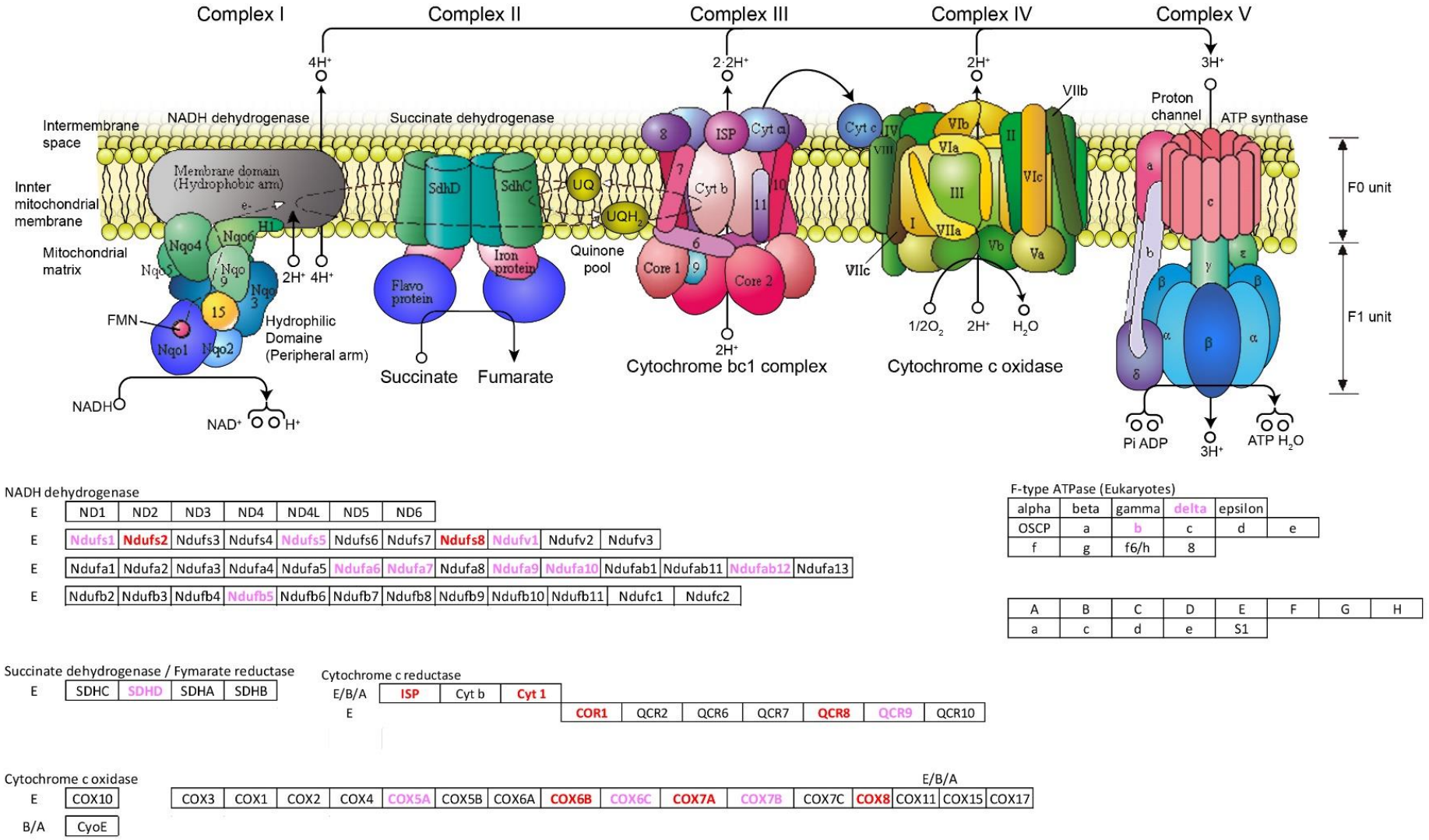


NADH dehydrogenase

| | | | | | | | | | | | | | | |
|---|---|---|---|---|---|---|---|---|---|---|---|---|---|---|
| E | ND1 | ND2 | ND3 | ND4 | ND4L | ND5 | ND6 | | | | | | | |
| E | Ndufs1 | Ndufs2 | Ndufs3 | Ndufs4 | Ndufs5 | Ndufs6 | Ndufs7 | Ndufs8 | Ndufv1 | Ndufv2 | Ndufv3 | | | |
| E | Ndufa1 | Ndufa2 | Ndufa3 | Ndufa4 | Ndufa5 | Ndufa6 | Ndufa7 | Ndufa8 | Ndufa9 | Ndufa10 | Ndufab1 | Ndufab11 | Ndufab12 | Ndufa13 |
| E | Ndufb2 | Ndufb3 | Ndufb4 | Ndufb5 | Ndufb6 | Ndufb7 | Ndufb8 | Ndufb9 | Ndufb10 | Ndufb11 | Ndufc1 | Ndufc2 | | |

F-type ATPase (Eukaryotes)

| | | | | | |
|---|---|---|---|---|---|
| alpha | beta | gamma | delta | epsilon | |
| OSCP | a | b | c | d | e |
| f | g | f6/h | 8 | | |

| | | | | | | | |
|---|---|---|---|---|---|---|---|
| A | B | C | D | E | F | G | H |
| a | c | d | e | S1 | | | |

Succinate dehydrogenase / Fymarate reductase

| | | | | |
|---|---|---|---|---|
| E | SDHC | SDHD | SDHA | SDHB |

Cytochrome c reductase

| | | | | | | | | | |
|---|---|---|---|---|---|---|---|---|---|
| E/B/A | ISP | Cyt b | Cyt 1 | | | | | | |
| E | COR1 | QCR2 | QCR6 | QCR7 | QCR8 | QCR9 | QCR10 | | |

Cytochrome c oxidase

| | | | | | | | | | | | | | | | | |
|---|---|---|---|---|---|---|---|---|---|---|---|---|---|---|---|---|
| E | COX10 | | | | | | | | | | | | | | | |
| B/A | CyoE | | | | | | | | | | | | | | | |
| E/B/A | COX3 | COX1 | COX2 | COX4 | COX5A | COX5B | COX6A | COX6B | COX6C | COX7A | COX7B | COX7C | COX8 | COX11 | COX15 | COX17 |

***Figure 44. Expression changes in eWAT induced by cold exposure of the several isoenzymes of the different complexes of the electron transport chain and the ATPase.*** On top of the figure, the different isoenzymes of each complex are shown. Below the scheme, all genes encoding for the different complex are indicated, as well as alterations in their gene expression level in cold exposed animals in comparison to room temperature exposed mice. Highlighted in **Black**: no changes in gene expression levels; Highlighted in **Red**: upregulated expression in cold exposure of 1.5-fold or higher; Highlighted in Pink: upregulated expression in cold exposure between 1.4- and 1.49-fold. Adapted from KEGG pathway.

| Transcript ID | Gene Symbol | Alias | Description | Pathway | Fold Change | p-value |
|---|---|---|---|---|---|---|
| 17408863 | Atp5f1 | b | ATP synthase, H+ transporting, mitochondrial F0 complex, subunit B1 | F-type ATPase | 1.44 | **0.008966** |
| 17271891 | Atp5h | delta | ATP synthase, H+ transporting, mitochondrial F0 complex, subunit d | F-type ATPase | 1.44 | **0.004618** |
| 17521996 | **COR1** | | ubiquinol-cytochrome c reductase core protein 1 | Cytochrome c reductase | **1.5** | **0.000136** |
| 17517727 | Cox5a | | cytochrome c oxidase subunit Va | Cytochrome c oxidase | 1.4 | **0.005596** |
| 17489223 | **Cox6b1** | | cytochrome c oxidase, subunit VIb polypeptide 1 | Cytochrome c oxidase | **1.63** | **0.002357** |
| 17547698 | Cox6c | | cytochrome c oxidase subunit VIc; predicted pseudogene 6265 | Cytochrome c oxidase | 1.42 | **0.003733** |
| 17476288 | **Cox7a1** | | cytochrome c oxidase subunit VIIa 1 | Cytochrome c oxidase | **2.07** | **0.006333** |
| 17548981 | Cox7b | | cytochrome c oxidase subunit VIIb | Cytochrome c oxidase | 1.44 | **0.015408** |
| 17548981 | Cox7b | | cytochrome c oxidase subunit VIIb | Cytochrome c oxidase | 1.44 | **0.015408** |
| 17497704 | **Cox8b** | | cytochrome c oxidase subunit VIIIb | Cytochrome c oxidase | **4.32** | **0.00011** |
| 17312396 | **Cyt1** | | cytochrome c-1 | Cytochrome c reductase | **1.7** | **0.000045** |
| 17291570 | **ISP** | | ubiquinol-cytochrome c reductase, Rieske iron-sulfur polypeptide 1 | Cytochrome c reductase | **1.7** | **0.000243** |
| 17225564 | Ndufa10 | | NADH dehydrogenase (ubiquinone) 1 alpha subcomplex 10 | NADH dehydrogenase | 1.41 | **0.002644** |
| 17236681 | Ndufa12 | | NADH dehydrogenase (ubiquinone) 1 alpha subcomplex, 12 | NADH dehydrogenase | 1.41 | **0.001577** |
| 17319619 | Ndufa6 | | NADH dehydrogenase (ubiquinone) 1 alpha subcomplex, 6 (B14) | NADH dehydrogenase | 1.41 | **0.008185** |
| 17319619 | Ndufa6 | | NADH dehydrogenase (ubiquinone) 1 alpha subcomplex, 6 (B14) | NADH dehydrogenase | 1.41 | **0.008185** |
| 17336190 | Ndufa7 | | NADH dehydrogenase (ubiquinone) 1 alpha subcomplex, 7 (B14.5a) | NADH dehydrogenase | 1.41 | 0.056813 |
| 17471166 | Ndufa9 | | NADH dehydrogenase (ubiquinone) 1 alpha subcomplex, 9 | NADH dehydrogenase | 1.43 | **0.00061** |
| 17396750 | Ndufb5 | | NADH dehydrogenase (ubiquinone) 1 beta subcomplex, 5 | NADH dehydrogenase | 1.49 | **0.002885** |
| 17223685 | Ndufs1 | | NADH dehydrogenase (ubiquinone) Fe-S protein 1 | NADH dehydrogenase | 1.4 | **0.005088** |
| 17229665 | **Ndufs2** | | NADH dehydrogenase (ubiquinone) Fe-S protein 2 | NADH dehydrogenase | **1.54** | **0.000358** |
| 17325719 | Ndufs5 | | NADH dehydrogenase [ubiquinone] iron-sulfur protein 5-like | NADH dehydrogenase | 1.4 | **0.005252** |
| 17361032 | **Ndufs8** | | NADH dehydrogenase (ubiquinone) Fe-S protein 8 | NADH dehydrogenase | **1.52** | **0.014121** |
| 17361056 | Ndufv1 | | NADH dehydrogenase (ubiquinone) flavoprotein 1 | NADH dehydrogenase | 1.4 | **0.000437** |
| 17262650 | **QCR8** | | ubiquinol-cytochrome c reductase, complex III subunit VII | Cytochrome c reductase | **1.5** | **0.00683** |
| 17260023 | QCR9 | | ubiquinol-cytochrome c reductase, complex III subunit X | Cytochrome c reductase | 1.49 | **0.000317** |
| 17517112 | SDHD | | succinate dehydrogenase complex, subunit D, integral membrane protein | Succinate dehydrogenase | 1.43 | **0.029554** |

***Table 22. Differentially expressed genes encoding enzymes involved in the respiratory chain in eWAT after cold exposure.*** Fold change values of gene expression in cold-exposed mice in comparison with the control group. Highlighted in **Bold**: statistically significant p-values. Highlighted in **Red**: upregulated expression in cold exposure of 1.5-fold or higher; Highlighted in Pink: upregulated expression in cold exposure between 1.4- and 1.49-fold.

## 2.7. Thermogenesis

Even though ATPases did not show differences in gene expression in eWAT between mice exposed to cold or to RT (Figure 45, Table 23), *Ucp1* was highly expressed in eWAT of cold challenged mice (about 392%) compared with the RT exposed mice (Figure 45, Table 23). This remarkable 4.92-fold change value presented by *Ucp1* indicated that this gene was the highest upregulated gene in eWAT.

The upregulation of the *Ucp1* was in agreement with the increased expression presented by several thermogenic genes. Among others, PGC1-α (*Ppargc1a*) or *Cidea* were upregulated 1.94- and 2.64-fold, respectively, and also *β-Klotho* receptor was upregulated 1.49-fold (Table 23). However, non-shivering thermogenesis activation (Figure 45, Table 23) in the eWAT depot was not as enhanced as in iWAT (Figure 34, Table 12).

| Transcript ID | Gene Symbol | Description | Fold Change | p-value |
|---|---|---|---|---|
| 17351457 | **Cidea** | cell death-inducing DNA fragmentation factor, alpha subunit-like effector A | **2.64** | **0.000126** |
| 17282970 | Dio2 | deiodinase, iodothyronine, type II | 1.28 | 0.097123 |
| 17437765 | **Klb** | klotho beta | **1.49** | 0.056466 |
| 17448001 | **Ppargc1a** | peroxisome proliferative activated receptor, gamma, coactivator 1 alpha | **1.94** | **0.014834** |
| 17502899 | **Ucp1** | uncoupling protein 1 (mitochondrial, proton carrier) | **4.92** | **0.010001** |

***Table 23. Expression analysis of thermogenic genes in eWAT.*** The table contains the fold change expression and statistical values for each gene. Highlighted in **Bold**: statistically significant p-values. Highlighted in **Red**: upregulated expression in cold exposure of 1.5-fold or higher; Highlighted in Pink: upregulated expression in cold exposure between 1.4- and 1.49-fold.

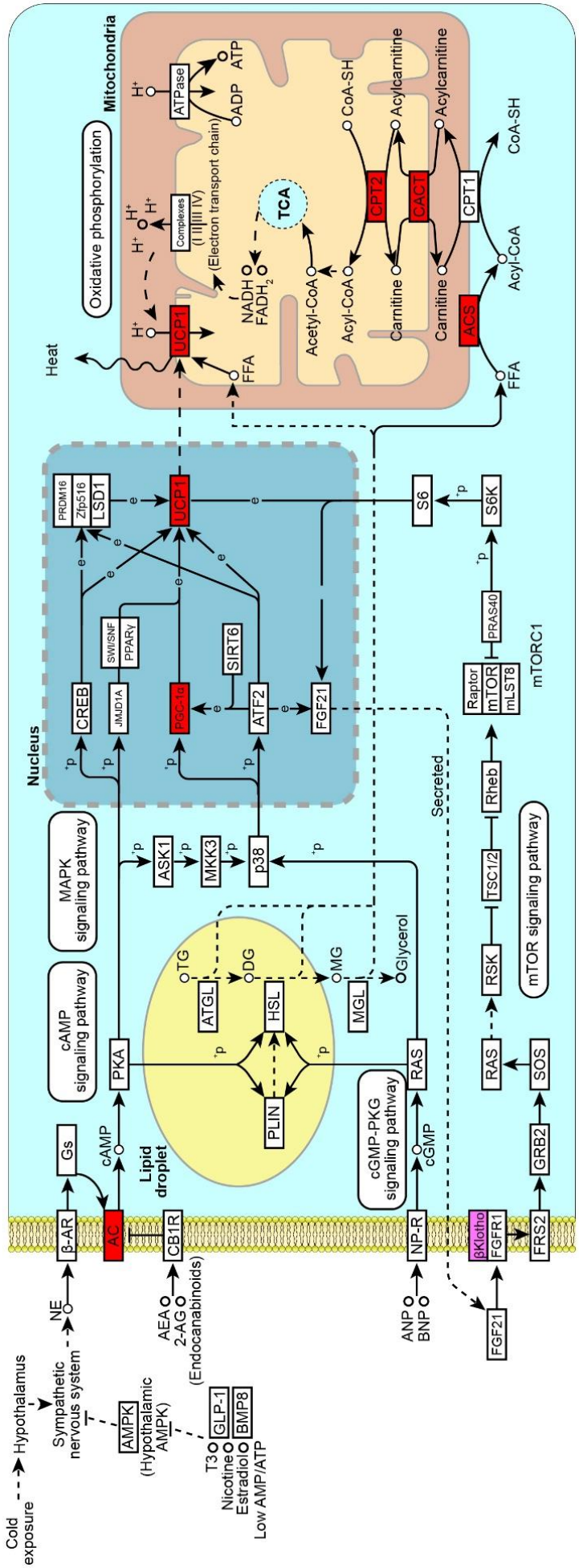


***Figure 45. Expression changes in eWAT of the thermogenesis and metabolic-related genes mediated by cold exposure.*** Enzymes that metabolize each process are framed. Highlighted in **Black**: no changes in gene expression levels; Highlighted in **Red**: upregulated expression in cold exposure of 1.5-fold or higher; Highlighted in **Pink**: upregulated expression in cold exposure between 1.4- and 1.49-fold. Adapted from KEGG pathway.

Data previously described in other studies suggested that eWAT is more resilient to browning than other depots such as iWAT and that even with cold exposure this depot does not perform thermogenesis (Chan et al., 2019; Ferrannini et al., 2016). However, as an increase in the expression of several thermogenesis-related genes was detected, the absolute expression levels of thermogenic genes were compared among fat depots, (eWAT, iWAT, and iBAT) (Table 24). The analysis of the levels of expression of *Cidea*, *Dio2*, *Klb*, *Ppargc1a,* and *Ucp1* in iWAT of cold-exposed mice determined the degree of expression of these genes during a browning activated process. Furthermore, the expression levels of these genes in iBAT of cold-exposed mice determined the levels in a well-described thermogenic depot during cold exposure. The comparison of the expression levels among depots showed that these thermogenic genes were slightly expressed in eWAT of RT-exposed mice (Table 24). These genes in iWAT of animals exposed at RT presented higher expression values than those obtained in eWAT (Table 24). Under cold exposure, the expression of these genes increased in both white adipose depots, but this upregulation was higher in iWAT, resulting in expression levels similar to those of iBAT (Table 24). In the iBAT depot, the expression levels of thermogenic genes in both RT and cold conditions were high in comparison with the expression levels of the other genes of the array (Table 24). In conclusion, despite eWAT presented a fold change increase after cold exposure of several thermogenic genes, their expression levels were still low, indicating that non-shivering thermogenesis was probably not enhanced in this fat depot.

| | | | | Expression levels | | | | | | | |
|---|---|---|---|---|---|---|---|---|---|---|---|
| | | | Mouse | 1 | 2 | 3 | 4 | 5 | 6 | 7 | 8 |
| Transcript ID | Gene Symbol | Description | Tissue | Room temperature | | | | Cold | | | |
| 17351457 | Cidea | Cell death-inducing DNA fragmentation factor, alpha subunit-like effector A | iBAT | 12.32 | 12.36 | 12.42 | 12.41 | 12.36 | 12.37 | 12.30 | 12.37 |
| | | | iWAT | 8.73 | 9.44 | 9.48 | 10.01 | 11.19 | 10.90 | 10.90 | 11.02 |
| | | | eWAT | 5.14 | 5.26 | 5.38 | 5.54 | 6.87 | 6.70 | 6.68 | 6.29 |
| 17282970 | Dio2 | Deiodinase, iodothyronine, type II | iBAT | 8.07 | 9.21 | 9.73 | 9.63 | 9.55 | 9.76 | 10.07 | 9.36 |
| | | | iWAT | 3.42 | 4.35 | 5.34 | 5.44 | 7.10 | 7.62 | 7.58 | 7.59 |
| | | | eWAT | 4.39 | 4.54 | 4.50 | 4.48 | 4.41 | 4.67 | 5.09 | 5.14 |
| 17448001 | Ppargc1a | Peroxisome proliferative activated receptor, gamma, coactivator 1 alpha | iBAT | 8.61 | 9.44 | 9.55 | 9.37 | 10.37 | 10.41 | 10.87 | 10.47 |
| | | | iWAT | 6.08 | 6.84 | 6.62 | 7.18 | 8.80 | 8.89 | 9.26 | 8.98 |
| | | | eWAT | 5.79 | 6.25 | 6.80 | 6.81 | 7.62 | 7.43 | 8.60 | 7.25 |
| 17502899 | Ucp1 | Uncoupling protein 1 | iBAT | 12.74 | 12.91 | 12.93 | 12.96 | 13.14 | 13.24 | 13.22 | 13.13 |
| | | | iWAT | 6.86 | 7.36 | 8.67 | 9.12 | 12.47 | 12.48 | 12.32 | 12.59 |
| | | | eWAT | 3.96 | 4.64 | 3.94 | 3.81 | 8.13 | 5.26 | 6.51 | 5.93 |

***Table 24. Gene expression levels of Cidea, Dio2, Klb, Ppargc1a, and Ucp1 in iBAT, iWAT, and eWAT of room temperature and cold-exposed mice.*** The expression levels of thermogenic genes were represented numerically for each mouse in each depot. Mice numbered from 1 to 4 were exposed to room temperature, while mice numbered from 5 to 8 were exposed to 4ºC for 4 days.

In agreement with the expression levels of thermogenic genes (Table 24), which suggested that non-shivering thermogenesis was not induced in the eWAT depot, no beige adipocytes were observed after the histological analysis of hematoxylin/eosin stained sections of eWAT of cold-exposed mice (Figure 46).

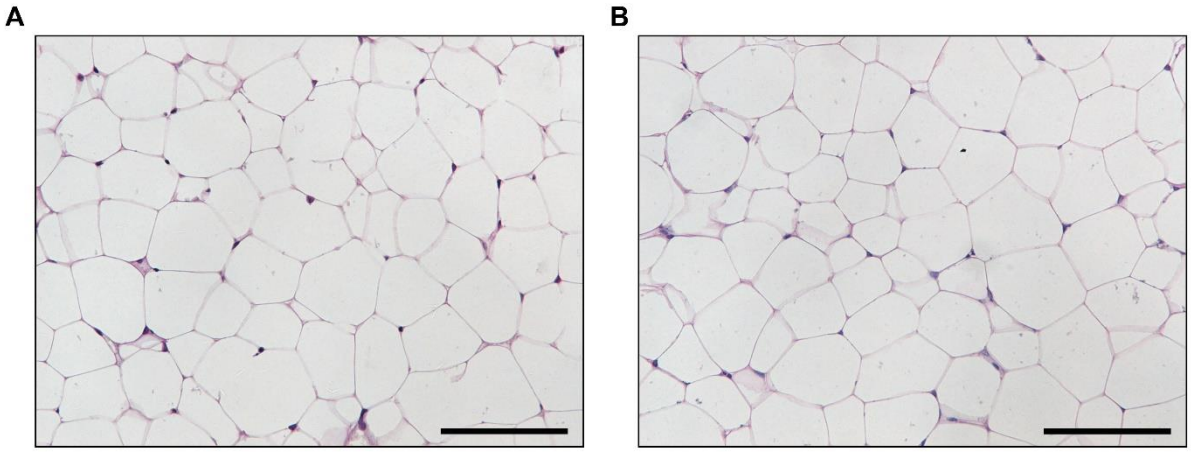


***Figure 46. Histological analysis of eWAT of animals exposed to cold or to room temperature.*** Hematoxylin/eosin staining of representative sections of eWAT of C57BL/6 mice exposed to either room temperature **(A)** or to cold for 4 days **(B)**. Scale bars: 100µm.

## 3. METABOLIC PATHWAY ANALYSIS OF iBAT

The metabolic pathways of the iBAT depot from cold-exposed mice were analyzed using the KEGG pathway map mmu01100 highlighting the upregulated and downregulated values (Figure 47). The obtained expression map of metabolic pathways showed a less coordinated response from this depot to cold exposure of mice (4ºC for 4 days). Despite the map presented several genes upregulated and downregulated, the identification of particular metabolic pathways upregulated or downregulated was not possible. As an example, only half of the steps of the glycolysis presented genes deregulated in iBAT, and some key steps of this process did not present deregulated genes (Figure 47).

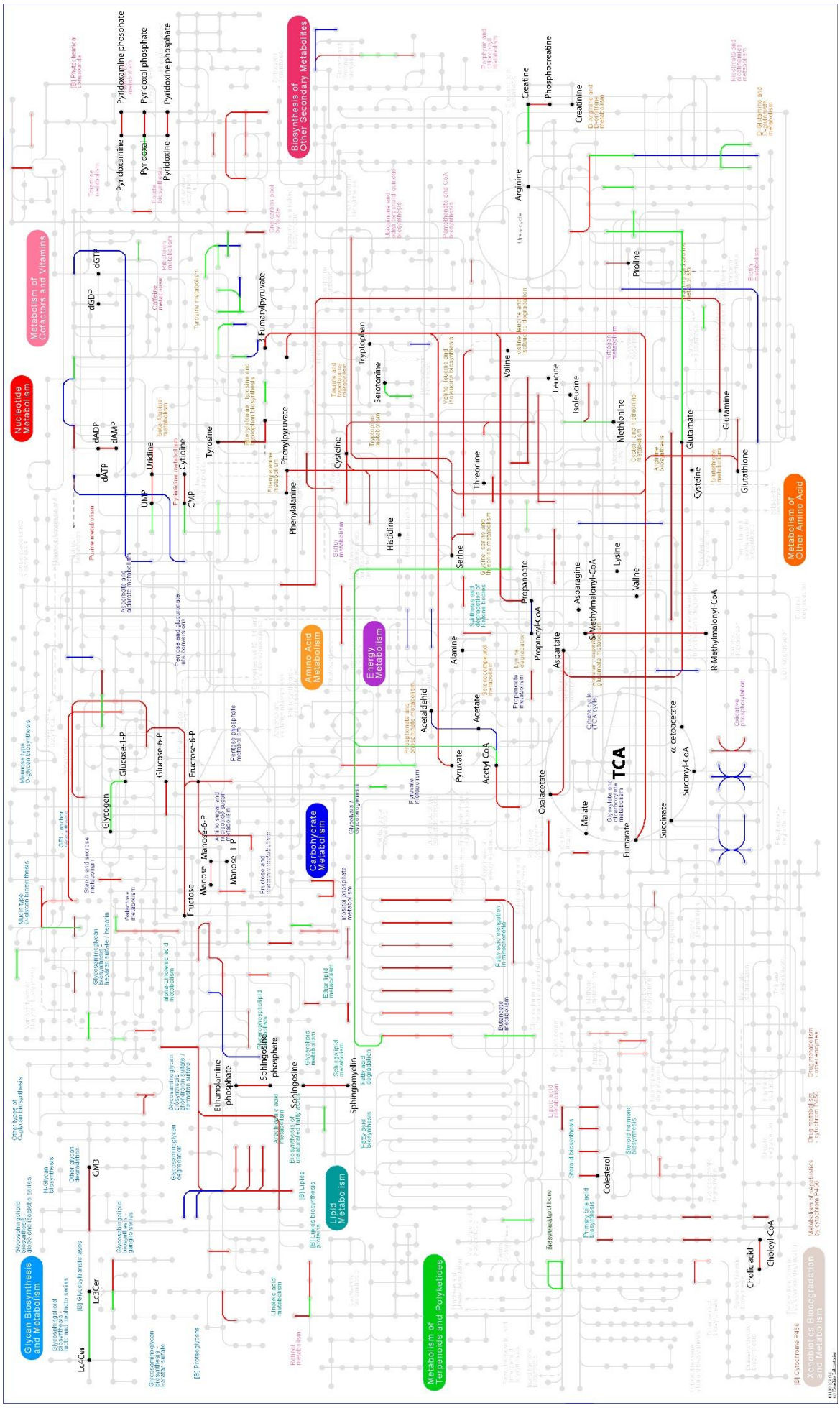


***Figure 47. Metabolic pathways in iBAT of cold-exposed mice.*** Metabolic pathways map mmu01100 from KEGG pathways indicating gene deregulation in iBAT of cold-exposed mice. Highlighted in **Bold**: metabolites; Highlighted in **Red**: upregulated expression in cold exposure of 1.5-fold or higher; Highlighted in **Green**: downregulated expression in cold exposure of -1.5-fold or lower; Highlighted in **Blue**: different isoforms presented divergent in fold change values. Adapted from KEGG pathways.

### 3.1. Glycolysis

As previously described in iWAT, glycolysis can be highly activated by cold. Analysis of the differences in gene expression in iBAT from RT or cold-exposed mice revealed that glycolysis was enhanced in cold-exposed animals (Figure 48, Table 25), but the degree of induction was lower than that observed in iWAT, not only for presenting a lower number of enzymes with upregulated expression but also for having lower fold change values in genes encoding key regulator enzymes (Figure 26, Table 2). In iBAT of cold-exposed mice, two of the essential genes that control the flow of this metabolic pathway, *hexokinase* and *phosphofructokinase* were significantly upregulated, presenting an increased expression of 1.69-fold for the *Hk1* and of 1.55- and 1.74-fold for *Pfkl* and *Pfkp,* respectively (Figure 48). Moreover, even though the expression of *pyruvate kinase* was not higher than 1.5-fold, the upregulation of 1.3-fold was statistically significant (Figure 48). Furthermore, expression of the isoform 1 of the *phosphoglycerate kinase* (*Pgam1*) was significantly increased about 4.38 times (Figure 48). Altogether, these data suggested that glycolysis seemed to be increased in cold-exposed mice.

When the expression of glucose transporters in this depot was evaluated, both GLUT8 and GLUT9 showed an upregulated expression, reaching fold change values of 1.5 and 1.76, respectively (Table 24). GLUT4 expression also present statistically significant differences, but the fold change increase was low (Table 25). All the other glucose transporters did not show clear deregulation in the expression values (Table 25).

| Transcript ID | Gene Symbol | Name | Description | Fold Change | p-value |
|---|---|---|---|---|---|
| 17549664 | Slc2a1 | GLUT1 | Solute carrier family 2 , member 1 | -1.25 | 0.159124 |
| 17396479 | Slc2a2 | GLUT2 | Solute carrier family 2 , member 2 | 1.04 | 0.792069 |
| 17470597 | Slc2a3 | GLUT3 | Solute carrier family 2 , member 3 | -1.04 | 0.608506 |
| 17265096 | Slc2a4 | GLUT4 | Solute carrier family 2 , member 4 | 1.16 | **0.029435** |
| 17421875 | Slc2a5 | GLUT5 | Solute carrier family 2 , member 5 | 1.24 | 0.574645 |
| 17383216 | Slc2a6 | GLUT6 | Solute carrier family 2 , member 6 | -1.22 | 0.235735 |
| 17421895 | Slc2a7 | GLUT7 | Solute carrier family 2 , member 7 | -1.11 | 0.524343 |
| 17384082 | Slc2a8 | **GLUT8** | Solute carrier family 2, , member 8 | **1.5** | **0.042195** |
| 17447646 | Slc2a9 | **GLUT9** | Solute carrier family 2 , member 9 | **1.76** | **0.019125** |
| 17379683 | Slc2a10 | GLUT10 | Solute carrier family 2 , member 10 | -1.07 | 0.457353 |
| 17232119 | Slc2a12 | GLUT12 | Solute carrier family 2 , member 12 | -1.08 | 0.713168 |
| 17320666 | Slc2a13 | GLUT13 | Solute carrier family 2 , member 13 | -1.27 | 0.293731 |

***Table 25. Gene expression analysis of glucose transporters in iBAT.*** Fold change values of gene expression in cold-exposed mice in comparison with the control group are shown. Highlighted in **Bold**: statistically significant p-values. Highlighted in **Red**: upregulated expression in cold exposure of 1.5-fold or higher.

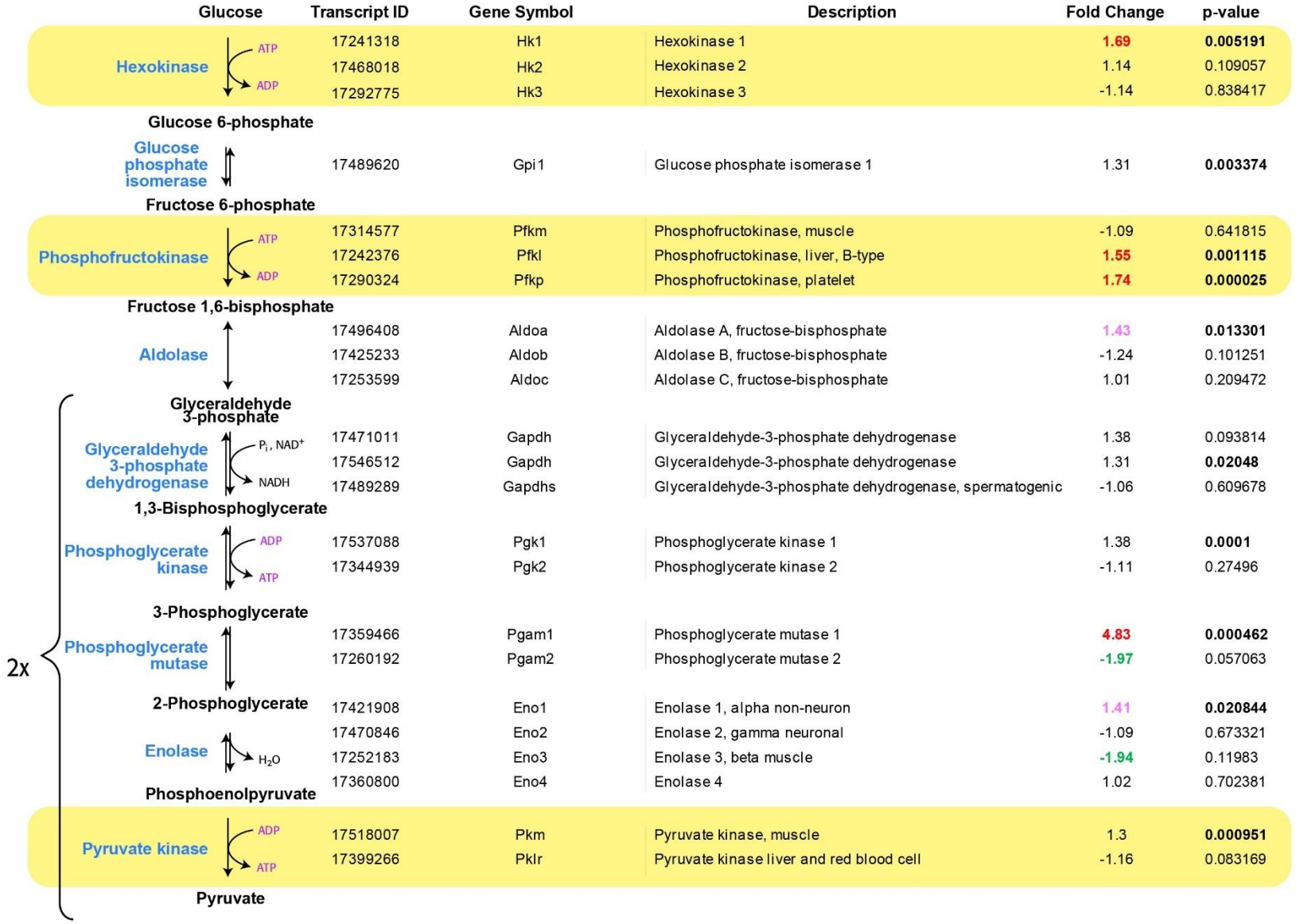


| Transcript ID | Gene Symbol | Description | Fold Change | p-value |
|---|---|---|---|---|
| 17241318 | Hk1 | Hexokinase 1 | **1.69** | **0.005191** |
| 17468018 | Hk2 | Hexokinase 2 | 1.14 | 0.109057 |
| 17292775 | Hk3 | Hexokinase 3 | -1.14 | 0.838417 |
| 17489620 | Gpi1 | Glucose phosphate isomerase 1 | 1.31 | **0.003374** |
| 17314577 | Pfkm | Phosphofructokinase, muscle | -1.09 | 0.641815 |
| 17242376 | Pfkl | Phosphofructokinase, liver, B-type | **1.55** | **0.001115** |
| 17290324 | Pfkp | Phosphofructokinase, platelet | **1.74** | **0.000025** |
| 17496408 | Aldoa | Aldolase A, fructose-bisphosphate | **1.43** | **0.013301** |
| 17425233 | Aldob | Aldolase B, fructose-bisphosphate | -1.24 | 0.101251 |
| 17253599 | Aldoc | Aldolase C, fructose-bisphosphate | 1.01 | 0.209472 |
| 17471011 | Gapdh | Glyceraldehyde-3-phosphate dehydrogenase | 1.38 | 0.093814 |
| 17546512 | Gapdh | Glyceraldehyde-3-phosphate dehydrogenase | 1.31 | **0.02048** |
| 17489289 | Gapdhs | Glyceraldehyde-3-phosphate dehydrogenase, spermatogenic | -1.06 | 0.609678 |
| 17537088 | Pgk1 | Phosphoglycerate kinase 1 | 1.38 | **0.0001** |
| 17344939 | Pgk2 | Phosphoglycerate kinase 2 | -1.11 | 0.27496 |
| 17359466 | Pgam1 | Phosphoglycerate mutase 1 | **4.83** | **0.000462** |
| 17260192 | Pgam2 | Phosphoglycerate mutase 2 | **-1.97** | 0.057063 |
| 17421908 | Eno1 | Enolase 1, alpha non-neuron | **1.41** | **0.020844** |
| 17470846 | Eno2 | Enolase 2, gamma neuronal | -1.09 | 0.673321 |
| 17252183 | Eno3 | Enolase 3, beta muscle | **-1.94** | 0.11983 |
| 17360800 | Eno4 | Enolase 4 | 1.02 | 0.702381 |
| 17518007 | Pkm | Pyruvate kinase, muscle | 1.3 | **0.000951** |
| 17399266 | Pklr | Pyruvate kinase liver and red blood cell | -1.16 | 0.083169 |

***Figure 48. Gene expression analysis of genes involved in glycolysis in iBAT.*** On the left part of the figure, a flow chart of the glycolysis pathway is shown. Key steps are highlighted in yellow. The steps of the glycolysis carried out twice per glucose molecule due to the generation of 2 molecules of glyceraldehyde 3-phosphate are indicated with a curly bracket and a "2x" sign. Fold change and statistical values are also specified on the right. Highlighted in **Bold**: statistically significant p-values. Highlighted in **Red**: upregulated expression in cold exposure of 1.5-fold or higher; Highlighted in Pink: upregulated expression in cold exposure between 1.4- and 1.49-fold; Highlighted in **Green**: downregulated expression in cold exposure of -1.5-fold or lower. Adapted from Stryer Biochemistry 8th Edition.

Pyruvate is produced in the last regulated step of the glycolysis (Figure 48). Pyruvate can then be metabolized to different products with different finalities (Figure 49). In iBAT samples of cold-exposed mice, the expression of none of the enzymes involved in the metabolism of pyruvate was upregulated more than 1.5-fold (Figure 49, Table 26). For example, *Ldhd* gene, which metabolizes the conversion of pyruvate to D-lactate, had a fold change value of -1.26 (Table 26). Similarly, the enzymes that produce L-Lactate from pyruvate, *Ldha*, *Ldhb,* and *Ldhc,* had a fold change of 1.24, 1.13 and -1.05, respectively (Table 26). In addition, expression of enzymes that metabolize the conversion of malate to pyruvate was also not altered, having the enzymes *Me1*, *Me2*, and *Me3* a fold change value of 1.07, 1.06, and 1.12, respectively (Table 26). However, the enzymes that convert acetyl-CoA to acetate, *Acss1* and *Acss2*, presented a deregulated expression of 1.68, and -1.87, respectively (Table 26).

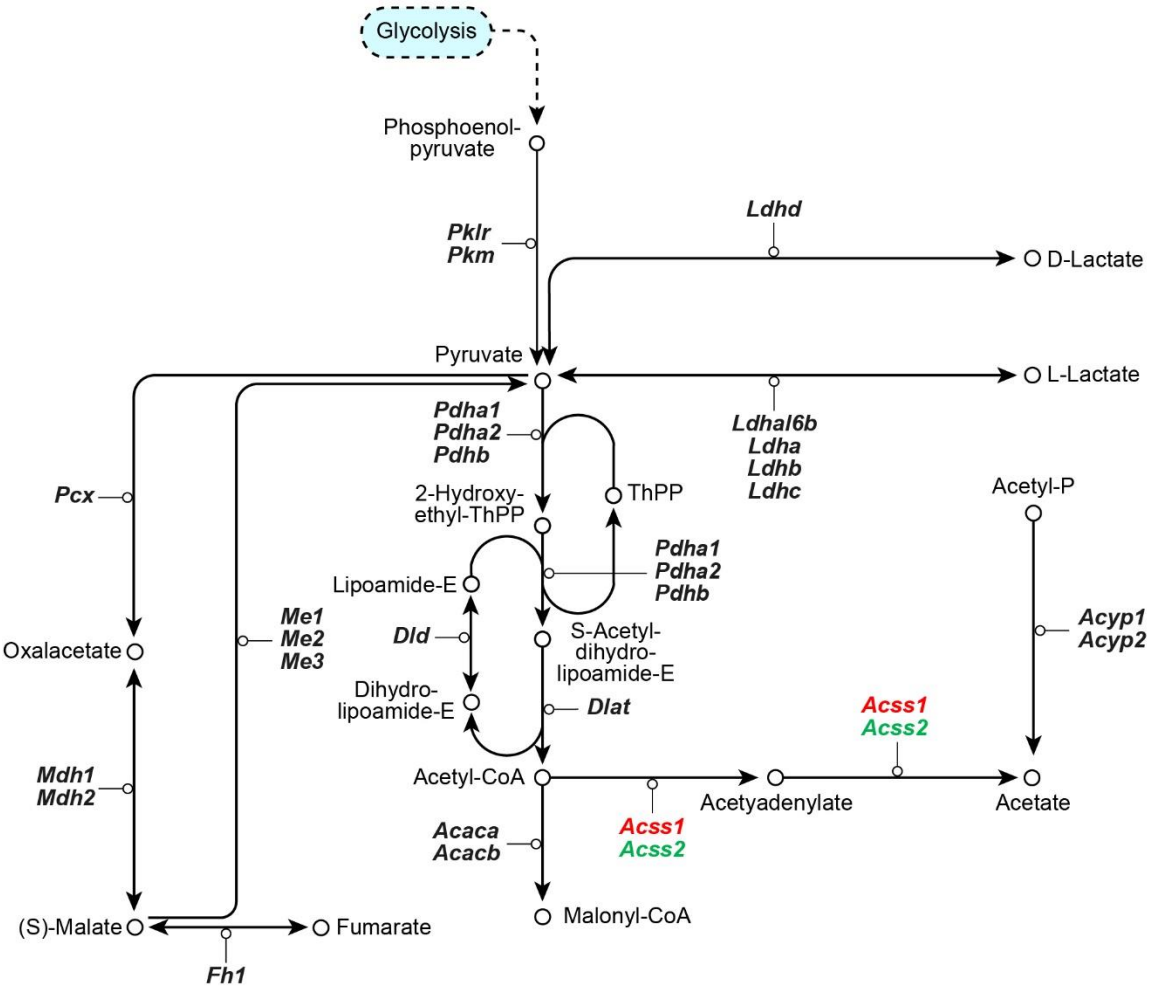


***Figure 49. Expression changes mediated by cold exposure of genes related to the pyruvate metabolism in iBAT.*** The enzymes that metabolize each process are emphasized in ***italic bold***. Highlighted in **Black**: no changes in gene expression levels; Highlighted in **Red**: upregulated expression in cold exposure of 1.5-fold or higher; Highlighted in **Green**: downregulated expression in cold exposure of -1.5-fold or lower.

| Transcript ID | Gene Symbol | Description | Fold Change | p-value |
|---|---|---|---|---|
| 17254395 | Acaca | acetyl-Coenzyme A carboxylase alpha; acetyl-CoA carboxylase 1-like | -1.34 | **0.000516** |
| 17440826 | Acacb | acetyl-Coenzyme A carboxylase beta | -1.06 | 0.851778 |
| 17392690 | **Acss1** | acyl-CoA synthetase short-chain family member 1 | **1.68** | **0.004643** |
| 17378359 | **Acss2** | acyl-CoA synthetase short-chain family member 2 | **-1.87** | **0.000435** |
| 17282689 | Acyp1 | acylphosphatase 1, erythrocyte (common) type | 1 | 0.909782 |
| 17261393 | Acyp2 | acylphosphatase 2, muscle type | 1.11 | 0.276052 |
| 17526861 | Dlat | dihydrolipoamide S-acetyltransferase | 1.14 | **0.002991** |
| 17280498 | Dld | dihydrolipoamide dehydrogenase | 1.02 | 0.596219 |
| 17230153 | Fh1 | fumarate hydratase 1 | -1.11 | **0.001358** |
| 17478225 | Ldha | lactate dehydrogenase A | 1.24 | **0.022728** |
| 17340493 | Ldhal6b | lactate dehydrogenase A-like 6B | -1.26 | 0.182726 |
| 17472517 | Ldhb | lactate dehydrogenase B | 1.13 | 0.08657 |
| 17478243 | Ldhc | lactate dehydrogenase C | -1.05 | 0.754488 |
| 17513135 | Ldhd | lactate dehydrogenase D | -1.26 | 0.253883 |
| 17260944 | Mdh1 | malate dehydrogenase 1, NAD (soluble) | -1.02 | 0.739543 |
| 17443310 | Mdh2 | malate dehydrogenase 2, NAD (mitochondrial) | 1.25 | **0.000656** |
| 17529398 | Me1 | malic enzyme 1, NADP(+)-dependent, cytosolic | 1.07 | 0.966533 |
| 17355391 | Me2 | malic enzyme 2, NAD(+)-dependent, mitochondrial | 1.06 | 0.97198 |
| 17480048 | Me3 | malic enzyme 3, NADP(+)-dependent, mitochondrial | 1.12 | 0.068221 |
| 17356216 | Pcx | pyruvate carboxylase | -1.25 | 0.128516 |
| 17545741 | Pdha1 | pyruvate dehydrogenase E1 alpha 1 | 1 | 0.693942 |
| 17410718 | Pdha2 | pyruvate dehydrogenase E1 alpha 2 | 1.02 | 0.790985 |
| 17303400 | Pdhb | pyruvate dehydrogenase (lipoamide) beta | -1.03 | 0.145859 |
| 17399266 | Pklr | pyruvate kinase liver and red blood cell | -1.16 | 0.083169 |
| 17518007 | Pkm | pyruvate kinase, muscle | 1.3 | **0.000951** |

***Table 26. Expression changes in genes encoding isoenzymes involved in pyruvate metabolism in iBAT.*** Fold change values of gene expression in cold-exposed mice in comparison with the control group. Highlighted in **Bold**: statistically significant p-values. Highlighted in **Red**: upregulated expression in cold exposure of 1.5-fold or higher; Highlighted in **Green**: downregulated expression in cold exposure of -1.5-fold or lower.

### 3.2. TCA cycle

The conversion of pyruvate to acetyl-CoA in iBAT was not enhanced at the gene expression level after cold challenge (Figure 49). None of the genes encoding for subunits of the enzymatic complex PDC presented important upregulation (Figure 49, Table 26). This complex is regulated by *PDH kinases* (*Pdk*) and *PDH phosphatases* (*Pdp*). In iBAT samples of cold-exposed mice, two different isoforms of *Pdk* showed a statistically significant upregulation, being *Pdk3* and *Pdk2* increased 1.37- and 1.56-fold, respectively (Table 27). None of the other isoforms, neither the regulatory subunit *Pdpr*, had a statistically significant change on their expression (Table 27).

| Transcript ID | Gene Symbol | Description | Fold Change | p-value |
|---|---|---|---|---|
| 17371847 | Pdk1 | pyruvate dehydrogenase kinase, isoenzyme 1 | -1.05 | 0.75494 |
| 17268120 | **Pdk2** | pyruvate dehydrogenase kinase, isoenzyme 2 | **1.56** | **0.001618** |
| 17543196 | Pdk3 | pyruvate dehydrogenase kinase, isoenzyme 3 | 1.37 | **0.010038** |
| 17464654 | Pdk4 | pyruvate dehydrogenase kinase, isoenzyme 4 | 1.08 | 0.241323 |
| 17423321 | Pdp1 | pyruvate dehyrogenase phosphatase catalytic subunit 1 | -1.1 | 0.81525 |
| 17504467 | Pdp2 | pyruvate dehyrogenase phosphatase catalytic subunit 2 | 1.19 | 0.161579 |
| 17505718 | Pdpr | pyruvate dehydrogenase phosphatase regulatory subunit | 1.13 | 0.172911 |

***Table 27. Changes in the expression levels in iBAT of the pyruvate dehydrogenase kinase and pyruvate dehydrogenase phosphatase isoenzymes induced by cold.*** Fold change values of gene expression in cold-exposed mice in comparison with the control group. Highlighted in **Bold**: statistically significant p-values. Highlighted in **Red**: upregulated expression in cold exposure of 1.5-fold or higher.

Despite some genes that encode for glycolytic regulatory enzymes were upregulated in iBAT, gene expression of the TCA cycle enzymes was moderately modified (Figure 50, Table 28). However, *aconitase 1* (*Aco1*) presented a statistically significant decreased expression of -1.4-fold (Figure 50, Table 28). The results obtained in iBAT of animals exposed to cold markedly differed from the ones obtained in iWAT and eWAT, in which several genes were statistically significant upregulated (Figure 28, Figure 39, Table 5, Table 16) .

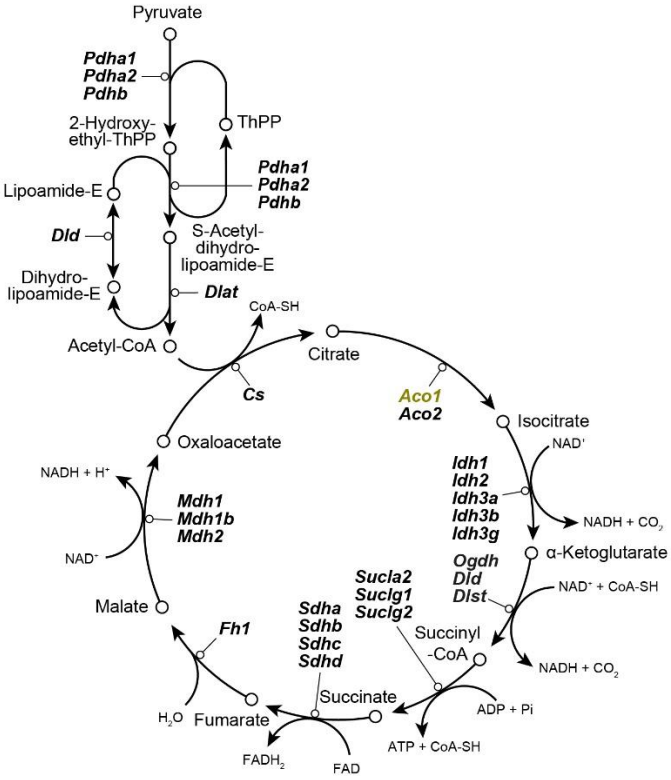


***Figure 50. Expression changes mediated by cold exposure of genes related to the metabolization of pyruvate to acetyl-CoA and the TCA in iBAT.*** The enzymes that metabolize each process are emphasized in ***italic bold***. Highlighted in **Black**: no changes in gene expression levels; Highlighted in **Yellow**; downregulated expression in cold exposure between -1.4- and -1.49-fold.

| Transcript ID | Gene Symbol | Description | Fold Change | p-value |
|---|---|---|---|---|
| 17412730 | Aco1 | aconitase 1 | -1.4 | **0.000331** |
| 17313394 | Aco2 | aconitase 2, mitochondrial | 1 | 0.547704 |
| 17238433 | Cs | citrate synthase | 1.06 | 0.138586 |
| 17280498 | Dld | dihydrolipoamide dehydrogenase | 1.02 | 0.596219 |
| 17277352 | Dlst | dihydrolipoamide S-succinyltransferase | 1.18 | **0.000429** |
| 17230153 | Fh1 | fumarate hydratase 1 | -1.11 | **0.001358** |
| 17223863 | Idh1 | isocitrate dehydrogenase 1 (NADP+), soluble | -1.27 | **0.014729** |
| 17492478 | Idh2 | isocitrate dehydrogenase 2 (NADP+), mitochondrial | -1.09 | 0.12816 |
| 17517390 | Idh3a | isocitrate dehydrogenase 3 (NAD+) alpha | 1.09 | **0.004851** |
| 17391608 | Idh3b | isocitrate dehydrogenase 3 (NAD+) beta | -1.05 | 0.074197 |
| 17542392 | Idh3g | isocitrate dehydrogenase 3 (NAD+), gamma | -1.06 | **0.026854** |
| 17260944 | Mdh1 | malate dehydrogenase 1, NAD (soluble) | -1.02 | 0.739543 |
| 17223747 | Mdh1b | malate dehydrogenase 1B, NAD (soluble) | -1.01 | 0.435833 |
| 17443310 | Mdh2 | malate dehydrogenase 2, NAD (mitochondrial) | 1.25 | **0.000656** |
| 17247080 | Ogdh | oxoglutarate (alpha-ketoglutarate) dehydrogenase (lipoamide) | 1.11 | **0.02256** |
| 17294377 | Sdha | succinate dehydrogenase complex, subunit A, flavoprotein (Fp) | -1.09 | **0.001851** |
| 17420897 | Sdhb | succinate dehydrogenase complex, subunit B, iron sulfur (Ip) | 1.12 | 0.698095 |
| 17229629 | Sdhc | succinate dehydrogenase complex, subunit C, integral membrane protein | 1.06 | 0.217129 |
| 17526843 | Sdhd | succinate dehydrogenase complex, subunit D, integral membrane protein | 1.01 | 0.571306 |
| 17517112 | Sdhd | succinate dehydrogenase complex, subunit D, integral membrane protein | -1.01 | 0.990773 |
| 17301899 | Sucla2 | succinate-Coenzyme A ligase, ADP-forming, beta subunit | 1.13 | **0.002078** |
| 17459716 | Suclg1 | succinate-CoenzymeA ligase, GDP-forming, alpha subunit | 1.13 | **0.0122** |
| 17548514 | Suclg2 | succinate-Coenzyme A ligase, GDP-forming, beta subunit | -1.27 | **0.041735** |

***Table 28. Changes in the expression levels of genes encoding isoenzymes involved in TCA induced by cold in iBAT.*** Fold change values of gene expression in cold-exposed mice in comparison with the control group are shown. Highlighted in **Bold**: statistically significant p-values. Highlighted in **Yellow**; downregulated expression in cold exposure between -1.4- and -1.49-fold.

### 3.3. Anaplerotic reactions

Despite the genes of TCA enzymes were not highly deregulated in iBAT, the statistically significant upregulation of the three genes that encoded enzymes which control the flow of the glycolysis suggested that the entrance of carbons from glycolysis into the TCA in the form of acetyl-CoA could be accelerated (Figure 50). To elucidate whether anaplerotic pathways could provide another entrance of carbon skeleton molecules into the TCA, we studied the BCAA degradation and their metabolic pathway to the TCA. The expression of several genes encoding for enzymes of the BCAA degradation pathway was modified (Figure 51, Table 29). Genes encoding for enzymes that mediate the degradation of isoleucine to acetyl-CoA such as *Bckdhd*, *Dbt*, and *Ehhadh* were upregulated 1.75, 1.53, and 1.92, respectively (Figure 51, Table 29). However, expression of the genes *Acadsb* and *Acaa1a*, which respectively mediate the conversion steps of 2-methyl-butanoyl-CoA to 2-methyl-but-2-enoyl-CoA and of 2-methyl-acetoacetyl-CoA to acetyl-CoA, were downregulated -1.44-fold and -1.42-fold, respectively (Figure 51, Table 29). The degradation of isoleucine can also generate succinyl-CoA through propionyl-CoA. The gene *Mcee* that encodes the enzyme that mediates this conversion, was significantly upregulated 1.69-fold (Figure 51, Table 29). Several of the genes encoding for enzymes involved in the degradation pathway of valine were also upregulated more than 1.5-fold (Figure 51, Table 29). However, expression of the genes *Aox1* and *Aldh2*, that encode proteins involved in the conversion step from methylmalonate semialdehyde to methylmalonate, was significantly downregulated -1,75- and -1.57-fold, respectively. Furthermore, *Acadsb* and *Hibadh* were downregulated -1.44- and -1.49-fold, respectively (Figure 51, Table 29). Finally, few genes encoding for enzymes that participate in the leucine degradation pathway were upregulated (Figure 51, Table 29). All this data suggested that in iBAT of cold-exposed mice the degradation of BCAA to acetyl-CoA or succinyl-CoA was slightly increased.

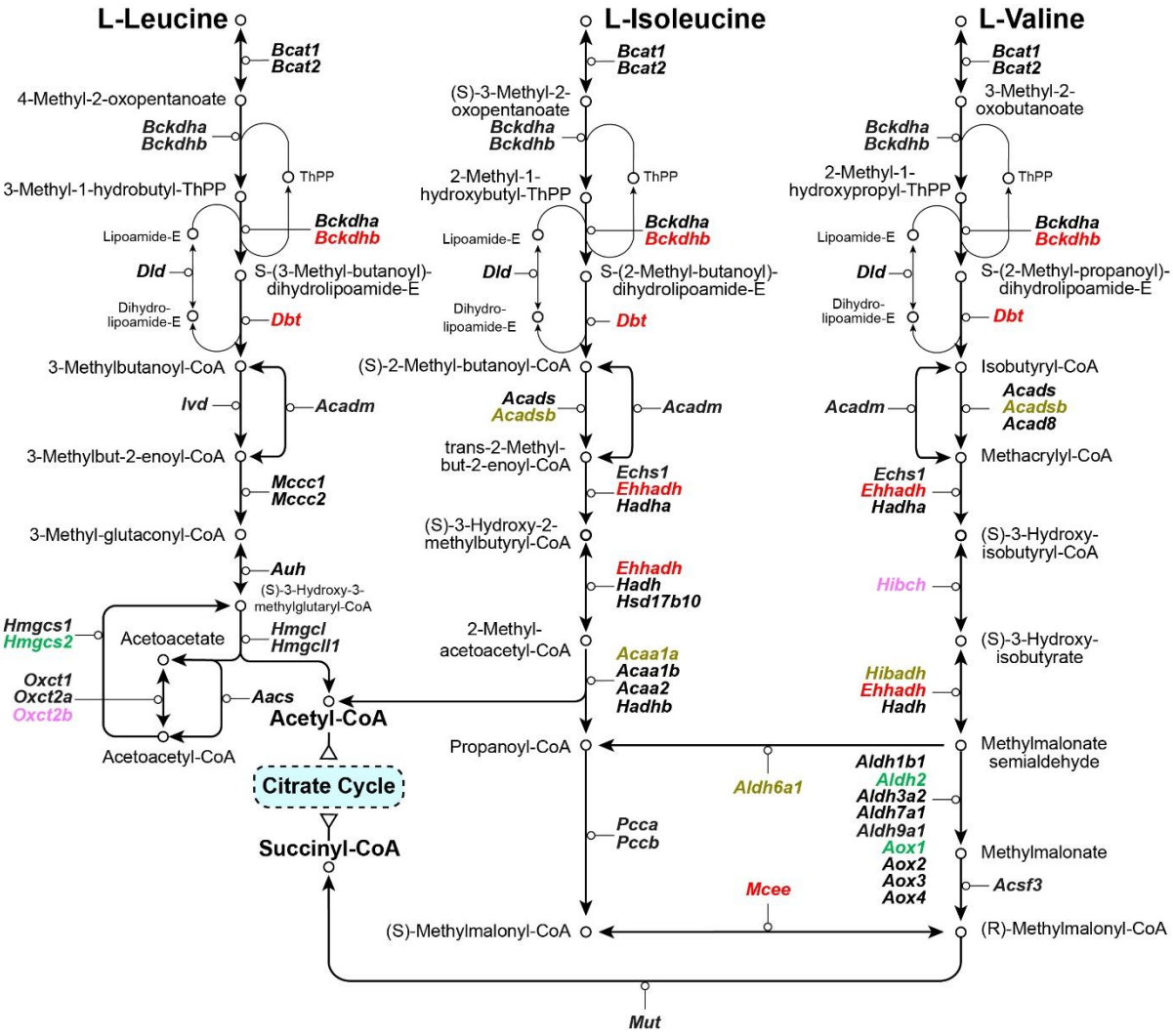


***Figure 51. Expression changes induced by cold exposure of genes involved in the branched-chain amino acids (leucine, isoleucine, and valine) degradation in iBAT.*** From left to right, degradation pathways for the leucine, isoleucine and valine amino acids. In ***italic bold,*** the enzymes that metabolize each process are highlighted. **Black**: no changes in gene expression levels; Highlighted in **Red**: upregulated expression in cold exposure of 1.5-fold or higher; Highlighted in **Pink**: upregulated expression in cold exposure between 1.4- and 1.49-fold; Highlighted in **Green**: downregulated expression in cold exposure of -1.5-fold or lower; Highlighted in **Yellow**: downregulated expression in cold exposure between -1.4- and -1.49-fold. Adapted from KEGG pathway.

| Transcript ID | Gene Symbol | Description | Fold Change | p-value |
|---|---|---|---|---|
| 17442719 | Aacs | acetoacetyl-CoA synthetase | 1.18 | 0.523469 |
| 17523042 | Acaa1a | acetyl-CoA acyltransferase 1A | -1.42 | **0.013254** |
| 17532063 | Acaa1b | acetyl-CoA acyltransferase 1B | 1.08 | 0.172756 |
| 17351811 | Acaa2 | acetyl-CoA acyltransferase 2 (mitochondrial 3-oxoacyl-CoA thiolase) | -1.16 | **0.019232** |
| 17525163 | Acad8 | acyl-CoA dehydrogenase family, member 8 | 1.06 | 0.202957 |
| 17411323 | Acadm | acyl-CoA dehydrogenase, medium chain | 1.05 | 0.138012 |
| 17451649 | Acads | acyl-CoA dehydrogenase, short chain | -1.1 | 0.07206 |
| 17484014 | Acadsb | acyl-CoA dehydrogenase, short/branched chain | -1.44 | **0.001584** |
| 17506443 | Acsf3 | acyl-CoA synthetase family member 3 | 1.2 | **0.006254** |
| 17413674 | Aldh1b1 | aldehyde dehydrogenase 1 family, member B1 | -1.08 | 0.335308 |
| 17441949 | Aldh2 | aldehyde dehydrogenase 2, mitochondrial | -1.75 | **0.006457** |
| 17250582 | Aldh3a2 | aldehyde dehydrogenase family 3, subfamily A2 | -1.08 | 0.553507 |
| 17277267 | Aldh6a1 | aldehyde dehydrogenase family 6, subfamily A1 | -1.43 | **0.001527** |
| 17354434 | Aldh7a1 | aldehyde dehydrogenase family 7, member A1 | 1.01 | 0.823546 |
| 17219096 | Aldh9a1 | aldehyde dehydrogenase 9, subfamily A1 | 1.01 | 0.733128 |
| 17212982 | Aox1 | aldehyde oxidase 1 | -1.57 | **0.004849** |
| 17213101 | Aox2 | aldehyde oxidase 3-like 1 | 1.11 | 0.726952 |
| 17213021 | Aox3 | aldehyde oxidase 3 | 1.12 | 0.492697 |
| 17213060 | Aox4 | aldehyde oxidase 4 | 1.01 | 0.862132 |
| 17292612 | Auh | AU RNA binding protein/enoyl-CoA hydratase | -1.26 | **0.001683** |
| 17472678 | Bcat1 | branched chain aminotransferase 1, cytosolic | 1.19 | 0.121898 |
| 17477897 | Bcat2 | branched chain aminotransferase 2, mitochondrial | 1.04 | 0.521225 |
| 17487982 | Bckdha | branched chain ketoacid dehydrogenase E1, alpha polypeptide | -1.09 | **0.008214** |
| 17519940 | Bckdhb | branched chain ketoacid dehydrogenase E1, beta polypeptide | 1.75 | **0.000141** |
| 17402025 | Dbt | dihydrolipoamide branched chain transacylase E2 | 1.53 | **0.002892** |
| 17280498 | Dld | dihydrolipoamide dehydrogenase | 1.02 | 0.596219 |
| 17497612 | Echs1 | enoyl CoA hydratase, short chain, 1, mitochondrial | 1.08 | 0.086897 |
| 17329220 | Ehhadh | enoyl-CoA, hydratase/3-hydroxyacyl CoA dehydrogenase | 1.92 | **0.003486** |
| 17410390 | Hadh | hydroxyacyl-CoA dehydrogenase | -1.03 | 0.987746 |
| 17446643 | Hadha | hydroxyacyl-CoA dehydrogenase/enoyl-CoA hydratase, alpha subunit | 1.15 | **0.000883** |
| 17435748 | Hadhb | hydroxyacyl-CoA dehydrogenase/enoyl-CoA hydratase, beta subunit | 1.03 | 0.795143 |
| 17466919 | Hibadh | 3-hydroxyisobutyrate dehydrogenase | -1.49 | **0.015359** |
| 17212792 | Hibch | 3-hydroxyisobutyryl-CoA hydrolase | -1.02 | 0.499146 |
| 17419980 | Hmgcl | 3-hydroxy-3-methylglutaryl-CoA lyase | 1.12 | 0.097257 |
| 17519550 | Hmgcll1 | 3-hydroxymethyl-3-methylglutaryl-CoA lyase-like 1 | 1.04 | 0.898365 |
| 17290173 | Hmgcs1 | 3-hydroxy-3-methylglutaryl-CoA synthase 1 | 1.19 | **0.042746** |
| 17400862 | Hmgcs2 | 3-hydroxy-3-methylglutaryl-CoA synthase 2 | -1.54 | 0.051867 |
| 17538852 | Hsd17b10 | hydroxysteroid (17-beta) dehydrogenase 10 | -1.11 | 0.797608 |
| 17374648 | Ivd | isovaleryl CoA dehydrogenase | 1.12 | 0.602489 |
| 17404750 | Mccc1 | methylcrotonoyl-CoA carboxylase 1 (alpha) | -1 | 0.249406 |
| 17295503 | Mccc2 | methylcrotonoyl-CoA carboxylase 2 (beta) | -1.19 | 0.070772 |
| 17478883 | Mcee | methylmalonyl CoA epimerase | 1.69 | **0.00009** |
| 17345004 | Mut | methylmalonyl-CoA mutase | -1.06 | 0.888995 |
| 17309802 | Oxct1 | 3-oxoacid CoA transferase 1 | 1.06 | 0.375321 |
| 17429685 | Oxct2a | 3-oxoacid CoA transferase 2A | 1.02 | 0.712624 |
| 17418154 | Oxct2b | 3-oxoacid CoA transferase 2B | 1.42 | **0.014035** |
| 17302889 | Pcca | propionyl-CoA carboxylase, alpha polypeptide | 1.33 | **0.000232** |
| 17530141 | Pccb | propionyl CoA carboxylase, beta polypeptide | -1.29 | **0.000485** |

**Table 29. Branched-chain amino acids degradation-related gene expression in iBAT.** Fold change values of gene expression in cold-exposed mice in comparison with the control group. Highlighted in **Bold**: statistically significant p-values. Highlighted in **Red**: upregulated expression in cold exposure of 1.5-fold or higher; Highlighted in **Green**: downregulated expression in cold exposure of -1.5-fold or lower; Highlighted in **Yellow**: downregulated expression in cold exposure between -1.4- and -1.49-fold.

Intermediate metabolites of TCA can be generated from other amino acids as well. The enzyme responsible for the conversion of aspartate to oxaloacetate and vice versa can be cytosolic or mitochondrial. The cytosolic form is the *glutamate oxaloacetate transaminase 1* (*Got1*), which was significantly upregulated (about 418%) in iBAT of cold-exposed mice

(Figure 52, Table 30). In addition, the mitochondrial form, the *glutamate oxaloacetate transaminase 2* (*Got2*), had an increased expression of 1.35-fold (Figure 52, Table 30). Regarding the conversion of malate to aspartate, the gene *Mdh2* was significantly upregulated 1.25-fold (Figure 52, Table 30).

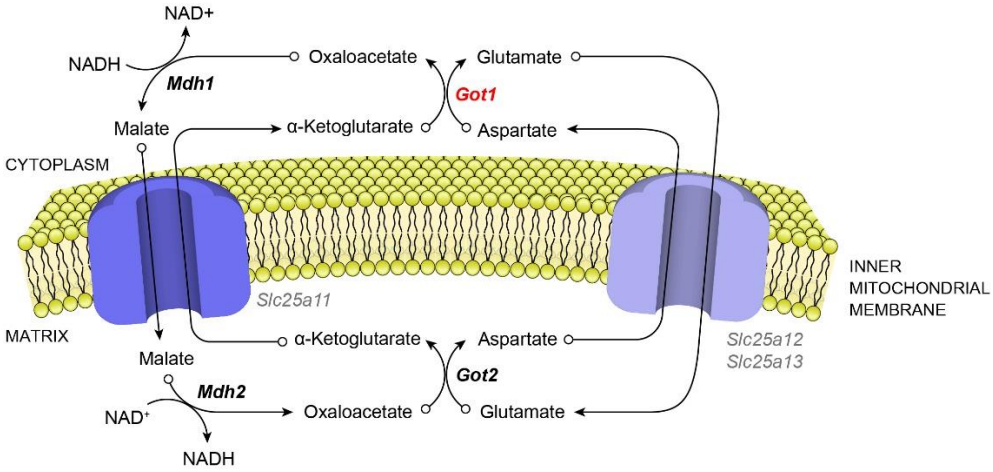


***Figure 52. Schematic representation of the gene expression changes mediated by cold exposure of the malate-aspartate shuttle in iBAT***. Representation of the malate-aspartate shuttle with the metabolites in regular black, the enzymes that metabolize each process in ***italic bold***, and the different transporters and channels in regular grey. Highlighted in **Bold**: no changes in gene expression levels; Highlighted in **Red**: upregulated expression in cold-exposed mice higher or equal than 1.5-fold.

| Transcript ID | Gene Symbol | Description | Fold Change | p-value |
|---|---|---|---|---|
| 17364932 | **Got1** | glutamate oxaloacetate transaminase 1, soluble | **4,18** | **0,000008** |
| 17512103 | Got2* | glutamate oxaloacetate transaminase 2, mitochondrial | 1,35 | **0,011914** |
| 17260944 | Mdh1 | malate dehydrogenase 1, NAD (soluble) | -1,02 | 0,739543 |
| 17443310 | Mdh2 | malate dehydrogenase 2, NAD (mitochondrial) | 1,25 | **0,000656** |
| 17265306 | Slc25a11 | solute carrier family 25 (mitochondrial carrier oxoglutarate carrier), member 11 | -1,14 | 0,390949 |
| 17386396 | Slc25a12 | solute carrier family 25 (mitochondrial carrier, Aralar), member 12 | -1,24 | 0,52712 |
| 17464672 | Slc25a13 | solute carrier family 25 (mitochondrial carrier, adenine nucleotide translocator), member 13 | 1,18 | 0,144719 |

***Table 30. Malate-aspartate shuttle related enzymes and their expression in iBAT.*** Fold change values of gene expression in cold-exposed mice in comparison with the control group. Highlighted in **Bold**: statistically significant p-values. Highlighted in **Red**: upregulated expression in cold exposure of 1.5-fold or higher. *This probe can detect different transcripts.

The degradation of other amino acids such as asparagine or glutamine was also analyzed (Figure 53). The expression of genes like *Shmt2* or *Cth* presented a significant upregulation of 1.52- and 2.42-fold, respectively. The degradation of amino acids mainly occurred for the BCAA. However, expression of genes related to serine was upregulated.

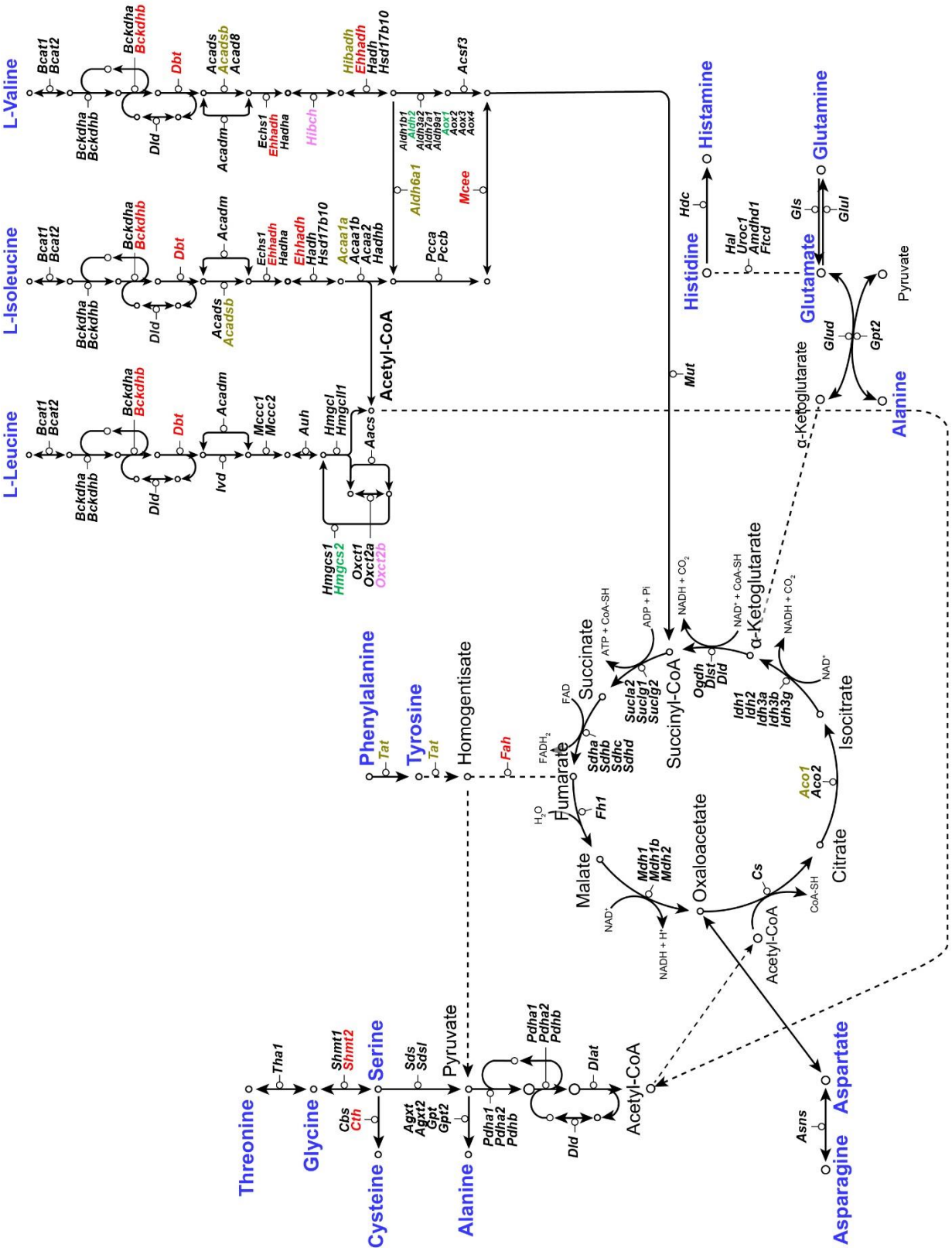


***Figure 53. Expression changes of genes related to the degradation of amino acids in iBAT after cold exposure.*** The enzymes that metabolize each process are emphasized in ***italic bold***. Highlighted in **Blue**: Amino acids; Highlighted in **Black**: no changes in gene expression levels; Highlighted in **Red**: upregulated expression in cold exposure of 1.5-fold or higher; Highlighted in **Pink**: upregulated expression in cold exposure between 1.4- and 1.49-fold. Highlighted in **Green**: downregulated expression in cold exposure of -1.5-fold or lower; Highlighted in **Yellow**: downregulated expression in cold exposure between -1.4- and -1.49-fold. Adapted from KEGG pathway. Dashed lines link same metabolites.

## 3.4. Triglycerides and Fatty acid metabolism

### *3.4.1. Mobilization of triacylglycerol*

Cold exposure has been reported to activate lipolysis via signaling through the β1 and β3-adrenergic receptors (Louis et al., 2000). In iBAT of cold-exposed mice, the expression of the β1-adrenergic receptor (*Adrb1*) was not modified (1.07-fold), but β3-adrenergic receptor gene (*Adrb3*) was a downregulated (about -1.53-fold) (Figure 54, Table 31). Despite this downregulation, the Gs protein that activates the *adenylate cyclase* to produce cAMP was slightly upregulated (about 1.23-fold) (Figure 54, Table 31). Moreover, genes encoding for the *adenylate cyclase 3, 4* and *10* were also upregulated, presenting a fold change of 2.66, 1.61 and 2.01, respectively (Figure 54, Table 31). However, the expression of transporters of fatty acids such as *Fabp1*, *Fabp2*, *Fabp3*, *Fabp4* or *Fabp7* was not modified (Figure 54, Table 31).

### *3.4.2. Fatty acid activation and transport to the mitochondria*

In iBAT of cold-exposed mice, the genes that encode for subunits of the *PKA* protein did not present any expression difference. Similarly, the expression levels of genes encoding for *perilipin*, *ATGL* or *HSL* were not modified between conditions (Figure 54, Table 31). However, since the activity of some of *PKA*, *perilipin* or *HS lipase* is regulated by a secondary metabolite or through phosphorylation, respectively, the fold change value of their gene expression is not as informative of their functionality as for other genes. Conversely, *monoglyceride lipase* (*MGL*) showed a significantly increased expression of 1.46-fold (Figure 54, Table 31). Anyway, upregulation of *adenylate cyclase* or MGL expression levels suggested activation of the triacylglycerol degradation to FA. Conversion of FA to fatty acyl-CoA thioester mediated by the isoenzymes of *acyl-CoA synthetase* was likely enhanced since the expression of *Acsl1* was increased 2.2-fold (Figure 54, Table 31). This activation is a first step to oxidize the FA. Then, *carnitine palmitoyltransferase 1* (*Cpt1*) transforms the fatty acyl-CoA thioester to fatty acyl-carnitine. The entrance of this molecule to the mitochondria is mediated through the *acyl-carnitine/carnitine transporter* (*Catc*), which was also slightly upregulated (1.37-fold) in iBAT of cold-exposed mice (Figure 54, Table 31). Altogether, these results suggested a general induction of the FA activation and transport to the mitochondria in iBAT of mice exposed to cold but not as marked as it was in iWAT of cold-exposed animals.

### *3.4.3. Fatty acid oxidation*

Although the results obtained in section 3.3.4.2. suggested FA activation and the transport to the mitochondria were increased in iBAT from cold-exposed mice, FA oxidation or β-oxidation were not too enhanced (Figure 54, Table 31). Expression of any gene coding for enzymes that remove successive two-carbon from the carboxyl end of the fatty acyl-CoA during several cycles to produce acetyl-CoA was modified (Figure 54, Table 31).

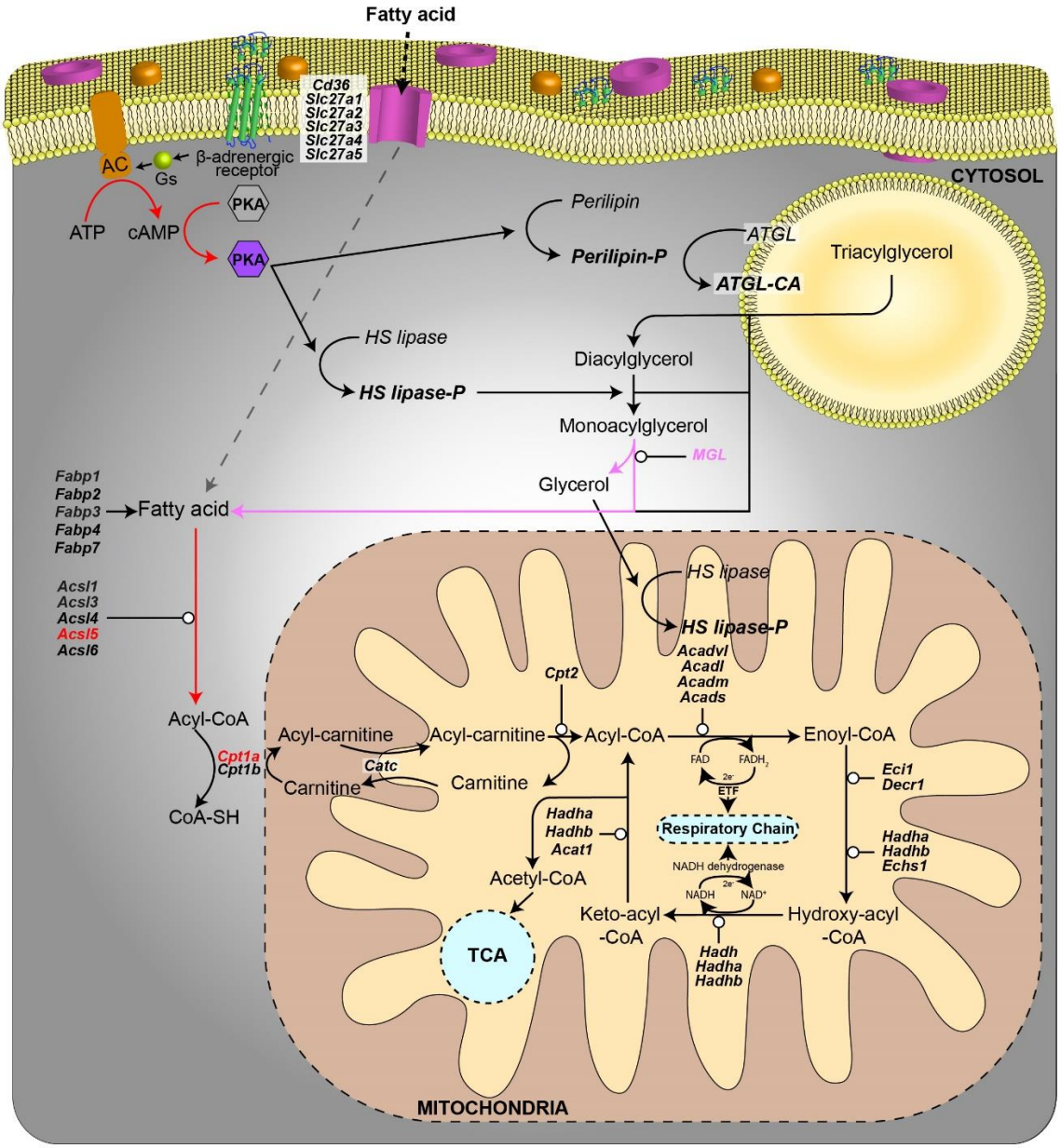


***Figure 54. Expression changes in iBAT of the thermogenesis and metabolic-related genes mediated by cold exposure.*** Schematic representation of a cell focusing on the triglycerides and fatty acids degradation pathways. In ***italic bold,*** the enzymes that metabolize each process are highlighted. **Black**: no changes in gene expression levels; **Red**: upregulated expression in cold exposure of 1.5-fold or higher; Pink: upregulated expression in cold exposure between 1.4- and 1.49-fold. Adapted from KEGG pathway.

| Transcript ID | Gene Symbol | Description | Fold Change | p-value |
|---|---|---|---|---|
| 17548916 | Acadl | acyl-Coenzyme A dehydrogenase, long-chain | 1.21 | 0.12823 |
| 17411323 | Acadm | acyl-Coenzyme A dehydrogenase, medium chain | 1.05 | 0.138012 |
| 17451649 | Acads | acyl-Coenzyme A dehydrogenase, short chain | -1.1 | 0.07206 |
| 17265129 | Acadvl | acyl-Coenzyme A dehydrogenase, very long chain | 1.09 | **0.008757** |
| 17527123 | Acat1 | acetyl-Coenzyme A acetyltransferase 1 | -1.13 | 0.051502 |
| 17500996 | Acsl1 | acyl-CoA synthetase long-chain family member 1 | 1.07 | 0.149462 |
| 17214685 | Acsl3 | acyl-CoA synthetase long-chain family member 3 | 1.11 | 0.122519 |
| 17545051 | Acsl4 | acyl-CoA synthetase long-chain family member 4 | -1.04 | 0.401806 |
| 17360462 | **Acsl5** | acyl-CoA synthetase long-chain family member 5 | **2.2** | **0.000071** |
| 17249640 | Acsl6 | acyl-CoA synthetase long-chain family member 6 | -1.04 | 0.804517 |
| 17247183 | Adcy1 | adenylate cyclase 1 | -1.17 | 0.246926 |
| 17294086 | Adcy2 | adenylate cyclase 2 | -1.01 | 0.98375 |
| 17273714 | **Adcy3** | adenylate cyclase 3 | **2.66** | **0.00048** |
| 17306877 | **Adcy4** | adenylate cyclase 4 | **1.61** | **0.035521** |
| 17325206 | Adcy5 | adenylate cyclase 5 | -1.12 | 0.582409 |
| 17321263 | Adcy6 | adenylate cyclase 6 | -1.22 | **0.043237** |
| 17503616 | Adcy7 | adenylate cyclase 7 | 1.18 | 0.22588 |
| 17317533 | Adcy8 | adenylate cyclase 8 | -1.05 | 0.323885 |
| 17327720 | **Adcy9** | adenylate cyclase 9 | **-1.76** | **0.022672** |
| 17218965 | **Adcy10** | adenylate cyclase 10 | **2.01** | **0.002505** |
| 17360599 | Adrb1 | adrenergic receptor, beta 1 | 1.07 | 0.878138 |
| 17354857 | Adrb2 | adrenergic receptor, beta 2 | -1.28 | 0.27135 |
| 17508544 | **Adrb3** | adrenergic receptor, beta 3 | **-1.53** | **0.02243** |
| 17521875 | Catc / Slc25a20 | solute carrier family 25, member 20 | 1.37 | **0.000426** |
| 17445715 | Cd36 | CD36 antigen | 1.03 | **0.035093** |
| 17355915 | **Cpt1a** | carnitine palmitoyltransferase 1a, liver | **1.86** | **0.011707** |
| 17320499 | Cpt1b | carnitine palmitoyltransferase 1b, muscle | 1.21 | **0.002842** |
| 17427961 | Cpt2 | carnitine palmitoyltransferase 2 | 1.23 | **0.001195** |
| 17423463 | Decr1 | 2,4-dienoyl CoA reductase 1, mitochondrial | 1.28 | **0.002655** |
| 17497612 | Echs1 | enoyl Coenzyme A hydratase, short chain, 1, mitochondrial | 1.08 | 0.086897 |
| 17334253 | Eci1 | enoyl-Coenzyme A delta isomerase 1 | -1.33 | **0.002042** |
| 17459455 | Fabp1 | fatty acid binding protein 1, liver | -1.17 | 0.329501 |
| 17402350 | Fabp2 | fatty acid binding protein 2, intestinal | -1.05 | 0.16597 |
| 17419215 | Fabp3 | fatty acid binding protein 3, muscle and heart | 1.14 | 0.281695 |
| 17404091 | Fabp4 | fatty acid binding protein 4, adipocyte | -1.02 | 0.36325 |
| 17233384 | Fabp7 | fatty acid binding protein 7, brain | 1.11 | 0.473748 |
| 17380306 | Gnas | GNAS (guanine nucleotide binding protein, alpha stimulating) complex locus | 1.23 | **0.001142** |
| 17410390 | Hadh | hydroxyacyl-Coenzyme A dehydrogenase | -1.03 | 0.987746 |
| 17446643 | Hadha | hydroxyacyl-Coenzyme A dehydrogenase | 1.15 | **0.000883** |
| 17435748 | Hadhb | hydroxyacyl-Coenzyme A dehydrogenase | 1.03 | 0.795143 |
| 17487927 | Lipe | lipase, hormone sensitive | -1.03 | 0.833708 |
| 17460665 | **Mgll** | monoglyceride lipase | **1.46** | **0.004611** |
| 17492406 | Plin1 | perilipin 1 | -1.22 | 0.434551 |
| 17426981 | **Plin2** | perilipin 2 | **1.59** | **0.000029** |
| 17346216 | Plin3 | perilipin 3 | 1.11 | 0.149327 |
| 17346125 | Plin4 | perilipin 4 | -1.13 | 0.539317 |
| 17346136 | Plin5 | perilipin 5 | 1.16 | 0.12574 |
| 17484909 | Pnpla2 | patatin-like phospholipase domain containing 2 | 1.15 | 0.128773 |
| 17503031 | Prkaca | protein kinase, cAMP dependent, catalytic, alpha | -1 | 0.284035 |
| 17502233 | Slc27a1 | solute carrier family 27 (fatty acid transporter), member 1 | 1.2 | 0.119463 |
| 17391089 | Slc27a2 | solute carrier family 27 (fatty acid transporter), member 2 | -1.22 | 0.740966 |
| 17407259 | Slc27a3 | solute carrier family 27 (fatty acid transporter), member 3 | -1.09 | 0.802461 |
| 17368904 | Slc27a4 | solute carrier family 27 (fatty acid transporter), member 4 | 1.17 | 0.273497 |
| 17486589 | Slc27a5 | solute carrier family 27 (fatty acid transporter), member 5 | -1.19 | 0.058655 |
| 17350856 | Slc27a6 | solute carrier family 27 (fatty acid transporter), member 6 | -1.16 | 0.418773 |

***Table 31. Cold-induced expression changes in genes involved in triglycerides and fatty acids degradation in iBAT.*** Fold change values of gene expression in cold-exposed mice in comparison with the control group are shown. Highlighted in **Bold**: statistically significant p-values. Highlighted in **Red**: upregulated expression in cold exposure of 1.5-fold or higher; Highlighted in **Pink**: upregulated expression in cold exposure between 1.4- and 1.49-fold; Highlighted in **Green**: downregulated expression in cold exposure of -1.5-fold or lower.

### 3.5. Oxidative phosphorylation

In iBAT of cold-exposed mice, the expression of only a few genes encoding for subunits of the different complexes presented an upregulated expression (Figure 55, Table 32). *Complex I* or *complex IV* not only presented few subunits upregulated but also some were downregulated (Figure 55, Table 32). Regarding the *complex V*, even though the mitochondrial ATPase *(F-type)* had only one subunit upregulated (the f subunit), the vacuolar ATPase presented the subunits *H*, *a*, *c*, and *d* with upregulated expression of about 1.56-, 1.73-, 1.61-, and 1.55-fold, respectively (Figure 55, Table 32). All these results suggested that the oxidative phosphorylation was not upregulated in terms of gene expression in iBAT of cold-exposed mice.

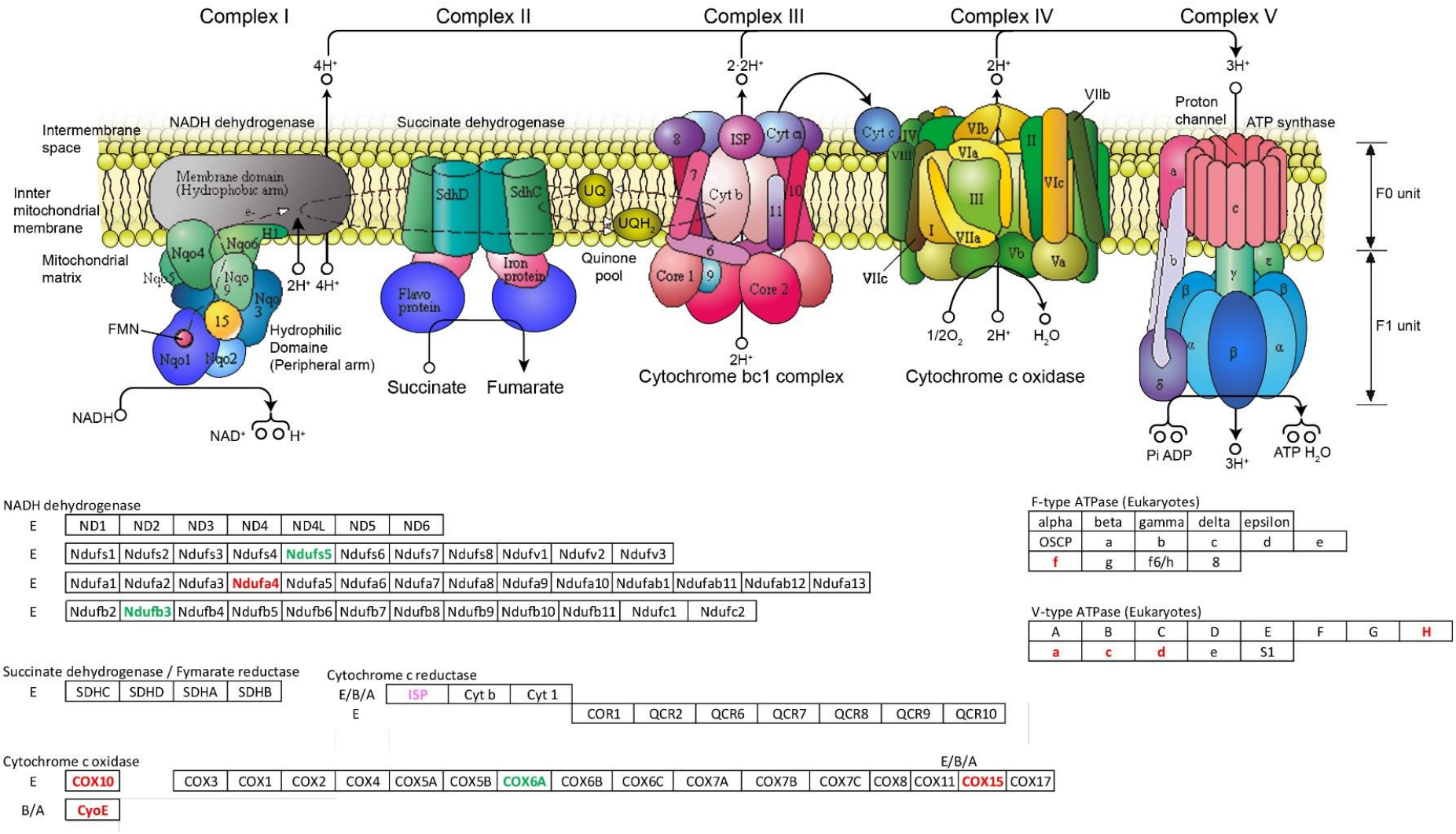


***Figure 55. Expression changes induced by cold exposure of the several isoenzymes of the different complexes of the electron transport chain and the ATPase in iBAT.*** On top of the figure, the different isoenzymes of each complex are showed. Below the scheme, all genes encoding for the different complexes are indicated, as well as alterations on their gene expression level in cold exposed animals in comparison to room temperature exposed mice. Highlighted in **Black**: no changes in gene expression levels; Highlighted in **Red**: upregulated expression in cold exposure of 1.5-fold or higher; Highlighted in Pink: upregulated expression in cold exposure between 1.4- and 1.49-fold; Highlighted in **Green**: downregulated expression in cold exposure of -1.5-fold or lower. Adapted from KEGG pathway.

| Transcript ID | Gene Symbol | Alias | Description | Pathway | Fold Change | p-value |
|---|---|---|---|---|---|---|
| 17455083 | Atp5j2 | f | ATP synthase, H+ transporting, mitochondrial F0 complex, subunit F2 | F-type ATPase | 1.52 | **0.014227** |
| 17442588 | Atp6v0a2 | a | ATPase, H+ transporting, lysosomal V0 subunit A2 | V-type ATPase | 1.73 | **0.000342** |
| 17549436 | Atp6v0c | c | ATPase, H+ transporting, lysosomal V0 subunit C | V-type ATPase | 1.61 | **0.002953** |
| 17423577 | Atp6v0d2 | d | ATPase, H+ transporting, lysosomal V0 subunit D2 | V-type ATPase | 1.55 | 0.166117 |
| 17210887 | Atp6v1h | H | ATPase, H+ transporting, lysosomal V1 subunit H | V-type ATPase | 1.56 | **0.001106** |
| 17264107 | Cox10 | | cytochrome c oxidase assembly protein 10 | Cytochrome c oxidase | 1.5 | **0.001264** |
| 17364954 | Cox15 | | cytochrome c oxidase assembly protein 15 | Cytochrome c oxidase | 1.59 | **0.015224** |
| 17496857 | Cox6a2 | | cytochrome c oxidase subunit VIa polypeptide 2 | Cytochrome c oxidase | -1.66 | 0.268726 |
| 17264107 | CyoE | | cytochrome c oxidase assembly protein 10 | Cytochrome c oxidase | 1.5 | **0.001264** |
| 17291570 | ISP | | ubiquinol-cytochrome c reductase, Rieske iron-sulfur polypeptide 1 | Cytochrome c reductase | 1.4 | **0.011457** |
| 17238054 | Ndufa4l2 | | NADH dehydrogenase (ubiquinone) 1 alpha subcomplex, 4-like 2 | NADH dehydrogenase | 1.65 | **0.001963** |
| 17213185 | Ndufb3 | | NADH dehydrogenase (ubiquinone) 1 beta subcomplex 3 | NADH dehydrogenase | -1.59 | **0.001783** |
| 17429803 | Ndufs5 | | NADH dehydrogenase (ubiquinone) Fe-S protein 5 | NADH dehydrogenase | -1.5 | 0.071732 |

***Table 32 Differentially expressed genes encoding enzymes involved in the respiratory chain in iBAT after cold exposure.*** Fold change values of gene expression in cold-exposed mice in comparison with the control group. Highlighted in **Bold**: statistically significant p-values. Highlighted in **Red**: upregulated expression in cold exposure of 1.5-fold or higher; Highlighted in **Pink**: upregulated expression in cold exposure between 1.4- and 1.49-fold; Highlighted in **Green**: downregulated expression in cold exposure of -1.5-fold or lower.

## 3.6. Thermogenesis

Despite the complexes from the electron respiratory chain were not upregulated in iBAT of cold-exposed mice, the expression of thermogenic genes was evaluated (Table 33). The expression of *Ucp1* in iBAT of cold-exposed mice was not highly increased, presenting only marginal upregulation of about 1.19-fold (Figure 56, Table 33). However, other thermogenic genes such as *Cidea* or *Dio2* did not present differences in its expression and the receptor β-Klotho presented a weak downregulation of about -1.35-fold in iBAT of cold-exposed mice (Figure 56, Table 33). Nevertheless, the expression of *Ppargc1a*, which codifies PGC1-α presented an upregulated expression of 1.96-fold (Figure 56, Table 33).

| Transcript ID | Gene Symbol | Description | Fold Change | p-value |
|---|---|---|---|---|
| 17351457 | Cidea | cell death-inducing DNA fragmentation factor, alpha subunit-like effector A | -1.01 | 0.387369 |
| 17282970 | Dio2 | deiodinase, iodothyronine, type II | 1.1 | 0.251483 |
| 17437765 | Klb | klotho beta | -1.35 | **0.000129** |
| 17448001 | Ppargc1a | peroxisome proliferative activated receptor, gamma, coactivator 1 alpha | 1.96 | **0.001886** |
| 17502899 | Ucp1 | uncoupling protein 1 (mitochondrial, proton carrier) | 1.19 | **0.00193** |

***Table 33.Expression of thermogenesis gene markers' in iBAT.*** **Bold**: statistically significant p-values. **Red**: upregulated expression in cold exposure of 1.5-fold or higher.

The variation of the expression of thermogenic genes in cold-exposed mice was heterogeneous, obtaining high upregulation for *Ppargc1a*, a low upregulation for *Ucp1* and no upregulation for *Cidea* or *Dio2*. The data of our gene expression analysis

determined that the highest absolute expression level among all the genes detected in the microarray was of 13.5, while the lowest was 0.32. As shown in Table 34, the genes presenting high absolute expression levels in iBAT of room temperature-exposed mice, such as *Cidea* or *Dio2*, did not increase more their expression (Table 33, 34). However, as *Ppargc1a* presented high expression but not maximal, cold exposure induced an increase in its expression.

| | | Expression levels | | | | | | | |
|---|---|---|---|---|---|---|---|---|---|
| | Mouse | 1 | 2 | 3 | 4 | 5 | 6 | 7 | 8 |
| Transcript ID | Gene Symbol | Room temperature | | | | Cold | | | |
| 17351457 | Cidea | 12.32 | 12.36 | 12.42 | 12.41 | 12.36 | 12.37 | 12.30 | 12.37 |
| 17282970 | Dio2 | 8.07 | 9.21 | 9.73 | 9.63 | 9.55 | 9.76 | 10.07 | 9.36 |
| 17437765 | Klb | 8.91 | 8.92 | 8.91 | 8.81 | 8.44 | 8.50 | 8.51 | 8.32 |
| 17448001 | Ppargc1a | 8.61 | 9.44 | 9.55 | 9.37 | 10.37 | 10.41 | 10.87 | 10.47 |
| 17502899 | Ucp1 | 12.74 | 12.91 | 12.93 | 12.96 | 13.14 | 13.24 | 13.22 | 13.13 |

***Table 34. Gene expression levels of Cidea, Dio2, Klb, Ppargc1a, and Ucp1 in iBAT of room temperature and cold-exposed mice.*** The expression levels were represented numerically for each gene.

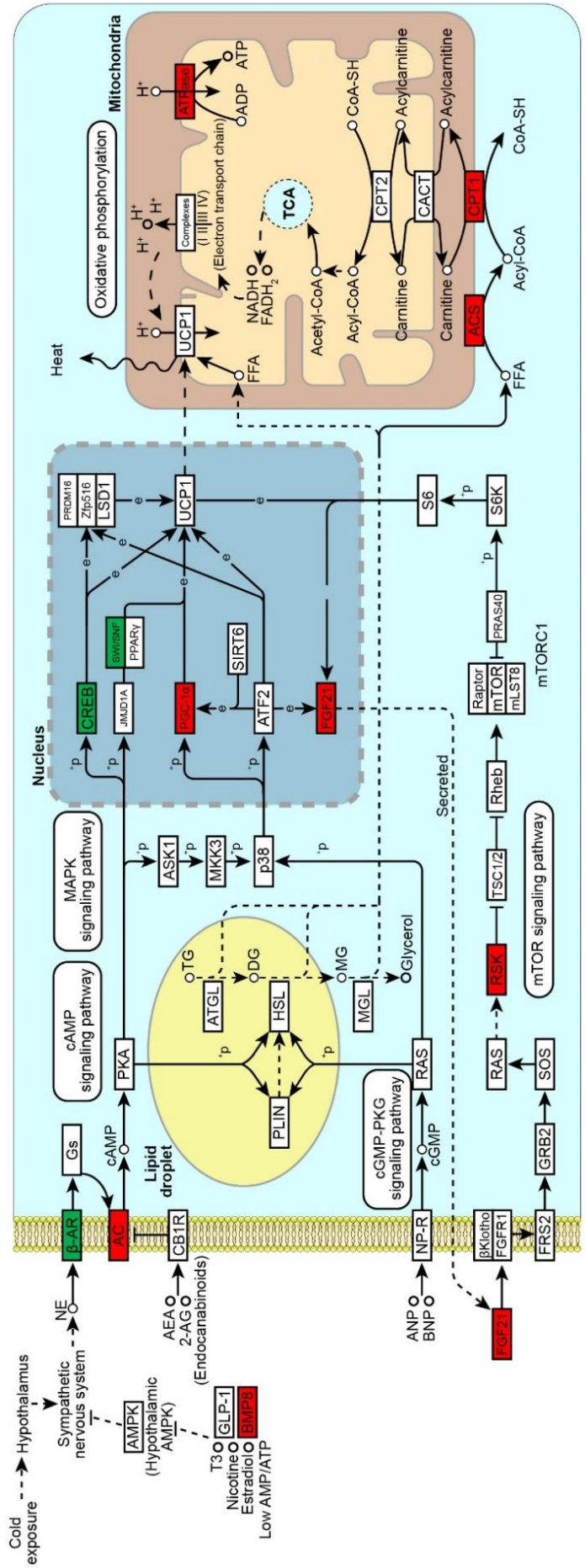


***Figure 56. Expression changes in iBAT mediated by cold exposure of the thermogenesis and related-genes.*** Enzymes that metabolize each process are framed. Highlighted in **Black**: no changes in gene expression levels; Highlighted in **Red**: upregulated expression in cold exposure of 1.5-fold or higher; Highlighted in **Green**: downregulated expression in cold exposure of -1.5-fold or lower. Adapted from KEGG pathway.

The induction of thermogenesis is related to consumption of lipids. To clarify if the low upregulation of *Ucp1* and the high upregulation of *Ppargc1a* were metabolically significant, a morphological analysis of different histological sections of iBAT samples of both cold and RT-exposed mice was performed. As observed in Figure 57, iBAT of cold-exposed mice (Figure 57B) did not present marked differences in lipid content in comparison with iBAT of room-temperature housed mice (Figure 57A).

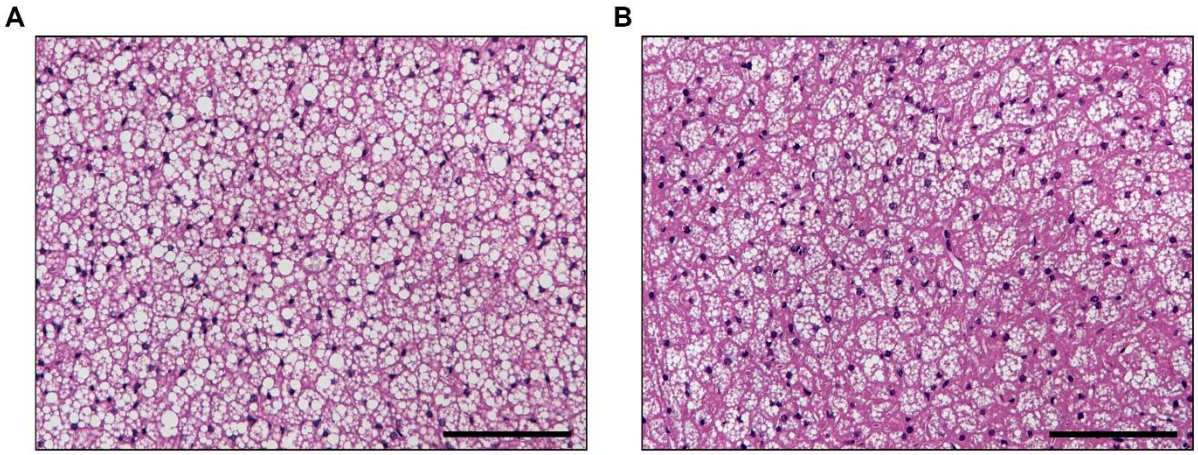


***Figure 57. Histological analysis of iBAT of animals exposed to cold or to room temperature***. Hematoxylin/eosin staining of representative sections of iWAT of C57BL/6 mice exposed to either **(A)** room temperature, or **(B)** cold challenge. Scale bars: 100µm.

In summary, the metabolic pathway analyses performed for iWAT, eWAT and iBAT depots showed marked differences in terms of gene expression during cold adaptation. Among the different depots studied, iWAT was the depot that responded the most from a metabolic point of view. This depot presented a high number of metabolic-related genes upregulated, in a marked and correlated response to cold. In contrast, the upregulation of genes related to metabolism in the eWAT depot was lower than in iWAT, but several important genes were clearly upregulated. Finally, iBAT depot presented a low number of upregulated genes, but as evidenced in the expression levels of thermogenic markers, despite not presenting differences these genes were already highly expressed. Altogether, these results indicated that a metabolic response was necessary to maintain or to induce non-shivering thermogenesis.

# Section III. Analysis of gene expression patterns in adipose tissue

# 1. GENE EXPRESSION PATTERN OF MOLECULAR FUNCTIONS

The results obtained from the metabolism analyses demonstrated a coordinated gene response to cold adaptation. These analyses revealed that several genes, such as the thermogenic genes, presented a similar expression pattern (Table 24). The analysis of genes co-expressed under different biological conditions could help to identify genes that are actively transcribed simultaneously, suggesting a possible co-regulation of said genes (Chou et al., 2007) and potentially indicating similar biological functions. In addition, the analysis of the different profiles of gene expression patterns has been also used to define complex biological processes, as it is suitable to group genes, "clusters", with similar expression pattern across samples (Ben-Dor et al., 2003). Thus, the functional analysis of clusters allows the unravelling of co-regulated networks of genes related to particular biological functions (Atias et al., 2009; Serin et al., 2016). Furthermore, the analysis of gene expression patterns has also been used to identify new molecular markers or potentially therapeutic genes (Alizadeh et al., 2000; Chang et al., 2002; Welsh et al., 2001).

## 1.1. Hierarchical clustering of the differentiated expressed genes

With the aim to study if the genes that presented similar expression pattern in the metabolic analyses, carried on in section II, were also co-expressed, *hierarchical clustering analysis* was performed. The hierarchical clustering analysis of adipose tissue samples of mice exposed either to cold or to RT demonstrated several different expression patterns across adipose depots (Figure 58). Specifically, five different clusters were detected (Figure 58).

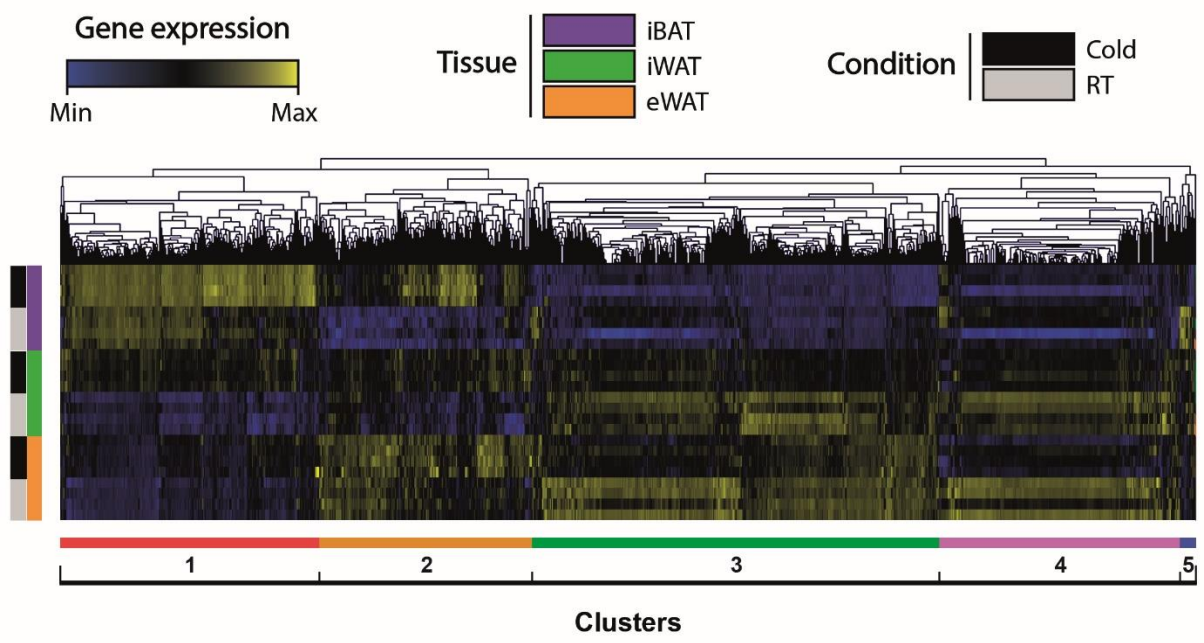


***Figure 58. Heatmap displaying hierarchical clustering for differentially expressed genes between cold and room temperature exposed adipose depot.*** The heatmap was constructed using Pearson correlation as the distance metric. Fold change values are presented using a color scale. Blue indicates low negative fold change values, black indicates neutral fold change and yellow indicates high fold change values. Five different clusters were detected and highlighted in red, orange, green, and pink in the heatmap.

To identify the different functions related to each gene expression profile, pathway enrichment, and gene ontology analyses were performed for each cluster.

### *1.1.1.* First Cluster

The gene expression pattern of the first cluster grouped the genes that did not show noteworthy expression differences in eWAT and iBAT samples of mice exposed to 4ºC or RT but presented an upregulated expression in iWAT of cold-exposed mice (Figure 59A).

The results from the *pathway enrichment analysis* highlighted that genes related to metabolism, such as *Acaa2*, *Cs*, *Got1*, *Pdk4*, or *Pfkm* among others, were highly enriched in the first cluster (Figure 59B). Moreover, the TCA with the respiratory electron transport chain appeared as the third most enriched pathway. These enriched pathways detected in this cluster were very similar to the ones obtained in the pathway enrichment analysis of all the DEGs, in which genes involved in metabolism were also highly enriched (Figure 22).

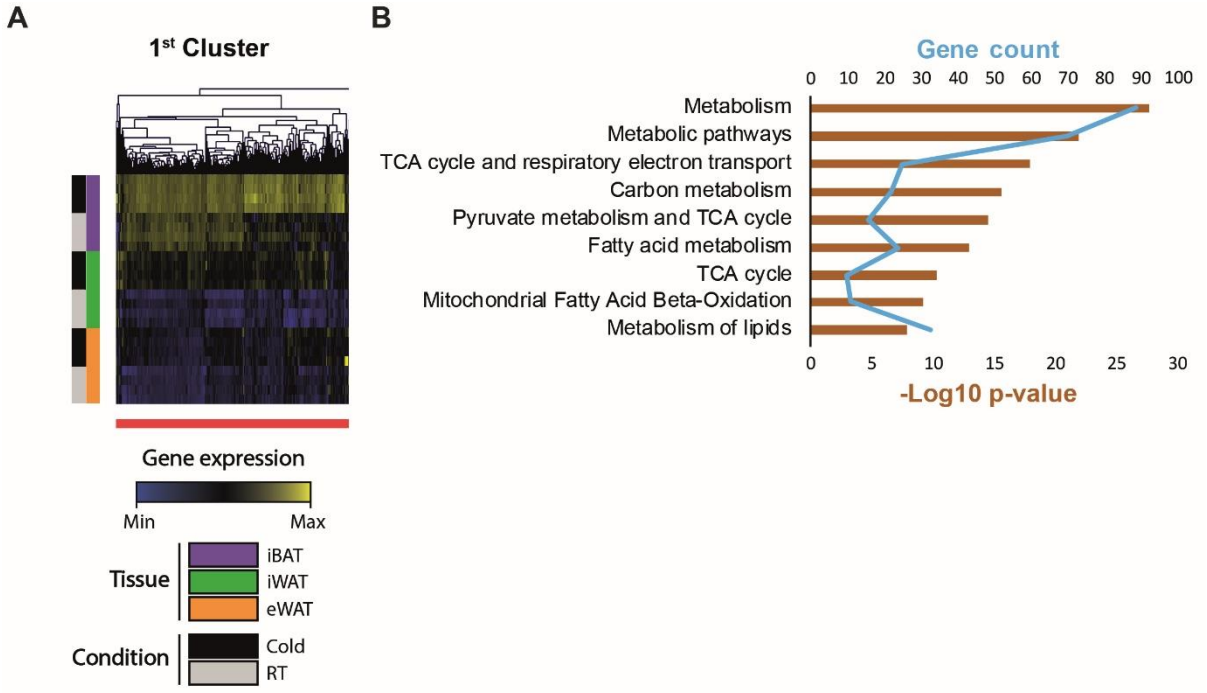


***Figure 59. Enriched pathways of the genes located in the 1st cluster.*** **(A)** Heatmap of the genes grouped in the first cluster. Fold change values are presented using a color scale. Blue indicates low negative fold change values, black indicates neutral fold change and yellow indicates high fold change values. **(B)** Enriched pathways in the genes of the first cluster. -$Log_{10}$ of the p-value is indicated using the bar chart and the gene number of each pathway enrichment is shown by the line chart. -$Log_{10}$ of 0.05 p-value is indicated by the dashed line.

The gene ontology analysis also highlighted the enrichment of metabolic genes, as "nucleotide metabolism", "coenzyme metabolism", "cofactor metabolism", the "generation of precursors metabolites and energy" or the "carbohydrate derivate metabolism" presented enriched genes (Figure 60).

The expression pattern observed in this cluster was similar to the expression profile presented by the thermogenic genes that were detected in the metabolic pathway analysis (Table 24). Specifically, genes involved in thermogenesis, genes specific of brown/beige adipocytes or genes related to mitochondria such as *Cpt1b*, *Cidea*, *Cox5a*, *Cox7a1*, *Cox8b*, *Cyc1*, *Dio2*, *Kcnk3*, *Otop1*, *Pdk4*, *Ppara*, *Ppargc1a*, *Shmt1*, *Slc25a20*, or *Ucp1* (Cheng et al., 2018; Li et al., 2016; Rajakumari et al., 2013; Shinoda et al., 2015) were grouped in this cluster.

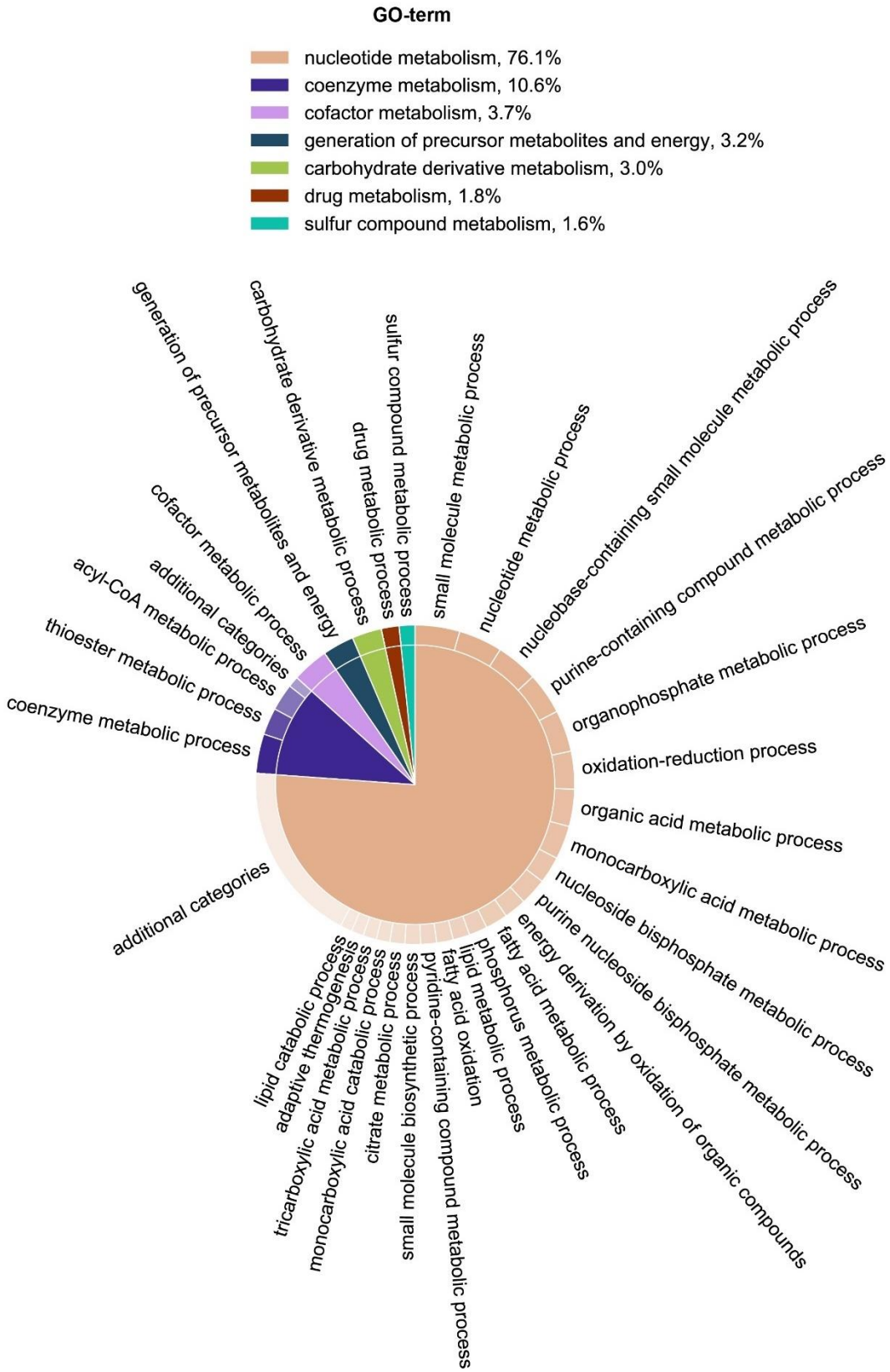


***Figure 60. Circular map summarizing Gene Ontology (GO) biological process of both upregulated and downregulated differentially expressed genes of the 1st Cluster.*** As the arch length of each slice is proportional to the p-value of the GO-term enrichment, the outside slices determine the importance of each GO which respects to the central big slice, which represents the upper-hierarchy GO-term which encompasses all the upregulated minor GO-term showed in the outside part of the graph.

### *1.1.2. Second Cluster*

The second cluster encompassed the genes that did not show differences in gene expression in eWAT of mice exposed to cold and RT but presented upregulation in iWAT and iBAT of mice exposed to cold (Figure 61A). The pathway enrichment analysis of the genes from the 2nd cluster (Figure 61A) did not present any significant result, and the gene ontology analysis of the same genes showed only 4 different enriched ontologies, which included under the upper-hierarchical GO-term "negative regulation of secretion by cell" the terms "ion transport", "transport" and "negative regulation of secretion by cell" (Figure 61B).

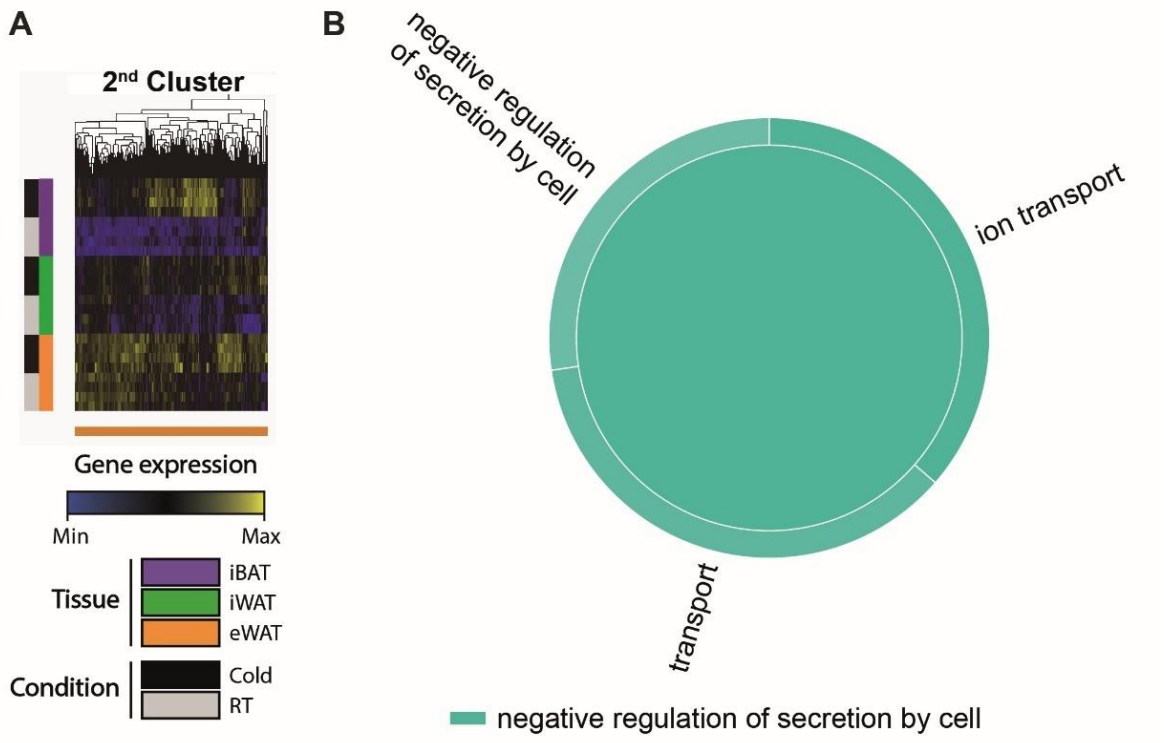


***Figure 61. Heatmap of differentially expressed genes of the 2nd Cluster and circular map summarizing its enriched biological process GO-terms.*** **(A)** Heatmap of the genes grouped in the second cluster. Fold change values are presented using a color scale. Blue indicates low negative fold change values, black indicates neutral fold change and yellow indicates high fold change values. **(B)** Circular map summarizing Gene Ontology (GO) biological process of both upregulated and downregulated differentially expressed genes of the 2nd Cluster. As the arch length of each slice is proportional to the p-value of the GO-term enrichment, the outside slices determine the importance of each GO which respects to the central big slice, which represents the upper-hierarchy GO-term which encompasses all the upregulated minor GO-term showed in the outside part of the graph.

### *1.1.3. Third Cluster*

The expression pattern of the third cluster presented genes with low expression levels in iBAT of mice exposed to cold or RT, but slightly downregulated expression in eWAT and iWAT of cold-exposed animals (Figure 62A). The functional analysis of the genes from the 3rd cluster presented several pathways enriched but none of them was a metabolic pathway (Figure 62B). However, several pathways related to G-protein signaling were enriched (Figure 62B). In addition, matrix-related pathways as "collagen chain trimerization", "extracellular matrix organization" or "assembly of collagen fibrils and other multimeric structures" were significantly enriched pathways (Figure 62B), suggesting that cold exposure triggered activation of genes related to cell and matrix remodeling in eWAT and iWAT.

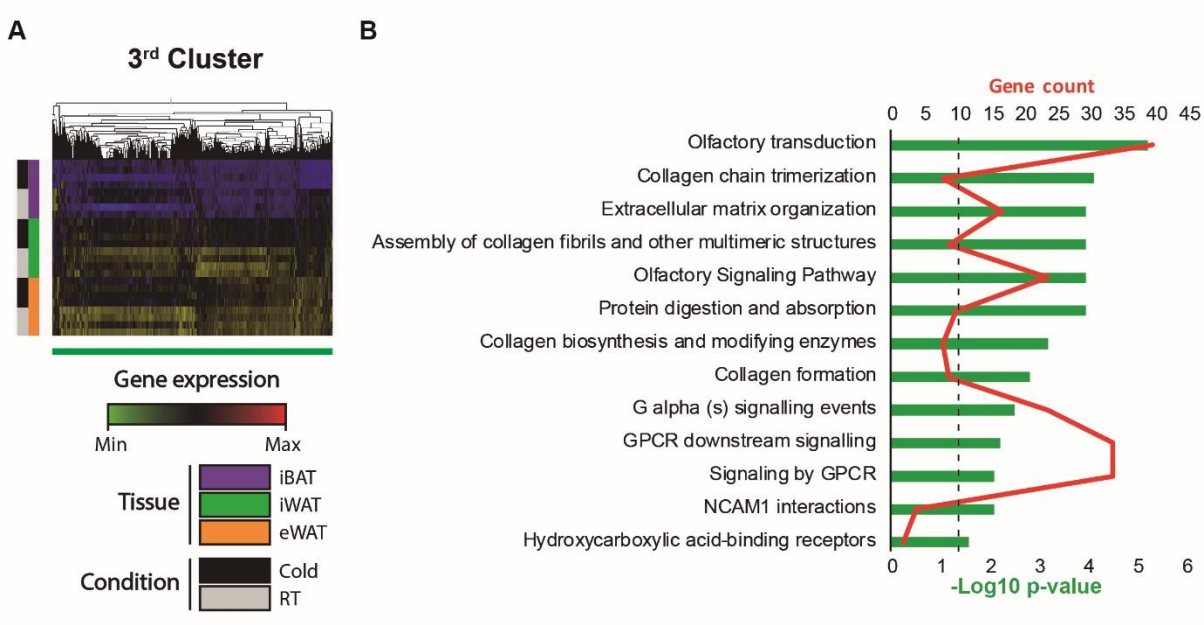


***Figure 62. Enriched pathways of the genes comprised in the 3rd cluster.*** **(A)** Heatmap of the genes grouped in the third cluster. Fold change values are presented using a color scale. Blue indicates low negative fold change values, black indicates neutral fold change and yellow indicates high fold change values. **(B)** Enriched pathways in the genes of the third cluster. $-Log_{10}$ of the p-value is indicated using the bar chart and the gene number of each pathway enrichment is shown by the line chart. $-Log_{10}$ of 0.05 p-value is indicated by the dashed line.

Gene ontology analysis detected "Cellular response to interferon-beta" and related ontologies highly enriched among the genes comprising the 3rd cluster (Figure 63). Additionally, "sensory perception of smell" was clearly enriched and "response to stimulus", "signalling" or "cell communication" also appeared among the significantly enriched biological processes (Figure 63).

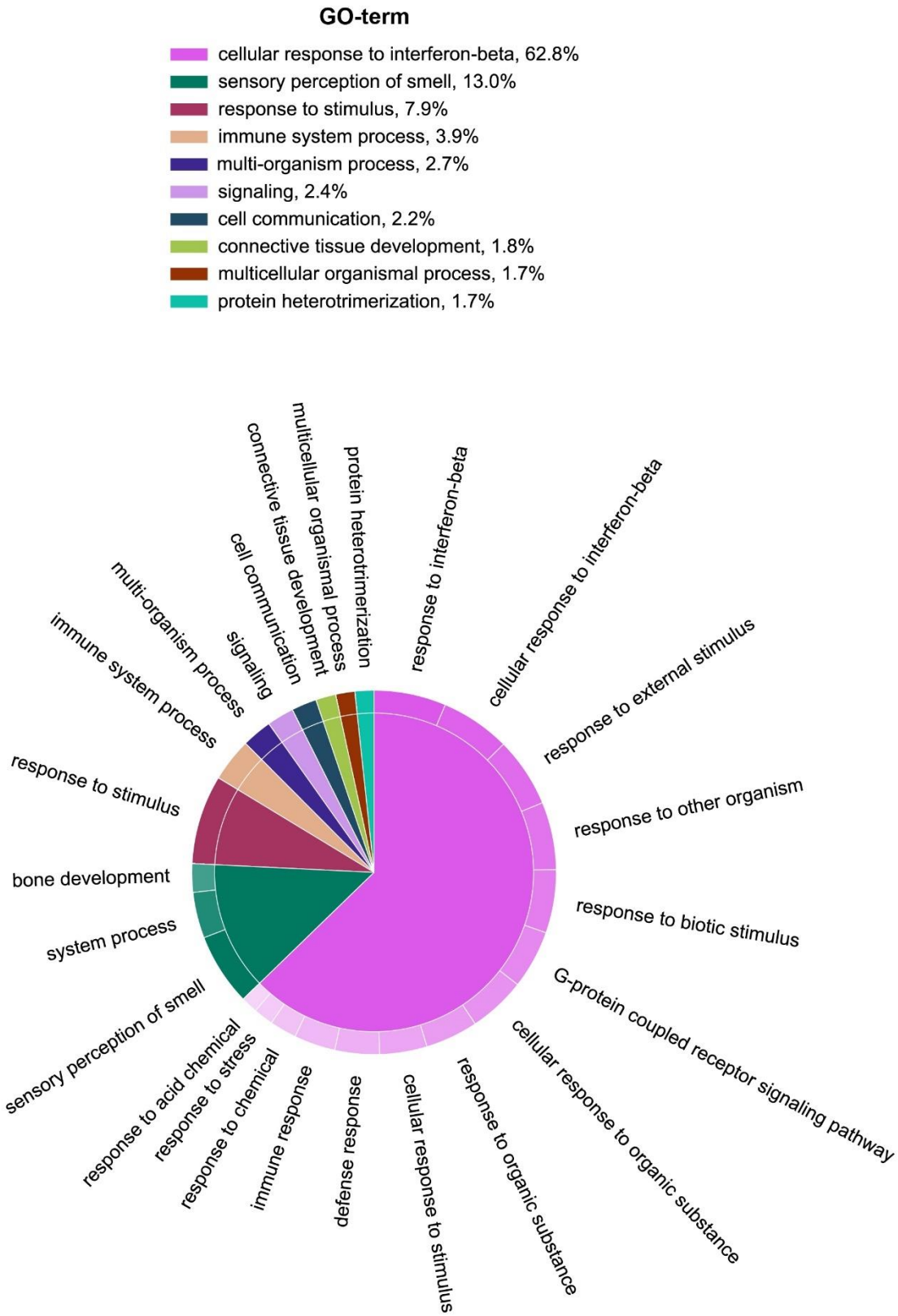


***Figure 63. Circular map summarizing Gene Ontology (GO) biological process of both upregulated and downregulated differential expressed genes of the 3rd Cluster.*** As the arch length of each slice is proportional to the p-value of the GO-term enrichment, the outside slices determine the importance of each GO which respects to the central big slice, which represents the upper-hierarchy GO-term which encompasses all the upregulated minor GO-term showed in the outside part of the graph.

### *1.1.4. Fourth Cluster*

The fourth cluster presented genes with low expression in iBAT and downregulated in iWAT and eWAT of cold-exposed (Figure 64A). The genes that grouped together in the 4th cluster presented "olfactory transduction" and "olfactory signalling pathway" as most enriched pathways (Figure 64B). Moreover, G protein related pathways such as "G alpha (s) signalling events", "GPCR downstream signalling" or "signalling by GPCR" were clearly enriched (Figure 64B).

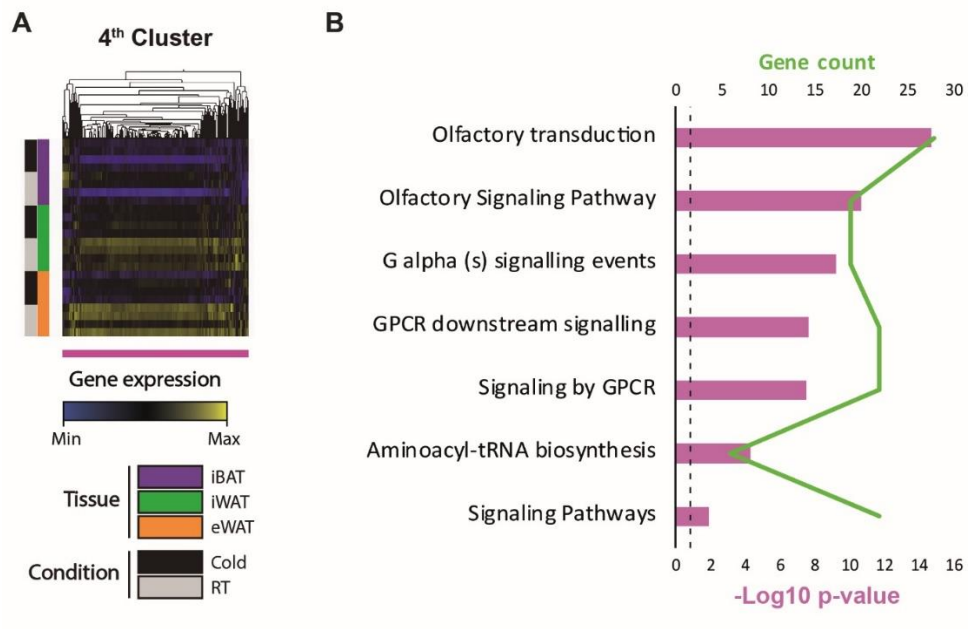


***Figure 64. Most significantly enriched pathways of the genes located in the 4th cluster.*** **(A)** Heatmap of the genes grouped in the fourth cluster. Fold change values are presented using a color scale. Blue indicates low negative fold change values, black indicates neutral fold change and yellow indicates high fold change values. **(B)** Enriched pathways in the genes of the fourth cluster. -$Log_{10}$ of the p-value is indicated using the bar chart and the gene number of each pathway enrichment is shown by the line chart. -$Log_{10}$ of 0.05 p-value is indicated by the dashed line.

The gene ontology analysis of the 4th cluster revealed the biological processes "sensory perception of smell", "G-protein coupled receptor signalling pathway", "signalling", "cell communication" and "multicellular organismal process" as significantly enriched ontologies (Figure 65).

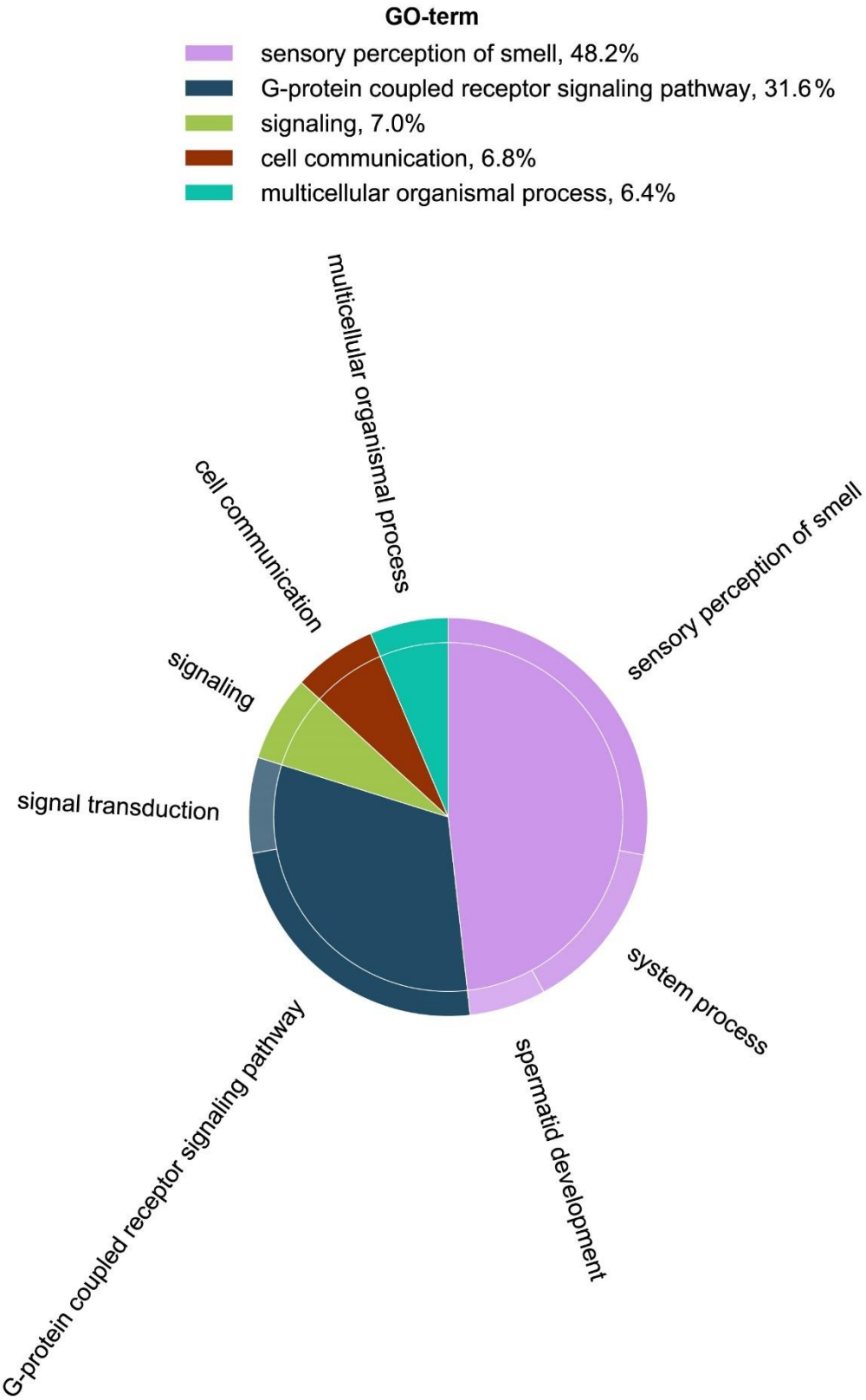


***Figure 65. Circular map summarizing Gene Ontology (GO) biological process of both upregulated and downregulated differential expressed genes of the 4th Cluster.*** As the arc length of each slice is proportional to the p-value of the GO-term enrichment, the outside slices determine the importance of each GO which respects to the central big slice, which represents the upper-hierarchy GO-term which encompasses all the upregulated minor GO-term showed in the outside part of the graph.

### *1.1.1. Fifth Cluster*

The fifth cluster did not present any pathway enrichment nor gene ontology among the 15 genes that composed the cluster (Figure 66).


***Figure 66. 5th cluster.*** **(A)** Heatmap of the genes grouped in the fifth cluster. Fold change values are presented using a color scale. Blue indicates low negative fold change values, black indicates neutral fold change and yellow indicates high fold change values.

Altogether, the results from the functional analysis of the different clusters evidenced that metabolic genes were predominantly located in the first cluster and presented a similar expression pattern (Figures 59, 60). Moreover, this cluster presented several important thermogenic genes, as well as genes related to brown/beige adipocytes and genes involved in the mitochondria.

## 1.2. Unravelling of new genes potentially involved in non-shivering thermogenesis

To unravel co-expressed genes of the first cluster potentially involved in non-shivering thermogenesis, a *pattern matching analysis* was performed. The p*attern matching analysis* consists of an algorithm that, given a template expression profile of a gene, matches the profiles of the genes of the data set using a Pearson correlation. Specifically, the pattern matching tool used was the *Pavlidis Template Matching* (PTM) (Pavlidis and Noble, 2001). As the strength of the linear relationship between the template and the profile of each gene its gene were statistical quantified using Pearson's correlation coefficient, a significant threshold value can be used to select genes.

With the aim of selecting genes with similar expression pattern, a threshold value of 0.05 was chosen for the genes involved in thermogenesis, mitochondria or related to brown/beige fat located in the first cluster (*Cpt1b*, *Cidea*, *Cox5a*, *Cox7a1*, *Cox8b*, *Cyc1*, *Dio2*, *Kcnk3*, *Otop1*, *Pdk4*, *Ppara*, *Ppargc1a*, *Shmt1*, *Slc25a20*, or *Ucp1*). Among the genes with similar profiles, *Atp4b* and *1700040L02Rik* presented high correlation with the profile of all the template genes (Figure 67).

As the gene expression was normalized to detect the different expression patterns, not all the genes of the first cluster presented statistical differences between animals exposed to cold or RT in the different depots. However, both *Atp4b* and *1700040L02Rik* showed a high significant upregulation in iBAT of cold-exposed mice (Figure 67), presenting *Atp4b* and *1700040L02Rik* a fold change increase of about 2.28 and 2.46, respectively (Table 36). In iWAT of animals exposed to cold, these genes were also upregulated (Figure 67), presenting *Atp4b* and *1700040L02Rik* genes an expression increase of 1.78- and 2.49-fold, respectively (Table 36). In contrast, the expression of *Atp4b* and *1700040L02Rik* did not differ between eWAT samples of mice exposed to either cold or RT (Figure 67). As this depot has been described as more resistant to browning than iWAT and to not induce non-shivering thermogenesis upon cold exposure, the fact that *Atp4b* and *1700040L02Rik* were not significantly upregulated further emphasised the potential thermogenic role of these genes (Chan et al., 2019; Ferrannini et al., 2016).

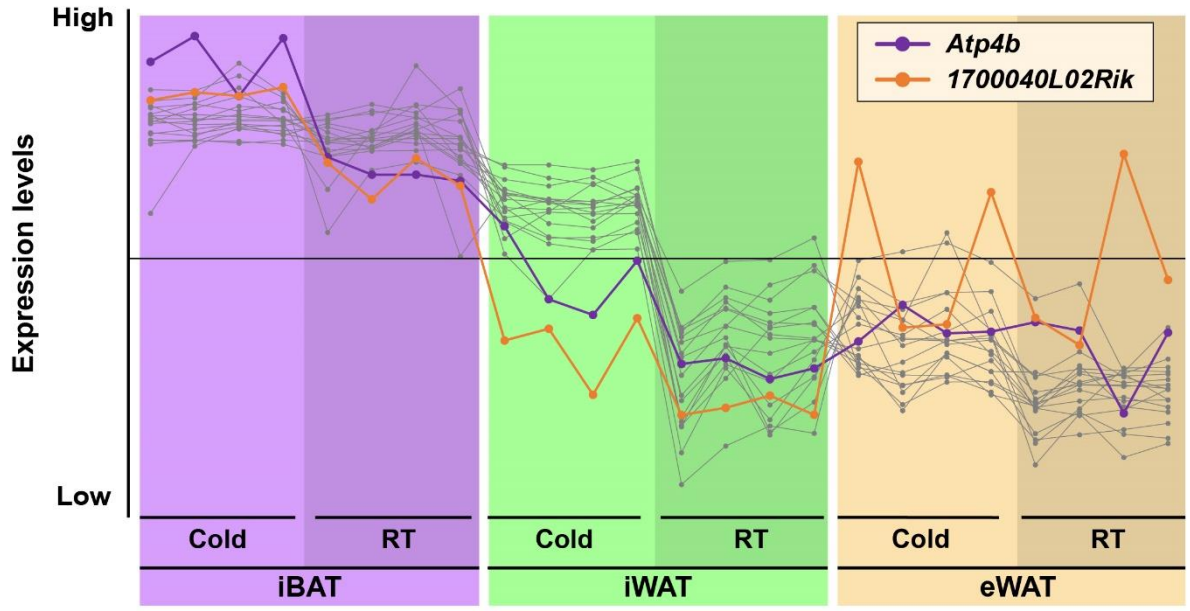


***Figure 67. Pattern matching analysis for the identification of novel genes potentially involved in non-shivering thermogenesis.*** A pattern matching analysis using the expression of *Cpt1b*, *Cidea*, *Cox5a*, *Cox7a1*, *Cox8b*, *Cyc1*, *Dio2*, *Kcnk3*, *Otop1*, *Pdk4*, *Ppara*, *Ppargc1a*, *Shmt1*, *Slc25a20*, and *Ucp1* as a template (grey line) identified co-expressed genes, among which the expression of *Atp4b* (purple line) and *1700040L02Rik* (orange line) were highly correlated.

| | | iBAT | | iWAT | | eWAT | |
|---|---|---|---|---|---|---|---|
| Transcript ID | Gene Symbol | Fold Change | p-value | Fold Change | p-value | Fold Change | p-value |
| 17507595 | Atp4b | **2.28** | **0.000258** | **1.78** | **0.004021** | -1.04 | 0.376462 |
| 17241676 | 1700040L02Rik | **2.46** | **0.00018** | **2.49** | **0.011902** | **1.88** | 0.720511 |

***Table 36. Gene expression fold-change differences of the selected genes in the different depots of mice exposed to cold.*** The genes *Atp4b* and *17000040L02Rik* presented upregulated expression in iBAT and iWAT, but not in eWAT. Highlighted in **Bold**: statistically significant p-values; Highlighted in **Red**: upregulated expression in cold exposure of 1.5-fold or higher.

Furthermore, an extensive and detailed bibliographic revision of the literature highlighted that there was no study describing a thermogenic role of *Atp4b* or *1700040L02R* in adipose tissue.

To gain insight into possible functions of genes, the usage of protein-protein interaction networks has become a very valuable technique in the last decade due to the huge amounts of protein-protein interaction data obtained by high-throughput technologies (Sun et al., 2018). To this end, a protein-protein interaction network was generated for ATP4B (Figure 68A). With the genes involved in this interactome of ATP4B, a functional analysis was performed (Figure 68B). The results obtained in this analysis revealed

enriched ATPase functions such as “potassium-transporting ATPase activity” or “cation-transporting ATPase activity” (Figure 68B). Using the same approach, another protein-protein interaction network was generated for 1700040L02Rik (Figure 68C). No enriched functions were detected in the protein-protein interaction network of 1700040L02Rik. In neither the interactome of ATP4B nor 1700040L02Rik connections with genes related to thermogenesis, brown/beige fat or mitochondrial biogenesis was detected (Figure 68A, C). No functions related to thermogenesis or metabolism were neither observed (Figure 8B).

Altogether, the transcriptomic analysis of eWAT, iWAT and iBAT samples of mice exposed either to cold or to RT unravel novel genes with a putative role in cold adaptation.

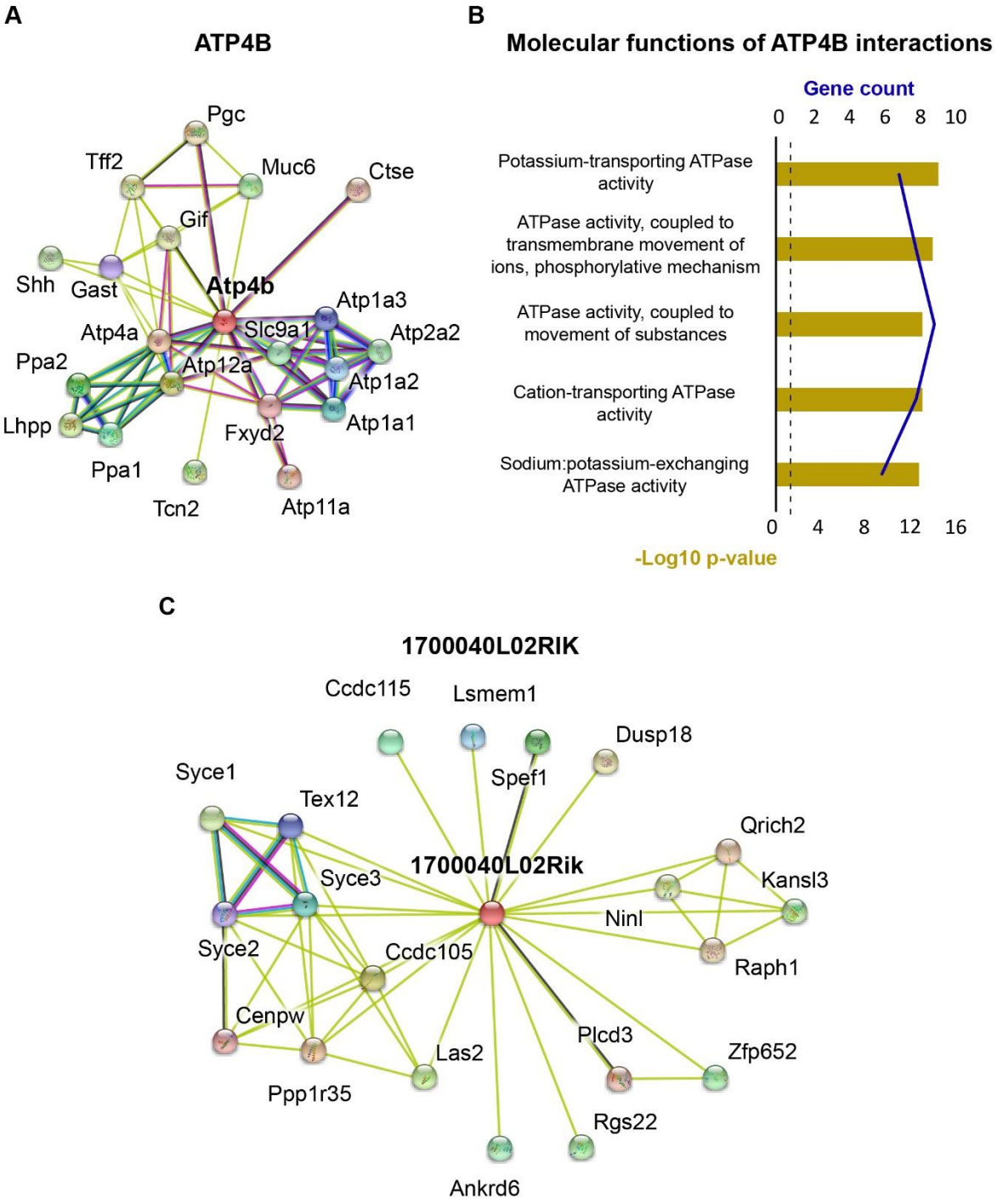


***Figure 68. Protein-protein interaction network for ATP4B and 1700040L02RIK and molecular functions enrichment analysis of ATP4B interactions.*** The interactions of **(A)** ATP4B and **(C)** 1700040L02RIK with other proteins were plotted using different supporting evidence: Cyan connection depicts known interactions from curated databases; Pink connection depicts known interactions experimentally determined; Green connection depicts predicted interaction by gene neighborhood; Red connection depicts predicted interaction by gene fusions; Blue connection depicts predicted interaction by co-occurrence; Yellow connection depicts potential interactions detected by text mining; Black connection depicts potential interactions detected by co-expression; light blue connection depicts potential interactions detected by protein homology. **(B)** Enriched molecular functions of genes interacting with ATP4B. $-Log_{10}$ of the p-value is indicated using the bar chart and the gene number of each enriched molecular function is shown by the line chart. $-Log_{10}$ of 0.05 p-value is indicated by the dashed line.

# Section IV. Study of the role of the overexpression of *Atp4b* and *1700040L02Rik* genes in adipose tissue

## 1. DESIGN AND GENERATION OF AAV VECTORS ENCODING THE GENES *Atp4b* AND *1700040L02Rik*

To examine the role of the overexpression of the genes *Atp4b* and *1700040L02Rik* in adipose tissue, a strategy using adeno-associated viral vectors (AAV) vectors was used. As both *Atp4b* and *1700040L02Rik* were highly expressed after cold exposure, the goal of our AAV strategy was to obtain a high expression of these genes in the adipose depots after transduction. It has been described that the systemic administration of AAV8 vectors results in highly efficient transduction of the different adipose tissue depots (Jimenez et al., 2013). In order to obtain high expression levels of *Atp4b* and *1700040L02Rik* in the transduced tissues, the codon-optimized (co) form of *Atp4b* and *1700040L02Rik* were expressed under CAG promotor. CAG promoter was synthesized for the first time by Dr. Jun-ichi Miyasaki´s lab by combining the following sequences: the cytomegalovirus (CMV) early enhancer element; the first exon and the first intron of the chicken ß-actin gene that play the role of promoter *per se*; and the splice acceptor of the rabbit ß globin gene. Moreover, to detarget transgene expression in the liver and in heart, 4 copies of the target sequence of the miR-122a and miR-1 (dmiRT) were added at the 3'-UTR of the expression cassette (Figure 69). As control, a null vector was also produced. This vector contained the promoter but not the sequence of the gene (Figure 69).

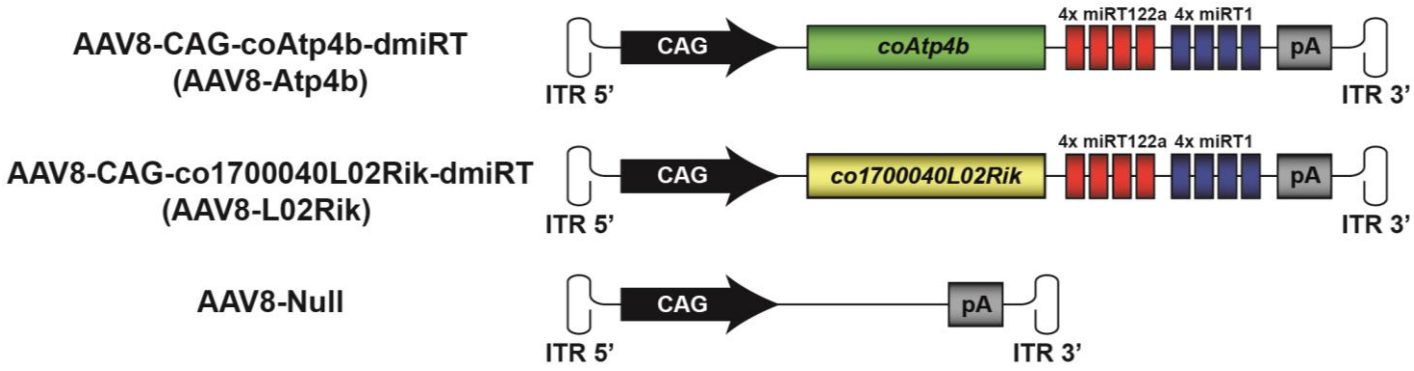


***Figure 69. Schematic representation of AAV constructs.*** AAV constructs designed with the selected genes. Target sequences of miR122a and miR1 were used to detarget transgene expression in the liver and heart. ITR: Inverted Terminal Repeats; CAG: hybrid promoter based on the promoter of β-actin of chicken and enhancer of the cytomegalovirus; 4xmiRT122a: target sequence of microRNA 122a (4 copies); 4xmiRT1: target sequence of microRNA 1 (4 copies); pA: poly A, polyadenylation sequence. Constructs are not represented on a scale.

## 2. EFFECTS OF THE SYSTEMIC ADMINISTRATION OF AAV8-CAG-co*Atp4b*-dmiRT AND AAV8-CAG-co*1700040L02Rik*-dmiRTs ON BODY WEIGHT, FOOD INTAKE, AND GLYCEMIA OF MICE

To study the role of the overexpression of genes *Atp4b* and *1700040L02Rik* in iWAT, eWAT, and iBAT, AAV8-CAG-co*Atp4b*-dmiRT (AAV8-Atp4b) and AAV8-CAG-co*1700040L02Rik*-dmiRT (AAV8-L02Rik) were administered systemically. To this end, 1,25x$10^{12}$ viral genomes (vg) of AAV8-Atp4b and 1,25x$10^{12}$ vg of AAV8-L02Rik were administered intravenously (i.v.) to 8-week-old male chow-fed C57Bl/6 mice. As control, another cohort of mice received 2,5x$10^{12}$ vg of AAV8-CAG-null vectors (Figure 70). In addition, since *Atp4b* and *1700040L02Rik* were selected by using as template the expression of genes that increase energy expenditure such the thermogenic genes *Cidea* or *Ucp1*, to study the possible antiobesogenic and anti-diabetic effects of these genes, a cohort of animals was also fed a high-fat diet (HFD), as it generates a well-characterized model of obesity (Surwit et al., 1998; Winzell and Ahrén, 2004) and was treated with AAV8-CAG-co*Atp4b*-dmiRT and AAV8-CAG-co*1700040L02Rik*-dmiRT (Figure 70).

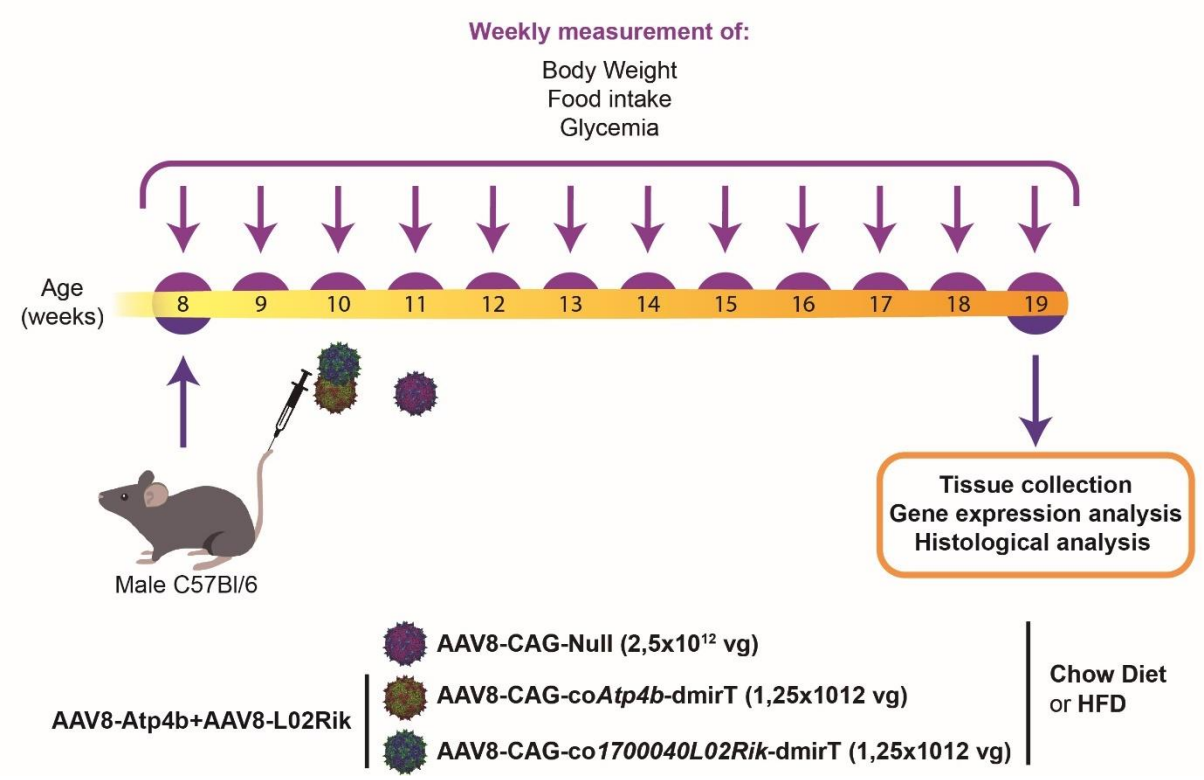


***Figure 70. Experimental design for the study of the role of the overexpression of the genes Atp4b and 1700040L02Rik in iWAT, eWAT, and iBAT.*** 8-week-old male C57Bl/6 mice fed either a HFD or chow diet were

administered i.v. with $1.25x10^{12}$ vg/mouse of AAV8-CAG-*Atp4b*-dmirT and $1.25x10^{12}$ vg/mouse of AAV8-CAG-*1700040L02Rik*-dmirT. Body weight, food intake, and glycemia were measured weekly. The control group of mice received $2.5x10^{12}$ vg of AAV8-CAG-Null vectors. HFD: high-fat diet; n=10-11 per group.

Following AAV-delivery, HFD-fed AAV8-Null-administered mice increased its body weight progressively and became obese by the end of the follow-up of approximately 80 days (Figure 71A, B). When challenged with HFD, animals administered with AAV8-Atp4b and AAV8-L02Rik presented a lower body weight gain compared to AAV8-null-injected HFD-fed mice (Figure 71A, B). This body weight gain difference between AAV8-Atp4b+AAV8-L02Rik-treated mice and AAV8-Null-administered mice was of 9.5% at the end of the experiment. Nevertheless, this difference was observed from the beginning of the experiment, being higher than 16% already at weeks 13 and 14 post-AAV administration (Figure 71B). No differences in neither body weight nor body weight gain were observed between chow-fed AAV8-Null-treated mice and chow-fed AAV8-Atp4b+AAV8-L02Rik-administered animals (Figure 71A, B). Control chow-fed mice presented an increase of 37% in their body weight at the end of the experiment, while the increase in the body weight of AAV8-Atp4b+AAV8-L02Rik-administered chow-fed mice was of about 32% (Figure 71B).

Food intake was analyzed to evaluate whether the reduction of body weight gain presented by the AAV8-Atp4b+AAV8-L02Rik-treated HFD-fed mice resulted in changes in the energy intake. No differences in food intake between animals administered with AAV8-Null or with AAV8-Atp4b+AAV8-L02Rik were found for neither chow nor HFD-fed mice (Figure 71C). Hence, as the energy intake was similar between groups, differences in body weight gain in HFD-fed mice were potentially produced by Atp4b- and 1700040L02Rik-mediated effects.

Glycemia of the animals administered with AAV8-Null or AAV8-Atp4b+AAV8-L02Rik fed a HFD was higher than that of chow-fed mice (Figure 71D). No differences in glycemia were observed between animals administered with AAV8-Null or AAV8-Atp4b+AAV8-L02Rik fed the same diet.

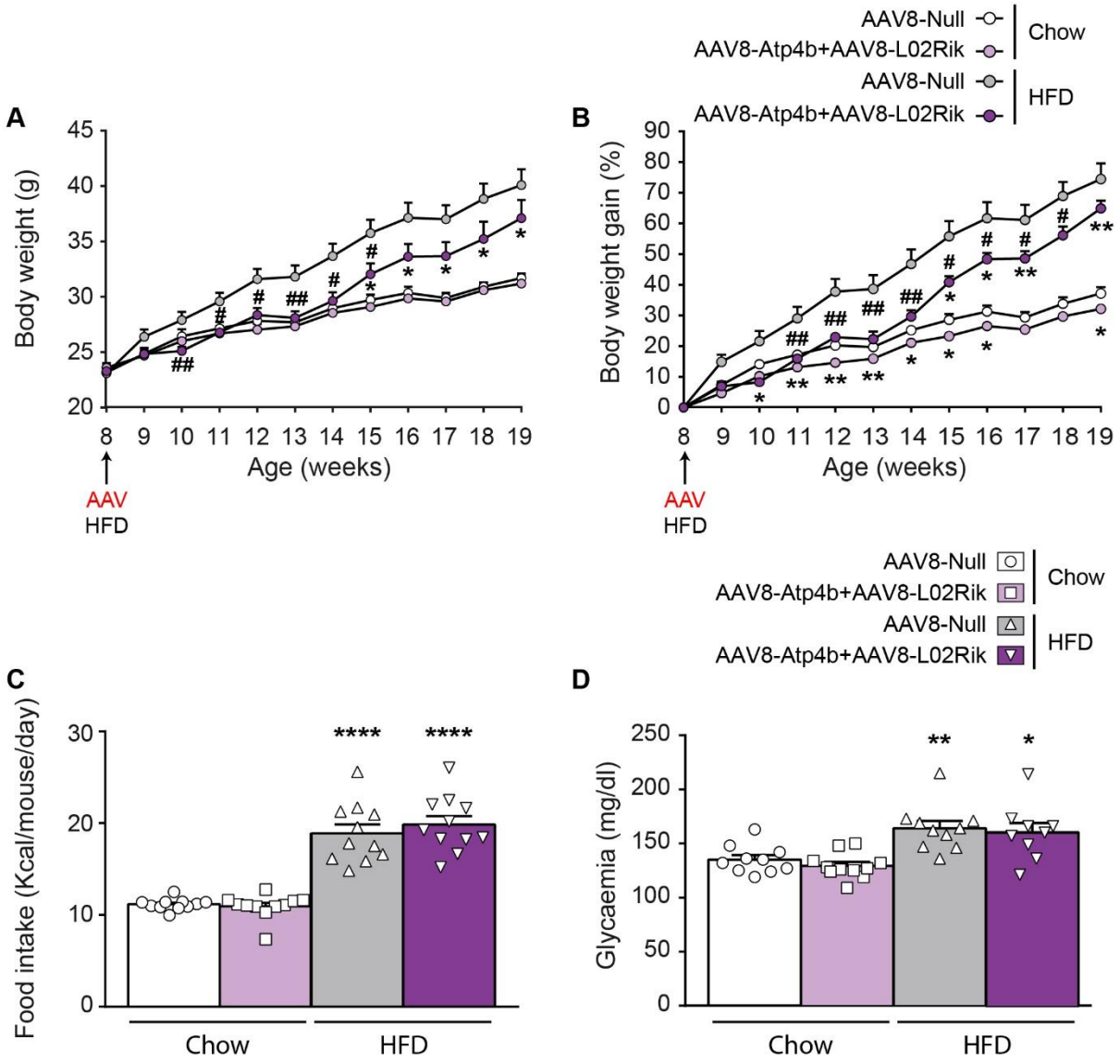


***Figure 71. Evaluation of body weight, food intake and glycemia of mice administered with AAV8-CAG-Atp4b-dmiRT and AAV8-CAG-1700040L02Rik-dmiRT vectors.*** Male C57Bl/6 mice were treated systemically with AAV8-Atp4b+AAV8-L02Rik or AAV8-CAG-Null vectors at 8 weeks of age and fed either chow or HFD diet. **(A)** Body weight evaluation and **(B)** evolution of the gain of body weight in percentage with regard to the initial value. **(C)** Glycemia 10-weeks-post AAV administration. **(D)** Daily food intake for the different experimental groups per animal. AAV: administration of AAV vectors; HFD, high-fat diet; g: grams. n = 9-11 mice per group. *P <0.05, **P <0.01, and ****P <0.0001 versus chow-fed AAV8-Null-injected group. #P <0.05 and ##P <0.01 versus HFD-fed AAV8-Null-injected group.

## 3. EFFECTS OF THE SYSTEMIC ADMINISTRATION OF AAV8-CAG-co*Atp4b*-dmiRT AND AAV8-CAG-co*1700040L02Rik*-dmiRTs ON ADIPOSE DEPOTS AND LIVER WEIGHTS

At the end of the experiment, adipose depots (eWAT, iWAT, and iBAT) together with the liver and skeletal muscle (gastrocnemius) were dissected and weighted. Animals fed a chow diet presented similar eWAT weight irrespective of the AAV treatment (Figure 72A, B). However, HFD-fed animals treated with AAV8-Null presented higher eWAT weight than HFD-fed AAV8-Atp4b+AAV8-L02Rik administered mice (Figure 72A). These differences in eWAT weight between mice fed a HFD treated AAV8-Atp4b+AAV8-L02Rik or AAV8-Null were increased upon animal weight normalization (Figure 72B). Similarly, the iWAT depot of chow-fed animals treated either with AAV8-Null or with AAV8-Atp4b+AAV8-L02Rik showed similar weight. iWAT weight of HFD-fed mice treated with AAV8-Atp4b+AAV8-L02Rik presented a tendency to be decreased in comparison with HFD-fed AAV8-Null-treated mice (Figure 72). Likewise, the weight of the iBAT depot was decreased in the animals fed a chow diet and administered with AAV8-Atp4b+AAV8-L02Rik in comparison with chow-fed mice treated with AAV8-Null (Figure 72).

A tendency of presenting lower iBAT weight was observed in the animals fed a HFD and administered with AAV8-Atp4b+AAV8-L02Rik when compared with AAV8-Null-administered mice (Figure 72A). This tendency was maintained after normalizing tissue weight by the weight of mice (Figure 72B). The weight of the liver of AAV8-Atp4b+AAV8-L02Rik-treated mice presented a reduction in comparison with control mice in both animals fed chow or HFD (Figure 72A). In animals fed a chow diet, the liver weight reduction was of 8%, but in the HFD-fed mice this difference was of about 24% (Figure 72A). The weight differences between chow-fed animals administered with AAV8-Atp4b+AAV8-L02Rik or AAV8-Null were increased upon normalizing tissue weight by the animal weight (Figure 72B). No difference in the weight of the gastrocnemius skeletal muscle was observed (Figure 72).

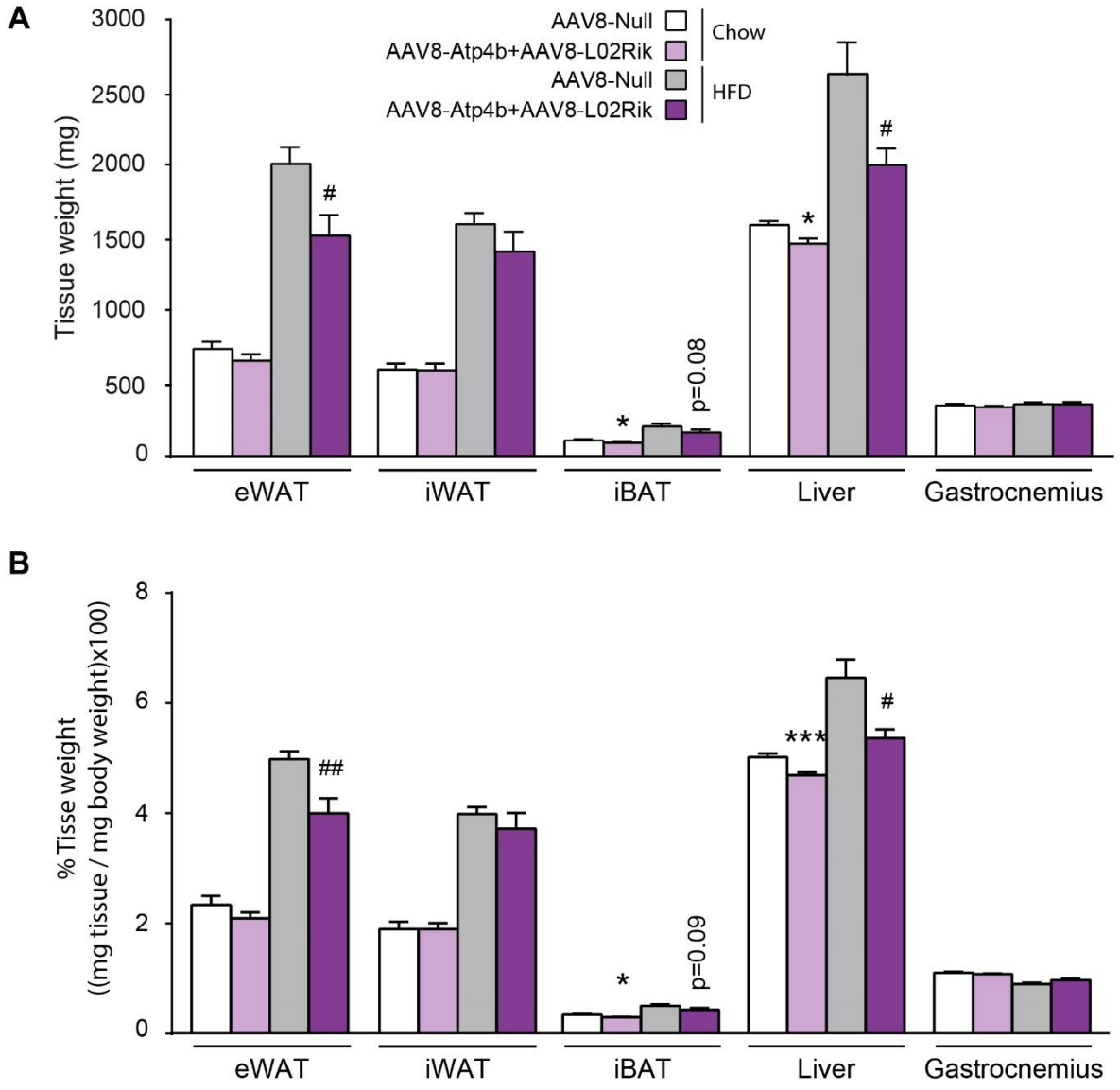


***Figure 72. Weight of adipose depots, liver, and gastrocnemius muscle.*** Male C57Bl/6 mice were treated systemically with AAV8-Atp4b+AAV8-L02Rik or AAV8-CAG-Null vectors at 8 weeks of age and fed either chow or HFD diet. At sacrifice, different **(A)** adipose tissue depots, the liver, and gastrocnemius skeletal muscle were weighted. **(B)** Tissue weight was also normalized by animal weight. mg: milligram. Results are expressed as mean ± SEM. n = 10-11 per group. *P <0.05, ***P<0.001 versus chow-fed AAV8-Null-injected group. #P <0.05, ##P<0.001 versus HFD-fed AAV8-Null-injected group. eWAT: epididymal white adipose tissue; iWAT: inguinal white adipose tissue; iBAT: interscapular brown adipose tissue.

## 4. co*Atp4b* AND co*1700040L02Rik* GENE EXPRESSION IN ANIMALS ADMINISTERED WITH AAV8-CAG-co*Atp4b*-dmiRT AND AAV8-CAG-co*1700040L02Rik*-dmiRT

Gene expression levels of codon-optimized coding sequences of *Atp4b (coAtp4b)* and *1700040L02Rik (co1700040L02Rik)* in WAT and BAT were analyzed by RT-qPCR (Figure 73). Results indicated that *coAtp4b* was highly overexpressed in eWAT, iWAT and iBAT

of mice administered with AAV8-Atp4b+AAV8-L02Rik (Figure 73A). Likewise, the expression of *co1700040L02Rik* was detected in eWAT, iWAT and iBAT of animals administered with AAV8-Atp4b+AAV8-L02Rik (Figure 73B).

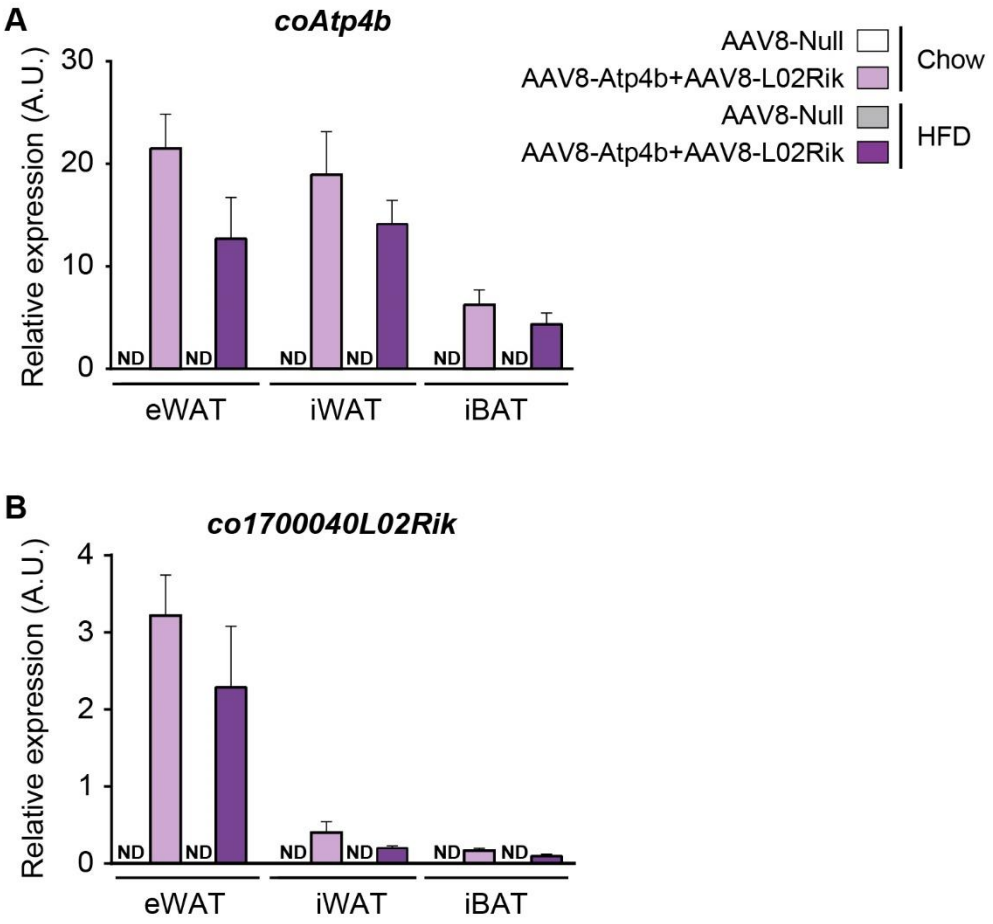


***Figure 73. Expression levels of Atp4b and 1700040L02Rik in the main adipose tissue depots.*** Male C57Bl/6 mice were treated systemically with AAV8-Atp4b+AAV8-L02Rik or AAV8-CAG-Null vectors at 8 weeks of age and fed either chow or HFD diet. Expression levels of codon optimized murine **(A)** Atp4b or **(B)** 1700040L02Rik in iWAT, eWAT, iBAT and liver 11 weeks post-AAV administration. ND: not detected; AU, arbitrary units. The results are expressed as the mean ± SEM. n = 7 per experimental group.

## 5. HISTOLOGICAL ANALYSIS OF eWAT, iWAT, AND iBAT OF ANIMALS ADMINISTERED WITH AAV8-CAG-co*Atp4b*-dmiRT AND AAV8-CAG-co*1700040L02Rik*-dmiRT

Histological analysis of iWAT, eWAT and iBAT stained with hematoxylin/eosin was performed to evaluate possible morphological changes of these tissues (Figure 74, 75, 76). Results indicated that the high-fat diet led to increased lipid accumulation in all the adipose depots of AAV8-Null administered mice (Figure 74, 75, 76). Furthermore, in white adipose depots of AAV8-Null administered HFD-fed mice, hypertropia of white adipocytes was observed (Figure 74, 75). In contrast, the adipocytes of the eWAT depot presented a reduced size in AAV8-Atp4b+AAV8-L02Rik-treated HFD-fed mice (Figure 74). The white adipocytes of the iWAT depot of mice fed either chow or HFD but treated with AAV8-Atp4b+AAV8-L02Rik also presented an important size reduction (Figure 75). In contrast, the histological analysis of iBAT did not show clear differences between mice administered with AAV8-Atp4b+AAV8-L02Rik or AAV8-Null (Figure 76).

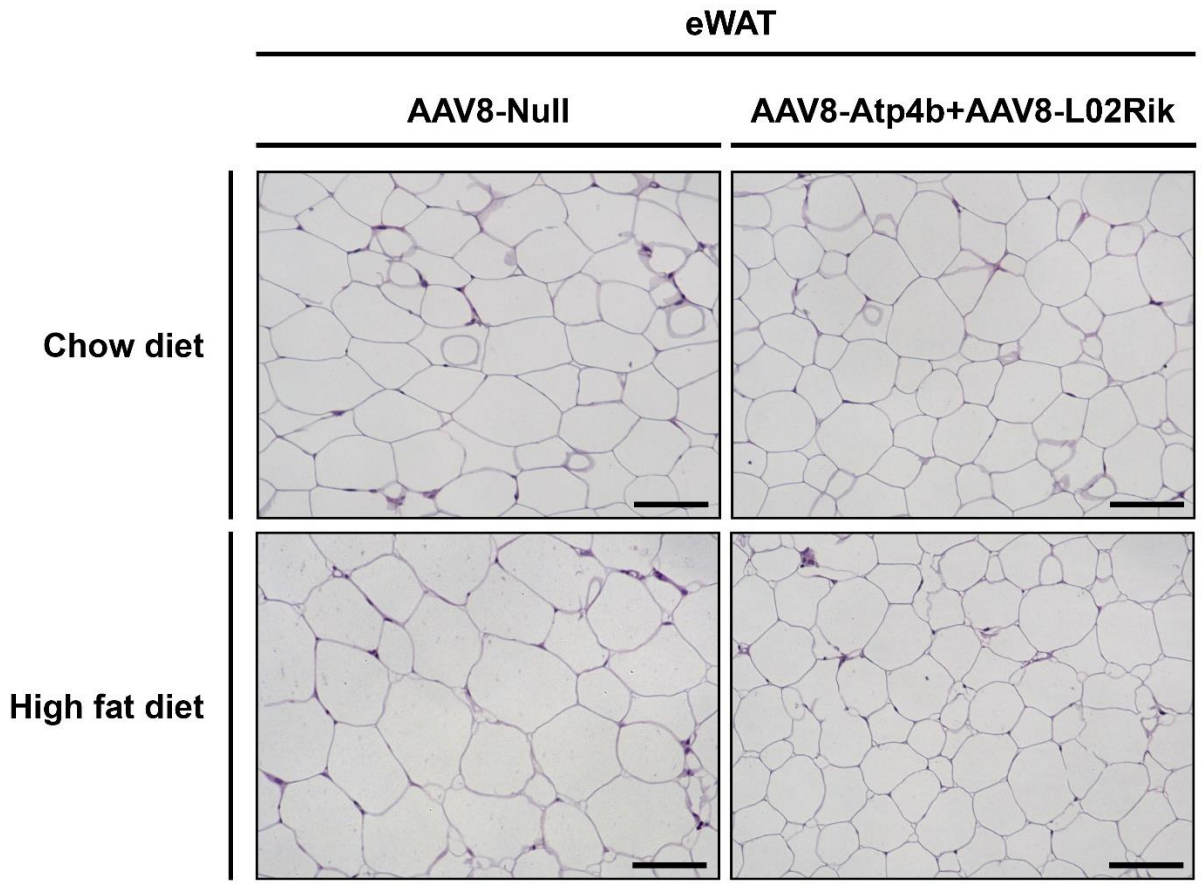


***Figure 74. Histological analysis of eWAT of animals treated with AAV8-Atp4b+AAV8-L02Rik.*** Hematoxylin/eosin staining of representative sections of eWAT of C57BL/6 mice fed either with chow diet or high-fat diet and treated with AAV8-Atp4b+AAV8-L02Rik or AAV8-Null. Scale bars: 100µm.

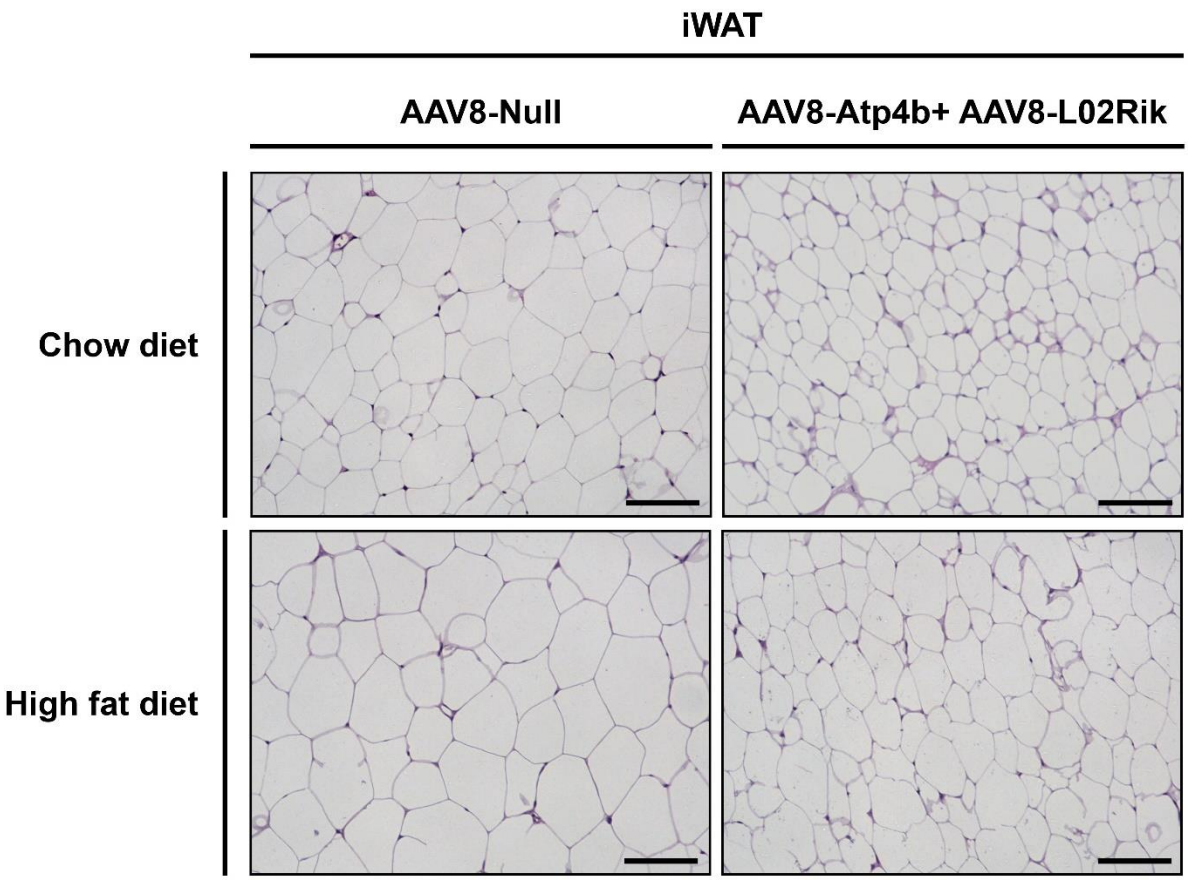


***Figure 75. Histological analysis of iWAT of animals treated with AAV8-Atp4b+AAV8-L02Rik***. Hematoxylin/eosin staining of representative sections of iWAT of C57BL/6 mice fed either with chow diet or high-fat diet and treated with AAV8-Atp4b+AAV8-L02Rik or AAV8-Null. Scale bars: 100µm.

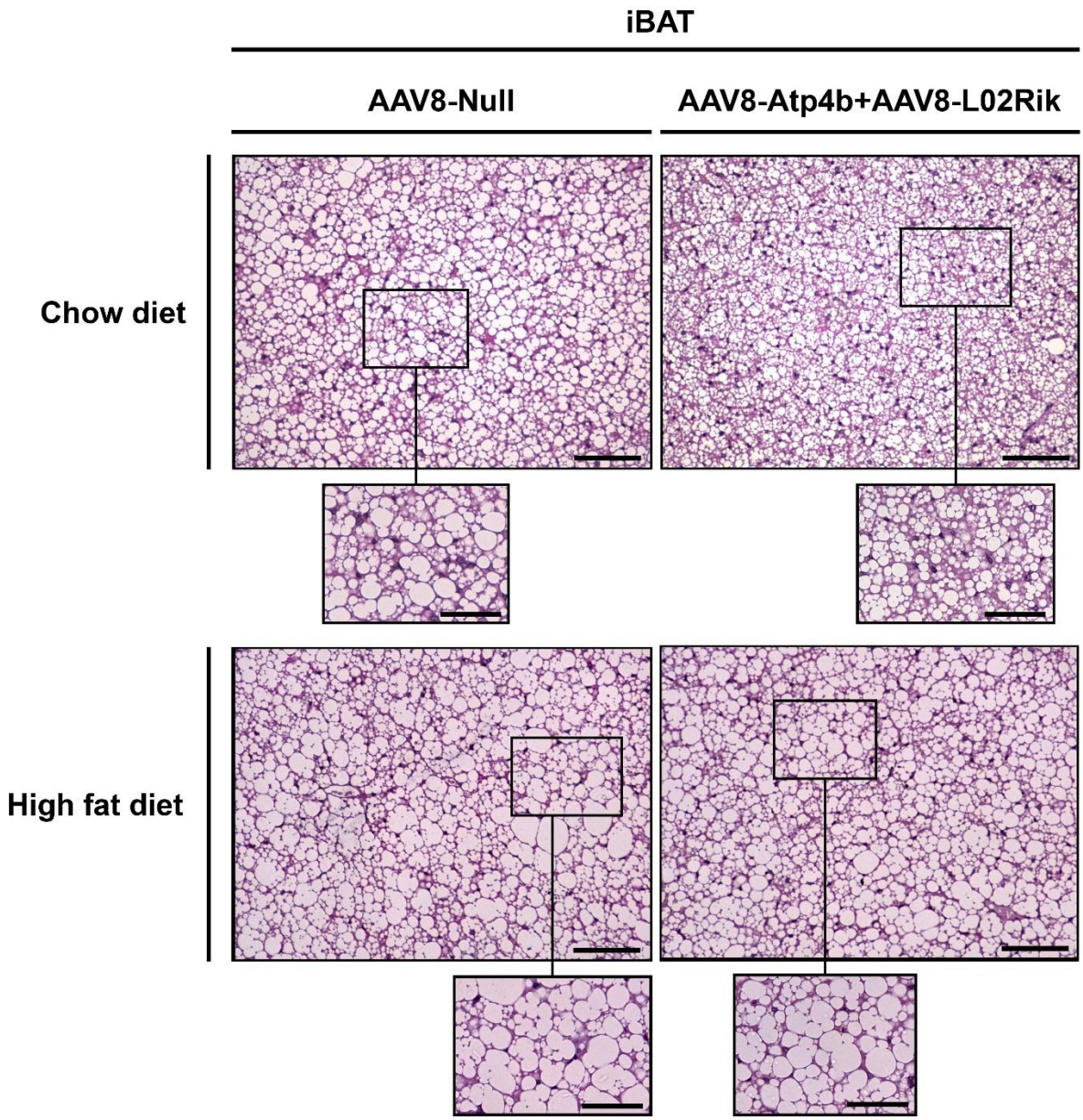


***Figure 76. Histological analysis of iBAT of animals treated with AAV8-Atp4b+AAV8-L02Rik.*** Hematoxylin/eosin staining of representative sections of iBAT of C57BL/6 mice fed either with chow diet or high-fat diet and treated with AAV8-Atp4b+AAV8-L02Rik or AAV8-Null. Scale bars: 100µm and 50µm (inset).

## 6. GENE EXPRESSION ANALYSIS OF THERMOGENIC MARKERS IN ANIMALS ADMINISTERED WITH AAV8-CAG-co*Atp4b*-dmiRT AND AAV8-CAG-co*1700040L02Rik*-dmiRT

The histological analysis of eWAT, iWAT and iBAT indicated the reduction of the lipid content in the eWAT and iWAT depots of the AAV8-Atp4b+AAV8-L02Rik-treated mice. Hence, the reduction in the lipid content together with the body weight gain reduction probably resulted in the induction of non-shivering thermogenesis. The expression levels of thermogenic markers such as *Ucp1* and *Cidea* were measured by RT-qPCR in iWAT and iBAT of AAV8-Atp4b+AAV8-L02Rik-treated and AAV8-Null-administered mice (Figure 77, 78).

The expression of *Ucp1* was increased in iWAT of AAV8-Atp4b+AAV8-L02Rik-treated mice, in both chow- and HFD-fed mice (Figure 77A). Especially, the expression of *Ucp1* was highly upregulated in HFD-fed mice treated with AAV8-Atp4b+AAV8-L02Rik (Figure 77A). Furthermore, AAV-mediated gene transfer of *coAtp4b* and *co1700040L02Rik* also produced an increment of the expression levels of *Cidea* (Figure 77B). In chow-fed mice treated with AAV8-Atp4b+AAV8-L02Rik, *Cidea* did not present any differences in gene expression levels when compared with animals administered with AAV8-Null (Figure 77B). The expression levels of this gene in the AAV8-Null-treated HFD-fed mice were barely detected by RT-qPCR (Figure 77B). However, the detection of animals expressing *Cidea* by RT-qPCR was increased in HFD-fed mice treated with AAV8-Atp4b+AAV8-L02Rik, indicating that the administration of these vectors increased the expression levels of *Cidea* (Figure 77B). Altogether, the expression of *Ucp1* and *Cidea* indicated induction of the non-shivering thermogenesis in AAV8-Atp4b+AAV8-L02Rik-treated mice.

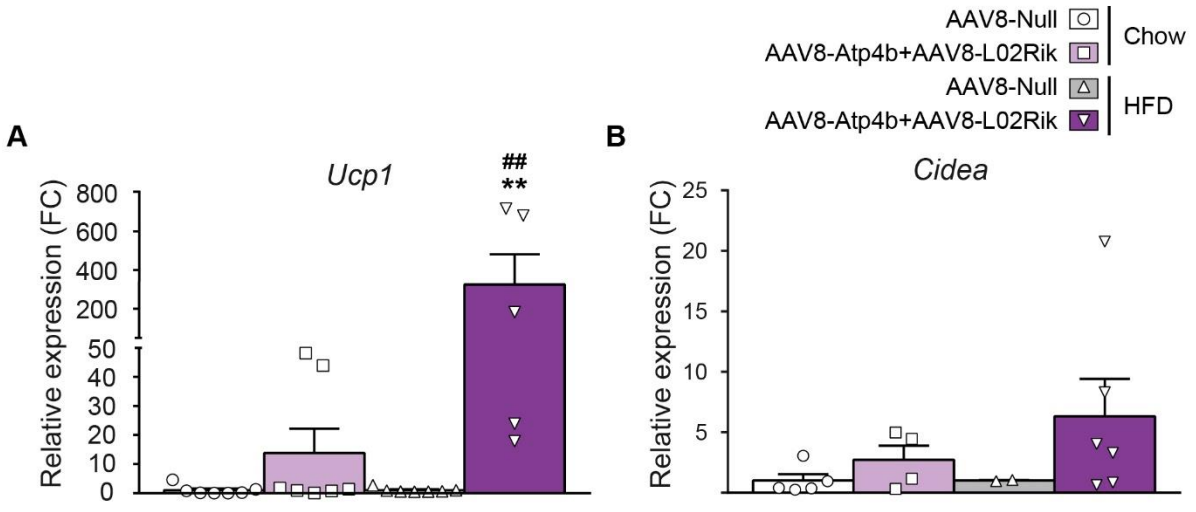


***Figure 77. Analysis of the expression of Ucp1 and Cidea in iWAT.*** Male C57Bl/6 mice were treated systemically with AAV8-Atp4b+AAV8-L02Rik or AAV8-CAG-Null vectors at 8 weeks of age and fed either chow or HFD diet. Expression levels of **(A)** *Ucp1* and **(B)** *Cidea* were evaluated. The results were expressed as the mean ± SEM. n = 7. **P <0.01 versus chow-fed AAV8-Null-injected group. ##P <0.001 versus HFD-fed AAV8-Null-injected group. FC: fold change.

The results obtained by the RT-qPCR analysis of iBAT were not similar to the ones obtained in iWAT. In agreement with the histological analysis of the iBAT depot (Figure 76), in which no differences in lipid deposition were observed, expression levels of *Ucp1* and *Cidea* remain unchanged among groups (Figure 78).

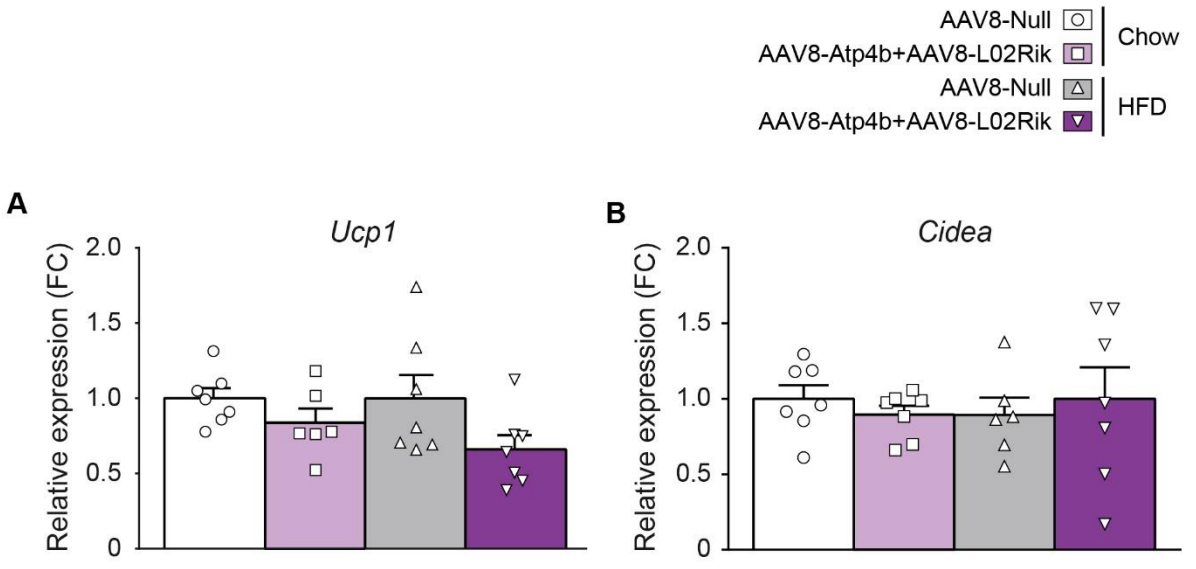


***Figure 78. Analysis of the expression of Ucp1 and Cidea in iBAT.*** Male C57Bl/6 mice fed chow or HFD were treated with AAV8-Atp4b+AAV8-L02Rik or AAV8-Null at 8 weeks of age. Expression levels of **(A)** *Ucp1* and **(B)** *Cidea* were evaluated. The results were expressed as the mean ± SEM. n = 7. FC: fold change.

## 7. HISTOLOGICAL ANALYSIS OF LIVER OF ANIMALS ADMINISTERED WITH AAV8-CAG-co*Atp4b*-dmiRT AND AAV8-CAG-co*1700040L02Rik*-dmiRT

As the liver also presented weight differences between groups, sections of this tissue were stained with hematoxylin/eosin and analyzed histologically (Figure 79). HFD-fed mice showed increased hepatic lipid content in comparison with chow-fed mice. In contrast, this lipid accumulation was decreased in mice fed a HFD and administered with AAV8-Atp4b+AAV8-L02Rik when compared with HFD-fed mice treated with the null vectors (Figure 79). The lipid content reduction between HFD-fed groups was in concordance with the liver weight reduction observed those mice (Figure 72). No differences were observed between chow-fed mice treated with either AAV8-Atp4b+AAV8-L02Rik or AAV8-Null (Figure 72).

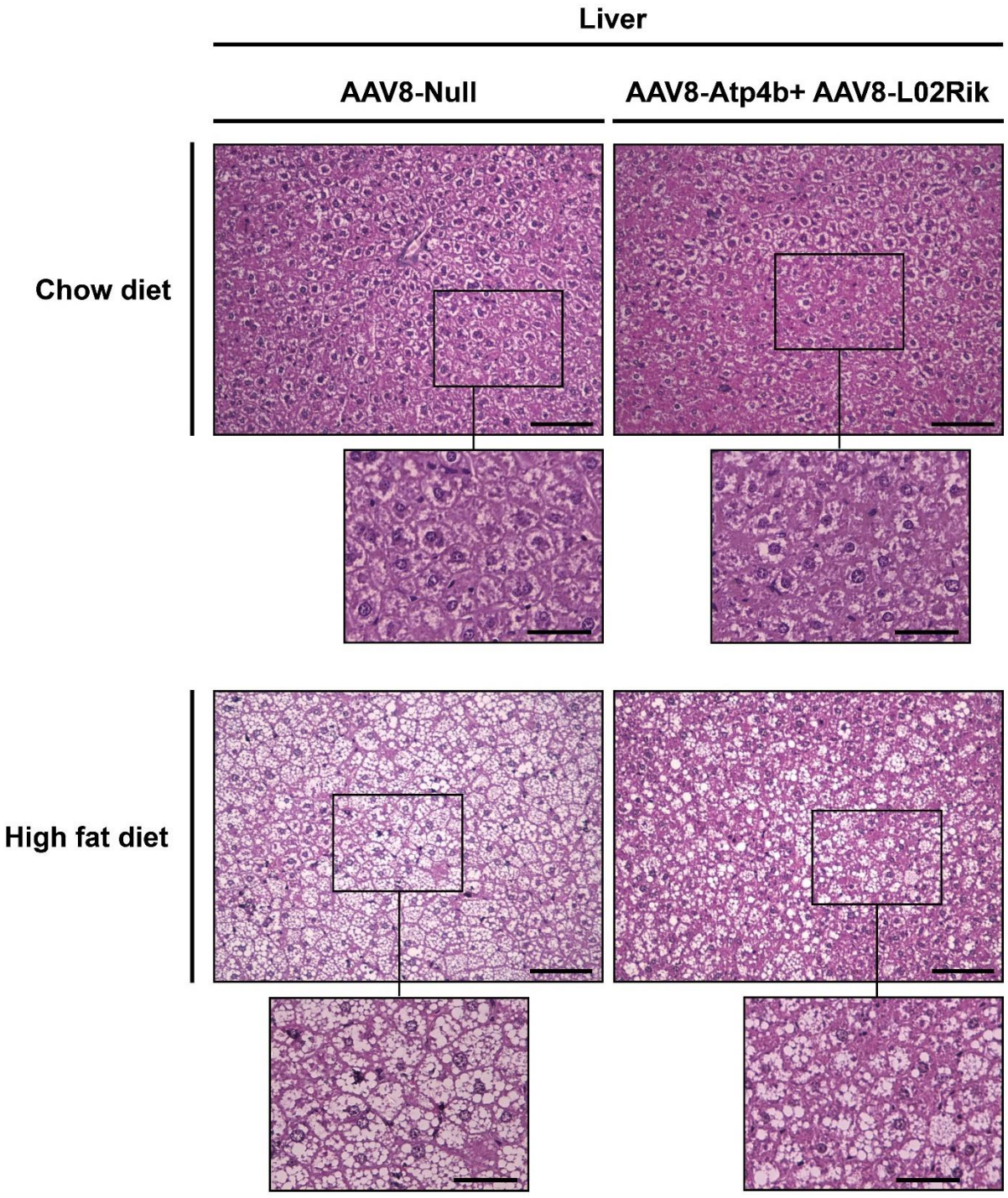


***Figure 79. Histological analysis of the liver of animals treated AAV8-Atp4b+AAV8-L02Rik.*** Hematoxylin/eosin staining of representative sections of the liver of C57BL/6 mice fed either with chow diet or high-fat diet and treated with AAV8-Atp4b+AAV8-L02Rik or AAV8-Null. Scale bars: 100µm and 50µm (inset).

Therefore, the overexpression of *Apt4b* and *1700040L02Rik* in adipose tissue resulted in the induction of non-shivering thermogenesis detected by the increased expression of genes such as *Ucp1* and *Cidea* in iWAT. The upregulation of these genes could mediate the reduction in the body weight gain indicating a potential newly described anti-obesogenic role of these genes. The detailed analysis of cold adaptation of different mice depots had allowed to unravel novel genes such as *Atp4b* and *1700040L02Rik* involved in the enhancement of thermogenesis in iWAT.

# V. DISCUSSION

Obesity and T2D are closely associated complex metabolic diseases. Both pathologies have reached epidemic proportions in both developed and developing countries. Obesity is caused mainly by the imbalance maintained over time between energy intake and expenditure. Energy expenditure represents the sum of the total energy consumed to maintain the normal function of the cells and organs, metabolism, physical activity and thermogenesis (Spiegelman & Flier, 2001). Despite the relevance for human health of these two diseases, the current treatments available for T2D and obesity are based on pharmacological therapies that present side effects and do not represent a real cure for these diseases. In order to overcome these disadvantages, new preventive or therapeutic approaches for T2D and obesity need to be developed.

According to recent studies, the activation of brown adipose tissue and the browning of white fat tissue are linked to a reduction in obesity and an improvement in insulin sensitivity in rodents and humans (Jimenez et al., 2018; Lee et al., 2014; Liu et al., 2015; Wang et al., 2015; Xue et al., 2016). Specifically, an inverse relationship between BAT activity and BMI has been established (Cypess et al., 2009; van Marken Lichtenbelt et al., 2009) and also between the activity of BAT and glycemia in humans (Matsushita et al., 2014). In addition, it has been shown that exposure to cold increases the activity of BAT in both humans and mice, reduces body weight and improves insulin sensitivity (Yoneshiro and Saito, 2015). Therefore, brown or beige adipocytes have become a potential therapeutic target for the treatment of obesity and T2D. In this sense, the study of the process of non-shivering thermogenesis in such adipocytes is of enormous importance to provide a better understanding to counteract obesity and T2D.

The studies carried out in this doctoral thesis have been focused on characterizing the adaptation of several adipose tissue depots to cold exposure. To this end, mice were housed at either 4ºC or 22ºC for 4 days and gene expression data of iBAT, iWAT, and eWAT were obtained using microarrays. Several analyses were then performed to study this process.

The *exploratory data analyses* (EDA) of the different adipose depots highlighted the importance of iWAT in the cold adaptability process of mice. *Principal component analysis,* which emphasizes the variance between depots and conditions, depicted clearly that the main source of variance among samples was the depot of origin. Similar results have also been obtained in other PCA analysis of gene expression profiles, metabolites or lipids of different adipose depots after cold exposure (Hao et al., 2015; Hoene et al., 2014; Lu et al., 2017). However, in Hao et al (Hao et al., 2015) in which mice were adapted to 4ºC or 30ºC, no differences were found in PC1 between white adipose depots. Furthermore,

the PCA from this study showed a plot composed of PC1 vs PC3, showing only ~35% of the variance instead of the ~70% showed in this thesis. However, in terms of cold adaptability, the results obtained in this thesis from the PCA also determined that iWAT was the depot with more variance between room temperature and cold-exposed mice samples as the two groups could be spatially localized separately. The other EDA performed in our analysis, the *correlation matrix*, presented results similar to the *correlation matrix* presented by Hao et al (Hao et al., 2015), though their matrix was not clustered. In both studies, the *correlation matrix* presented a strong similarity between eWAT samples of mice exposed either to cold or RT. Furthermore, iWAT of mice housed at room temperature also presented high similarity to eWAT. However, iWAT samples from cold-exposed mice only partially resemble the iBAT samples. Nevertheless, some differences can be detected between both studies, as their results (Hao et al., 2015) suggested a very similar and more variable pattern between iWAT exposed to cold and iBAT than ours.

The results obtained from the EDA analyses indicated that iWAT tissue played a key role in cold adaptation of mice from 22ºC to 4ºC. The functional analysis was used to determine with biological processes were being activated transcriptionally. This analysis revealed that iWAT was the depot that presented the strongest and most coordinated differential gene expression. The functional analysis of this depot of cold-exposed mice in comparison with mice housed at RT showed that metabolism-related genes were the most affected in terms of gene expression pattern after cold exposure. Specifically, the metabolism-affected genes were not related only to a specific pathway but related to different ones. The eWAT and iBAT depots presented a lower number of metabolic genes upregulated. The upregulation of metabolic genes during cold exposure in several adipose depots has been described by several authors (Bartelt et al., 2011; Jia et al., 2016a; Moura et al., 2005; Shimizu et al., 1993; Sustarsic et al., 2018; Yu et al., 2015, Yu et al, 2002). Overall, the pathway more affected by cold in mice upon cold exposure has been described as being non-shivering thermogenesis both in iWAT and iBAT (Baba et al., 2007; Gospodarska et al., 2015; Jia et al., 2016a; Nedergaard et al., 1980; Okada et al., 2016; Sun et al., 2014; Xue et al., 2009; Yu et al., 2015). In our study, an important upregulation of non-shivering thermogenesis-related genes such as *Cidea, Dio2, Ppargc1a*, or *Ucp1* was detected in iWAT. Furthermore, eWAT also presented an upregulation of some thermogenic genes. However, this upregulation was not detected in the iBAT, which is the main described depot thermogenically active. It has been reported that browning of iWAT is especially notorious when cold exposure is produced when mice are initially housed at 21ºC

(Kalinovich et al., 2017). In this situation, UCP1 gene expression was only weakly increased in iBAT but markedly augmented in beige adipocytes of the iWAT depot (Kalinovich et al., 2017). The response in iBAT in this cold adaptation differed from the situation in which mice are exposed to cold after being housed at 30ºC. When mice were exposed to cold after being housed at 21ºC, *Ucp1* levels did not get upregulated in iBAT but rather this tissue increased its mass through proliferation of brown adipocytes (Kalinovich et al., 2017). However, in cold adaptation of mice being initially housed at 30ºC, a large increase in the *Ucp1* levels was observed, indicating activation of iBAT (Kalinovich et al., 2017). The data presented by Kalinovich (Kalinovich et al., 2017) supported the results obtained in our study. The expression of *Ucp1* was clearly increased in iWAT but not in iBAT. In the eWAT depot, the upregulation of *Ucp1* was low. Epididymal white adipose tissue has been described as being more resistant to browning and to express low levels of brown fat regulators genes (Chan et al., 2019; Ferrannini et al., 2016).

It has been shown that adipose depots exhibit a wide range of metabolic activity (Zhang et al., 2018) which may explain the differences in metabolic activation detected among depots. The upregulation of metabolism is associated with the upregulation of non-shivering thermogenesis because metabolic pathways have been described as being important to maintain heat generation, leading the disruption of pathways such as glycolysis (Albert et al., 2016) or FA oxidation (Ellis et al., 2010; Lee et al., 2015) to cold intolerance. Moreover, several metabolites have been described as being important or critical for thermogenesis. Among others, fatty acid release from lipolysis has been considered for long-time to activate thermogenesis in mice, rats and humans (Blondin et al., 2017; Labbé et al., 2015; Li et al., 2014). However, recent studies suggested that intracellular lipolysis is not critical in cold-induced thermogenesis in iBAT (Schreiber et al., 2017; Shin et al., 2017). Nevertheless, it was proposed from the studies of Scheiber et al (Schreiber et al., 2017) and Shin et al (Shin et al., 2017) that WAT lipolysis could release FA, reaching BAT from circulation and therefore, compensating the defective lipolysis. Also, it has been observed that the administration of high levels of FA activates UCP1 in iBAT (Prusiner et al., 1968). Other authors have recently highlighted the importance of glucose uptake. Glycolysis has been described as being required for at least short-term thermogenesis of the BAT tissue (Inokuma et al., 2005; Jeanguillaume et al., 2013; Jeong et al., 2018). Moreover, lactate has been described as playing a role inducing non-shivering thermogenesis (Carriere et al., 2014; Jeong et al., 2018; Vergnes and Reue, 2014).

As detected in the functional analysis, genes related to metabolism were enriched in iWAT. In this depot, several pathways such as glycolysis, TCA, lipolysis, and degradation of some amino acids presented upregulated genes. The upregulation of genes of these pathways occurred in parallel with the increment in the expression levels of non-shivering thermogenic genes. This thermogenic activation needs a readily available proton gradient to work properly (Ouellet et al., 2012; Petersen et al., 2017; Townsend and Tseng, 2014; Wu et al., 2013). Therefore, is not a coincidence the upregulation of the metabolism in this cell context.

It has been described that after cold exposure, human BAT depots increase glucose uptake up to 12-fold, while in brown adipocytes insulin-stimulated glucose uptake increases only up to 5-fold (Orava et al., 2011). The detected browning process that occurred in iWAT somehow mimicked some BAT responses to cold-exposure as glucose stimulation. In the iWAT depot of cold-exposed mice, the upregulation of several glucose transporters such as GLUT4, GLUT5 or GLUT8 possibly increased the glucose uptake. The upregulation of GLUT4 in iWAT of cold-exposed mice has also been described also by other authors (Jia et al., 2016b; Rosell et al., 2014). These upregulations are important for producing a thermogenic response, as the knockdown of individual glucose transporters such as GLUT1 and GLUT4 in cultured brown adipocytes has been described as preventing an increase in oxygen consumption following acute adrenergic stimulation (Winther et al., 2018). Furthermore, the GLUT4 inhibitor indinavir has been shown to produce a dose-dependent reduction of thermogenesis in human brown adipocytes *in vitro* (Lee et al., 2016). Genetically engineered mice lacking mTORC2, which presented defective glucose uptake and glycolysis in brown adipocytes, were cold intolerant (Albert et al., 2016).

Once glucose is internalized in the cell it gets metabolized through the glycolysis. In iWAT depot samples of mice exposed to cold nearly all the steps of this pathway presented upregulated genes, with a noteworthy upregulation of the genes that control the flow pace, such as *hexokinase*, *phosphofructokinase*, and *pyruvate kinase*. The upregulated expression of *hexokinase 2* was of high importance, as the phosphorylation of glucose to glucose-6-phosphate prevents this molecule exiting the cell. Another remarkable upregulation was the higher expression presented by the *phosphofructokinase* (*Pfkm*, *Pfkl*), as this enzyme set the pace of glycolysis. Finally, the upregulation of the *pyruvate kinase* (*Pkm*) would be also important. This enzyme controls the glycolysis outflow as the formation of pyruvate is an irreversible step. *In vitro* studies using siRNA-mediated knockdown of the genes *Hk2* and *Pkm*, which are two of the three enzymes that control

glycolysis pace, produced impairment in oxygen consumption in brown adipocytes (Winther et al., 2018).

The upregulation of the isoform B and D of the *lactate dehydrogenase* was also detected in iWAT of cold-exposed mice. This upregulation is important for cold adaptation because the knockdown of the LDH activity in C57BL6/129SVJ mice has been described as blocking the increase of BAT temperature in Norepinephrine (NE)-induced thermogenesis (Jeong et al., 2018). Furthermore, Jeong et al (Jeong et al., 2018) described how the inhibition of MCT1 activity, a transporter of both pyruvate and lactate to mitochondria, blocked short-term NE-induced thermogenesis. Moreover, several authors have described the upregulation of this transporter under cold-exposure or NE-induced thermogenesis (Carriere et al., 2014; Jeong et al., 2018). In iWAT of cold-exposed mice, the expression of MCT1 was upregulated 2.2-fold. Furthermore, the lactate concentrations can regulate the *phosphofructokinase* as this enzyme is strongly inhibited at acidic cellular pH (Erecińska et al., 2002; Trivedi and Danforth, 1966).

It had been though that intracellular triglycerides were the main energy source for thermogenesis, and therefore intracellular lipolysis and mitochondrial β-oxidation have been described for years as required for generating or maintaining the mitochondrial proton gradient that is used by *Ucp1* (Cannon and Nedergaard, 2004; Townsend and Tseng, 2014). This hypothesis was based on studies that demonstrate that the disruption of mitochondrial β-oxidation blocked non-shivering thermogenesis (Gonzalez-Hurtado et al., 2018; Guerra et al., 1998; Lee et al., 2015) or that the *Cpt2*-KO mice were cold intolerant (Lee et al., 2015). However, the studies performed by Schreiber et al (Schreiber et al., 2017) and Shin et al (Shin et al., 2017) concluded that the FA molecules produced intracellularly are not critical in cold-induced non-shivering thermogenesis of BAT, but that this molecule may be released from the iWAT lipolysis to the circulating system to reach finally the BAT. In any case, lipolysis in WAT can potentially affect the thermogenic process. In iWAT of cold-exposed mice, lipolysis seemed to be highly induced, as many genes encoding for enzymes that participate in this process were upregulated. The upregulation of genes related to the degradation of triglycerides occurred in parallel with the upregulation of genes participating in β-oxidation. The induction of lipolysis in iWAT during cold exposure has also been described by other authors (Xue et al., 2009). Altogether, the activation of lipolysis and β-oxidation in iWAT of cold-exposure mice would produce NADH and $FADH_2$ to maintain the protonmotive power used by UCP1 to

generate heat. Moreover, the increased degradation of triglycerides to FA could allow the release of this molecule to the bloodstream.

The molecules of acetyl-CoA produced by the β-oxidation as well as from pyruvate could enter the TCA. The majority of the TCA-related genes were upregulated in iWAT of cold-exposed mice, suggesting an enhanced production of NADH and $FADH_2$ in this cycle.

The analysis of the metabolic changes 4 hours after cold exposure in C57Bl/6 mice highlighted altered levels of different amino acids in iBAT during this period (Lu et al., 2017). Though in our study mice were exposed to cold for 4 days, which is a period of time that cannot be considered immediate early stages of the thermogenic process, an upregulation of genes related to amino acids degradation was also observed. In particular, an increment in the degradation of BCAA was detected in the different adipose depots analyzed, but with a different degree of upregulation. In iWAT, genes related to the degradation of leucine, isoleucine, and valine were clearly upregulated. Upregulation of genes related to serine metabolism was also detected. This amino acid has been described as presenting increased levels during cold exposure in iBAT depot of rats (López-Soriano and Alemany, 1987). Other authors have described how this amino acid activates *Pkm* (Chaneton et al., 2012). The knockdown in cultured brown adipocytes with siRNAs of *Pkm* led to an impairment in oxygen consumption (Winther et al., 2018). Altogether, the upregulation of genes related to glycolysis, TCA, lipolysis, and amino acids degradation demonstrated the coordinated metabolic response that is produced in iWAT of animals exposed to cold for 4 days after being housed at 22ºC.

In eWAT, different glucose transporters were also deregulated as in iWAT when samples from mice at RT were compared with cold-exposed mice samples. In the epididymal depot, GLUT5, GLUT8, and GLUT9 were upregulated, while GLUT13 was downregulated. These glucose transporters are not as characterized as GLUT1 or GLUT4, and no role in cold adaptation has been described for them. The glycolysis in eWAT presented also differences in comparison with iWAT. Genes that were upregulated in iWAT such as *Hk2, Pfkm* or *Pfkl* were not upregulated in this tissue. *Pkm* was only upregulated 1.4-fold in comparison with iWAT, in which this upregulation was 1.88-fold. The pyruvate produced by these pathways could then be metabolized to lactate by the *lactate dehydrogenase* enzyme as observed in iWAT, a molecule which is somehow involved in the thermogenic process. In eWAT of cold-exposed mice, neither *Ldha*, *Ldhb* nor *Ldhc* were upregulated.

When the expression of genes related to triglycerides degradation was studied, no major differences were detected. However, several key proteins of this process are regulated post-transcriptionally, through phosphorylation or by another mechanism. For this reason its complicated to conclude that the production of FA was not increased in eWAT. Furthermore, the mitochondrial β-oxidation in this adipose depot presented several related genes that were upregulated. No differences in white adipocytes size were observed in the histological analysis of sections of eWAT. Altogether, these results suggested that the degradation of FA was enhanced, but further research is needed to conclude if triglycerides were being mobilized and converted to FA. The upregulation of some genes related to glycolysis and β-oxidation suggested a mildly increased production of acetyl-CoA, which can enter the TCA cycle. This process presented several enzymes upregulated but with mild fold change, suggesting that probably the generation of NADH and $FADH_2$ was slightly incremented. However, as the cycle was not highly activated, a mild increase in the expression of genes related to anaplerotic pathways such as the degradation of isoleucine or valine was observed. These pathways could generate an increased flux of succinyl-CoA into the TCA in eWAT depot. However, the degradation of leucine to acetyl-CoA was not apparently upregulated.

This slight activation of the metabolism in the eWAT depot correlated with the mild expression of thermogenic markers, which, despite presenting high fold changes increased values, had relatively moderate expression levels in comparison with iWAT or iBAT depots.

On the other hand, gene expression analysis of metabolic-related genes in the iBAT depot differed from the results obtained in the analysis of iWAT and eWAT, as this depot was already thermogenically activated, presenting high expression levels for thermogenic- and metabolic-related genes (Kalinovich et al., 2017). In this depot, only two glucose transporters, GLUT8 and GLUT9, presented upregulated expression. GLUT8 was upregulated in the three adipose tissue depots and GLUT9 presented an increase expression in eWAT and iBAT, suggesting a potential role of these two transporters in cold adaptation of adipose tissue depots. Several genes encoding enzymes of the glycolysis were upregulated in iBAT, the expression of genes of key processes such has *Hk1*, *Pfkl* or *Pfkp* being highly upregulated. The expression of the gene encoding the hypoxia-inducible factor-1α (HIF-1α) was upregulated 1.5-fold in this depot. HIF-1α-dependent regulation of glycolysis has been described as necessary for maximum glucose metabolism in brown adipocytes (Basse et al., 2017). Despite the upregulation of this protein, glycolysis did not

seem to be highly enhanced as the muscular pyruvate kinase isoform, which mediates the key step of producing pyruvate, only presented a 1.3-fold change increase.

When lipolysis was analyzed, only a few genes related to this pathway presented an upregulated expression. However, among these genes, two isoforms of the adenylate cyclase were detected. These proteins could trigger the activation of several proteins through the activation of PKA due to the possible increase in the intracellular cAMP levels. Furthermore, the gene *Plin2* which encodes for perilipin, a target of the PKA, was also upregulated. This gene participates in the mobilization of triglycerides. Other genes encoding enzymes that contribute to the degradation of triglycerides such as *Mgll* were also detected. Importantly, upregulated genes, such as Acsl5 or Cpt1a, coding enzymes related to the conversion of FA and to the entrance of this molecule into the mitochondria were also detected. However, no enzymes participating in β-oxidation presented expression that increased under cold exposure. An upregulation in the expression of genes encoding enzymes related with the degradation of triglycerides in iBAT due to cold exposure has also been described by other authors (Nie et al., 2015; Sustarsic et al., 2018). Proteomic studies of BAT remodeling during cold exposure have also described increased levels of lipolytic enzymes (Yu et al., 2015).

On the other hand, no gene related to TCA cycle presented an increased expression. The only gene that presented a deregulated expression was *Aco1*, which had its expression slightly downregulated under cold exposure. However, mice housed at 29ºC subsequently exposed to 5ºC presented increased expression of genes related to the TCA cycle, which could be explained by the differences in iBAT activation discussed by Kalinovich et al (Kalinovich et al., 2017; Sustarsic et al., 2018).

The degradation of leucine, isoleucine, and valine presented several enzymes with its expression deregulated, indicating that the genes of these pathways were differentially regulated between cold- and RT-exposed mice.

In conclusion, as iBAT already presented high metabolic gene expression levels in RT housed mice, cold exposure did not mainly furhter enhance expression of these genes. Several genes related with glycolysis were upregulated but one key step presented only a slight increase in its gene. Genes related to the TCA cycle were not upregulated. Moreover, several genes of the degradation of BCAA to acetyl-CoA or succinyl-CoA were downregulated. The degradation of triglycerides was possibly enhanced but no gene encoding enzymes related with the β-oxidation was upregulated though the entrance of

FA into the mitochondria was upregulated. However, the analysis of the expression levels of thermogenic genes suggested that non-shivering thermogenesis was already induced in the animals exposed at room temperature. Thus, the results obtained in iBAT were in agreement with the model proposed by Kalinovhich et al (Kalinovich et al., 2017). Altogether, these data suggested that the iBAT tissue was already highly activated in mice exposed at RT, limiting the upregulation of metabolic genes.

It is noteworthy to mention that the transcriptomic analysis of this doctoral thesis has only studied gene expression changes but not post-transcriptional modifications, which can be essential for the proper activation/function several of the related proteins.

The detailed study of the adipose tissue depots response to cold exposure allowed the detection of different coordinated levels of thermogenic and metabolic induction. The fact that genes related to thermogenesis and metabolism presented a similar expression pattern among samples endorsed the utilization of *pattern matching analysis tools* to unravel *Atp4b* and *1700040L02Rik* as novel genes potentially involved in thermogenesis.

The overexpression of *Atp4b* and *1700040L02Rik* in adipose tissue by means of AAV vectors induced non-shivering thermogenesis in iWAT in HFD-fed mice, leading to body weight gain reduction, decreased eWAT and liver weight, amelioration of white adipocyte hypertrophy, and reduced hepatic steatosis. Given that expression of *1700040L02Rik* was much more lower than the expression of *Atp4b* in adipose tissue, the phenotype would have been likely produced by the overexpression of *Atp4b*. However, more studies are needed to evaluate the therapeutic potential of this gene. Overall, these results reveal a new function for the *Atp4b* as a gene involved in the induction of non-shivering thermogenesis in iWAT.

In conclusion, the results from this doctoral thesis allowed a better understanding of the response of adipose tissue depots to cold exposure in mice. Among the different adipose depots, exploratory data analysis of the gene expression levels of mice exposed from 22ºC to 4ºC determined that iWAT was the depot that responded most significantly to cold exposure. Moreover, as observed in the pathway enrichment and gene ontology analysis, this response was highly coordinated, presenting a high number of genes related to metabolic pathways highly affected. The detailed study of the metabolic pathways led to detect a high induction of non-shivering thermogenesis, unraveling that both energy production and energy consumption mechanisms were highly synchronized. This in detail

study of the adipose tissue also allowed the identification of novel genes potentially involved in non-shivering thermogenesis.

# VI. CONCLUSIONS

1. Mice exposed to cold for 4 days presented transcriptional changes in the adipose tissue depots. The exploratory data analysis presented the iWAT as a key depot in cold adaptation.

2. Pathway enrichment and gene ontology analyses presented several metabolic pathways and terms, respectively, highly enriched among all the differentially expressed genes. These functions were mainly enriched in iWAT.

3. Genes related to glycolysis, TCA cycle, degradation of BCAA, and lipolysis were mainly upregulated in the inguinal depot.

4. Gene markers of non-shivering thermogenesis were highly upregulated in the iWAT depot. Moreover, histological sections of this depot revealed the appearance of beige adipocytes.

5. eWAT presented a lower number of metabolic-related differentially expressed genes than iWAT, and their upregulation was mild. Similarly, iBAT also presented a low number of differentially expressed genes related to metabolic pathways in comparison with the inguinal depot.

6. Five different clusters of genes were identified based on different expression profiles. One of these clusters contained most of the thermogenic and metabolic-related genes.

7. This cluster also comprised a subset of genes not described as being involved in cold adaptation, allowing the unraveling of novel genes potentially involved in thermogenesis, such as *Atp4b* and *1700040L02Rik*.

8. The genetic engineering of adipose tissue with AAV8 vectors encoding *Atp4b* and *L02Rik* reduced the body weight gain of HFD-fed mice. Furthermore, this treatment also decreased the adiposity of eWAT and hepatic steatosis.

9. Mice administered with AAV8 vectors encoding *Atp4b* and *L02Rik* counteracted HFD-induced hypertrophy of white adipocytes. Moreover, their overexpression induced the expression of non-shivering thermogenic markers in iWAT but not in iBAT.

10. In conclusion, the results of this thesis provided a better understanding of the adaptation of white and brown adipose tissue to cold exposure. In particular, a high induction of non-shivering thermogenesis was detected in iWAT, and the transcriptomic analyses revealed that both energy production and energy consumption mechanisms were highly synchronized. Furthermore, the bioinformatic analysis of gene expression profiles unraveled novel genes potentially involved in non-shivering thermogenesis.

# VII. MATERIALS AND METHODS

# 1. MATERIALS

## 1.1. Animals

In the studies of this doctoral thesis, consanguine male mice of the strain C57Bl/6JOlaHsd of 8 weeks of age were used (*Envigo, Huntingdon, Cambs, UK*). Mice were housed in a specific pathogen-free facility (*SER-CBATEG,* Universitat Autònoma de Barcelona*, CA, ES*) and kept under controlled conditions of temperature (22 ºC ± 2), light (light-dark cycles of 12 h) and humidity and were fed *ad libitum* with a standard diet (2018S *Teklad Global Diets*, *Envigo, Huntingdon, Cambs, UK*) or a high fat diet (HFD) (TD.88137 *Teklad Global Diets*, *Envigo, Huntingdon, Cambs, UK*).

Prior to sampling, mice were anesthetized by inhalation anesthesia (Isoflurane, *IsoFlo®, Abbott Laboratories, Chicago, IL, USA*) and euthanized by decapitation. Tissue samples were obtained in the morning and were immediately stored in 4% formaldehyde ($CH_2O$, pH 7) (*Panreac, Barcelona, CAT, ES*) or frozen in liquid nitrogen ($N_2$) and then stored at -80 ºC. Blood samples were centrifuged at 12000g for 10 min and the obtained serum was kept at -80°C. All the experimental procedures were carried out under the current legislation and approved by the Ethics Committee on Animal and Experimentation of the Universitat Autònoma de Barcelona (UAB).

## 1.2. Bacterial strains

The strain Escherichia coli *XL2Blue* (*Agilent Technologies, Santa Clara, CA, USA*) was used to obtain and amplify the different plasmids used in this thesis. Since all the plasmids contained the ampicillin resistance selection gene, the bacterial cultures were grown in LB medium (*Miller's LB Broth, Laboratorios Conda, Madrid, MAD, ES*) with 50 µg/mL ampicillin. When cells were grown in a solid medium, 2% agar was added to the LB media.

## 1.3. Plasmids

For the generation of the AAV construct of interest, the plasmids pMA-co*1700040L02Rik* and pMA-co*Atp4b*, which encoded for codon-optimized coding sequences of murine sequence of *1700040L02Rik* and *Atp4b*, respectively, were acquired from GeneArt (*Thermo Fisher Scientific, Waltham, MA, USA*). The plasmids generated and used in this study are summarized in Table 37.

| Name | Promoter | Gen of interest | dmiRT | PolyA |
|---|---|---|---|---|
| pAAV-CAG-co1700040L02Rik-dmiRT | CAG | co1700040L02Rik | Yes | Rabbit β-globin |
| pAAV-CAG-coApold1-dmiRT | CAG | coApold1 | Yes | Rabbit β-globin |
| pAAV-CAG-coAtp4b-dmiRT | CAG | coAtp4b | Yes | Rabbit β-globin |
| pAAV-CAG-coChac1-dmiRT | CAG | coChac1 | Yes | Rabbit β-globin |
| pAAV-CAG-coMarc1-dmiRT | CAG | coMarc1 | Yes | Rabbit β-globin |
| pAAV-CAG-Null | CAG | none | No | Rabbit β-globin |

Table 37. List of generated plasmids

CAG is a hybrid promoter formed with the cytomegalovirus early enhancer element, the promoter, the first exon and the first intron of the chicken ß-actin gene, and the splice acceptor of the rabbit ß globin gene. This promoter mediates a strong and ubiquitous expression of the transgene (Okabe et al., 1997).

Table 38 summarizes the strategies followed to generate the plasmids.

| Name | | Cloning strategy | Source |
|---|---|---|---|
| pAAV-CAG-mmo1700040L02Rik-dmiRT | Backbone | pAAV-CAG-eGFP-dmiRT digested with NheI and NotI | CBATEG |
| | Insert | pMA-mmo1700040L02Rik digested with NheI and NotI | GeneArt |
| pAAV-CAG-mmoApold1-dmiRT | Backbone | pAAV-CAG-eGFP-dmiRT digested with NheI and NotI | CBATEG |
| | Insert | pMA-mmoApold1 digested with NheI and NotI | GeneArt |
| pAAV-CAG-mmoAtp4b-dmiRT | Backbone | pAAV-CAG-eGFP-dmiRT digested with NheI and NotI | CBATEG |
| | Insert | pMA-mmoAtp4b digested with NheI and NotI | GeneArt |
| pAAV-CAG-mmoChac1-dmiRT | Backbone | pAAV-CAG-eGFP-dmiRT digested with NheI and NotI | CBATEG |
| | Insert | pMA-mmoChac1 digested with NheI and NotI | GeneArt |
| pAAV-CAG-mmoMarc1-dmiRT | Backbone | pAAV-CAG-eGFP-dmiRT digested with NheI and NotI | CBATEG |
| | Insert | pMA-mmoMarc1 digested with NheI and NotI | GeneArt |
| pAAV-CAG-Null | | CBATEG | CBATEG |

mmo: mus musculus optimized codon sequence; CAG: CMV early enhancer/chicken β-actin promoter; eGFP: enhanced Green Fluorescent Protein; dmiRT: target sequence of microRNA 1 and microRNA 122a

Table 38. Strategies used in the generation of plasmids.

## 1.4. Reagents

Reagents used in molecular biology techniques were obtained from *Roche* (*Hoffmann-La Roche, Basel, CH), Thermo Fisher Scientific* (*Waltham, MA, USA*), *Bio-Rad Laboratories* (*Hercules, CA, USA*), *Sigma-Aldrich Corporation* (*St. Louis, MO, USA*), *Promega Corporation* (*Madison, WI, USA*), *BASF* (*Ludwigshafen, RP, DE*), *Qiagen* (*Hilden, NW, DE*) and *MP Biomedicals* (*Santa Ana, CA, USA*). Culture media and antibiotics were obtained from *Fisher Scientific* (*Thermo Fisher Scientific, Waltham, MA, USA*) and fetal bovine serum (FBS) and *F68 Pluronic*® from *Gibco* (*Thermo Fisher Scientific, Waltham, MA, USA*).

# 2. METHODS

## 2.1. Acute cold exposure

8 weeks-old male C57Bl/6JOlaHsd mice were divided into two groups that were either exposed during 4 days to 4ºC in a humidity and temperature-controlled refrigerator room (MDB123T0 02F, *Zanotti Appliance, Valencia, VA, ES*) or to room temperature (RT). Each mouse was housed individually, and the bedding of the cage was removed to keep mice from nesting to help regulate body temperature. Day and night cycles were maintained with 12 hours of light and 12 hours of darkness. Body weight and blood glucose were measured before and after exposing the animals to cold.

## 2.2. Basic DNA techniques

### *2.2.1. Plasmid DNA preparation*

Small amounts of plasmid equivalent to 3-4 µg were obtained from mini preparations (minipreps), performed according to the alkaline lysis protocol (Birnboim and Doly, 1979). To this end, bacteria transformed with plasmid DNA were cultured for 12-16 h at 37ºC and 250 rpm in 3 mL of LB culture medium and ampicillin. From 1.5 mL of the grown medium, bacteria were precipitated and resuspended in an RNase/TE solution (10 mM EDTA, 50 mM Tris-HCl, pH 8). Then, alkaline lysis (1% SDS, 200 mM NaOH) followed by selective precipitation of denatured proteins and genomic DNA with an acidic solution of potassium acetate (3 M KAc, pH 5.5) were carried out. During this process, bacterial RNA was degraded by the addition of RNase (100 µg/ml).

Large amounts of DNA were obtained by performing maxi preparations (maxipreps, from which 1 mg of plasmid is obtained as maximum), mega preparations (megapreps, to obtain a maximum of 2.5 mg of plasmid) or giga preparations (gigapreps, from which a maximum of 12 mg of plasmid is obtained), from 200, 500 or 1500 mL of culture medium respectively. The different protocols for extracting DNA in large quantities are also based on alkaline lysis, although in these cases, DNA purification was performed using the *GeneJET Endo-Free Plasmid Maxiprep Kit* absorption columns (*Thermo Fisher Scientific, Waltham, MA, USA*) for the maxipreps, the *Endo-Free Plasmid Mega Kit* or *Endo-Free Plasmid Giga Kit* columns (*Thermo Fisher Scientific, Waltham, MA, USA*) for the mega or gigapreps, respectively.

### *2.2.2. DNA digestion with restriction enzymes*

Specific conditions of temperature, pH and ionic strength are required by each restriction enzyme to ensure the correct digestion of DNA. In all the enzymatic digestions performed in this thesis, the commercial instructions were followed (*Thermo Fisher Scientific, Waltham, MA, USA*). As all the DNA digestions were carried out using two restriction enzymes with buffer incompatibilities (NheI + NotI), first DNA was digested overnight (16 h) at the optimum temperature with 2.5 units of NheI for each µg of DNA in the specific buffer supplied by the manufacturer. Then, digested DNA was precipitated to purify it of salts and the enzyme used. For the precipitation of digested DNA, the double amount of volume of absolute ethanol ($C_2H_5OH$) and 10% of the volume of 3M of sodium acetate pH 5.2 were added to later centrifuge it at maximum speed. After removing the supernatant, 70% ethanol was added to facilitate the dilution of the sodium acetate and it was centrifuged again at maximum speed. Finally, the supernatant was removed, and the pellet was resuspended in the appropriate volume of water. Once digested, DNA was precipitated and it was then re-digested with the second enzymatic reaction (NotI).

The digested DNA was loaded into 1 or 2% electrophoretic agarose gel, depending on the size of the expected bands. Then, the different DNA bands migrated, and the band of interest was cut and purified by the *GeneJET® Gel Extraction kit* (*Thermo Fisher Scientific, Waltham, MA, USA*) following the manufacturer's instructions. The DNA was eluted in 30 µL of elution buffer and quantified in the *Nanodrop 1000* spectrophotometer (*Thermo Fisher Scientific, Waltham, MA, USA*).

### *2.2.3. Dephosphorylation of DNA fragments*

To avoid self-ligation, dephosphorylation of the plasmid was necessary to eliminate the phosphate residues of the 5 'end. For dephosphorylation, one unit of alkaline phosphatase (*FastAP Thermosensitive Alkaline Phosphatase* (1 U/µl), *Thermo Fisher Scientific, Waltham, MA, USA*) was used for every 1-5 µg of DNA in its commercial buffer. Following the commercial protocol, the dephosphorylation reaction was carried out for 10 min at 37°C. Subsequently, alkaline phosphatase was inactivated at 75ºC for 5 min.

### *2.2.4. Ligation of DNA fragments*

The ligation was performed due to the action of the enzyme DNA ligase of bacteriophage T4 (*New England Biolabs, Ipswich, MA, USA*). For the ligation, the DNA fragments of interest were added at different molar ratios of vector:insert (1:5, 1:10 and 1:20) with the T4 DNA ligase enzyme and the corresponding buffer following the protocol established by the manufacturer. Three types of controls were used to check whether the ligations were performed correctly and its efficiency: vector control, ligase control and insert control (Table 39).

| Name | Vector control | Ligase control | Insert control |
|---|---|---|---|
| Dephosphorilated vector | X | X | |
| Insert | | | X |
| Ligase | | X | X |
| Ligase buffer | X | X | X |
| $H_2O$ | X | X | X |

Table 39. Controls of ligation used in the studies.

Both vector and insert control determined if the cut of the band of interest in the electrophoresis gel was correctly performed and no remaining parental vector plasmid was still present. Furthermore, the ligase control provided information on whether the dephosphorylation of the vector was performed correctly or not. The absence of growth colonies of bacteria transformed from each of the controls suggested that the ligation had occurred correctly. The absence of colonies in the vector and insert controls demonstrated that both, the vector DNA and the insert DNA, were well linearized and did not contain resistance to the antibiotic. In contrast, the absence of colonies in the ligase control demonstrated that the dephosphorylation of the vector worked correctly and the self-ligation of the linear fragment containing the resistance to the antibiotic did not occur.

### *2.2.5. Transformation of competent E.Coli XL2-blue cells*

Plasmid DNA was electroporated into competent bacteria to introduce the genetic material. To this aim, 40 µL of *E.Coli XL2-Blue* bacteria ($2x10^{10}$ bacteria/mL) was mixed with 1 µL (approximately 10 ng) of ligated or control DNA. After incubating the mix

during 5 min on ice, the bacteria cells were electroporated at 2500 V with an electroporator (*Bio-Rad, Hercules, CA, USA*). Subsequently, cells were diluted in 100 µL of LB medium, spread on LB plates with ampicillin and incubated at 37°C overnight.

### *2.2.6. Separation and visualization of DNA fragments*

To separate, identify and purify DNA fragments, the usage of electrophoretic agarose gel is the standard method. To separate DNA fragments between 0.2 and 7 Kb, 1% agarose gels were used. Agarose gels were prepared by dissolving agarose in 1x TAE electrophoresis buffer (40 mM pH 8.3 tris-acetate and 1 nM EDTA). Samples were loaded on the gel with 1x loading buffer (*Thermo Fisher Scientific, Waltham, MA, USA*) and run with 1x TAE electrophoresis buffer at 80 V. The visualization of DNA in the gel was achieved by the addition of low concentrations of fluorescent ethidium bromide to the gel (0.5 µg/mL), which is intercalated between the DNA helices. The presence of DNA was visualized using ultraviolet (UV) light of low wavelength (310 nm) through a transilluminator and a camera system (*Syngene, Scientific Digital Imaging, Cambridge, UK*). The 1 kb GeneRuler and the 100 bp GeneRuler (*Thermo Fisher Scientific, Waltham, MA, USA*) were used as molecular DNA markers.

## 2.3. Culture of eukaryotic cells

### 2.3.1.HEK293 cells

Human embryonic kidney 293 (HEK293) cells were used to assess the cloned transgene *in vitro* expression. HEK293 were also used to produce AAV viral vectors. These cells were maintained in DMEM culture medium (*Fisher Scientific*, *Thermo Fisher Scientific, Waltham, MA, USA*) with 2mM of glutamine and 10% of Fetal Bovine Serum (FBS) (heat inactivated) in an incubator adjusted to 37°C and 8.5% $CO_2$. When the cells reached a 70% confluence, they were trypsinized and plated at different dilutions to continue their maintenance in culture until their use.

### 2.3.2.Transfection of cultured cells

Plasmids were transfected by using Lipofectamine (Lipofectamine™2000, *Invitrogen, Carlsbad, CA, USA*), which increases the transfection efficiency of DNA into the cells by

forming a hydrophobic lipofectamine-DNA complex. A lipofectamine/DNA ratio of 10 µL of lipofectamine (1 mg/mL) per 4 µg of DNA per-well of 6-well culture plates was used. For optimal transfection, HEK293 cells were transfected when they were 70-80% confluent. The culture of the transfected cells was terminated at 24-48 h after transfection for the analysis of the samples.

## 2.4. Production, purification and titering of adeno-associated vectors

### *2.4.1. Production and purification*

Infectious single-stranded AAV8 viral vector particles were generated in adherent HEK293 cells cultured in Roller Bottles (RB) (*Greiner Bio-One, Kremsmünster, KI, AT*) by a triple transfection protocol (Ayuso et al., 2010). These cells express the adenoviral E1 gene of adenovirus serotype 5 as it is stably integrated into its genome. HEK293 cells were cultured in RB in DMEM medium supplemented with 10% FBS + 1% Penicillin/Streptomycin until they reached 80% of confluence. Before transfection, DMEM medium was changed to IMDM medium supplemented with 2% FBS + 1% Penicillin/Streptomycin. Then, each RB was co-transfected with 30 mL of calcium phosphate with 150 µg of each of the following plasmids: 1) pAAV-CAG-co*1700040L02Rik*-dmirt or pAAV-CAG-co*Atp4b*-dmirt or pAAV-CAG-Null; 2) a pREP / CAP packaging plasmid coding for the AAV Rep2 and Cap8 genes; and 3) an adenoviral accessory plasmid called pWeiAD containing the genes coding for the helper functions of the adenovirus. Plasmids pREP/CAP and pWeiAD were provided by Dr. K.A. High, from the Children's Hospital of Philadelphia, USA and amplified in Plasmid Factory (*PlasmidFactory GmbH & Co. KG, Bielefeld, NW, DE*). Finally, 16 h post-transfection, IMDM medium was changed to DMEM medium supplemented with 1% Penicillin/Streptomycin (at this point, cells were cultured without FBS).

Three days post-transfection, cells were harvested and centrifuged at 2,500 g for 15 min at 4°C. The medium was stored at 4°C and the cell pellet was resuspended in TMS (50 mM Tris-HCl, 150 mM NaCl, and 2 mM MgCl 2, pH 8.0) and sonicated to lyse the cells and release the cytoplasmatic viral vectors. The lysate was centrifuged at 2,500 g for 30 min and the resulting supernatant was added to the culture medium previously stored at 4°C. Next, the viral particles from the supernatant were precipitated by incubating them during 15h in 8% PEG 8000 (*Sigma-Aldrich Corporation, Saint Louis, MI, US*) at 4°C. After this period, viral vectors were precipitated by centrifugation at 4,000 g for 30 min.

The new pellet, which contained the viral vectors from both the culture medium and the cell lysate, was reconstituted with TMS, treated with benzonane (*Merck KGaA, Darmstadt, HE, DE*) for 1 h at 37°C and finally centrifuged at 10,000 g for 10 min. The resulting supernatant was loaded in 37.5mL ultra-clear tubes (*Beckman Coulter, Brea, CA, USA*) containing a discontinuous gradient of CsCl of density 1.5 (5 ml) and 1.3 g/ml (10 ml). Then, the tubes were centrifuged at 125.000 g for 17 h in an SW32T rotor (*Beckman Coulter, Brea, CA, USA*). The bands containing the vectors (Figure 80) were collected with 18 G needles and transferred to 12.5 mL ultra-clear tubes. CsCl at 1.379 g/mL was used to fill the empty volume of the 12.5 mL tube to generate a continuous gradient (Figure 80). These tubes were centrifuged at 250.000 g in an SW40Ti (*Beckman Coulter, Brea, CA, USA*) rotor for 48 h. Finally, AAV vectors that have encapsidated the transgene (Full capsids), were collected and dialyzed with PBS + 0.001% Pluronic® F68 through a 10 kDa membrane (Slide-A-Lyzer Dialysis Products, *Pierce*, *Thermo Fisher Scientific, Waltham, MA, USA*) and subsequently filtered using 0.22 µm filters (*Millipore, Burlington, MA, USA*).

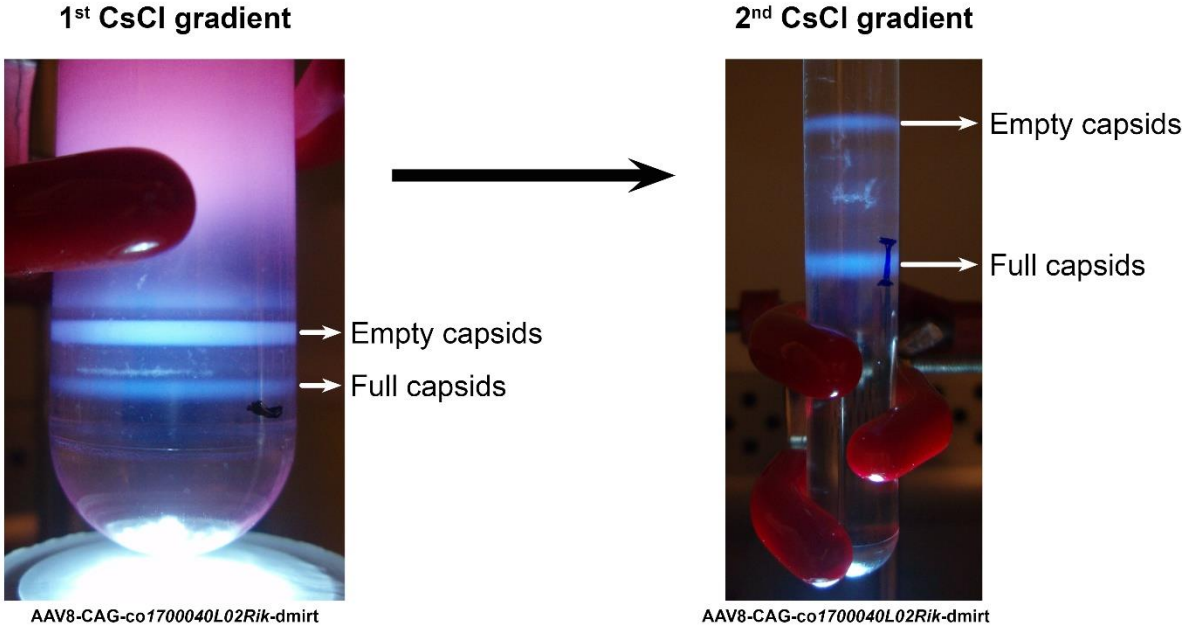


**Figure 80. Purification of AAV vectors**. Representative image of the first and second CsCl gradient, obtained from the purification of AAV8-CAG-co*1700040L02Rik*-dmirt.The first CsCl gradient allows to separate the vectors that contain the transgene (Full capsids), from most impurities and empty capsids. The second gradient of CsCl allows to separate similar density impurities to that of the full AAVs, of intermediate species and of empty AAVs.

### *2.4.2. Titering of viral genomes by PicoGreen*

The viral genomes of the different batches of generated rAAV vectors were determined by *PicoGreen* (*Invitrogen, Carlsbad, CA, USA*). The quantification or titration of each vector was performed in parallel with a reference vector of known concentration to guarantee the validity of the results. *PicoGreen* is a fluorescent probe that has a high sensitivity to double-stranded DNA and emits very little fluorescence in the presence of proteins, single-stranded DNA or RNA. In order to measure viral genomes of the viral vectors with *PicoGreen*, first, the AAV capsids have to be lysed so that the positive and negative single strands encapsidated within the AAV vectors associate together and form double-stranded DNA. DNA of known concentration (lambda phage) supplied by the manufacturer (P11496, *Invitrogen, Carlsbad, CA, USA*) was used to generate a calibration curve.

In order to ensure that the titer of the viral vectors was not overestimated due to the presence of external DNA to the capsids in the final viral preparation, the same vector was processed in parallel without lysis, in order to subtract this contribution to the laboratory encapsidated viral genomes.

Then, in a 0.5 µL microcentrifuge tube, 2 µL of the sample was mixed with 8 µL of PBS + 0.001% PF68 and 10 µL of lysis buffer (20 mM TRIS-HCl, 200 mM NaCl, and 0.2% SDS, pH: 7.4). The mix was incubated 1 h at 70°C (lysed samples). In parallel, the same sample volume was mixed with 8 µl of PBS + 0.001% PF68 and 10 µL of TE. These samples were kept at room temperature (non-lysed samples). Finally, 180 µL of TE were added to both the 20 µL of lysed and non-lysed samples. A serial dilution of the reference DNA was performed with TE to generate a calibration curve.

In a black 96-well plate, 180 µL of *PicoGreen* probe diluted in TE at 1X final concentration was added to each well. Then, 20 µL of each concentration of the reference DNA, 20 µL of the lysed sample and 20 µL of the non-lysed sample were added in triplicate.

The fluorescence was measured at 535 nm with a previous excitation at 485 nm in a Synergy HTX (*BioTek Instrument Inc., Winooski, VT, USA*) fluorometer. To the fluorescence of each digested sample (with the viral genomes forming double-stranded DNA) the fluorescence of the same undigested sample was subtracted (corresponding to the background signal). The fluorescence of the TE (background signal) was then deducted to the fluorescence of the reference DNA.

The concentration of viral genomes per mL was obtained by interpolating the fluorescence from the linear regression of the calibration curve obtained from the different concentrations of the reference DNA and their respective fluorescence. Titers of the different vectors used in this thesis are shown in Table 40.

| Viral vectors | Titer (vg/mL) |
|---|---|
| pAAV-CAG-co*1700040L02Rik*-dmirt | $1.45 \cdot 10^{13}$ |
| pAAV-CAG-co*Atp4b*-dmirt | $5.5 \cdot 10^{13}$ |
| pAAV-CAG-Null | $3.85 \cdot 10^{13}$ |

Table 40. Titers of the AAV vectors used in this thesis

## 2.5. Quantification of viral particles by *Sypro Ruby Protein Gel Staining*

The usage of *SDS-PAGE* protein electrophoresis together with a subsequent analysis with *Sypro Ruby Protein Gel Staining* (*Invitrogen, Carlsbad, CA, USA*) and with the value of viral genomes obtained by PicoGreen, allows calculating the percentage of full vectors (relation: viral genome / viral particles). Furthermore, this method allows visualization in the gel of the degree of contamination of non-viral proteins that could affect the efficiency of transduction *in vivo*.

The appropriate volume of the vector of interest containing $3x10^{10}$ vg and different dilutions of the reference vector of known concentration were mixed with 4x Laemmli buffer to a final volume of 20 µL. After 5 min of boiling, the samples were loaded in a 10% Bis-Tris Gel 15 mm 15-well gel (*Invitrogen, Carlsbad, CA, USA*) and run at 120 V for 2 h and 30 min.

The proteins in the gel were fixed with a mixture of Milli-Q water ($H_2O$), methanol ($CH_3OH$) and acetic acid ($CH_3COOH$). The gel was then incubated in 100 mL of *Sypro Ruby Protein Gel Staining* (*Invitrogen, Carlsbad, CA, USA*) overnight. The next day, the gel was washed with a mixture of Milli-Q water ($H_2O$), methanol ($CH_3OH$) and acetic acid ($CH_3COOH$) and finally only Milli-Q water ($H_2O$). The fluorescence of the proteins was detected with a UV transilluminator.

The titer of the viral particles was obtained by densitometry. From the intensity of the VP3 protein of each dilution of the reference vector, a calibration curve was generated to quantify the viral particles of the different preparations.

## 2.6. Intravenous administration of AAV8

The necessary quantity of the vectors AAV8-CAG-co*1700040L02Rik*-dmirt, AAV8-CAG-co*Atp4b*-dmirt, and AAV8-CAG-Null were diluted depending on the experiment to a final volume of 200 µL with phosphate buffered saline (PBS) with 0.001% F68 Pluronic® (*Gibco, Thermo Fisher Scientific, Waltham, MA, USA*) and administered intravenously in the lateral caudal vein without exerting pressure at the moment of the injection. Prior to administration, the animals were exposed to 250 W infrared light (*Philips, Amsterdam, AMS, NL*) for a few minutes to induce vasodilation and facilitate visualization and access to the caudal vein. To facilitate the injection, the animals were placed in a methacrylate restrainer (*Harvard Apparatus, Cambridge, MA, USA*) to immobilize them.

## 2.7. Determination of food intake

Food intake was determined by calculating the average kilocalories consumed per day per cage, with all the animals in each cage being from the same experimental group. First, the ingested food was obtained by the difference between the amount of food added initially and the food remaining 7 days later. Then, the amount of weekly consumed food was multiplied by the kilocalories of the diet and divided by 7 days. Finally, the average kilocalories consumed per day were calculated.

## 2.8. Isolation of total RNA

Tissue was homogenized in 1 mL of QIAzol (*Qiagen, Hilden, NW, DE*) for adipose depots or 1 mL of Tripure (*Hoffmann-La Roche, Basel, CH*) for other tissues. Next, the *Rneasy Mini Kit* (*Qiagen, Hilden, NW, DE*) was used to extract total RNA. To eliminate possible contaminations of genomic DNA, all samples were treated with DNAse from the *RNase-Free DNase Set* (*Qiagen, Hilden, NW, DE*) in the purification columns. Samples were then eluted in 30 µL of RNase-Free Distilled Water, except those of liver, which as they contained a large amount of RNA were eluted in 50 µL. Finally, the concentration and purity of the extracted RNA were measured by determining the absorbance at 230, 260, and 280 nm with a Nanodrop (ND-1000, *Thermo Fisher Scientific, Waltham, MA, USA*).

## 2.9. Analysis of messenger RNA expression by RT-qPCR

### *2.9.1. Reverse transcription of RNA to complementary DNA*

The commercial kit *Transcriptor First Strand cDNA Synthesis Kit* (*Hoffmann-La Roche, Basel, CH*) and the *Master Cycler Eppendorf Gradient S* thermocycler (*Eppendorf, Hamburg, HH, DE*) were used, following the manufacturer's instructions, to perform a reverse transcription reaction of RNA to obtain complementary DNA (cDNA). A total amount of 1 µg of RNA was mixed with Oligo-dT and random oligonucleotide hexamers as primers of the reaction and was incubated as shown in Table 41 - First incubation. Then, RNase inhibitors, reaction buffer, deoxynucleotides, and the reverse transcriptase were added to the mix and the second stage of incubation was carried out (Table 41 – Second incubation). A sample of each experimental group was used as a negative control of the reaction, as no reverse transcriptase was added to the mix with the aim of detecting possible contamination with genomic DNA of the extracted RNA. Once the reverse transcription was completed, cDNAs were diluted 1/10 and frozen at -20°C.

| | Temperature | Duration |
|---|---|---|
| First incubation | 65ºC | 10 min |
| | 4ºC | Pause |
| Second incubation | 25ºC | 15 min |
| | 55ºC | 45 min |
| | 85ºC | 5 min |
| | 4ºC | Stop |

Table 41. Steps of the Reverse transcription reaction.

### *2.9.2. Real-time quantitative PCR*

Real-time quantitative PCR (RT-qPCR) is the most widely used method for the analysis of mRNA expression. RT-qPCR was performed to quantify the expression of the genes listed below with their respective primers (Table 42), in a LightCycler® 480 Instrument II thermal block cycler (*Hoffmann-La Roche, Basel, CH*) using LightCycler® 480 SYBR Green I Master (*Hoffmann-La Roche, Basel, CH*) as a reagent. SYBR Green I interacts with the secondary structure of the DNA double helix and is energetically coupled to its nucleic acids, significantly increasing its fluorescent emission rate as PCR increases DNA number, which allows quantification.

| Gene | Primer Forward | Primer Reverse |
|---|---|---|
| co*Atp4b* | TGAAGGCCAAGATCCAGAAG | TGCTGATTCTCAGGTTGTGG |
| co*1700040L02Rik* | CTGGAATCCGAGATGAGAGA | TTCTGCATGGAGATCAGCAC |
| *Ucp1* | GGATTGGCCTCTACGACTCAG | TGTAGGCTGCCCAATGAACA |
| *Cidea* | CCTACGACATCCGATGCACA | GTATGTGCCCGCATAGACCA |
| *Ppargc1a* | ATGAATGCAGCGGTCTTAGC | GGACGTCTTTGTGGCTTTTG |
| *Rplp0* | TCCCACCTTGTCTCCAGTCT | ACTGGTCTAGGACCCGAGAAG |

Table 42. List of primers used in RT-qPCR

Each RT-qPCR reaction (LightCycler® 480 SYBR Green I Master, *Hoffmann-La Roche, Basel, CH*) had a final volume of 10 µl, containing (Table 43):

| SYBR Green Reaction |
|---|
| **5 µL** 2x *LightCycler® 480 SYBR Green I Master* |
| **0.2 µL** *primer forward* (10 M) |
| **0.2 µL** *primer reverse* (10 M) |
| **2.6 µL** $H_2O$ Milli-Q |
| **2 µL** cDNA (dil. 1/10) |

Table 43. SYBR Green reaction components

2 µl of diluted cDNA samples were loaded in triplicate into 384-well plates together with 8 µl of the mix containing SYBR Green, primers, and water. Once the plate was loaded, the amplification reaction was carried out with the LightCycler® 480 Instrument II thermal block cycler. This reaction consisted of a 5 min preincubation at 95°C with a temperature variation of 4.8°C/sec for an initial denaturation. Subsequently, 45 cycles of amplification were carried out in 4 stages: denaturation (10 sec at 95°C to 4.8°C/sec), annealing (10 sec at 60°C to 2.5°C/sec), amplification (10 sec at 72°C to 4.8°C/sec) and 30 sec at 60°C. After amplification, a denaturing curve of the amplified or melted DNA was made by performing a temperature ramp of 5 s at 95ºC to 4.8ºC/s, followed by 1 min at 65ºC at 2.5ºC/s to finish at a temperature of 97ºC to 0.11ºC/s. Finally, the plate was cooled down to 4°C with a temperature variation of 2.5°C/s for 30s.

The results of the LightCycler® 480 Instrument II were reviewed and interpreted in order to detect and eliminate possible errors produced when loading the plate or in the amplification process. The mean of the triplicates and their standard deviation were calculated, eliminating those triplicates that presented a standard deviation higher than

0.3. These results were expressed as Cycle threshold or Ct, defined as the fractional PCR cycle in which fluorescence levels intersect the threshold line, which is the level of detection at which a reaction reaches a fluorescent intensity above background levels. Data were normalized by the Cts of a reference gene, in our case the *Rplp0* gene (*Ribosomal protein lateral stalk subunit P0*), of each sample, to quantify the relative expression of the different genes of interest compared to the reference gene. Thus, the delta-delta-Ct ($2^{-\Delta\Delta Ct}$) method described by Livak (Livak and Schmittgen, 2001) was used to calculate the results. In this widely used method, optimal duplication is assumed in each cycle of RT-qPCR with an amplification rate of 100%. The Cts indicates the cycle number to which the amount of the cDNA of the target gene has been amplified and both the test and reference samples are adjusted to the Cts of the normalizing gene. The resulting value serves to determine the difference of expression with respect to a control group. In the case that the control group did not present amplification of Cts, Cts of the gene of interest were normalized directly with Cts of the housekeeping of the sample itself, resulting in arbitrary units of the gene of interest.

## 2.10. Analysis of mRNA expression with microarrays

### *2.10.1. cDNA synthesis and array hybridization*

For the analysis of the mRNA expression, using microarrays, extracted RNA samples were sent to Progenika Biopharma (*Progenika Biopharma, Grifols, Barcelona, CAT, ES*), which measured RNA concentrations with Nanodrop and RNA quality with the Agilent 2100 Bioanalyzer (*Agilent Technologies, Santa Clara, CA, USA*).

From this point, 300ng of RNA were used to synthesize cDNA with the *GeneChip WT Plus Reagent kit* (*Affymetrix, Thermo Fisher Scientific, Waltham, MA, USA*) following the manufacturer's instructions. From the obtained cDNA, 5.5 µg were fragmented using UDG (*Uracil DNA Glycosylase*) and APE1 (*Apurinic/apyrimidinic endonuclease 1*). Fragmented cDNA was then labeled with terminal transferase using the *WT Terminal Labeling kit* (*Affymetrix, Thermo Fisher Scientific, Waltham, MA, USA*).

The *GeneTitan Hybridization Wash and Stain kit* for *WT array plates* (*Affymetrix, Thermo Fisher Scientific, Waltham, MA, USA*) were then used following the manufacturer's instructions. This kit contained a hybridization cocktail which included labeled, fragmented target and hybridization controls. Labeled samples were hybridized to Affymetrix GeneChip™ Mouse Gene 2.1 ST (*Affymetrix, Thermo Fisher Scientific,*

*Waltham, MA, USA*). Finally, the Expression Console™ Software version 1.4.0.38 (Affymetrix, *Thermo Fisher Scientific, Waltham, MA, USA*) was used to perform quality control of the obtained files from the array hybridization.

### *2.10.2. Array normalization*

The Expression Console™ Software version 1.4.0.38 (*Affymetrix*, *Thermo Fisher Scientific, Waltham, MA, USA*) was also used to normalize the data of all the microarrays altogether using the *Robust Multi-array Average* (RMA) algorithm. First, RMA performed a background correction to remove artifacts and noise, and next, it transformed the data to log2 values and data was quantile normalized to compare values across microarrays. Finally, using a linear model, RMA fitted the normalized values to obtain the expression values measured for each probe set on each array. This software was used after normalizing the data to annotate the different probes set values. Finally, expression values were exported to text files.

### *2.10.3. Array quality control*

The Affymetrix GeneChip® technology contains two main types of probes of 25 base pairs (Mei et al., 2003). One probe named "perfect match probes" or PM is designed to be totally complementary to its DNA target. The other probe named "mismatch probes" or MM contains a single mismatch to its DNA target in the middle of the oligonucleotide. This total or partial complementary sequence of the probes ensures a good match between target and probes, detecting cross-activation of probes.

To ensure that all the aforementioned processes were performed properly, quality control of the normalized data was completed using the Expression Console™ Software version 1.4.0.38 (*Affymetrix*, *Thermo Fisher Scientific, Waltham, MA, USA*) (Figure 81). The first set of quality assessment metrics were based on probe level data, in which the mean of the raw intensity for all the PM probes prior to intensity transformation (*PM mean*) and the mean of the raw intensities used to calculate the background prior to intensity transformation (*BGRD mean*) were analyzed. As shown in Figure 81A, all the PM probes and background probe calculations were stable, indicating normal chip brightness and correct background intensities. Next, the probeset summarization-based metrics were assessed (Figure 81B). In this section, the signal values for the positives controls to the

negatives were compared by analyzing the area under the curve (*Pos vs neg AUC*), being 1 a perfect separation and 0.5 no separation. In gene arrays, values between 0.8 and 0.9 are typical, indicating a good quality of the RNA sample. Besides, the mean of the absolute deviation of the residuals from the median was also analyzed (*Mad residual mean*). This analysis, that showed concordance among all the arrays, compared the intensities obtained from large numbers of probes versus the model obtained with the prediction of the RMA algorithm to detect problematic chips. Finally, the mean absolute relative log expression (RLE) was calculated by analyzing the difference in log base 2 between the median signal value for each probeset all over the chips with the estimated signal (*RLE mean*). Moreover, box plots of the relative log expression for all the probesets indicated no outlier chip (Figure 81C), as a box with a median significantly deviated from 0 indicate skewness in the raw intensities not properly corrected by normalization. Our data went through these quality control tests as no chip presented any high difference among the others in any studied parameter.

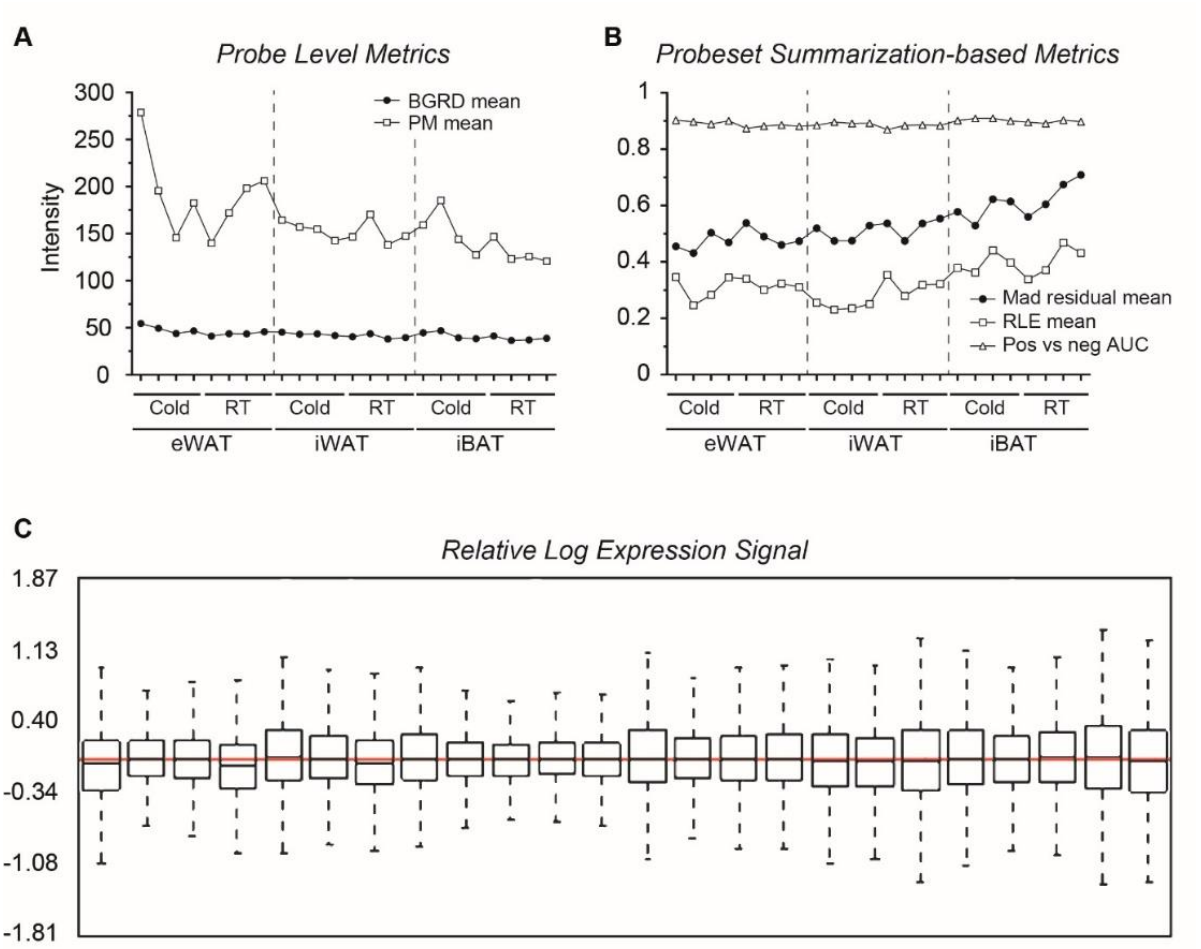


***Figure 81. Quality control assessment of microarray data.*** Several parameters were analyzed as quality control. As quality control on a probe level data, the mean of raw intensity values of perfect match probes prior to intensity transformation (*PM mean*) and the mean of the raw intensities used to calculate the background prior to intensity transformation (*BGRD mean*) were checked **(A)**. Furthermore, the probeset summarization-based metrics were analyzed, checking the area under de curve of the signal values of positive vs negative controls (*Pos vs neg AUC*), the mean of the absolute deviation of the residuals from the median (*Mad residual mean*) and the difference in $\log_2$ between the median signal value for each probeset all over the chips with the estimated signal (*RLE mean*) **(B)**. Finally, a box plots of the relative log expression for all the probeset was also plotted **(C)**.

## 2.11. Histological analysis

Immediately after euthanase, a portion of iBAT, iWAT, eWAT, and liver was fixed in 4% paraformaldehyde for 12-24h, and then were embedded in paraffin and sectioned into 2-3 µm thick sections. The slices were deparaffined by 2 xylol washes for 10 min, 2 washes of 5 min with 100% ethanol and 2 washes of 5 min with 96% ethanol.

Then, the slices were stained with hematoxylin, washed with distilled water and re-stained with eosin. The samples were then dehydrated and mounted on a slide to be analyzed with a Nikon Eclipse E90i microscope (*Nikon, Minato, TYO, JP*) and captured by a video camera Nikon DS-Fi1 (*Nikon, Minato, TYO, JP*) connected to the monitor.

## 2.12. Bioinformatic analysis

### *2.12.1. Differential Expression Analysis*

The Transcriptome Analysis Console (TAC) version 3.1.0.5 (*Affymetrix, Thermo Fisher Scientific, Waltham, MA, USA*) was used to perform statistical tests for differential gene expression. To this aim, expression values exported in *cph* files from the Expression Console™ Software were uploaded to TAC and the different samples from cold or room temperature-exposed mice were compared between them for each tissue independently. Fold change, Anova and FDR values were calculated.

### *2.12.2. Functional analysis*

Gene Ontology (GO) and pathway enrichment analysis of different sets of data were performed using Targetmine (Chen et al., 2011) (https://targetmine.mizuguchilab.org/). The correction of Benjamini Hochberg method was applied to decrease the false discovery rate. The adjusted p-value cut-off was set to 0.05, considering lower values as statistically significant.

To summarize and remove redundant GO terms obtained from the results of TargetMine, the REVIGO algorithm (Supek et al., 2011) implemented in the REVIGO web server (http://revigo.irb.hr/) was used. The version of the Gene Ontology used by REVIGO was the monthly release of January 2017. The remaining terms after removing redundant GO terms were plotted using CirGO Software Version 1.0 01/03/2018 (Kuznetsova et al., 2019) (https://github.com/IrinaVKuznetsova/CirGO). CirGO is a software that allows the visualization of the most enriched GO terms in a comprehensive hierarchically clustering format.

### *2.12.3. Hierarchical clustering analysis*

Hierarchical clustering analysis was performed using the MultiExperimentViewer (Mev) software version 4.9.0 (http://mev.tm4.org/). This analysis was run with average linkage as the linkage method and the distance metric selection was the Euclidean method. For a better clustering and visualization data was mean normalized by the following formula:

$$x' = \frac{x - average\ (x)}{\max(x) - \min(x)}$$

#### *2.12.4. Pattern template matching*

To detect co-expressed genes, data were first mean-normalized as it was done for hierarchical clustering analyses to avoid detecting patterns due to differences in expression levels but to detect expression pattern. Then, the MultiExperimentViewer (Mev) software version 4.9.0 (http://mev.tm4.org/) and its implemented tool Pavlidis template matching (PTM) (Pavlidis and Noble, 2001) were used to calculate the correlation coefficient between the expression pattern of genes used as template and the other genes of the microarray.

### 2.12.5. Exploratory data analysis

#### *2.12.5.1. Principal component analysis*

The principal component analysis was generated using ClustVis (Metsalu and Vilo, 2015) (https://biit.cs.ut.ee/clustvis/). After analyzing the variance captured by each principal component (PC), it was corroborated that plotting PC1 vs PC2 was adequate to capture enough variation.

#### *2.12.5.2. Correlation matrix*

The correlation matrix was generated using Python version 3.7 importing as python libraries: pandas, seaborn and matplotlib with its module pyplot. The correlation coefficients between variables from the expression values exported from the Expression Console™ Software (*Affymetrix*, *Thermo Fisher Scientific, Waltham, MA, USA*) were calculated using the Pearson correlation methods as data had a normal distribution.

### *2.13. Pathway visualization*

Using the "C*olor pathway"* tool of the *KEGG Mapper* (Kanehisa et al., 2012) webpage (https://www.genome.jp/kegg/mapper.html), the differentially expressed genes (DEG) of each adipose depot was mapped into the different KEGG maps. Specifically, the main used maps are summarized in Table 44. The different affected pathways were then reconstructed using Adobe Illustrator CC 2017 software (*Adobe Systems Incorporated, San José, CA, USA*) and colored for each adipose depot depending on the fold change values of the related enzymes.

| KEGG pathway | Name |
|---|---|
| mmu00190 | Oxidative phosphorylation |
| mmu00250 | Alanine, aspartate and glutamate metabolism |
| mmu00280 | Valine, leucine and isoleucine metabolism |
| mmu00620 | Pyruvate metabolism |
| mmu0640 | Propanoate metabolism |
| mmu01100 | Metabolic pathways |
| mmu01200 | Carbon metabolism |
| mmu01212 | Fatty acids metabolism |
| mmu04714 | Thermogenesis |
| mmu00061 | Fatty acids biosynthesis |
| mmu00062 | Fatty acids elongation |
| mmu00071 | Fatty acids degradation |
| mmu00072 | Synthesis and degradation of keton bodies |
| mmu00330 | Arginine and proline metabolism |

Table 44. KEGG pathways used to analyze the different metabolic pathways affected by cold exposure in the different adipose depots.

## 2.14.Statistical analysis

The results were expressed as the mean ± standard error of the mean (SEM). The analysis of the results between the different experimental groups was performed using the two-factor ANOVA table for comparisons of more than 2 groups. The differences were considered significant when $p \leq 0.05$ (95% confidence interval).

# VIII. BIBLIOGRAPHY

Abarca-Gómez, L., Abdeen, Z.A., Hamid, Z.A., Abu-Rmeileh, N.M., Acosta-Cazares, B., Acuin, C., Adams, R.J., Aekplakorn, W., Afsana, K., Aguilar-Salinas, C.A., et al. (2017). Worldwide trends in body-mass index, underweight, overweight, and obesity from 1975 to 2016: a pooled analysis of 2416 population-based measurement studies in 128·9 million children, adolescents, and adults. Lancet 390, 2627–2642.

Adab, P., Pallan, M., and Whincup, P.H. (2018). Is BMI the best measure of obesity? BMJ k1274.

Ahmadian, M., Wang, Y., and Sul, H.S. (2010). Lipolysis in adipocytes. Int. J. Biochem. Cell Biol. 42, 555–559.

Albert, V., Svensson, K., Shimobayashi, M., Colombi, M., Munoz, S., Jimenez, V., Handschin, C., Bosch, F., and Hall, M.N. (2016). mTORC2 sustains thermogenesis via Akt-induced glucose uptake and glycolysis in brown adipose tissue. EMBO Mol. Med. 8, 232–246.

Algire, C., Medrikova, D., and Herzig, S. (2013). White and brown adipose stem cells: From signaling to clinical implications. Biochim. Biophys. Acta - Mol. Cell Biol. Lipids 1831, 896–904.

Alizadeh, A.A., Eisen, M.B., Davis, R.E., Ma, C., Lossos, I.S., Rosenwald, A., Boldrick, J.C., Sabet, H., Tran, T., Yu, X., et al. (2000). Distinct types of diffuse large B-cell lymphoma identified by gene expression profiling. Nature 403, 503–511.

Allegra, S.R., Gmuer, C., and O'Leary, G.P. (1983). Endocrine activity in a large hibernoma. Hum. Pathol. 14, 1044–1052.

American Diabetes Association (2019a). Lifestyle Management: Standards of Medical Care in Diabetes - 2019. Diabetes Care 42, S46–S60.

American Diabetes Association (2019b). Pharmacologic Approaches to Glycemic Treatment: Standards of Medical Care in Diabetes - 2019. Diabetes Care 42, S90–S102.

American Diabetes Association (2019c). Classification and Diagnosis of Diabetes: Standards of Medical Care in Diabetes - 2019. Diabetes Care 42, S13–S28.

American Diabetes Association (2019d). Obesity Management for the Treatment of Type 2 Diabetes: Standards of Medical Care in Diabetes - 2019. Diabetes Care 42, S81–S89.

Anthonsen, M.W., Rönnstrand, L., Wernstedt, C., Degerman, E., and Holm, C. (1998). Identification of Novel Phosphorylation Sites in Hormone-sensitive Lipase That Are Phosphorylated in Response to Isoproterenol and Govern Activation Properties in Vitro. J. Biol. Chem. 273, 215–221.

Arch, J.R.S. (2008). The discovery of drugs for obesity, the metabolic effects of leptin and variable receptor pharmacology: perspectives from β3-adrenoceptor agonists. Naunyn. Schmiedebergs. Arch. Pharmacol. 378, 225–240.

Armani, A., Mammi, C., Marzolla, V., Calanchini, M., Antelmi, A., Rosano, G.M.C., Fabbri, A., and Caprio, M. (2010). Cellular models for understanding adipogenesis, adipose dysfunction, and obesity. J. Cell. Biochem. 110, 564–572.

Arner, P. (1999). Catecholamine-induced lipolysis in obesity. Int. J. Obes. 23, S10–S13.

Arner, P., Petrus, P., Esteve, D., Boulomié, A., Näslund, E., Thorell, A., Gao, H., Dahlman, I., and Rydén, M. (2018). Screening of potential adipokines identifies S100A4 as a marker of pernicious adipose tissue and insulin resistance. Int. J. Obes. 42, 2047–2056.

Aroda, V.R., Edelstein, S.L., Goldberg, R.B., Knowler, W.C., Marcovina, S.M., Orchard, T.J., Bray, G.A., Schade, D.S., Temprosa, M.G., White, N.H., et al. (2016). Long-term Metformin Use and Vitamin B12 Deficiency in the Diabetes Prevention Program Outcomes Study. J. Clin. Endocrinol. Metab. 101, 1754–1761.

Ashcroft, F.M., and Rorsman, P. (2012). Diabetes Mellitus and the β Cell: The Last Ten Years. Cell 148, 1160–1171.

Astrup, A., Carraro, R., Finer, N., Harper, A., Kunesova, M., Lean, M.E.J., Niskanen, L., Rasmussen, M.F., Rissanen, A., Rössner, S., et al. (2012). Safety, tolerability and sustained weight loss over 2 years with the once-daily human GLP-1 analog, liraglutide. Int. J. Obes. 36, 843–854.

Atias, O., Chor, B., and Chamovitz, D.A. (2009). Large-scale analysis of Arabidopsis transcription reveals a basal co-regulation network. BMC Syst. Biol. 3, 86.

Ausina, P., Da Silva, D., Majerowicz, D., Zancan, P., and Sola-Penna, M. (2018). Insulin specifically regulates expression of liver and muscle phosphofructokinase isoforms. Biomed. Pharmacother. 103, 228–233.

Ayuso, E., Mingozzi, F., and Bosch, F. (2010a). Production, Purification and Characterization of Adeno-Associated Vectors. Curr. Gene Ther. 10, 423–436.

Ayuso, E., Mingozzi, F., Montane, J., Leon, X., Anguela, X.M., Haurigot, V., Edmonson, S.A., Africa, L., Zhou, S., High, K.A., et al. (2010b). High AAV vector purity results in serotype- and tissue-independent enhancement of transduction efficiency. Gene Ther. 17, 503–510.

Baba, S., Engles, J.M., Huso, D.L., Ishimori, T., and Wahl, R.L. (2007). Comparison of Uptake of Multiple Clinical Radiotracers into Brown Adipose Tissue Under Cold-Stimulated and Nonstimulated Conditions. J. Nucl. Med. 48, 1715–1723.

Balakrishnan, B., and Jayandharan, G.R. (2014). Basic biology of adeno-associated virus (AAV) vectors used in gene therapy. Curr. Gene Ther. 14, 86–100.

Ballinger, M.A., and Andrews, M.T. (2018). Nature's fat-burning machine: brown adipose tissue in a hibernating mammal. J. Exp. Biol. 221, jeb162586.

Barbatelli, G., Murano, I., Madsen, L., Hao, Q., Jimenez, M., Kristiansen, K., Giacobino, J.P., De Matteis, R., and Cinti, S. (2010). The emergence of cold-induced brown adipocytes in mouse white fat depots is determined predominantly by white to brown adipocyte transdifferentiation. Am J Physiol Endocrinol Metab 298, 1244–1253.

Bartelt, A., Bruns, O.T., Reimer, R., Hohenberg, H., Ittrich, H., Peldschus, K., Kaul, M.G., Tromsdorf, U.I., Weller, H., Waurisch, C., et al. (2011). Brown adipose tissue activity controls triglyceride clearance. Nat. Med. 17, 200–205.

Basse, A.L., Isidor, M.S., Winther, S., Skjoldborg, N.B., Murholm, M., Andersen, E.S., Pedersen, S.B., Wolfrum, C., Quistorff, B., and Hansen, J.B. (2017). Regulation of glycolysis in brown adipocytes by HIF-1α. Sci. Rep. 7, 4052.

Ben-Dor, A., Chor, B., Karp, R., and Yakhini, Z. (2003). Discovering Local Structure in Gene Expression Data: The Order-Preserving Submatrix Problem. J. Comput. Biol. 10, 373–384.

Bhagavan, N.V., and Chung-Eun, H. (2015). Essentials of Medical Biochemistry. In Essentials of Medical Biochemistry, (Elsevier), pp. i–iii.

Billes, S.K., Sinnayah, P., and Cowley, M.A. (2014). Naltrexone/bupropion for obesity: An investigational combination pharmacotherapy for weight loss. Pharmacol. Res. 84, 1–11.

Billings, L.K., and Florez, J.C. (2010). The genetics of type 2 diabetes: What have we learned from GWAS? Ann. N. Y. Acad. Sci. 1212, 59–77.

Birkenfeld, A.L., and Shulman, G.I. (2014). Nonalcoholic fatty liver disease, hepatic insulin resistance, and type 2 Diabetes. Hepatology 59, 713–723.

Birnboim, H.C., and Doly, J. (1979). A rapid alkaline extraction procedure for screening recombinant plasmid DNA. Nucleic Acids Res. 7, 1513–1523.

Black, H. (2003). The burden of cardiovascular disease: following the link from hypertension to myocardial infarction and heart failure. Am. J. Hypertens. 16, 4–6.

Blondin, D.P., Frisch, F., Phoenix, S., Guérin, B., Turcotte, É.E., Haman, F., Richard, D., and Carpentier, A.C. (2017). Inhibition of Intracellular Triglyceride Lipolysis Suppresses Cold-Induced Brown Adipose Tissue Metabolism and Increases Shivering in Humans. Cell Metab. 25, 438–447.

Bond, L.M., Miyazaki, M., O'Neill, L.M., Ding, F., and Ntambi, J.M. (2016). Fatty Acid Desaturation and Elongation in Mammals. In Biochemistry of Lipids, Lipoproteins and Membranes, (Elsevier), pp. 185–208.

Booth, A., Magnuson, A., Fouts, J., and Foster, M.T. (2016). Adipose tissue: an endocrine organ playing a role in metabolic regulation. Horm. Mol. Biol. Clin. Investig. 26, 25–42.

Braga, M., Reddy, S.T., Vergnes, L., Pervin, S., Grijalva, V., Stout, D., David, J., Li, X., Tomasian, V., Reid, C.B., et al. (2014). Follistatin promotes adipocyte differentiation, browning, and energy metabolism. J. Lipid Res. 55, 375–384.

Brondani, L.A., de Souza, B.M., Duarte, G.C.K., Kliemann, L.M., Esteves, J.F., Marcon, A.S., Gross, J.L., Canani, L.H., and Crispim, D. (2012). The UCP1 −3826A/G Polymorphism Is Associated with Diabetic Retinopathy and Increased UCP1 and MnSOD2 Gene Expression in Human Retina. Investig. Opthalmology Vis. Sci. 53, 7449.

Brosnan, J.T., and Brosnan, M.E. (2006). Branched-Chain Amino Acids: Enzyme and Substrate Regulation. J. Nutr. 136, 207S-211S.

Brown, G.C. (1992). Control of respiration and ATP synthesis in mammalian mitochondria and cells. Biochem. J. 284 ( Pt 1, 1–13.

Brunton, S.A. (2015). The potential role of sodium glucose co-transporter 2 inhibitors in the early treatment of type 2 diabetes mellitus. Int. J. Clin. Pract. 69, 1071–1087.

Butler, A.E., Janson, J., Bonner-Weir, S., Ritzel, R., Rizza, R.A., and Butler, P.C. (2003). Beta-cell deficit and increased beta-cell apoptosis in humans with type 2 diabetes. Diabetes 52, 102–110.

Calderon-Dominguez, M., Alcalá, M., Sebastián, D., Zorzano, A., Viana, M., Serra, D., and Herrero, L. (2017). Brown Adipose Tissue Bioenergetics: A New Methodological Approach. Adv. Sci. 4, 1600274.

Cannon, B., and Nedergaard, J. (2004). Brown adipose tissue: function and physiological significance. Physiol. Rev. 84, 277–359.

Carpio, C., Villasante, C., Galera, R., Romero, D., de Cos, A., Hernanz, A., and García-Río, F. (2016). Systemic inflammation and higher perception of dyspnea mimicking asthma in obese subjects. J. Allergy Clin. Immunol. 137, 718-726.e4.

Carriere, A., Jeanson, Y., Berger-Muller, S., Andre, M., Chenouard, V., Arnaud, E., Barreau, C., Walther, R., Galinier, A., Wdziekonski, B., et al. (2014). Browning of White Adipose Cells by Intermediate Metabolites: An Adaptive Mechanism to Alleviate Redox Pressure. Diabetes 63, 3253–3265.

Carter, B.J. (2004). Adeno-associated virus and the development of adeno-associated virus vectors: a historical perspective. Mol. Ther. 10, 981–989.

Caspard, H., Jabbour, S., Hammar, N., Fenici, P., Sheehan, J.J., and Kosiborod, M. (2018). Recent trends in the prevalence of type 2 diabetes and the association with abdominal obesity lead to growing health disparities in the USA: An analysis of the NHANES surveys from 1999 to 2014. Diabetes, Obes. Metab. 20, 667–671.

Cassard-Doulcier, A.-M., Gelly, C., De! Ric Bouillaud, F.!, and Ricquier, D. (1998). A 211-bp enhancer of the rat uncoupling protein-1 (UCP-1) gene controls specific and regulated expression in brown adipose tissue.

Cawthorn, W.P., Scheller, E.L., and MacDougald, O.A. (2012). Adipose tissue stem cells: the great WAT hope. Trends Endocrinol. Metab. 23, 270–277.

Centers for Disease Control and Prevention (2017). National Diabetes Statistics Report, 2017 (Atlanta, GA).

Cereijo, R., Gavaldà-Navarro, A., Cairó, M., Quesada-López, T., Villarroya, J., Morón-Ros, S., Sánchez-Infantes, D., Peyrou, M., Iglesias, R., Mampel, T., et al. (2018). CXCL14, a Brown Adipokine that Mediates Brown-Fat-to-Macrophage Communication in Thermogenic Adaptation. Cell Metab. 28, 750-763.e6.

Cerf, M.E. (2015). High fat programming of beta cell compensation, exhaustion, death and dysfunction. Pediatr. Diabetes 16, 71–78.

Chakrabarti, P., Kim, J.Y., Singh, M., Shin, Y.-K., Kim, J., Kumbrink, J., Wu, Y., Lee, M.-J., Kirsch, K.H., Fried, S.K., et al. (2013). Insulin Inhibits Lipolysis in Adipocytes via the Evolutionarily Conserved mTORC1-Egr1-ATGL-Mediated Pathway. Mol. Cell. Biol. 33, 3659–3666.

Chan, M., Lim, Y.C., Yang, J., Namwanje, M., Liu, L., and Qiang, L. (2019). Identification of a natural beige adipose depot in mice. J. Biol. Chem. 294, 6751–6761.

Chaneton, B., Hillmann, P., Zheng, L., Martin, A.C.L., Maddocks, O.D.K., Chokkathukalam, A., Coyle, J.E., Jankevics, A., Holding, F.P., Vousden, K.H., et al. (2012). Serine is a natural ligand and allosteric activator of pyruvate kinase M2. Nature 491, 458–462.

Chang, B.-D., Swift, M.E., Shen, M., Fang, J., Broude, E. V, and Roninson, I.B. (2002). Molecular determinants of terminal growth arrest induced in tumor cells by a chemotherapeutic agent. Proc. Natl. Acad. Sci. 99, 389–394.

Chartoumpekis, D. V, Habeos, I.G., Ziros, P.G., Psyrogiannis, A.I., Kyriazopoulou, V.E., and Papavassiliou, A.G. (2011). Brown adipose tissue responds to cold and adrenergic stimulation by induction of FGF21. Mol. Med. 17, 736–740.

Chen, Y.-A., Tripathi, L.P., and Mizuguchi, K. (2011). TargetMine, an Integrated Data Warehouse for Candidate Gene Prioritisation and Target Discovery. PLoS One 6, e17844.

Cheng, D. (2005). Prevalence, predisposition and prevention of type II diabetes. Nutr. Metab. (Lond). 2, 29.

Cheng, Y., Jiang, L., Keipert, S., Zhang, S., Hauser, A., Graf, E., Strom, T., Tschöp, M., Jastroch, M., and Perocchi, F. (2018). Prediction of Adipose Browning Capacity by Systematic Integration of Transcriptional Profiles. Cell Rep. 23, 3112–3125.

Chondronikola, M., Volpi, E., Borsheim, E., Porter, C., Annamalai, P., Enerback, S., Lidell, M.E., Saraf, M.K., Labbe, S.M., Hurren, N.M., et al. (2014). Brown Adipose Tissue Improves Whole-Body Glucose Homeostasis and Insulin Sensitivity in Humans. Diabetes 63, 4089–4099.

Chou, J.W., Zhou, T., Kaufmann, W.K., Paules, R.S., and Bushel, P.R. (2007). Extracting gene expression patterns and identifying co-expressed genes from microarray data reveals biologically responsive processes. BMC Bioinformatics 8, 427.

Chusyd, D.E., Wang, D., Huffman, D.M., and Nagy, T.R. (2016). Relationships between Rodent White Adipose Fat Pads and Human White Adipose Fat Depots. Front. Nutr. 3.

Cinti, S. (2005). The adipose organ. Prostaglandins, Leukot. Essent. Fat. Acids 73, 9–15.

Cinti, S. (2009). Transdifferentiation properties of adipocytes in the adipose organ. Am. J. Physiol. Metab. 297, E977–E986.

Cinti, S. (2012). The adipose organ at a glance. Dis. Model. Mech. 5, 588–594.

Cinti, S. (2018). White, brown, beige and pink: A rainbow in the adipose organ. Curr. Opin. Endocr. Metab. Res.

Clapham, J.C., and Arch, J.R.S. (2007). Thermogenic and metabolic antiobesity drugs: rationale and opportunities. Diabetes, Obes. Metab. 9, 259–275.

Cornelis, M.C., Zaitlen, N., Hu, F.B., Kraft, P., and Price, A.L. (2015). Genetic and environmental components of family history in type 2 diabetes. Hum. Genet. 134, 259–267.

Cowie, C., Cowie, C., Casagrande, S., Menke, A., Cissell, M., Eberhardt, M., Meigs, J., Gregg, E., Knowler, W., Barrett-Connor, E., et al. (2017). Classification and Diagnosis of Diabetes. In Diabetes in America, 3rd Ed, (Pub No. 17-1468), p.

Cypess, A.M., Lehman, S., Williams, G., Tal, I., Rodman, D., Goldfine, A.B., Kuo, F.C., Palmer, E.L., Tseng, Y.-H., Doria, A., et al. (2009). Identification and Importance of Brown Adipose Tissue in Adult Humans. N. Engl. J. Med. 360, 1509–1517.

Cypess, A.M., White, A.P., Vernochet, C., Schulz, T.J., Xue, R., Sass, C.A., Huang, T.L., Roberts-Toler, C., Weiner, L.S., Sze, C., et al. (2013). Anatomical localization, gene expression profiling and functional characterization of adult human neck brown fat. Nat. Med. 19, 635–639.

da Silva, F.B.L., Gomes, D.L., and de Carvalho, K.M.B. (2016). Poor diet quality and postoperative time are independent risk factors for weight regain after Roux-en-Y gastric bypass. Nutrition 32, 1250–1253.

de Luis, D.A., Izaola, O., Primo, D., and Aller, R. (2018). Role of rs670 variant of APOA1 gene on lipid profile, insulin resistance and adipokine levels in obese subjects after weight loss with a dietary intervention. Diabetes Res. Clin. Pract. 142, 139–145.

DeFronzo, R.A. (2004). Pathogenesis of type 2 diabetes mellitus. Med. Clin. North Am. 88, 787–835.

Dempersmier, J., Sambeat, A., Gulyaeva, O., Paul, S.M., Hudak, C.S.S., Raposo, H.F., Kwan, H.-Y., Kang, C., Wong, R.H.F., and Sul, H.S. (2015). Cold-Inducible Zfp516 Activates UCP1 Transcription to Promote Browning of White Fat and Development of Brown Fat. Mol. Cell 57, 235–246.

Deyle, D.R., and Russell, D.W. (2009). Adeno-associated virus vector integration. Curr. Opin. Mol. Ther. 11, 442–447.

Dimas, A.S., Lagou, V., Barker, A., Knowles, J.W., Mägi, R., Hivert, M.-F., Benazzo, A., Rybin, D., Jackson, A.U., Stringham, H.M., et al. (2014). Impact of Type 2 Diabetes Susceptibility Variants on Quantitative Glycemic Traits Reveals Mechanistic Heterogeneity. Diabetes 63, 2158–2171.

Donath, M.Y., and Halban, P.A. (2004). Decreased beta-cell mass in diabetes: significance, mechanisms and therapeutic implications. Diabetologia 47, 581–589.

Donath, M.Y., Böni-Schnetzler, M., Ellingsgaard, H., Halban, P.A., and Ehses, J.A. (2010). Cytokine production by islets in health and diabetes: Cellular origin, regulation and function. Trends Endocrinol. Metab. 21, 261–267.

Dooko, C.B.A., De Wit, S., Neuhaus, J., Palfreeman, A., Pepe, R., Pankow, J.S., and Neaton, J.D. (2014). Interleukin-6, High Sensitivity C-Reactive Protein, and the Development of Type 2 Diabetes Among HIV-Positive Patients Taking Antiretroviral Therapy. JAIDS J. Acquir. Immune Defic. Syndr. 67, 538–546.

Doonan, S., Barra, D., and Bossa, F. (1984). Structural and genetic relationships between cytosolic and mitochondrial isoenzymes. Int. J. Biochem. 16, 1193–1199.

Duarte, R.L. de M., and Magalhães-da-Silveira, F.J. (2015). Factors predictive of obstructive sleep apnea in patients undergoing pre-operative evaluation for bariatric surgery and referred to a sleep laboratory for polysomnography. J. Bras. Pneumol. 41, 440–448.

Duncan, R.E., Ahmadian, M., Jaworski, K., Sarkadi-Nagy, E., and Sul, H.S. (2007). Regulation of Lipolysis in Adipocytes. Annu. Rev. Nutr. 27, 79–101.

Dutchak, P.A., Katafuchi, T., Bookout, A.L., Choi, J.H., Yu, R.T., Mangelsdorf, D.J., and Kliewer, S.A. (2012). Fibroblast Growth Factor-21 Regulates PPARγ Activity and the Antidiabetic Actions of Thiazolidinediones. Cell 148, 556–567.

Dyson, P.A. (2010). The therapeutics of lifestyle management on obesity. Diabetes, Obes. Metab. 12, 941–946.

Earley, L.F., Powers, J.M., Adachi, K., Baumgart, J.T., Meyer, N.L., Xie, Q., Chapman, M.S., and Nakai, H. (2017). Adeno-associated Virus (AAV) Assembly-Activating Protein Is Not an Essential Requirement for Capsid Assembly of AAV Serotypes 4, 5, and 11. J. Virol. 91, 1980–1996.

Eknoyan, G. (2007). Adolphe Quetelet (1796 1874) the average man and indices of obesity. Nephrol. Dial. Transplant. 23, 47–51.

Eliassen, A.H., Colditz, G.A., Rosner, B., Willett, W.C., and Hankinson, S.E. (2006). Adult Weight Change and Risk of Postmenopausal Breast Cancer. JAMA 296, 193.

Ellis, J.M., Li, L.O., Wu, P.-C., Koves, T.R., Ilkayeva, O., Stevens, R.D., Watkins, S.M., Muoio, D.M., and Coleman, R.A. (2010). Adipose Acyl-CoA Synthetase-1 Directs Fatty Acids toward ß-Oxidation and Is Required for Cold Thermogenesis. Cell Metab. 12, 53–64.

Enerbäck, S., Jacobsson, A., Simpson, E.M., Guerra, C., Yamashita, H., Harper, M.-E., and Kozak, L.P. (1997). Mice lacking mitochondrial uncoupling protein are cold-sensitive but not obese. Nature 387, 90–94.

Erecińska, M., Deas, J., and Silver, I.A. (2002). The Effect of pH on Glycolysis and Phosphofructokinase Activity in Cultured Cells and Synaptosomes. J. Neurochem. 65, 2765–2772.

Esposito, K., Giugliano, F., Di Palo, C., Giugliano, G., Marfella, R., D'Andrea, F., D'Armiento, M., and Giugliano, D. (2004). Effect of Lifestyle Changes on Erectile Dysfunction in Obese Men. JAMA 291, 2978.

Eto, H., Suga, H., Matsumoto, D., Inoue, K., Aoi, N., Kato, H., Araki, J., and Yoshimura, K. (2009). Characterization of Structure and Cellular Components of Aspirated and Excised Adipose Tissue. Plast. Reconstr. Surg. 124, 1087–1097.

Farmer, S.R. (2006). Transcriptional control of adipocyte formation. Cell Metab. 4, 263–273.

Felson, D.T. (1992). Weight Loss Reduces the Risk for Symptomatic Knee Osteoarthritis in Women. Ann. Intern. Med. 116, 535.

Ferrannini, G., Namwanje, M., Fang, B., Damle, M., Li, D., Liu, Q., Lazar, M.A., and Qiang, L. (2016). Genetic backgrounds determine brown remodeling of white fat in rodents. Mol. Metab. 5, 948–958.

Ferrari, F.K., Samulski, T., Shenk, T., and Samulski, R.J. (1996). Second-strand synthesis is a rate-limiting step for efficient transduction by recombinant adeno-associated virus vectors. J. Virol. 70, 3227–3234.

Ford, G.C., Eichele, G., and Jansonius, J.N. (1980). Three-dimensional structure of a pyridoxal-phosphate-dependent enzyme, mitochondrial aspartate aminotransferase. Proc. Natl. Acad. Sci. U. S. A. 77, 2559–2563.

Gao, G.-P., Alvira, M.R., Wang, L., Calcedo, R., Johnston, J., and Wilson, J.M. Novel adeno-associated viruses from rhesus monkeys as vectors for human gene therapy.

Gesta, S., Tseng, Y.-H., and Kahn, C.R. (2007). Developmental origin of fat: tracking obesity to its source. Cell 131, 242–256.

Ghouri, N., Clifton, P., Craigie, A.M., Anderson, A.S., Christensen, P., Waters, L., Williams, C., Coco, G. Lo, and Ricciardelli, L.A. (2018). Consequences and comorbidities associated with obesity. In Advanced Nutrition and Dietetics in Obesity, K.W.P.R.F. Catherine Hankey PhD RD, ed. (John Wiley & Sons Ltd.), pp. 39–84.

Golay, A., and Ybarra, J. (2005). Link between obesity and type 2 diabetes. Best Pract. Res. Clin. Endocrinol. Metab. 19, 649–663.

Gonçalves, L.F., Machado, T.Q., Castro-Pinheiro, C., de Souza, N.G., Oliveira, K.J., and Fernandes-Santos, C. (2017). Ageing is associated with brown adipose tissue remodelling and loss of white fat browning in female C57BL/6 mice. Int. J. Exp. Pathol. 98, 100–108.

Gonzalez-Hurtado, E., Lee, J., Choi, J., and Wolfgang, M.J. (2018). Fatty acid oxidation is required for active and quiescent brown adipose tissue maintenance and thermogenic programing. Mol. Metab. 7, 45–56.

Gospodarska, E., Nowialis, P., and Kozak, L.P. (2015). Mitochondrial turnover: a phenotype distinguishing brown adipocytes from interscapular brown adipose tissue and white adipose tissue. J. Biol. Chem. 290, 8243–8255.

Graves, R.A., Tontonoz, P., and Spiegelman, B.M. (1992). Analysis of a tissue-specific enhancer: ARF6 regulates adipogenic gene expression. Mol. Cell. Biol. 12, 1202–1208.

Greenway, F.L., Fujioka, K., Plodkowski, R.A., Mudaliar, S., Guttadauria, M., Erickson, J., Kim, D.D., and Dunayevich, E. (2010). Effect of naltrexone plus bupropion on weight loss in overweight and obese adults (COR-I): a multicentre, randomised, double-blind, placebo-controlled, phase 3 trial. Lancet 376, 595–605.

Greenwood, D.C., Threapleton, D.E., Evans, C.E.L., Cleghorn, C.L., Nykjaer, C., Woodhead, C., and Burley, V.J. (2014). Association between sugar-sweetened and artificially sweetened soft drinks and type 2 diabetes: systematic review and dose–response meta-analysis of prospective studies. Br. J. Nutr. 112, 725–734.

Gregg, E.W., Sattar, N., and Ali, M.K. (2016). The changing face of diabetes complications. Lancet Diabetes Endocrinol. 4, 537–547.

Grimpo, K., Völker, M.N., Heppe, E.N., Braun, S., Heverhagen, J.T., and Heldmaier, G. (2014). Brown adipose tissue dynamics in wild-type and UCP1-knockout mice: in vivo insights with magnetic resonance. J. Lipid Res. 55, 398–409.

Guerra, C., Koza, R.A., Walsh, K., Kurtz, D.M., Wood, P.A., and Kozak, L.P. (1998). Abnormal nonshivering thermogenesis in mice with inherited defects of fatty acid oxidation. J. Clin. Invest. 102, 1724–1731.

Guerra, C., Navarro, P., Valverde, A.M., Arribas, M., Brüning, J., Kozak, L.P., Kahn, C.R., and Benito, M. (2001). Brown adipose tissue–specific insulin receptor knockout shows diabetic phenotype without insulin resistance. J. Clin. Invest. 108, 1205–1213.

Guilherme, A., Virbasius, J. V., Puri, V., and Czech, M.P. (2008). Adipocyte dysfunctions linking obesity to insulin resistance and type 2 diabetes. Nat. Rev. Mol. Cell Biol. 9, 367–377.

Gustafson, B., Hedjazifar, S., Gogg, S., Hammarstedt, A., and Smith, U. (2015). Insulin resistance and impaired adipogenesis. Trends Endocrinol. Metab. 26, 193–200.

Hagberg, C.E., Li, Q., Kutschke, M., Bhowmick, D., Kiss, E., Shabalina, I.G., Harms, M.J., Shilkova, O., Kozina, V., Nedergaard, J., et al. (2018). Flow Cytometry of Mouse and Human Adipocytes for the Analysis of Browning and Cellular Heterogeneity. Cell Rep. 24, 2746-2756.e5.

Hajer, G.R., Van Haeften, T.W., and Visseren, F.L.J. (2008). Adipose tissue dysfunction in obesity, diabetes, and vascular diseases. Eur. Heart J. 29, 2959–2971.

Halban, P. a (2008). Cell therapy for type 2 diabetes: is it desirable and can we get it? Diabetes. Obes. Metab. 10 Suppl 4, 205–211.

Hall, M.E., Wang, Z., do Carmo, J., Kamimura, D., and Hall, J.E. (2018). Obesity and Metabolic Syndrome Hypertension. In Disorders of Blood Pressure Regulation Phenotypes, Mechanisms, Therapeutic Options, pp. 705–722.

Hameed, I., Masoodi, S.R., Mir, S.A., Nabi, M., Ghazanfar, K., and Ganai, B.A. (2015). Type 2 diabetes mellitus: From a metabolic disorder to an inflammatory condition. World J. Diabetes 6, 598.

Hansen, J.B., and Kristiansen, K. (2006). Regulatory circuits controlling white versus brown adipocyte differentiation. Biochem. J. 398, 153–168.

Hao, Q., Yadav, R., Basse, A.L., Petersen, S., Sonne, S.B., Rasmussen, S., Zhu, Q., Lu, Z., Wang, J., Audouze, K., et al. (2015a). Transcriptome profiling of brown adipose tissue during cold exposure reveals extensive regulation of glucose metabolism. Am. J. Physiol. Metab. 308, E380–E392.

Harper, A.E., Miller, R.H., and Block, K.P. (1984). Branched-Chain Amino Acid Metabolism. Annu. Rev. Nutr. 4, 409–454.

Hirata, R.K., and Russell, D.W. (2000). Design and packaging of adeno-associated virus gene targeting vectors. J. Virol. 74, 4612–4620.

Hiroshima, Y., Yamamoto, T., Watanabe, M., Baba, Y., and Shinohara, Y. (2018). Effects of cold exposure on metabolites in brown adipose tissue of rats. Mol. Genet. Metab. Reports 15, 36–42.

Ho, K.K.Y. (2018). Diet-induced thermogenesis: fake friend or foe? J. Endocrinol. 238, R185–R191.

Hodson, L. (2014). Adipose tissue oxygenation. Adipocyte 3, 75–80.

Hoene, M., Li, J., Häring, H.-U., Weigert, C., Xu, G., and Lehmann, R. (2014). The lipid profile of brown adipose tissue is sex-specific in mice. Biochim. Biophys. Acta - Mol. Cell Biol. Lipids 1841, 1563–1570.

Holman, R.R., Paul, S.K., Bethel, M.A., Matthews, D.R., and Neil, H.A.W. (2008). 10-Year Follow-up of Intensive Glucose Control in Type 2 Diabetes. N. Engl. J. Med. 359, 1577–1589.

Huang, B., Gudi, R., Wu, P., Harris, R.A., Hamilton, J., and Popov, K.M. (1998). Isoenzymes of pyruvate dehydrogenase phosphatase. DNA-derived amino acid sequences, expression, and regulation. J. Biol. Chem. 273, 17680–17688.

Huang, B., Wu, P., Bowker-Kinley, M.M., and Harris, R.A. (2002). Regulation of pyruvate dehydrogenase kinase expression by peroxisome proliferator-activated receptor-alpha ligands, glucocorticoids, and insulin. Diabetes 51, 276–283.

Huttunen, P., Hirvonen, J., and Kinnula, V. (1981). The occurrence of brown adipose tissue in outdoor workers. Eur. J. Appl. Physiol. Occup. Physiol. 46, 339–345.

Iacobellis, G., Corradi, D., and Sharma, A.M. (2005). Epicardial adipose tissue: anatomic, biomolecular and clinical relationships with the heart. Nat. Clin. Pract. Cardiovasc. Med. 2, 536–543.

Imamura, M., and Maeda, S. (2011). Genetics of type 2 diabetes: the GWAS era and future perspectives. Endocr. J. 58, 723–739.

Inokuma, K. -i., Ogura-Okamatsu, Y., Toda, C., Kimura, K., Yamashita, H., and Saito, M. (2005). Uncoupling Protein 1 Is Necessary for Norepinephrine-Induced Glucose Utilization in Brown Adipose Tissue. Diabetes 54, 1385–1391.

International Diabetes Federation (2017). IDF Diabetes Atlas (Brussels, Belgium).

Inzucchi, S.E., Bergenstal, R.M., Buse, J.B., Diamant, M., Ferrannini, E., Nauck, M., Peters, A.L., Tsapas, A., Wender, R., and Matthews, D.R. (2012). Management of Hyperglycemia in Type 2 Diabetes: A Patient-Centered Approach: Position Statement of the American Diabetes Association (ADA) and the European Association for the Study of Diabetes (EASD). Diabetes Care 35, 1364–1379.

Jackness, C., Karmally, W., Febres, G., Conwell, I.M., Ahmed, L., Bessler, M., McMahon, D.J., and Korner, J. (2013). Very Low–Calorie Diet Mimics the Early Beneficial Effect of Roux-en-Y Gastric Bypass on Insulin Sensitivity and ß-Cell Function in Type 2 Diabetic Patients. Diabetes 62, 3027–3032.

James, D.E., Brown, R., Navarro, J., and Pilch, P.F. (1988). Insulin-regulatable tissues express a unique insulin-sensitive glucose transport protein. Nature 333, 183–185.

Jannasch, F., Kröger, J., and Schulze, M.B. (2017). Dietary Patterns and Type 2 Diabetes: A Systematic Literature Review and Meta-Analysis of Prospective Studies. J. Nutr. 147, 1174–1182.

Jeanguillaume, C., Metrard, G., Ricquier, D., Legras, P., Bouchet, F., Lacoeuille, F., Hindre, F., Morel, O., and Rakotonirina, H. (2013). Visualization of Activated BAT in Mice, with FDG-PET and Its Relation to UCP1. Adv. Mol. Imaging 03, 19–22.

Jeong, J.H., Chang, J.S., and Jo, Y.-H. (2018). Intracellular glycolysis in brown adipose tissue is essential for optogenetically induced nonshivering thermogenesis in mice. Sci. Rep. 8, 6672.

Jespersen, N.Z., Larsen, T.J., Peijs, L., Daugaard, S., Homøe, P., Loft, A., de Jong, J., Mathur, N., Cannon, B., Nedergaard, J., et al. (2013). A Classical Brown Adipose Tissue mRNA Signature Partly Overlaps with Brite in the Supraclavicular Region of Adult Humans. Cell Metab. 17, 798–805.

Jia, R., Luo, X.-Q., Wang, G., Lin, C.-X., Qiao, H., Wang, N., Yao, T., Barclay, J.L., Whitehead, J.P., Luo, X., et al. (2016). Characterization of cold-induced remodelling reveals depot-specific differences across and within brown and white adipose tissues in mice. Acta Physiol. 217, 311–324.

Jimenez, V., Munoz, S., Casana, E., Mallol, C., Elias, I., Jambrina, C., Ribera, A., Ferre, T., Franckhauser, S., and Bosch, F. (2013). In Vivo Adeno-Associated Viral Vector-Mediated Genetic Engineering of White and Brown Adipose Tissue in Adult Mice. Diabetes 62, 4012–4022.

Jimenez, V., Jambrina, C., Casana, E., Sacristan, V., Muñoz, S., Darriba, S., Rodó, J., Mallol, C., Garcia, M., León, X., et al. (2018). FGF21 gene therapy as treatment for obesity and insulin resistance. EMBO Mol. Med. 10, e8791.

Kahn, S.E., Hull, R.L., and Utzschneider, K.M. (2006). Mechanisms linking obesity to insulin resistance and type 2 diabetes. Nature 444, 840–846.

Kalinovich, A. V., de Jong, J.M.A., Cannon, B., and Nedergaard, J. (2017). UCP1 in adipose tissues: two steps to full browning. Biochimie 134, 127–137.

Kanehisa, M., Goto, S., Sato, Y., Furumichi, M., and Tanabe, M. (2012). KEGG for integration and interpretation of large-scale molecular data sets. Nucleic Acids Res. 40, D109–D114.

Kanker, W., and Fonds, O. (2007). Food, Nutrition, Physical Activity, and the Prevention of Cancer: a Global Perspective (Washington DC).

Karaderi, T., Drong, A.W., and Lindgren, C.M. (2015). Insights into the Genetic Susceptibility to Type 2 Diabetes from Genome-Wide Association Studies of Obesity-Related Traits. Curr. Diab. Rep. 15, 83.

Kasim, N.B., Huri, H.Z., Vethakkan, S.R., Ibrahim, L., and Abdullah, B.M. (2016). Genetic polymorphisms associated with overweight and obesity in uncontrolled Type 2 diabetes mellitus. Biomark. Med. 10, 403–415.

Keipert, S., Kutschke, M., Ost, M., Schwarzmayr, T., van Schothorst, E.M., Lamp, D., Brachthäuser, L., Hamp, I., Mazibuko, S.E., Hartwig, S., et al. (2017). Long-Term Cold Adaptation Does Not Require FGF21 or UCP1. Cell Metab. 26, 437-446.e5.

Kir, S., White, J.P., Kleiner, S., Kazak, L., Cohen, P., Baracos, V.E., and Spiegelman, B.M. (2014). Tumour-derived PTH-related protein triggers adipose tissue browning and cancer cachexia. Nature 513, 100–104.

Kirov, S.A., Talan, M.I., Kosheleva, N.A., and Engel, B.T. (1996). Nonshivering thermogenesis during acute cold exposure in adult and aged C57BL/6J mice. Exp. Gerontol. 31, 409–419.

Knowler, W.C., Barrett-Connor, E., Fowler, S.E., Hamman, R.F., Lachin, J.M., Walker, E.A., Nathan, D.M., and Diabetes Prevention Program Research Group (2002). Reduction in the incidence of type 2 diabetes with lifestyle intervention or metformin. N. Engl. J. Med. 346, 393–403.

Kolb, H., and Martin, S. (2017). Environmental/lifestyle factors in the pathogenesis and prevention of type 2 diabetes. BMC Med. 15, 131.

Kopecky, J., Clarke, G., Enerbäck, S., Spiegelman, B., and Kozak, L.P. (1995). Expression of the mitochondrial uncoupling protein gene from the aP2 gene promoter prevents genetic obesity. J. Clin. Invest. 96, 2914–2923.

Koppen, A., and Kalkhoven, E. (2010). Brown vs white adipocytes: The PPARγ coregulator story. FEBS Lett. 584, 3250–3259.

Kotterman, M.A., and Schaffer, D. V (2014). Engineering adeno-associated viruses for clinical gene therapy. Nat. Rev. Genet. 15, 445–451.

Kurokawa, N., Young, E.H., Oka, Y., Satoh, H., Wareham, N.J., Sandhu, M.S., and Loos, R.J.F. (2008). The ADRB3 Trp64Arg variant and BMI: a meta-analysis of 44 833 individuals. Int. J. Obes. 32, 1240–1249.

Kusminski, C.M., Bickel, P.E., and Scherer, P.E. (2016). Targeting adipose tissue in the treatment of obesity-associated diabetes. Nat. Rev. Drug Discov. 15, 639–660.

Kuznetsova, I., Lugmayr, A., Siira, S.J., Rackham, O., and Filipovska, A. (2019). CirGO: an alternative circular way of visualising gene ontology terms. BMC Bioinformatics 20, 84.

Labbé, S.M., Caron, A., Bakan, I., Laplante, M., Carpentier, A.C., Lecomte, R., and Richard, D. (2015). In vivo measurement of energy substrate contribution to cold-induced brown adipose tissue thermogenesis. FASEB J. 29, 2046–2058.

Ladenheim, E. (2015). Liraglutide and obesity: a review of the data so far. Drug Des. Devel. Ther. 1867.

Larose, M., Cassard-Doulcier, A.-M., Fleury, C., Serra, F., Champigny, O., Bouillaud, F., and Ricquier, D. (1996). Essential cis -Acting Elements in Rat Uncoupling Protein Gene Are in an Enhancer Containing a Complex Retinoic Acid Response Domain. J. Biol. Chem. 271, 31533–31542.

Leahy, J.L. (2005). Pathogenesis of Type 2 Diabetes Mellitus. Arch. Med. Res. 36, 197–209.

Lee, J., Ellis, J.M., and Wolfgang, M.J. (2015). Adipose Fatty Acid Oxidation Is Required for Thermogenesis and Potentiates Oxidative Stress-Induced Inflammation. Cell Rep. 10, 266–279.

Lee, P., Bova, R., Schofield, L., Bryant, W., Dieckmann, W., Slattery, A., Govendir, M.A., Emmett, L., and Greenfield, J.R. (2016). Brown Adipose Tissue Exhibits a Glucose-Responsive Thermogenic Biorhythm in Humans. Cell Metab. 23, 602–609.

Lee, P., Smith, S., Linderman, J., Courville, A.B., Brychta, R.J., Dieckmann, W., Werner, C.D., Chen, K.Y., and Celi, F.S. (2014). Temperature-Acclimated Brown Adipose Tissue Modulates Insulin Sensitivity in Humans. Diabetes 63, 3686–3698.

Lee, Y.-H., Petkova, A.P., Mottillo, E.P., and Granneman, J.G. (2012). In Vivo Identification of Bipotential Adipocyte Progenitors Recruited by β3-Adrenoceptor Activation and High-Fat Feeding. Cell Metab. 15, 480–491.

Lehner, R., and Quiroga, A.D. (2016). Fatty Acid Handling in Mammalian Cells. In Biochemistry of Lipids, Lipoproteins and Membranes, (Elsevier), pp. 149–184.

Lerat, H., Imache, M.R., Polyte, J., Gaudin, A., Mercey, M., Donati, F., Baudesson, C., Higgs, M.R., Picard, A., Magnan, C., et al. (2017). Hepatitis C virus induces a prediabetic state by directly impairing hepatic glucose metabolism in mice. J. Biol. Chem. 292, 12860–12873.

Lettieri-Barbato, D. (2019). Redox control of non-shivering thermogenesis. Mol. Metab.

Li, F., Wu, R., Cui, X., Zha, L., Yu, L., Shi, H., and Xue, B. (2016). Histone Deacetylase 1 (HDAC1) Negatively Regulates Thermogenic Program in Brown Adipocytes via Coordinated Regulation of Histone H3 Lysine 27 (H3K27) Deacetylation and Methylation.

Li, H., Malani, N., Hamilton, S.R., Schlachterman, A., Bussadori, G., Edmonson, S.E., Shah, R., Arruda, V.R., Mingozzi, F., Fraser Wright, J., et al. (2011). Assessing the potential for AAV vector genotoxicity in a murine model. Blood 117, 3311–3319.

Li, P., Zhu, Z., Lu, Y., and Granneman, J.G. (2005). Metabolic and cellular plasticity in white adipose tissue II: role of peroxisome proliferator-activated receptor-α. Am. J. Physiol. Metab. 289, E617–E626.

Li, Y., Fromme, T., Schweizer, S., Schottl, T., and Klingenspor, M. (2014). Taking control over intracellular fatty acid levels is essential for the analysis of thermogenic function in cultured primary brown and brite/beige adipocytes. EMBO Rep. 15, 1069–1076.

Lidell, M.E., Betz, M.J., Leinhard, O.D., Heglind, M., Elander, L., Slawik, M., Mussack, T., Nilsson, D., Romu, T., Nuutila, P., et al. (2013). Evidence for two types of brown adipose tissue in humans. Nat. Med.

Lidell, M.E. (2019). Brown Adipose Tissue in Human Infants. Handb. Exp. Pharmacol. 251, 107–123.

Lim, E.L., Hollingsworth, K.G., Aribisala, B.S., Chen, M.J., Mathers, J.C., and Taylor, R. (2011). Reversal of type 2 diabetes: normalisation of beta cell function in association with decreased pancreas and liver triacylglycerol. Diabetologia 54, 2506–2514.

Lim, S., Honek, J., Xue, Y., Seki, T., Cao, Z., Andersson, P., Yang, X., Hosaka, K., and Cao, Y. (2012). Cold-induced activation of brown adipose tissue and adipose angiogenesis in mice. Nat. Protoc. 7, 606–615.

Lin, S.-C., and Li, P. (2004). CIDE-A, a novel link between brown adipose tissue and obesity. Trends Mol. Med. 10, 434–439.

Lisowski, L., Tay, S.S., and Alexander, I.E. (2015). Adeno-associated virus serotypes for gene therapeutics. Curr. Opin. Pharmacol. 24, 59–67.

Liu, X., Magee, D., Wang, C., McMurphy, T., Slater, A., During, M., and Cao, L. (2014). Adipose tissue insulin receptor knockdown via a new primate-derived hybrid recombinant AAV serotype. Mol. Ther. - Methods Clin. Dev. 1, 8.

Liu, X., Wang, S., You, Y., Meng, M., Zheng, Z., Dong, M., Lin, J., Zhao, Q., Zhang, C., Yuan, X., et al. (2015). Brown Adipose Tissue Transplantation Reverses Obesity in Ob/Ob Mice. Endocrinology 156, 2461–2469.

Livak, K.J., and Schmittgen, T.D. (2001). Analysis of Relative Gene Expression Data Using Real-Time Quantitative PCR and the 2 C T Method. METHODS 25, 402–408.

Livhits, M., Mercado, C., Yermilov, I., Parikh, J.A., Dutson, E., Mehran, A., Ko, C.Y., and Gibbons, M.M. (2011). Patient behaviors associated with weight regain after laparoscopic gastric bypass. Obes. Res. Clin. Pract. 5, e258–e265.

Loher, H., Kreis, R., Boesch, C., and Christ, E. (2016). The Flexibility of Ectopic Lipids. Int. J. Mol. Sci. 17, 1554.

López-Soriano, F.J., and Alemany, M. (1987). Effect of cold-temperature exposure and acclimation on amino acid pool changes and enzyme activities of rat brown adipose tissue. Biochim. Biophys. Acta - Gen. Subj. 925, 265–271.

Louis, S.N., Jackman, G.P., Nero, T.L., Iakovidis, D., and Louis, W.J. (2000). Role of beta-adrenergic receptor subtypes in lipolysis. Cardiovasc. Drugs Ther. 14, 565–577.

Lowell, B.B., S-Susulic, V., Hamann, A., Lawitts, J.A., Himms-Hagen, J., Boyer, B.B., Kozak, L.P., and Flier, J.S. (1993). Development of obesity in transgenic mice after genetic ablation of brown adipose tissue. Nature 366, 740–742.

Lu, X., Solmonson, A., Lodi, A., Nowinski, S.M., Sentandreu, E., Riley, C.L., Mills, E.M., and Tiziani, S. (2017). The early metabolomic response of adipose tissue during acute cold exposure in mice. Sci. Rep. 7, 3455.

Mallol, C., Casana, E., Jimenez, V., Casellas, A., Haurigot, V., Jambrina, C., Sacristan, V., Morró, M., Agudo, J., Vilà, L., et al. (2017). AAV-mediated pancreatic overexpression of Igf1 counteracts progression to autoimmune diabetes in mice. Mol. Metab. 6, 664–680.

Marchington, J.M., Mattacks, C.A., and Pond, C.M. (1989). Adipose tissue in the mammalian heart and pericardium: Structure, foetal development and biochemical properties. Comp. Biochem. Physiol. Part B Comp. Biochem. 94, 225–232.

Martino, A.T., Suzuki, M., Markusic, D.M., Zolotukhin, I., Ryals, R.C., Moghimi, B., Ertl, H.C.J., Muruve, D.A., Lee, B., and Herzog, R.W. (2011). The genome of self-complementary adeno-associated viral vectors increases Toll-like receptor 9-dependent innate immune responses in the liver. Blood 117, 6459–6468.

Matsushita, M., Yoneshiro, T., Aita, S., Kameya, T., Sugie, H., and Saito, M. (2014). Impact of brown adipose tissue on body fatness and glucose metabolism in healthy humans. Int. J. Obes. 38, 812–817.

McCarty, D.M., Monahan, P.E., and Samulski, R.J. (2001). Self-complementary recombinant adeno-associated virus (scAAV) vectors promote efficient transduction independently of DNA synthesis. Gene Ther. 8, 1248–1254.

McCarty, D.M., Young, S.M., and Samulski, R.J. (2004). Integration of adeno-associated virus (AAV) and recombinant AAV vectors. Annu. Rev. Genet. 38, 819–845.

McCarty, D.M. (2008). Self-complementary AAV Vectors; Advances and Applications. Mol. Ther. 16, 1648–1656.

McGarry, J.D. (2002). Banting Lecture 2001: Dysregulation of Fatty Acid Metabolism in the Etiology of Type 2 Diabetes. Diabetes 51, 7–18.

McNelis, J.C., and Olefsky, J.M. (2014). Macrophages, Immunity, and Metabolic Disease. Immunity 41, 36–48.

Mei, R., Hubbell, E., Bekiranov, S., Mittmann, M., Christians, F.C., Shen, M.-M., Lu, G., Fang, J., Liu, W.-M., Ryder, T., et al. (2003). Probe selection for high-density oligonucleotide arrays. Proc. Natl. Acad. Sci. 100, 11237–11242.

Mekonnen, T., Tariku, A., and Abebe, S.M. (2018). Overweight/obesity among school aged children in Bahir Dar City: cross sectional study. Ital. J. Pediatr. 44, 17.

Metsalu, T., and Vilo, J. (2015). ClustVis: a web tool for visualizing clustering of multivariate data using Principal Component Analysis and heatmap. Nucleic Acids Res. 43, W566–W570.

Miller, D.G., Petek, L.M., and Russell, D.W. (2004). Adeno-associated virus vectors integrate at chromosome breakage sites. Nat. Genet. 36, 767–773.

Mo, Q., Salley, J., Roshan, T., Baer, L.A., May, F.J., Jaehnig, E.J., Lehnig, A.C., Guo, X., Tong, Q., Nuotio-Antar, A.M., et al. (2017). Identification and characterization of a supraclavicular brown adipose tissue in mice. JCI Insight 2.

Moisan, A., Lee, Y.-K., Zhang, J.D., Hudak, C.S., Meyer, C.A., Prummer, M., Zoffmann, S., Truong, H.H., Ebeling, M., Kiialainen, A., et al. (2014). White-to-brown metabolic conversion of human adipocytes by JAK inhibition. Nat. Cell Biol. 17, 57–67.

Morais, M., Faria, G., Preto, J., and Costa-Maia, J. (2016). Gallstones and Bariatric Surgery: To Treat or Not to Treat? World J. Surg. 40, 2904–2910.

Morris, A.P., Voight, B.F., Teslovich, T.M., Ferreira, T., Segrè, A. V, Steinthorsdottir, V., Strawbridge, R.J., Khan, H., Grallert, H., Mahajan, A., et al. (2012). Large-scale association analysis provides insights into the genetic architecture and pathophysiology of type 2 diabetes. Nat. Genet. 44, 981–990.

Moura, M.A.F., Festuccia, W.T.L., Kawashita, N.H., Garófalo, M.A.R., Brito, S.R.C., Kettelhut, I.C., and Migliorini, R.H. (2005). Brown adipose tissue glyceroneogenesis is activated in rats exposed to cold. Pflugers Arch. - Eur. J. Physiol. 449, 463–469.

Mulvihill, E.E., and Drucker, D.J. (2014). Pharmacology, Physiology, and Mechanisms of Action of Dipeptidyl Peptidase-4 Inhibitors. Endocr. Rev. 35, 992–1019.

Murano, I., Barbatelli, G., Giordano, A., and Cinti, S. (2009). Noradrenergic parenchymal nerve fiber branching after cold acclimatisation correlates with brown adipocyte density in mouse adipose organ. J. Anat. 214, 171–178.

Murín, R., Mohammadi, G., Leibfritz, D., and Hamprecht, B. (2009). Glial Metabolism of Valine. Neurochem. Res. 34, 1195–1203.

Muthuri, S.K., Francis, C.E., Wachira, L.-J.M., LeBlanc, A.G., Sampson, M., Onywera, V.O., and Tremblay, M.S. (2014). Evidence of an Overweight/Obesity Transition among School-Aged Children and Youth in Sub-Saharan Africa: A Systematic Review. PLoS One 9, e92846.

Naumer, M., Sonntag, F., Schmidt, K., Nieto, K., Panke, C., Davey, N.E., Popa-Wagner, R., and Kleinschmidt, J.A. (2012). Properties of the Adeno-Associated Virus Assembly-Activating Protein. J. Virol. 86, 13038–13048.

Nedergaard, J., Alexson, S., and Cannon, B. (1980). Cold adaptation in the rat: increased brown fat peroxisomal beta-oxidation relative to maximal mitochondrial oxidative capacity. Am. J. Physiol. Physiol. 239, C208–C216.

Nedergaard, J., and Cannon, B. (2013). UCP1 mRNA does not produce heat. Biochim. Biophys. Acta - Mol. Cell Biol. Lipids 1831, 943–949.

Ng, M.C.Y. (2015). Genetics of Type 2 Diabetes in African Americans. Curr. Diab. Rep. 15, 74.

Nie, Y., Yan, Z., Yan, W., Xia, Q., and Zhang, Y. (2015). Cold exposure stimulates lipid metabolism, induces inflammatory response in the adipose tissue of mice and promotes the osteogenic differentiation of BMMSCs via the p38 MAPK pathway in vitro.

Nolan, C.J., Damm, P., and Prentki, M. (2011). Type 2 diabetes across generations: From pathophysiology to prevention and management. Lancet 378, 169–181.

O'Neill, S.M., Hinkle, C., Chen, S.-J., Sandhu, A., Hovhannisyan, R., Stephan, S., Lagor, W.R., Ahima, R.S., Johnston, J.C., and Reilly, M.P. (2014). Targeting adipose tissue via systemic gene therapy. Gene Ther. 21, 653–661.

Odom, J., Zalesin, K.C., Washington, T.L., Miller, W.W., Hakmeh, B., Zaremba, D.L., Altattan, M., Balasubramaniam, M., Gibbs, D.S., Krause, K.R., et al. (2010). Behavioral Predictors of Weight Regain after Bariatric Surgery. Obes. Surg. 20, 349–356.

Ohno, H., Shinoda, K., Spiegelman, B.M., and Kajimura, S. (2012). PPARγ agonists Induce a White-to-Brown Fat Conversion through Stabilization of PRDM16 Protein. Cell Metab. 15, 395–404.

Okabe, M., Ikawa, M., Kominami, K., Nakanishi, T., and Nishimune, Y. (1997). 'Green mice' as a source of ubiquitous green cells. FEBS Lett. 407, 313–319.

Okada, K., LeClair, K.B., Zhang, Y., Li, Y., Ozdemir, C., Krisko, T.I., Hagen, S.J., Betensky, R.A., Banks, A.S., and Cohen, D.E. (2016). Thioesterase superfamily member 1 suppresses cold thermogenesis by limiting the oxidation of lipid droplet-derived fatty acids in brown adipose tissue. Mol. Metab. 5, 340–351.

Olds, T., Maher, C., Zumin, S., Péneau, S., Lioret, S., Castetbon, K., Bellisle, de Wilde, J., Hohepa, M., Maddison, R., et al. (2011). Evidence that the prevalence of childhood overweight is plateauing: data from nine countries. Int. J. Pediatr. Obes. 6, 342–360.

Orava, J., Nuutila, P., Lidell, M.E., Oikonen, V., Noponen, T., Viljanen, T., Scheinin, M., Taittonen, M., Niemi, T., Enerbäck, S., et al. (2011). Different Metabolic Responses of Human Brown Adipose Tissue to Activation by Cold and Insulin. Cell Metab. 14, 272–279.

Ouellet, V., Labbé, S.M., Blondin, D.P., Phoenix, S., Guérin, B., Haman, F., Turcotte, E.E., Richard, D., and Carpentier, A.C. (2012). Brown adipose tissue oxidative metabolism contributes to energy expenditure during acute cold exposure in humans. J. Clin. Invest. 122, 545–552.

Pacak, C.A., Mah, C.S., Thattaliyath, B.D., Conlon, T.J., Lewis, M.A., Cloutier, D.E., Zolotukhin, I., Tarantal, A.F., and Byrne, B.J. (2006). Recombinant Adeno-Associated Virus Serotype 9 Leads to Preferential Cardiac Transduction In Vivo. Circ. Res. 99.

Park, A. (2014). Distinction of white, beige and brown adipocytes derived from mesenchymal stem cells. World J. Stem Cells 6, 33.

Paschos, G.K., Tang, S.Y., Theken, K.N., Li, X., Verginadis, I., Lekkas, D., Herman, L., Yan, W., Lawson, J., and FitzGerald, G.A. (2018). Cold-Induced Browning of Inguinal White Adipose Tissue Is Independent of Adipose Tissue Cyclooxygenase-2. Cell Rep. 24, 809–814.

Pastors, J.G., Warshaw, H., Daly, A., Franz, M., and Kulkarni, K. (2002). The Evidence for the Effectiveness of Medical Nutrition Therapy in Diabetes Management. Diabetes Care 25, 608–613.

Pavlidis, P., and Noble, W.S. (2001). Analysis of strain and regional variation in gene expression in mouse brain. Genome Biol. 2, RESEARCH0042.

Petersen, C., Nielsen, M.D., Andersen, E.S., Basse, A.L., Isidor, M.S., Markussen, L.K., Viuff, B.M., Lambert, I.H., Hansen, J.B., and Pedersen, S.F. (2017). MCT1 and MCT4 Expression and Lactate Flux Activity Increase During White and Brown Adipogenesis and Impact Adipocyte Metabolism. Sci. Rep. 7, 13101.

Petrovic, N., Walden, T.B., Shabalina, I.G., Timmons, J.A., Cannon, B., and Nedergaard, J. (2010). Chronic Peroxisome Proliferator-activated Receptor γ (PPARγ) Activation of Epididymally Derived White Adipocyte Cultures Reveals a Population of Thermogenically Competent, UCP1-containing Adipocytes Molecularly Distinct from Classic Brown Adipocytes. J. Biol. Chem. 285, 7153–7164.

Pi-Sunyer, X., Astrup, A., Fujioka, K., Greenway, F., Halpern, A., Krempf, M., Lau, D.C.W., le Roux, C.W., Violante Ortiz, R., Jensen, C.B., et al. (2015). A Randomized, Controlled Trial of 3.0 mg of Liraglutide in Weight Management. N. Engl. J. Med. 373, 11–22.

Pond, C.M. (1992). An evolutionary and functional view of mammalian adipose tissue. Proc. Nutr. Soc. 51, 367–377.

Prasad, R.B., and Groop, L. (2015). Genetics of type 2 diabetes—pitfalls and possibilities. Genes (Basel). 6, 87–123.

Printz, R.L., Koch, S., Potter, L.R., O'Doherty, R.M., Tiesinga, J.J., Moritz, S., and Granner, D.K. (1993). Hexokinase II mRNA and gene structure, regulation by insulin, and evolution. J. Biol. Chem. 268, 5209–5219.

Prusiner, S.B., Cannon, B., and Lindberg, O. (1968). Oxidative metabolism in cells isolated from brown adipose tissue. 1. Catecholamine and fatty acid stimulation of respiration. Eur. J. Biochem. 6, 15–22.

Pryor, R., and Cabreiro, F. (2015). Repurposing metformin: an old drug with new tricks in its binding pockets. Biochem. J. 471, 307–322.

Rajakumari, S., Wu, J., Ishibashi, J., Lim, H.-W., Giang, A.-H., Won, K.-J., Reed, R.R., and Seale, P. (2013). EBF2 Determines and Maintains Brown Adipocyte Identity. Cell Metab. 17, 562–574.

Rao, R.R., Long, J.Z., White, J.P., Svensson, K.J., Lou, J., Lokurkar, I., Jedrychowski, M.P., Ruas, J.L., Wrann, C.D., Lo, J.C., et al. (2014). Meteorin-like Is a Hormone that Regulates Immune-Adipose Interactions to Increase Beige Fat Thermogenesis. Cell 157, 1279–1291.

Reaven, G.M., Hollenbeck, C., Jeng, C.Y., Wu, M.S., and Chen, Y.D. (1988). Measurement of plasma glucose, free fatty acid, lactate, and insulin for 24 h in patients with NIDDM. Diabetes 37, 1020–1024.

Renehan, A.G., Tyson, M., Egger, M., Heller, R.F., and Zwahlen, M. (2008). Body-mass index and incidence of cancer: a systematic review and meta-analysis of prospective observational studies. Lancet 371, 569–578.

Rivera, J.Á., de Cossío, T.G., Pedraza, L.S., Aburto, T.C., Sánchez, T.G., and Martorell, R. (2014). Childhood and adolescent overweight and obesity in Latin America: a systematic review. Lancet Diabetes Endocrinol. 2, 321–332.

Robiou-du-Pont, S., Bonnefond, A., Yengo, L., Vaillant, E., Lobbens, S., Durand, E., Weill, J., Lantieri, O., Balkau, B., Charpentier, G., et al. (2013). Contribution of 24 obesity-associated genetic variants to insulin resistance, pancreatic beta-cell function and type 2 diabetes risk in the French population. Int. J. Obes. 37, 980–985.

Rodriguez, A.R., Plascencia-Villa, G., Witt, C.M., Yu, J.-J., José-Yacamán, M., Chambers, J.P., Perry, G., Guentzel, M.N., and Arulanandam, B.P. (2015). Chlamydia pneumoniae promotes dysfunction of pancreatic beta cells. Cell. Immunol. 295, 83–91.

Rosell, M., Kaforou, M., Frontini, A., Okolo, A., Chan, Y.-W., Nikolopoulou, E., Millership, S., Fenech, M.E., MacIntyre, D., Turner, J.O., et al. (2014). Brown and white adipose tissues: intrinsic differences in gene expression and response to cold exposure in mice. Am. J. Physiol. Metab. 306, E945–E964.

Rosen, E.D., and Spiegelman, B.M. (2000). Molecular regulation of adipogenesis. Annu. Rev. Cell Dev. Biol. 16, 145–171.

Rosengren, A.H., Braun, M., Mahdi, T., Andersson, S.A., Travers, M.E., Shigeto, M., Zhang, E., Almgren, P., Ladenvall, C., Axelsson, A.S., et al. (2012). Reduced Insulin Exocytosis in Human Pancreatic -Cells With Gene Variants Linked to Type 2 Diabetes. Diabetes 61, 1726–1733.

Ross, S.R., Graves, R.A., Greenstein, A., Platt, K.A., Shyu, H.L., Mellovitz, B., and Spiegelman, B.M. (1990). A fat-specific enhancer is the primary determinant of gene expression for adipocyte P2 in vivo. Proc. Natl. Acad. Sci. U. S. A. 87, 9590–9594.

Rothberg, A.E., McEwen, L.N., Kraftson, A.T., Fowler, C.E., and Herman, W.H. (2014). Very-low-energy diet for type 2 diabetes: An underutilized therapy? J. Diabetes Complications 28, 506–510.

Rowland, L.A., Bal, N.C., Kozak, L.P., and Periasamy, M. (2015). Uncoupling Protein 1 and Sarcolipin Are Required to Maintain Optimal Thermogenesis, and Loss of Both Systems Compromises Survival of Mice under Cold Stress. J. Biol. Chem. 290, 12282–12289.

Saito, M., Okamatsu-Ogura, Y., Matsushita, M., Watanabe, K., Yoneshiro, T., Nio-Kobayashi, J., Iwanaga, T., Miyagawa, M., Kameya, T., Nakada, K., et al. (2009). High Incidence of Metabolically Active Brown Adipose Tissue in Healthy Adult Humans: Effects of Cold Exposure and Adiposity. Diabetes 58, 1526–1531.

Sam, S. (2018). Differential effect of subcutaneous abdominal and visceral adipose tissue on cardiometabolic risk. Horm. Mol. Biol. Clin. Investig. 33, 1–9.

Samulski, R.J., Berns, K.I., Tan, M., and Muzyczka, N. (1982). Cloning of adeno-associated virus into pBR322: rescue of intact virus from the recombinant plasmid in human cells. Proc. Natl. Acad. Sci. U. S. A. 79, 2077–2081.

Samulski, R.J., and Muzyczka, N. (2014). AAV-Mediated Gene Therapy for Research and Therapeutic Purposes. Annu. Rev. Virol. *1*, 427–451.

Sattar, N., and Gill, J.M. (2014). Type 2 diabetes as a disease of ectopic fat? BMC Med. 12, 123.

Scallan, C.D. (2006). Human immunoglobulin inhibits liver transduction by AAV vectors at low AAV2 neutralizing titers in SCID mice. Blood 107, 1810–1817.

Schäfer, S.A., Machicao, F., Fritsche, A., Häring, H.U., and Kantartzis, K. (2011). New type 2 diabetes risk genes provide new insights in insulin secretion mechanisms. Diabetes Res. Clin. Pract. 93, S9–S24.

Schreiber, R., Diwoky, C., Schoiswohl, G., Feiler, U., Wongsiriroj, N., Abdellatif, M., Kolb, D., Hoeks, J., Kershaw, E.E., Sedej, S., et al. (2017). Cold-Induced Thermogenesis Depends on ATGL-Mediated Lipolysis in Cardiac Muscle, but Not Brown Adipose Tissue. Cell Metab. 26, 753-763.e7.

Schulz, T.J., Huang, T.L., Tran, T.T., Zhang, H., Townsend, K.L., Shadrach, J.L., Cerletti, M., McDougall, L.E., Giorgadze, N., Tchkonia, T., et al. (2011). Identification of inducible brown adipocyte progenitors residing in skeletal muscle and white fat. Proc. Natl. Acad. Sci. 108, 143–148.

Schwingshackl, L., Hoffmann, G., Lampousi, A.-M., Knüppel, S., Iqbal, K., Schwedhelm, C., Bechthold, A., Schlesinger, S., and Boeing, H. (2017). Food groups and risk of type 2 diabetes mellitus: a systematic review and meta-analysis of prospective studies. Eur. J. Epidemiol. 32, 363–375.

Seale, P., Kajimura, S., Yang, W., Chin, S., Rohas, L.M., Uldry, M., Tavernier, G., Langin, D., and Spiegelman, B.M. (2007). Transcriptional Control of Brown Fat Determination by PRDM16. Cell Metab. 6, 38–54.

Seale, P., Conroe, H.M., Estall, J., Kajimura, S., Frontini, A., Ishibashi, J., Cohen, P., Cinti, S., and Spiegelman, B.M. (2011). Prdm16 determines the thermogenic program of subcutaneous white adipose tissue in mice. J. Clin. Invest. 121, 96–105.

Segula, D. (2014). Complications of obesity in adults: a short review of the literature. Malawi Med. J. 26, 20–24.

Seino, Y., Fukushima, M., and Yabe, D. (2010). GIP and GLP-1, the two incretin hormones: Similarities and differences. J. Diabetes Investig. 1, 8–23.

Serin, E.A.R., Nijveen, H., Hilhorst, H.W.M., and Ligterink, W. (2016). Learning from Co-expression Networks: Possibilities and Challenges. Front. Plant Sci. 7, 1–18.

Sharp, L.Z., Shinoda, K., Ohno, H., Scheel, D.W., Tomoda, E., Ruiz, L., Hu, H., Wang, L., Pavlova, Z., Gilsanz, V., et al. (2012). Human BAT Possesses Molecular Signatures That Resemble Beige/Brite Cells. PLoS One 7, e49452.

Shimizu, Y., Nikami, H., Tsukazaki, K., Machado, U.F., Yano, H., Seino, Y., and Saito, M. (1993). Increased expression of glucose transporter GLUT-4 in brown adipose tissue of fasted rats after cold exposure. Am. J. Physiol. Metab. 264, E890–E895.

Shimizu, I., Aprahamian, T., Kikuchi, R., Shimizu, A., Papanicolaou, K.N., MacLauchlan, S., Maruyama, S., and Walsh, K. (2014). Vascular rarefaction mediates whitening of brown fat in obesity. J. Clin. Invest. 124, 2099–2112.

Shin, H., Ma, Y., Chanturiya, T., Cao, Q., Wang, Y., Kadegowda, A.K.G., Jackson, R., Rumore, D., Xue, B., Shi, H., et al. (2017). Lipolysis in Brown Adipocytes Is Not Essential for Cold-Induced Thermogenesis in Mice. Cell Metab. 26, 764-777.e5.

Shinoda, K., Luijten, I.H.N., Hasegawa, Y., Hong, H., Sonne, S.B., Kim, M., Xue, R., Chondronikola, M., Cypess, A.M., Tseng, Y.-H., et al. (2015). Genetic and functional characterization of clonally derived adult human brown adipocytes HHS Public Access. Nat Med 21, 389–394.

Shore, A.M., Karamitri, A., Kemp, P., Speakman, J.R., and Graham, N.S. (2013). Cold-Induced Changes in Gene Expression in Brown Adipose Tissue, White Adipose Tissue and Liver. PLoS One 8, 68933.

Smith, R.E., Roberts, J.C., and Hittelman, K.J. (1966). Nonphosphorylating Respiration of Mitochondria from Brown Adipose Tissue of Rats. Science (80-. ). 154, 653–654.

Smith, R.H. (2008). Adeno-associated virus integration: virus versus vector. Gene Ther. 15, 817–822.

Smith, R.J., Nathan, D.M., Arslanian, S.A., Groop, L., Rizza, R.A., and Rotter, J.I. (2010a). Individualizing Therapies in Type 2 Diabetes Mellitus Based on Patient Characteristics: What We Know and What We Need to Know. J. Clin. Endocrinol. Metab. 95, 1566–1574.

Smith, S.R., Weissman, N.J., Anderson, C.M., Sanchez, M., Chuang, E., Stubbe, S., Bays, H., and Shanahan, W.R. (2010b). Multicenter, Placebo-Controlled Trial of Lorcaserin for Weight Management. N. Engl. J. Med. 363, 245–256.

Smorlesi, A., Frontini, A., Giordano, A., and Cinti, S. (2012). The adipose organ: white-brown adipocyte plasticity and metabolic inflammation. Obes. Rev. 13, 83–96.

Snyder, R.O., Audit, M., and Francis, J.D. (2011). rAAV vector product characterization and stability studies. Methods Mol. Biol. 807, 405–428.

Song, Y.-M., Sung, J., Smith, G.D., and Ebrahim, S. (2004). Body Mass Index and Ischemic and Hemorrhagic Stroke. Stroke 35, 831–836.

Sonntag, F., Schmidt, K., and Kleinschmidt, J.A. (2010). A viral assembly factor promotes AAV2 capsid formation in the nucleolus. Proc. Natl. Acad. Sci. 107, 10220–10225.

Sramkova, D., Krejbichova, S., Vcelak, J., Vankova, M., Samalikova, P., Hill, M., Kvasnickova, H., Dvorakova, K., Vondra, K., Hainer, V., et al. (2007). The UCP1 gene polymorphism A-3826G in relation to DM2 and body composition in Czech population. Exp. Clin. Endocrinol. Diabetes 115, 303–307.

Srivastava, A., Lusby, E.W., and Berns, K.I. (1983). Nucleotide sequence and organization of the adeno-associated virus 2 genome. J. Virol. 45, 555–564.

Srivastava, A. (2016). In vivo tissue-tropism of adeno-associated viral vectors. Curr. Opin. Virol. 21, 75–80.

Stefan, N., Pfannenberg, C., and Häring, H.-U. (2009). The importance of brown adipose tissue. N. Engl. J. Med. 361, 416–417; author reply 418-21.

Steinthorsdottir, V., Thorleifsson, G., Sulem, P., Helgason, H., Grarup, N., Sigurdsson, A., Helgadottir, H.T., Johannsdottir, H., Magnusson, O.T., Gudjonsson, S.A., et al. (2014). Identification of low-frequency and rare sequence variants associated with elevated or reduced risk of type 2 diabetes. Nat. Genet. 46, 294–298.

Strissel, K.J., Denis, G. V, and Nikolajczyk, B.S. (2014). Immune regulators of inflammation in obesity-associated type 2 diabetes and coronary artery disease. Curr. Opin. Endocrinol. Diabetes Obes. 21, 330–338.

Sumithran, P., and Proietto, J. (2014). Benefit-Risk Assessment of Orlistat in the Treatment of Obesity. Drug Saf. 37, 597–608.

Sun, K., Kusminski, C.M., Luby-Phelps, K., Spurgin, S.B., An, Y.A., Wang, Q.A., Holland, W.L., and Scherer, P.E. (2014). Brown adipose tissue derived VEGF-A modulates cold tolerance and energy expenditure. Mol. Metab. 3, 474–483.

Sun, P., Tan, X., Guo, S., Zhang, J., Sun, B., Du, N., Wang, H., and Sun, H. (2018). Protein Function Prediction Using Function Associations in Protein–Protein Interaction Network. IEEE Access 6, 30892–30902.

Supek, F., Bošnjak, M., Škunca, N., and Šmuc, T. (2011). REVIGO Summarizes and Visualizes Long Lists of Gene Ontology Terms. PLoS One 6, e21800.

Surwit, R.S., Wang, S., Petro, A.E., Sanchis, D., Raimbault, S., Ricquier, D., and Collins, S. (1998). Diet-induced changes in uncoupling proteins in obesity-prone and obesity-resistant strains of mice. Proc. Natl. Acad. Sci. U. S. A. 95, 4061–4065.

Sustarsic, E.G., Ma, T., Lynes, M.D., Larsen, M., Karavaeva, I., Havelund, J.F., Nielsen, C.H., Jedrychowski, M.P., Moreno-Torres, M., Lundh, M., et al. (2018). Cardiolipin Synthesis in Brown and Beige Fat Mitochondria Is Essential for Systemic Energy Homeostasis. Cell Metab. 28, 159-174.e11.

Tahrani, A.A., Bailey, C.J., Del Prato, S., and Barnett, A.H. (2011). Management of type 2 diabetes: new and future developments in treatment. Lancet (London, England) 378, 182–197.

Tamboli, R.A., Breitman, I., Marks-Shulman, P.A., Jabbour, K., Melvin, W., Williams, B., Clements, R.H., Feurer, I.D., and Abumrad, N.N. (2014). Early weight regain after gastric bypass does not affect insulin sensitivity but is associated with elevated ghrelin. Obesity 22, 1617–1622.

Tanne, D., Medalie, J.H., and Goldbourt, U. (2005). Body Fat Distribution and Long-Term Risk of Stroke Mortality. Stroke 36, 1021–1025.

Taylor, R. (2008). Pathogenesis of type 2 diabetes: tracing the reverse route from cure to cause. Diabetologia 51, 1781–1789.

Tchkonia, T., Thomou, T., Zhu, Y., Karagiannides, I., Pothoulakis, C., Jensen, M.D., and Kirkland, J.L. (2013). Mechanisms and Metabolic Implications of Regional Differences among Fat Depots. Cell Metab. 17, 644–656.

Tedeschi, P.M., Markert, E.K., Gounder, M., Lin, H., Dvorzhinski, D., Dolfi, S.C., Chan, L.L.-Y., Qiu, J., DiPaola, R.S., Hirshfield, K.M., et al. (2013). Contribution of serine, folate and glycine metabolism to the ATP, NADPH and purine requirements of cancer cells. Cell Death Dis. 4, e877–e877.

The European Association for the Study of Obesity (2018). Obesity Statistics.

Townsend, K.L., and Tseng, Y.-H. (2014). Brown fat fuel utilization and thermogenesis. Trends Endocrinol. Metab. 25, 168–177.

Trivedi, B., and Danforth, W.H. (1966). Effect of pH on the kinetics of frog muscle phosphofructokinase. J. Biol. Chem. 241, 4110–4112.

Tseng, Y.-H., Kokkotou, E., Schulz, T.J., Huang, T.L., Winnay, J.N., Taniguchi, C.M., Tran, T.T., Suzuki, R., Espinoza, D.O., Yamamoto, Y., et al. (2008). New role of bone morphogenetic protein 7 in brown adipogenesis and energy expenditure. Nature 454, 1000–1004.

Tuomilehto, J. (2013). The Emerging Global Epidemic of Type 1 Diabetes. Curr. Diab. Rep. 13, 795–804.

Turner, R.C., Cull, C.A., Frighi, V., and Holman, R.R. (1999). Glycemic control with diet, sulfonylurea, metformin, or insulin in patients with type 2 diabetes mellitus: progressive requirement for multiple therapies (UKPDS 49). UK Prospective Diabetes Study (UKPDS) Group. JAMA 281, 2005–2012.

Ueta, C.B., Fernandes, G.W., Capelo, L.P., Fonseca, T.L., Maculan, F.D., Gouveia, C.H.A., Brum, P.C., Christoffolete, M.A., Aoki, M.S., Lancellotti, C.L., et al. (2012). β1 Adrenergic receptor is key to cold- and diet-induced thermogenesis in mice. J. Endocrinol. 214, 359–365.

UKPDS Group (1990). UK prospective diabetes study 7: Response of fasting plasma glucose to diet therapy in newly presenting type II diabetic patients. Metabolism 39, 905–912.

Unick, J.L., Beavers, D., Bond, D.S., Clark, J.M., Jakicic, J.M., Kitabchi, A.E., Knowler, W.C., Wadden, T.A., Wagenknecht, L.E., and Wing, R.R. (2013). The Long-term Effectiveness of a Lifestyle Intervention in Severely Obese Individuals. Am. J. Med. 126, 236-242.e2.

Valdmanis, P.N., Lisowski, L., and Kay, M.A. (2012). rAAV-Mediated Tumorigenesis: Still Unresolved After an AAV Assault. Mol. Ther. 20, 2014–2017.

Valle, A., Guevara, R., García-Palmer, F.J., Roca, P., and Oliver, J. (2008). Caloric Restriction Retards the Age-Related Decline in Mitochondrial Function of Brown Adipose Tissue. Rejuvenation Res. 11, 597–604.

van Marken Lichtenbelt, W.D., Vanhommerig, J.W., Smulders, N.M., Drossaerts, J.M.A.F.L., Kemerink, G.J., Bouvy, N.D., Schrauwen, P., and Teule, G.J.J. (2009). Cold-activated brown adipose tissue in healthy men. N. Engl. J. Med. 360, 1500–1508.

Vergnes, L., and Reue, K. (2014). Adaptive Thermogenesis in White Adipose Tissue: Is Lactate the New Brown(ing)? Diabetes 63, 3175–3176.

Verrotti, A., Scaparrotta, A., Agostinelli, S., Di Pillo, S., Chiarelli, F., and Grosso, S. (2011). Topiramate-induced weight loss: A review. Epilepsy Res. 95, 189–199.

Vimaleswaran, K.S., Radha, V., Ghosh, S., Majumder, P.P., Rao, M.R.S., and Mohan, V. (2010). A Haplotype at the UCP1 Gene Locus Contributes to Genetic Risk for Type 2 Diabetes in Asian Indians (CURES-72). Metab. Syndr. Relat. Disord. 8, 63–68.

Vitali, A., Murano, I., Zingaretti, M.C., Frontini, A., Ricquier, D., and Cinti, S. (2012). The adipose organ of obesity-prone C57BL/6J mice is composed of mixed white and brown adipocytes. J. Lipid Res. 53, 619–629.

Voight, B.F., Scott, L.J., Steinthorsdottir, V., Morris, A.P., Dina, C., Welch, R.P., Zeggini, E., Huth, C., Aulchenko, Y.S., Thorleifsson, G., et al. (2010). Twelve type 2 diabetes susceptibility loci identified through large-scale association analysis. Nat. Genet. 42, 579–589.

Wabitsch, M., Moss, A., and Kromeyer-Hauschild, K. (2014). Unexpected plateauing of childhood obesity rates in developed countries. BMC Med. 12, 17.

Wang, L., Wang, H., Bell, P., McCarter, R.J., He, J., Calcedo, R., Vandenberghe, L.H., Morizono, H., Batshaw, M.L., and Wilson, J.M. (2010). Systematic Evaluation of AAV Vectors for Liver directed Gene Transfer in Murine Models. Mol. Ther. 18, 118–125.

Wang, M., Yu, M., Fang, L., and Hu, R.-Y. (2015). Association between sugar-sweetened beverages and type 2 diabetes: A meta-analysis. J. Diabetes Investig. 6, 360–366.

Wang, S., Liang, X., Yang, Q., Fu, X., Rogers, C.J., Zhu, M., Rodgers, B.D., Jiang, Q., Dodson, M. V, and Du, M. (2015). Resveratrol induces brown-like adipocyte formation in white fat through activation of AMP-activated protein kinase (AMPK) α1. Int. J. Obes. 39, 967–976.

Webb, V.L., and Wadden, T.A. (2017). Intensive Lifestyle Intervention for Obesity: Principles, Practices, and Results. Gastroenterology 152, 1752–1764.

Weber, C., and Chand, B. (2018). Weight Regain Following Bariatric Surgery and Revisional Surgery. In Complications in Bariatric Surgery, (Cham: Springer International Publishing), pp. 147–165.

Welsh, J.B., Zarrinkar, P.P., Sapinoso, L.M., Kern, S.G., Behling, C.A., Monk, B.J., Lockhart, D.J., Burger, R.A., and Hampton, G.M. (2001). Analysis of gene expression

profiles in normal and neoplastic ovarian tissue samples identifies candidate molecular markers of epithelial ovarian cancer. Proc. Natl. Acad. Sci. 98, 1176–1181.

WHO Expert Committee (1995). Physical status: the use and interpretation of anthropometry.

Williamson, D.F., Thompson, T.J., Thun, M., Flanders, D., Pamuk, E., and Byers, T. (2000). Intentional weight loss and mortality among overweight individuals with diabetes. Diabetes Care 23, 1499–1504.

Wing, R.R., Lang, W., Wadden, T.A., Safford, M., Knowler, W.C., Bertoni, A.G., Hill, J.O., Brancati, F.L., Peters, A., and Wagenknecht, L. (2011). Benefits of Modest Weight Loss in Improving Cardiovascular Risk Factors in Overweight and Obese Individuals With Type 2 Diabetes. Diabetes Care 34, 1481–1486.

Winther, S., Isidor, M.S., Basse, A.L., Skjoldborg, N., Cheung, A., Quistorff, B., and Hansen, J.B. (2018). Restricting glycolysis impairs brown adipocyte glucose and oxygen consumption. Am. J. Physiol. Metab. 314, E214–E223.

Winzell, M.S., and Ahrén, B. (2004). The high-fat diet-fed mouse: a model for studying mechanisms and treatment of impaired glucose tolerance and type 2 diabetes. Diabetes 53 Suppl 3, S215-9.

Wohlt, J.E., Clark, J.H., Derrig, R.G., and Davis, C.L. (1977). Valine, Leucine, and Isoleucine Metabolism by Lactating Bovine Mammary Tissue. J. Dairy Sci. 60, 1875–1882.

World Health Organization (2016). Global Report on Diabetes.

World Health Organization (2018a). Obesity and overweight.

World Health Organization (2018b). World Health Statistics 2018- Monitoring Health for the SDG's (Sustainable development goals). 4, 25.

Wu, J., Boström, P., Sparks, L.M., Ye, L., Choi, J.H., Giang, A.-H., Khandekar, M., Virtanen, K.A., Nuutila, P., Schaart, G., et al. (2012). Beige Adipocytes Are a Distinct Type of Thermogenic Fat Cell in Mouse and Human. Cell 150, 366–376.

Wu, J., Cohen, P., and Spiegelman, B.M. (2013). Adaptive thermogenesis in adipocytes: Is beige the new brown? Genes Dev. 27, 234–250.

Xie, Q., Bu, W., Bhatia, S., Hare, J., Somasundaram, T., Azzi, A., and Chapman, M.S. (2002). The atomic structure of adeno-associated virus (AAV-2), a vector for human gene therapy. Proc. Natl. Acad. Sci. 99, 10405–10410.

Xue, B., Rim, J.-S., Hogan, J.C., Coulter, A.A., Koza, R.A., and Kozak, L.P. (2007). Genetic variability affects the development of brown adipocytes in white fat but not in interscapular brown fat. J. Lipid Res. 48, 41–51.

Xue, Y., Petrovic, N., Cao, R., Larsson, O., Lim, S., Chen, S., Feldmann, H.M., Liang, Z., Zhu, Z., Nedergaard, J., et al. (2009). Hypoxia-Independent Angiogenesis in Adipose Tissues during Cold Acclimation. Cell Metab. 9, 99–109.

Xue, Y., Xu, X., Zhang, X.-Q., Farokhzad, O.C., and Langer, R. (2016). Preventing diet-induced obesity in mice by adipose tissue transformation and angiogenesis using targeted nanoparticles. Proc. Natl. Acad. Sci. 113, 5552–5557.

Yki-Järvinen, H. (2004). Thiazolidinediones. N. Engl. J. Med. 351, 1106–1118.

Yoneda, S., Uno, S., Iwahashi, H., Fujita, Y., Yoshikawa, A., Kozawa, J., Okita, K., Takiuchi, D., Eguchi, H., Nagano, H., et al. (2013). Predominance of ß-Cell Neogenesis Rather Than Replication in Humans With an Impaired Glucose Tolerance and Newly Diagnosed Diabetes. J. Clin. Endocrinol. Metab. 98, 2053–2061.

Yoneshiro, T., and Saito, M. (2015). Activation and recruitment of brown adipose tissue as anti-obesity regimens in humans. Ann. Med. 47, 133–141.

Young, P., Cawthorne, M.A., Levy, A.L., and Wilson, K. (1984). Reduced maximum capacity of glycolysis in brown adipose tissue of genetically obese, diabetic (db/db) mice and its restoration following treatment with a thermogenic beta-adrenoceptor agonist. FEBS Lett. 176, 16–20.

Yu, J., Zhang, S., Cui, L., Wang, W., Na, H., Zhu, X., Li, L., Xu, G., Yang, F., Christian, M., et al. (2015). Lipid droplet remodeling and interaction with mitochondria in mouse brown adipose tissue during cold treatment. Biochim. Biophys. Acta - Mol. Cell Res. 1853, 918–928.

Yu, X.X., Lewin, D.A., Forrest, W., and Adams, S.H. (2002). Cold elicits the simultaneous induction of fatty acid synthesis and ß-oxidation in murine brown adipose tissue: prediction from differential gene expression and confirmation in vivo. FASEB J. 16, 155–168.

Zafrir, B. (2013). Brown Adipose Tissue: Research Milestones of a Potential Player in Human Energy Balance and Obesity. Horm. Metab. Res. 45, 774–785.

Zhang, F., Hao, G., Shao, M., Nham, K., An, Y., Wang, Q., Zhu, Y., Kusminski, C.M., Hassan, G., Gupta, R.K., et al. (2018). An Adipose Tissue Atlas: An Image-Guided Identification of Human-like BAT and Beige Depots in Rodents. Cell Metab. 27, 252-262.e3.

Zhang, S., Zeng, X., Ren, M., Mao, X., and Qiao, S. (2017). Novel metabolic and physiological functions of branched chain amino acids: a review. J. Anim. Sci. Biotechnol. 8, 10.

Zhou, Z., Yon Toh, S., Chen, Z., Guo, K., Peng Ng, C., Ponniah, S., Lin, S.-C., Hong, W., and Li, P. (2003). Cidea-deficient mice have lean phenotype and are resistant to obesity. Nat. Genet. 35, 49–56.

Zincarelli, C., Soltys, S., Rengo, G., and Rabinowitz, J.E. (2008). Analysis of AAV Serotypes 1–9 Mediated Gene Expression and Tropism in Mice After Systemic Injection. Mol. Ther. 16, 1073–1080.

Zinman, B., Wanner, C., Lachin, J.M., Fitchett, D., Bluhmki, E., Hantel, S., Mattheus, M., Devins, T., Johansen, O.E., Woerle, H.J., et al. (2015). Empagliflozin, Cardiovascular Outcomes, and Mortality in Type 2 Diabetes. N. Engl. J. Med. 373, 2117–2128.

# IX. APPENDIX

## List of genes included in this study

| *Gene Symbol* | **Description** |
|---|---|
| ***1700040L02Rik*** | *RIKEN cDNA 1700040L02 gene* |
| ***5033411D12Rik*** | *RIKEN cDNA 5033411D12 gene* |
| ***8430408G22Rik*** | *RIKEN cDNA 8430408G22 gene* |
| ***Aacs*** | *Acetoacetyl-coa synthetase* |
| ***Acaa1a*** | *Acetyl-coa acyltransferase 1A* |
| ***Acaa1b*** | *Acetyl-coa acyltransferase 1B* |
| ***Acaa2*** | *Acetyl-coa acyltransferase 2 (mitochondrial 3-oxoacyl-coa thiolase)* |
| ***Acaca*** | *Acetyl-Coenzyme A carboxylase alpha* |
| ***Acacb*** | *Acetyl-Coenzyme A carboxylase beta* |
| ***Acad8*** | *Acyl-coa dehydrogenase family, member 8* |
| ***Acadl*** | *Acyl-Coenzyme A dehydrogenase, long-chain* |
| ***Acadm*** | *Acyl-coa dehydrogenase, medium chain* |
| ***Acads*** | *Acyl-coa dehydrogenase, short chain* |
| ***Acadsb*** | *Acyl-coa dehydrogenase, short/branched chain* |
| ***Acadvl*** | *Acyl-Coenzyme A dehydrogenase, very long chain* |
| ***Acat1*** | *Acetyl-Coenzyme A acetyltransferase 1* |
| ***Acly*** | *ATP citrate lyase* |
| ***Aco1*** | *Aconitase 1* |
| ***Aco2*** | *Aconitase 2, mitochondrial* |
| ***Acot11*** | *Acyl-coa thioesterase 11* |
| ***Acsf3*** | *Acyl-coa synthetase family member 3* |
| ***Acsl1*** | *Acyl-coa synthetase long-chain family member 1* |
| ***Acsl3*** | *Acyl-coa synthetase long-chain family member 3* |
| ***Acsl4*** | *Acyl-coa synthetase long-chain family member 4* |
| ***Acsl5*** | *Acyl-coa synthetase long-chain family member 5* |
| ***Acsl6*** | *Acyl-coa synthetase long-chain family member 6* |
| ***Acss1*** | *Acyl-coa synthetase short-chain family member 1* |
| ***Acss2*** | *Acyl-coa synthetase short-chain family member 2* |
| ***Acyp1*** | *Acylphosphatase 1, erythrocyte (common) type* |
| ***Acyp2*** | *Acylphosphatase 2, muscle type* |
| ***Adcy1*** | *Adenylate cyclase 1* |
| ***Adcy10*** | *Adenylate cyclase 10* |
| ***Adcy2*** | *Adenylate cyclase 2* |
| ***Adcy3*** | *Adenylate cyclase 3* |
| ***Adcy4*** | *Adenylate cyclase 4* |
| ***Adcy5*** | *Adenylate cyclase 5* |

| | |
|---|---|
| ***Adcy6*** | *Adenylate cyclase 6* |
| ***Adcy7*** | *Adenylate cyclase 7* |
| ***Adcy8*** | *Adenylate cyclase 8* |
| ***Adcy9*** | *Adenylate cyclase 9* |
| ***Adrb1*** | *Adrenergic receptor, beta 1* |
| ***Adrb2*** | *Adrenergic receptor, beta 2* |
| ***Adrb3*** | *Adrenergic receptor, beta 3* |
| ***Agxt*** | *Alanine-glyoxylate aminotransferase* |
| ***Agxt2*** | *Alanine-glyoxylate aminotransferase 2* |
| ***Alb*** | *Albumin* |
| ***Aldh1b1*** | *Aldehyde dehydrogenase 1 family, member B1* |
| ***Aldh2*** | *Aldehyde dehydrogenase 2, mitochondrial* |
| ***Aldh3a2*** | *Aldehyde dehydrogenase family 3, subfamily A2* |
| ***Aldh6a1*** | *Aldehyde dehydrogenase family 6, subfamily A1* |
| ***Aldh7a1*** | *Aldehyde dehydrogenase family 7, member A1* |
| ***Aldh9a1*** | *Aldehyde dehydrogenase 9, subfamily A1* |
| ***Aldoa*** | *Aldolase A, fructose-bisphosphate* |
| ***Aldob*** | *Aldolase B, fructose-bisphosphate* |
| ***Aldoc*** | *Aldolase C, fructose-bisphosphate* |
| ***Amdhd1*** | *Amidohydrolase domain containing 1* |
| ***Amt*** | *Aminomethyltransferase* |
| ***Angpt1*** | *Angiopoietin 1* |
| ***Aox1*** | *Aldehyde oxidase 1* |
| ***Aox2*** | *Aldehyde oxidase 3-like 1* |
| ***Aox3*** | *Aldehyde oxidase 3* |
| ***Aox4*** | *Aldehyde oxidase 4* |
| ***Aqp1*** | *Aquaporin 1* |
| ***Asns*** | *Asparagine synthetase* |
| ***Atp4b*** | *ATPase, H+/K+ exchanging, beta polypeptide* |
| ***Atp5a1*** | *ATP synthase, H+ transporting, mitochondrial F1 complex, alpha subunit 1* |
| ***Atp5b*** | *ATP synthase, H+ transporting mitochondrial F1 complex, beta subunit* |
| ***Atp5d*** | *ATP synthase, H+ transporting, mitochondrial F1 complex, delta subunit* |
| ***Atp5e*** | *ATP synthase, H+ transporting, mitochondrial F1 complex, epsilon subunit* |
| ***Atp5f1*** | *ATP synthase, H+ transporting, mitochondrial F0 complex, subunit B1* |
| ***Atp5g1*** | *ATP synthase, H+ transporting, mitochondrial F0 complex, subunit c1 (subunit 9)* |
| ***Atp5g2*** | *ATP synthase, H+ transporting, mitochondrial F0 complex, subunit C2 (subunit 9)* |
| ***Atp5g3*** | *ATP synthase, H+ transporting, mitochondrial F0 complex, subunit C3 (subunit 9)* |
| ***Atp5h*** | *ATP synthase, H+ transporting, mitochondrial F0 complex, subunit d* |

| | |
|---|---|
| ***Atp5j2*** | *ATP synthase, H+ transporting, mitochondrial F0 complex, subunit F2* |
| ***Atp5k*** | *ATP synthase, H+ transporting, mitochondrial F1F0 complex, subunit e* |
| ***Atp5o*** | *ATP synthase, H+ transporting, mitochondrial F1 complex, O subunit* |
| ***Atp6v0a2*** | *ATPase, H+ transporting, lysosomal V0 subunit A2* |
| ***Atp6v0c*** | *ATPase, H+ transporting, lysosomal V0 subunit C* |
| ***Atp6v0d2*** | *ATPase, H+ transporting, lysosomal V0 subunit D2* |
| ***Atp6v1h*** | *ATPase, H+ transporting, lysosomal V1 subunit H* |
| ***Auh*** | *AU RNA binding protein/enoyl-CoA hydratase* |
| ***B3galt2*** | *UDP-Gal:betaGlcNAc beta 1,3-galactosyltransferase, polypeptide 2* |
| ***Bcat1*** | *Branched chain aminotransferase 1, cytosolic* |
| ***Bcat2*** | *Branched chain aminotransferase 2, mitochondrial* |
| ***Bckdha*** | *Branched chain ketoacid dehydrogenase E1, alpha polypeptide* |
| ***Bckdhb*** | *Branched chain ketoacid dehydrogenase E1, beta polypeptide* |
| ***Bmp8b*** | *Bone morphogenetic protein 8b* |
| ***Cad*** | *Carbamoyl-phosphate synthetase 2, aspartate transcarbamylase, and dihydroorotase* |
| ***Car3*** | *Carbonic anhydrase 3* |
| ***Casq1*** | *Calsequestrin 1* |
| ***Catc / Slc25a20*** | *Solute carrier family 25, member 20* |
| ***Cbs*** | *Cystathionine beta-synthase* |
| ***Ccl8*** | *Chemokine (C-C motif) ligand 8* |
| ***Cd274*** | *CD274 antigen* |
| ***Cd36*** | *CD36 antigen* |
| ***Chkb*** | *Choline kinase beta* |
| ***Cidea*** | *Cell death-inducing DNA fragmentation factor, alpha subunit-like effector A* |
| ***Ckb*** | *Creatine kinase, brain* |
| ***Cntfr*** | *Ciliary neurotrophic factor receptor* |
| ***co1700040L02Rik*** | *RIKEN cDNA 1700040L02 gene* |
| ***coAtp4b*** | *Codon optimized atpase, H+/K+ exchanging, beta polypeptide* |
| ***Col1a2*** | *Collagen, type I, alpha 2* |
| ***Col3a1*** | *Collagen, type III, alpha 1* |
| ***COR1*** | *Ubiquinol-cytochrome c reductase core protein 1* |
| ***Cox10*** | *Cytochrome c oxidase assembly protein 10* |
| ***Cox11*** | *Cytochrome c oxidase assembly protein 11* |
| ***Cox15*** | *Cytochrome c oxidase assembly protein 15* |
| ***Cox17*** | *Cytochrome c oxidase assembly protein 17* |
| ***Cox4i1*** | *Cytochrome c oxidase subunit IV isoform 1* |
| ***Cox5a*** | *Cytochrome c oxidase subunit Va* |

| | |
|---|---|
| ***Cox6a2*** | *Cytochrome c oxidase subunit via polypeptide 2* |
| ***Cox6b1*** | *Cytochrome c oxidase, subunit vib polypeptide 1* |
| ***Cox6b2*** | *Cytochrome c oxidase subunit vib polypeptide 2* |
| ***Cox6c*** | *Cytochrome c oxidase subunit vic* |
| ***Cox7a1*** | *Cytochrome c oxidase subunit viia 1* |
| ***Cox7a2*** | *Cytochrome c oxidase subunit viia 2* |
| ***Cox7b*** | *Cytochrome c oxidase subunit viib* |
| ***Cox8b*** | *Cytochrome c oxidase subunit viiib* |
| ***Cpne5*** | *Copine V* |
| ***Cpt1a*** | *Carnitine palmitoyltransferase 1a, liver* |
| ***Cpt1b*** | *Carnitine palmitoyltransferase 1b, muscle* |
| ***Cpt2*** | *Carnitine palmitoyltransferase 2* |
| ***Cs*** | *Citrate synthase* |
| ***Cth*** | *Cystathionase (cystathionine gamma-lyase)* |
| ***CyoE*** | *Cytochrome c oxidase assembly protein 10* |
| ***Cyp2b10*** | *Cytochrome P450, family 2, subfamily b, polypeptide 10* |
| ***Cyt1*** | *Cytochrome c-1* |
| ***Dbt*** | *Dihydrolipoamide branched chain transacylase E2* |
| ***Decr1*** | *2,4-dienoyl coa reductase 1, mitochondrial* |
| ***Dio2*** | *Deiodinase, iodothyronine, type II* |
| ***Dlat*** | *Dihydrolipoamide S-acetyltransferase* |
| ***Dld*** | *Dihydrolipoamide dehydrogenase* |
| ***Dlst*** | *Dihydrolipoamide S-succinyltransferase* |
| ***Echs1*** | *Enoyl coa hydratase, short chain, 1, mitochondrial* |
| ***Eci1*** | *Enoyl-Coenzyme A delta isomerase 1* |
| ***Ehhadh*** | *Enoyl-coa, hydratase/3-hydroxyacyl coa dehydrogenase* |
| ***Elovl1*** | *Elongation of very long chain fatty acids (FEN1/Elo2, SUR4/Elo3, yeast)-like 1* |
| ***Elovl2*** | *Elongation of very long chain fatty acids (FEN1/Elo2, SUR4/Elo3, yeast)-like 2* |
| ***Elovl3*** | *Elongation of very long chain fatty acids (FEN1/Elo2, SUR4/Elo3, yeast)-like 3* |
| ***Elovl4*** | *Elongation of very long chain fatty acids (FEN1/Elo2, SUR4/Elo3, yeast)-like 4* |
| ***Elovl5*** | *ELOVL family member 5, elongation of long chain fatty acids (yeast)* |
| ***Elovl6*** | *ELOVL family member 6, elongation of long chain fatty acids (yeast)* |
| ***Elovl7*** | *ELOVL family member 7, elongation of long chain fatty acids (yeast)* |
| ***Eno1*** | *Enolase 1, alpha non-neuron* |
| ***Eno2*** | *Enolase 2, gamma neuronal* |
| ***Eno3*** | *Enolase 3, beta muscle* |
| ***Eno4*** | *Enolase 4* |
| ***Fabp1*** | *Fatty acid binding protein 1, liver* |

| | |
|---|---|
| ***Fabp2*** | *Fatty acid binding protein 2, intestinal* |
| ***Fabp3*** | *Fatty acid binding protein 3, muscle and heart* |
| ***Fabp3-ps1*** | *Fatty acid binding protein 3, muscle and heart, pseudogene 1* |
| ***Fabp4*** | *Fatty acid binding protein 4, adipocyte* |
| ***Fabp7*** | *Fatty acid binding protein 7, brain* |
| ***Fads1*** | *Fatty acid desaturase 1* |
| ***Fads2*** | *Fatty acid desaturase 2* |
| ***Fads3*** | *Fatty acid desaturase 3* |
| ***Fasn*** | *Fatty acid synthase* |
| ***Fgf21*** | *Fibroblast growth factor 21* |
| ***Fh1*** | *Fumarate hydratase 1* |
| ***Folr2*** | *Folate receptor 2 (fetal)* |
| ***Ftcd*** | *Formiminotransferase cyclodeaminase* |
| ***Gapdh*** | *Glyceraldehyde-3-phosphate dehydrogenase* |
| ***Gapdhs*** | *Glyceraldehyde-3-phosphate dehydrogenase, spermatogenic* |
| ***Gbp10*** | *Guanylate-binding protein 10* |
| ***Gcsh*** | *Glycine cleavage system protein H (aminomethyl carrier)* |
| ***Gldc*** | *Glycine decarboxylase* |
| ***Gls*** | *Glutaminase* |
| ***Glud1*** | *Glutamate dehydrogenase 1* |
| ***Glul*** | *Glutamate-ammonia ligase (glutamine synthetase)* |
| ***Gm10106*** | *Predicted gene 10106* |
| ***Gm10722*** | *Predicted gene 10722* |
| ***Gm10801*** | *Predicted gene, 10801* |
| ***Gm14527*** | *Predicted gene 14527* |
| ***Gm15241*** | *Predicted gene 15241* |
| ***Gm17535*** | *Predicted gene, 17535* |
| ***Gm20736*** | *Predicted gene, 20736* |
| ***Gm20824*** | *Predicted gene, 20824* |
| ***Gm21088*** | *Predicted gene, 21088* |
| ***Gm21627*** | *Predicted gene, 21627* |
| ***Gm22577*** | *Predicted geme, 22577* |
| ***Gmpr*** | *Guanosine monophosphate reductase* |
| ***Gnas*** | *GNAS (guanine nucleotide binding protein, alpha stimulating) complex locus* |
| ***Got1*** | *Glutamate oxaloacetate transaminase 1, soluble* |
| ***Got2*** | *Glutamate oxaloacetate transaminase 2, mitochondrial* |
| ***Gpi1*** | *Glucose phosphate isomerase 1* |
| ***Gpr81*** | *G protein-coupled receptor 81* |

| | |
|---|---|
| ***Gpt*** | *Glutamic pyruvic transaminase, soluble* |
| ***Gpt2*** | *Glutamic pyruvate transaminase (alanine aminotransferase) 2* |
| ***Gyk*** | *Glycerol kinase* |
| ***Gys2*** | *Glycogen synthase 2* |
| ***Hacd1*** | *3-hydroxyacyl-coa dehydratase 1* |
| ***Hacd2*** | *3-hydroxyacyl-coa dehydratase 2* |
| ***Hacd3*** | *3-hydroxyacyl-coa dehydratase 4* |
| ***Hacd4*** | *3-hydroxyacyl-coa dehydratase 3* |
| ***Hadh*** | *Hydroxyacyl-coa dehydrogenase* |
| ***Hadha*** | *Hydroxyacyl-coa dehydrogenase/enoyl-coa hydratase, alpha subunit* |
| ***Hadhb*** | *Hydroxyacyl-coa dehydrogenase/enoyl-coa hydratase, beta subunit* |
| ***Hal*** | *Histidine ammonia lyase* |
| ***Hcn2*** | *Hyperpolarization-activated, cyclic nucleotide-gated K+ 2* |
| ***Hdc*** | *Histidine decarboxylase* |
| ***Hibadh*** | *3-hydroxyisobutyrate dehydrogenase* |
| ***Hibch*** | *3-hydroxyisobutyryl-coa hydrolase* |
| ***Hmgcl*** | *3-hydroxy-3-methylglutaryl-coa lyase* |
| ***Hmgcll1*** | *3-hydroxymethyl-3-methylglutaryl-coa lyase-like 1* |
| ***Hmgcs1*** | *3-hydroxy-3-methylglutaryl-coa synthase 1* |
| ***Hmgcs2*** | *3-hydroxy-3-methylglutaryl-coa synthase 2* |
| ***Hsd17b10*** | *Hydroxysteroid (17-beta) dehydrogenase 10* |
| ***Hsd17b12*** | *Hydroxysteroid (17-beta) dehydrogenase 12* |
| ***Idh1*** | *Isocitrate dehydrogenase 1 (NADP+), soluble* |
| ***Idh2*** | *Isocitrate dehydrogenase 2 (NADP+), mitochondrial* |
| ***Idh3a*** | *Isocitrate dehydrogenase 3 (NAD+) alpha* |
| ***Idh3b*** | *Isocitrate dehydrogenase 3 (NAD+) beta* |
| ***Idh3g*** | *Isocitrate dehydrogenase 3 (NAD+), gamma* |
| ***Ifi44*** | *Interferon-induced protein 44* |
| ***Ighv1-9*** | *Immunoglobulin heavy variable v1-9* |
| ***Igh-VJ558*** | *Immunoglobulin heavy chain (J558 family)* |
| ***ISP*** | *Ubiquinol-cytochrome c reductase, Rieske iron-sulfur polypeptide 1* |
| ***Ivd*** | *Isovaleryl coa dehydrogenase* |
| ***Klb*** | *Klotho beta* |
| ***Kng2*** | *Kininogen 2* |
| ***Lctl*** | *Lactase-like* |
| ***Ldha*** | *Lactate dehydrogenase A* |
| ***Ldhal6b*** | *Lactate dehydrogenase A-like 6B* |
| ***Ldhb*** | *Lactate dehydrogenase B* |

| | |
|---|---|
| ***Ldhc*** | *Lactate dehydrogenase C* |
| ***Ldhd*** | *Lactate dehydrogenase D* |
| ***Letmd1*** | *LETM1 domain containing 1* |
| ***Lipe*** | *Lipase, hormone sensitive* |
| ***LOC630751*** | *Interferon-inducible gtpase 1-like* |
| ***Lum*** | *Lumican* |
| ***Mccc1*** | *Methylcrotonoyl-coa carboxylase 1 (alpha)* |
| ***Mccc2*** | *Methylcrotonoyl-coa carboxylase 2 (beta)* |
| ***Mcee*** | *Methylmalonyl coa epimerase* |
| ***Mdh1*** | *Malate dehydrogenase 1, NAD (soluble)* |
| ***Mdh1b*** | *Malate dehydrogenase 1B, NAD (soluble)* |
| ***Mdh2*** | *Malate dehydrogenase 2, NAD (mitochondrial)* |
| ***Me1*** | *Malic enzyme 1, NADP(+)-dependent, cytosolic* |
| ***Me2*** | *Malic enzyme 2, NAD(+)-dependent, mitochondrial* |
| ***Me3*** | *Malic enzyme 3, NADP(+)-dependent, mitochondrial* |
| ***Mfsd2a*** | *Major facilitator superfamily domain containing 2A* |
| ***Mgll*** | *Monoglyceride lipase* |
| ***Mpc1*** | *Mitochondrial pyruvate carrier 1** |
| ***Mpc2*** | *Mitochondrial pyruvate carrier 2* |
| ***Mpzl2*** | *Myelin protein zero-like 2* |
| ***mt-Tl2*** | *Mitochondrially encoded trna leucine 2* |
| ***mt-Ts2*** | *Mitochondrially encoded trna serine 2* |
| ***mt-Tt*** | *Mitochondrially encoded trna threonine* |
| ***Mut*** | *Methylmalonyl-coa mutase* |
| ***Ndufa10*** | *NADH dehydrogenase (ubiquinone) 1 alpha subcomplex 10* |
| ***Ndufa12*** | *NADH dehydrogenase (ubiquinone) 1 alpha subcomplex, 12* |
| ***Ndufa3*** | *NADH dehydrogenase (ubiquinone) 1 alpha subcomplex, 3* |
| ***Ndufa4*** | *NADH dehydrogenase (ubiquinone) 1 alpha subcomplex, 4* |
| ***Ndufa4l2*** | *NADH dehydrogenase (ubiquinone) 1 alpha subcomplex, 4-like 2* |
| ***Ndufa5*** | *NADH dehydrogenase (ubiquinone) 1 alpha subcomplex, 5* |
| ***Ndufa6*** | *NADH dehydrogenase (ubiquinone) 1 alpha subcomplex, 6 (B14)* |
| ***Ndufa7*** | *NADH dehydrogenase (ubiquinone) 1 alpha subcomplex, 7 (B14.5a)* |
| ***Ndufa8*** | *NADH dehydrogenase (ubiquinone) 1 alpha subcomplex, 8* |
| ***Ndufa9*** | *NADH dehydrogenase (ubiquinone) 1 alpha subcomplex, 9* |
| ***Ndufab1*** | *NADH dehydrogenase (ubiquinone) 1, alpha/beta subcomplex, 1* |
| ***Ndufb10*** | *NADH dehydrogenase (ubiquinone) 1 beta subcomplex, 10* |
| ***Ndufb11*** | *NADH dehydrogenase (ubiquinone) 1 beta subcomplex, 11* |
| ***Ndufb3*** | *NADH dehydrogenase (ubiquinone) 1 beta subcomplex 3* |

| | |
|---|---|
| ***Ndufb4c*** | *NADH dehydrogenase (ubiquinone) 1 beta subcomplex 4* |
| ***Ndufb5*** | *NADH dehydrogenase (ubiquinone) 1 beta subcomplex, 5* |
| ***Ndufb6*** | *NADH dehydrogenase (ubiquinone) 1 beta subcomplex, 6* |
| ***Ndufb7*** | *NADH dehydrogenase (ubiquinone) 1 beta subcomplex, 7* |
| ***Ndufb8*** | *NADH dehydrogenase (ubiquinone) 1 beta subcomplex 8* |
| ***Ndufc1*** | *NADH dehydrogenase (ubiquinone) 1, subcomplex unknown, 1* |
| ***Ndufc2*** | *NADH dehydrogenase [ubiquinone] 1 subunit C2-like* |
| ***Ndufs1*** | *NADH dehydrogenase (ubiquinone) Fe-S protein 1* |
| ***Ndufs2*** | *NADH dehydrogenase (ubiquinone) Fe-S protein 2* |
| ***Ndufs3*** | *NADH dehydrogenase (ubiquinone) Fe-S protein 3* |
| ***Ndufs4*** | *NADH dehydrogenase (ubiquinone) Fe-S protein 4* |
| ***Ndufs5*** | *NADH dehydrogenase (ubiquinone) Fe-S protein 5* |
| ***Ndufs8*** | *NADH dehydrogenase (ubiquinone) Fe-S protein 8* |
| ***Ndufv1*** | *NADH dehydrogenase (ubiquinone) flavoprotein 1* |
| ***Ndufv2*** | *NADH dehydrogenase (ubiquinone) flavoprotein 2* |
| ***Ndufv3*** | *NADH dehydrogenase (ubiquinone) flavoprotein 3* |
| ***Ntrk3*** | *Neurotrophic tyrosine kinase, receptor, type 3* |
| ***Ogdh*** | *Oxoglutarate (alpha-ketoglutarate) dehydrogenase (lipoamide)* |
| ***Oxct1*** | *3-oxoacid coa transferase 1* |
| ***Oxct2a*** | *3-oxoacid coa transferase 2A* |
| ***Oxct2b*** | *3-oxoacid coa transferase 2B* |
| ***Pax8*** | *Paired box gene 8* |
| ***Pcca*** | *Propionyl-coa carboxylase, alpha polypeptide* |
| ***Pccb*** | *Propionyl coa carboxylase, beta polypeptide* |
| ***Pcx*** | *Pyruvate carboxylase* |
| ***Pdha1*** | *Pyruvate dehydrogenase E1 alpha 1* |
| ***Pdha2*** | *Pyruvate dehydrogenase E1 alpha 2* |
| ***Pdhb*** | *Pyruvate dehydrogenase (lipoamide) beta* |
| ***Pdk1*** | *Pyruvate dehydrogenase kinase, isoenzyme 1* |
| ***Pdk2*** | *Pyruvate dehydrogenase kinase, isoenzyme 2* |
| ***Pdk3*** | *Pyruvate dehydrogenase kinase, isoenzyme 3* |
| ***Pdk4*** | *Pyruvate dehydrogenase kinase, isoenzyme 4* |
| ***Pdp1*** | *Pyruvate dehyrogenase phosphatase catalytic subunit 1* |
| ***Pdp2*** | *Pyruvate dehyrogenase phosphatase catalytic subunit 2* |
| ***Pdpr*** | *Pyruvate dehydrogenase phosphatase regulatory subunit* |
| ***Pfkl*** | *Phosphofructokinase, liver, B-type* |
| ***Pfkm*** | *Phosphofructokinase, muscle* |
| ***Pfkp*** | *Phosphofructokinase, platelet* |

| | |
|---|---|
| ***Pgam1*** | *Phosphoglycerate mutase 1* |
| ***Pgam2*** | *Phosphoglycerate mutase 2* |
| ***Pgk1*** | *Phosphoglycerate kinase 1* |
| ***Pgk2*** | *Phosphoglycerate kinase 2* |
| ***Phospho1*** | *Phosphatase, orphan 1* |
| ***Pipox*** | *Pipecolic acid oxidase* |
| ***Pklr*** | *Pyruvate kinase liver and red blood cell* |
| ***Pkm*** | *Pyruvate kinase, muscle* |
| ***Plin1*** | *Perilipin 1* |
| ***Plin2*** | *Perilipin 2* |
| ***Plin3*** | *Perilipin 3* |
| ***Plin4*** | *Perilipin 4* |
| ***Plin5*** | *Perilipin 5* |
| ***Pnpla2*** | *Patatin-like phospholipase domain containing 2* |
| ***Ppargc1a*** | *Peroxisome proliferative activated receptor, gamma, coactivator 1 alpha* |
| ***Ppif*** | *Peptidylprolyl isomerase F (cyclophilin F)* |
| ***Prkaca*** | *Protein kinase, camp dependent, catalytic, alpha* |
| ***Qcr2*** | *Ubiquinol cytochrome c reductase core protein 2* |
| ***Qcr6*** | *Ubiquinol-cytochrome c reductase hinge protein* |
| ***Qcr8*** | *Ubiquinol-cytochrome c reductase, complex III subunit VII* |
| ***Qcr9*** | *Ubiquinol-cytochrome c reductase, complex III subunit X* |
| ***Rplp0*** | *Ribosomal protein lateal stalk subunit P0* |
| ***Rps15*** | *Ribosomal protein S15* |
| ***Scd1*** | *Stearoyl-Coenzyme A desaturase 1* |
| ***Scd2*** | *Stearoyl-Coenzyme A desaturase 2* |
| ***Scd3*** | *Stearoyl-coenzyme A desaturase 3* |
| ***Scd4*** | *Stearoyl-coenzyme A desaturase 4* |
| ***Sdha*** | *Succinate dehydrogenase complex, subunit A, flavoprotein (Fp)* |
| ***Sdhb*** | *Succinate dehydrogenase complex, subunit B, iron sulfur (Ip)* |
| ***Sdhc*** | *Succinate dehydrogenase complex, subunit C, integral membrane protein* |
| ***Sdhd*** | *Succinate dehydrogenase complex, subunit D, integral membrane protein* |
| ***Shmt1*** | *Serine hydroxymethyltransferase 1 (soluble)* |
| ***Shmt2*** | *Serine hydroxymethyltransferase 2 (mitochondrial)* |
| ***Slc25a11*** | *Solute carrier family 25 (mitochondrial carrier oxoglutarate carrier), member 11* |
| ***Slc25a12*** | *Solute carrier family 25 (mitochondrial carrier, Aralar), member 12* |
| ***Slc25a13*** | *Solute carrier family 25 (mitochondrial carrier, adenine nucleotide translocator), member 13* |
| ***Slc25a34*** | *Solute carrier family 25, member 34* |

| | |
|---|---|
| ***Slc27a1*** | *Solute carrier family 27 (fatty acid transporter), member 1* |
| ***Slc27a2*** | *Solute carrier family 27 (fatty acid transporter), member 2* |
| ***Slc27a3*** | *Solute carrier family 27 (fatty acid transporter), member 3* |
| ***Slc27a4*** | *Solute carrier family 27 (fatty acid transporter), member 4* |
| ***Slc27a5*** | *Solute carrier family 27 (fatty acid transporter), member 5* |
| ***Slc27a6*** | *Solute carrier family 27 (fatty acid transporter), member 6* |
| ***Slc2a1*** | *Solute carrier family 2, member 1* |
| ***Slc2a10*** | *Solute carrier family 2, member 10* |
| ***Slc2a12*** | *Solute carrier family 2, member 12* |
| ***Slc2a13*** | *Solute carrier family 2, member 13* |
| ***Slc2a2*** | *Solute carrier family 2, member 2* |
| ***Slc2a3*** | *Solute carrier family 2, member 3* |
| ***Slc2a4*** | *Solute carrier family 2, member 4* |
| ***Slc2a5*** | *Solute carrier family 2, member 5* |
| ***Slc2a6*** | *Solute carrier family 2, member 6* |
| ***Slc2a7*** | *Solute carrier family 2, member 7* |
| ***Slc2a8*** | *Solute carrier family 2, member 8* |
| ***Slc2a9*** | *Solute carrier family 2, member 9* |
| ***St3gal5*** | *ST3 beta-galactoside alpha-2,3-sialyltransferase 5* |
| ***Sucla2*** | *Succinate-Coenzyme A ligase, ADP-forming, beta subunit* |
| ***Suclg1*** | *Succinate-coenzymea ligase, GDP-forming, alpha subunit* |
| ***Suclg2*** | *Succinate-Coenzyme A ligase, GDP-forming, beta subunit* |
| ***Svep1*** | *Sushi, von Willebrand factor type A, EGF and pentraxin domain containing 1* |
| ***Tacr2*** | *Tachykinin receptor 2* |
| ***Tecr*** | *Trans-2,3-enoyl-coa reductase* |
| ***Tha1*** | *Threonine aldolase 1* |
| ***Ucp1*** | *Uncoupling protein 1 (mitochondrial, proton carrier)* |
| ***Uroc1*** | *Urocanase domain containing 1* |
| ***Vat1l*** | *Vesicle amine transport protein 1 homolog-like (T. Californica)* |